

Photon-Pair Generation in Photonic Crystal Waveguides

Dissertation
zur Erlangung des akademischen Grades
doctor rerum naturalium (Dr. rer. nat.)

vorgelegt dem Rat der Physikalisch-Astronomischen Fakultät
der Friedrich-Schiller-Universität Jena

von Master of Science in Photonics Sina Saravi
geboren am 3. Mai 1988 in Amol, Iran

Gutachter:

1. Prof. Dr. Thomas Pertsch, Friedrich-Schiller-Universität Jena, Germany
2. Prof. Dr. Kurt Busch, Humboldt-Universität zu Berlin, Germany
3. Prof. Dr. Costantino De Angelis, Università degli Studi di Brescia, Italy

Tag der Disputation: 29. November 2018

Contents

1	Introduction, state of the art, and aim	1
1.1	Sources of quantum light	2
1.2	State of the art of integrated photon-pair sources	6
1.3	Aim and structure of the thesis and collaborations	12
2	Periodic waveguides for parametric three-wave mixing (TWM)	15
2.1	Fundamentals of waveguided three-wave mixing	16
2.2	Periodic waveguides: fundamentals and phase-matching	23
2.3	Standard photonic crystal slab waveguides (PCSWs)	32
2.4	A double-slot PCSW: an ideal structure for TWM	39
2.5	Summary of the results and related publications	46
3	Second-harmonic generation (SHG) in the presence of loss	47
3.1	Unconjugated reciprocity theorem for SHG in PCSWs	48
3.2	SHG experiment in a lithium niobate ridge waveguide	55
3.3	SHG in a PCSW: nonlinear simulation and analysis	59
3.4	Effect of loss on slow-light-enhanced SHG	63
3.5	Summary of the results and related publications	68
4	Spontaneous parametric down-conversion (SPDC)	69
4.1	SPDC theory for lossless and guided signal and idler modes	70
4.2	Controlling spectral entanglement: counterpropagating factorizable pair example	74
4.3	Controlling modal and path entanglement: path-entangled Bell state example	79
4.4	Summary of the results and related publications	83
5	Atom-mediated SPDC	84
5.1	Green's function method for SPDC	86
5.2	Atoms as detectors	88
5.3	Atom-mediated SPDC with evanescent modes	91
5.4	Summary of the results and related publications	96
6	Conclusion and outlook	97
	Deutschsprachige zusammenfassung	101

List of own contributions	103
Bibliography	105
Appendix A Details and methods of the simulations	126
Appendix B Intermediate calculations in the formulation of atom-mediated SPDC	135
Appendix C Green's function of an infinite periodic waveguide	139
Abbreviations and conventions	143
Acknowledgement	145
Ehrenwörtliche Erklärung	147

Chapter 1

Introduction, state of the art, and aim

Using the superposition and entanglement of quantum states, quantum information science [1] has offered a new paradigm for the creation of devices that in principle can surpass the performance and limits of conventional devices in computing [2, 3], communication [4, 5], and metrology [6, 7]. Many different platforms have been used for the implementation of quantum protocols, e.g. atoms [8, 9] and ions [10], superconducting circuits [11], photons [12, 13], spins of electrons [14] and nuclei [15], solid-state emitters [16, 17], and phonons in an optomechanical system [18]. Each platform has its own strengths that makes it suitable for specific applications, but it is becoming clearer that a fully functioning quantum system will be a hybrid one that combines different systems [19]. Among these different physical objects, photons are highly suitable carriers of quantum information, as they are resistant to dephasing caused by the noise of the environment. This allows photons to carry quantum information over long distances and enables photonic based technologies to operate at room temperature. Moreover, photons have a high information capacity due to the many degrees of freedom of a photon's quantum state, such as spectrum, polarization, and spatial profile, which can be used for superposition and entanglement [20]. These properties make photons a key enabler of quantum technologies [21, 12, 13], especially for the implementation of secure quantum optical networks that are close to commercialization [22]. In the realm of quantum simulators, heavy research is being done on the implementation of optical quantum simulators [12], and table-top setups are already capable of implementing quantum imaging schemes [23].

An important property of the optical quantum technology is its potential for integration, providing a path to miniaturization, practical large-scale implementation, and more cost efficiency that eventually leads to commercialization. The existing fabrication technology based on lithography, which has been perfected over the past decades for the fabrication of integrated electronic circuits with nanometer sized details, has been adapted over the past two decades for the fabrication of integrated optical circuits on different material platforms that can run quantum operations [21, 16, 12, 24, 25, 26, 27]. Components of a quantum optical circuit can in general be divided in four categories: sources of quantum light, elements to manipulate the state of light, memories to store the quantum state of photons, and single photon detectors, all of which need to be made efficient, miniaturized, and compatible to an integrated platform. Recent reviews exist on the development of all these components [27, 25, 26]. My interest in this thesis is in the integrated sources of quantum light.

1.1 Sources of quantum light

Controlled generation of single photons and entangled photon-pairs is of vital importance for implementation of most quantum protocols. Single photons are needed for optical quantum computers and simulators [28] and some quantum cryptography protocols [29]. Entangled photon-pairs lay at the heart of secure quantum communication protocols and are also needed for implementing quantum repeaters [30], which make long distance communication possible. Multiple entangled photon-pairs can also be used to construct multiphoton entangled states, with three or more photons entangled, through the process of entanglement swapping [31], and these states have applications in fundamental tests of quantum mechanics and quantum information processing [32].

An ideal source of quantum light should output pure quantum states of single or entangled photons on demand [21, 33, 24, 13, 26, 34]. Pure means the produced quantum state should be the same every time, as opposed to a mixed state where the source outputs different states probabilistically. Moreover, such a source should produce a defined number of photons. From a practical point of view, aside from being efficient and miniaturized, a source should also be reproducible, such that the structure with defined properties can be fabricated in a controlled way. An integrated platform, aside from allowing for scalability, also increases the chance for reproducibility, as the chances for random misalignments and environmental effects are minimized when all components are fixed together on a chip. The properties stated above will ensure the indistinguishability of photons produced from one or different sources, such that two photons can interfere at a beamsplitter and bunch into its output channels. This interference is the foundation of most quantum operations, e.g. for quantum gates in computers and simulators [28] or for quantum repeaters in communication [30]. Finally, since a photon can store information in different degrees of freedom, we want to have control over these degrees and their entanglements. This includes controlling properties like the central frequency, spectral bandwidth, polarization, and propagation direction of the photons, creating entanglement in one or more of these degrees simultaneously, or controlling the extent of entanglement from maximally entangled to fully unentangled in these degrees. Henceforth, a source should offer us versatility in its design, so that we can "tune" the source geometry before implementation to produce photons with our desired properties.

There are different physical implementation of sources of quantum light that can generate single and entangled photons in a controlled way [35, 33], but in general they can be divided in two main categories: Single-emitters and nonlinear sources. For both cases, having the source on an integrated platform capable of nanostructuring is of enormous advantage, as certain nanostructures allow us to manipulate the optical modes of the system, in turn enabling us to control the underlying light-matter interactions. This eventually allows us to engineer the output and bring it closer to our ideal. The focus of my work will be the nonlinear sources, for which I will explain this point in detail in this chapter, along with their state of the art of integrated implementation. For comparison, a very short overview of the single-emitter sources is given first.

Single-emitter sources: Single-emitter sources encompass objects such as atoms [36] or solid-state emitters [37], with the latter being suitable for integration. Single-emitters are mainly used as a source of single photons, but can also generate entangled photon-pairs [38]. In general, in these systems, an external source puts the emitter into an excited state and afterwards, through relaxation into a lower energy state, a single photon is emitted. The main advantage of these sources is their

capability in generation of highly pure states, which can also be done on demand [39]. Integration of solid-state emitters into nanostructured optical systems has seen enormous advancements in the last decade. Of specially high interest are vacancy centers in a diamond platform [17] and InGaAs quantum dots (QDs) in a GaAs platform [40]. Integrated structures such as photonic crystal slab waveguides (PCSWs) and photonic crystal (PC) cavities [41, 42, 16, 40], micro pillars [43], and nanobeam cavities [44] have been used to engineer the radiation dynamics of such sources, through the control they provide over the density of states (DOS) of the optical modes and their field profiles. Given the sensitivity of the electronic band structure of an emitter to local environmental fluctuations, solid-state emitters are commonly susceptible to inhomogeneous broadening [40, 37], which then requires the emitters to be individually tuned to make them identical [45]. Moreover, interaction with the phonons of the solid can affect the coherence of the emitter's state. Although, there are some solid-state emitters that can have a stable quantum operation at room temperature [37], cryogenic temperatures are often used to improve the indistinguishability of single-photons [46, 39], which in turn creates complexity in implementation.

1.1.1 Nonlinear sources of photon-pairs

The second category of quantum light sources are the nonlinear sources of photon-pairs, which are the main focus of this thesis. A nonlinear material can be pumped with a strong pump beam and through nonlinear interaction, mediated usually through the $\chi^{(2)}$ or $\chi^{(3)}$ nonlinearity, a pair of entangled photons can be generated, called signal and idler. In the process of spontaneous parametric down-conversion (SPDC) in a $\chi^{(2)}$ material, a pump photon "spontaneously" splits into a pair of lower frequency photons such that conservation of energy is satisfied through $\omega_p = \omega_i + \omega_s$, where ω_p , ω_i , and ω_s are the frequencies of the pump, idler, and signal fields, respectively [47]. In the process of spontaneous four-wave mixing (SFWM) in a $\chi^{(3)}$ material, two pump photons mix and split into a pair of signal and idler photons, where the frequencies of all photons are usually close to each other satisfying $2\omega_p = \omega_i + \omega_s$ [48]. Sources of photon-pairs have first been developed in non-integrated platforms and are still in use when integration is not needed, where bulk crystals are used for SPDC [49, 50, 51, 52] and often optical fibres are used for SFWM [48, 53, 54, 55]. In general, irrespective of the underlying process, a waveguide (WG) structure is a more efficient system than the bulk, as it can maintain a high electric field intensity of the pump in a single mode over a long interaction length due to the guiding mechanism [56], and the process gets even more efficient for WGs that can confine modes to a very small cross-section [57]. Integration, especially on a platform capable of nanostructuring, allows for the creation of such WGs with varying degrees of confinement, which not only results in highly efficient sources, but ones that are stable and well controlled [24, 26, 27, 25, 34]. Henceforth, the focus of this work is on integrated WG sources of photon-pairs, and from this point on the properties of sources are described assuming an underlying nonlinear WG platform.

For SPDC and SFWM to be efficient in a WG structure, the electric field profiles of the guided modes have to be matched. More importantly, the wave-vectors k of the modes involved should satisfy the phase-matching condition [58], which is $k_p = k_i + k_s$ for SPDC and $2k_p = k_i + k_s$ for SFWM, where for a WG structure k is a scalar. A fundamental characteristic of these processes is, that the properties of the generated photons and their entanglements in different degrees of freedom are in

principle widely tunable, through controlling a combination of the conservation of energy condition, the phase-matching condition, and the properties of the optical modes of the medium. In an integrated nonlinear WG source, the degrees of freedom can in general be categorized in the three categories of polarization/modal, spatial/path, and spectral [24, 26, 27, 34], which can be controlled as follows:

Polarization/modal: The modal and polarization degree of freedom (DOF) are often not separable in an integrated platform, and can be controlled through the phase-matching condition. If phase-matching is satisfied between an almost transverse electric (TE) mode at ω_S and an almost transverse magnetic (TM) mode at ω_I , a horizontally polarized signal and a vertically polarized idler photon are generated in a biphoton state of $|\psi\rangle = |H_S, V_I\rangle$. A maximally polarization-entangled state has the form $|\psi\rangle = |H_S, V_I\rangle \pm |V_S, H_I\rangle$ and is usually created through post-processing outside the source with birefringent wave-plates and beamsplitters [59, 60]. Integration allows us to avoid this outside post-processing. One way is integrating the post/middle-processing elements with the source on the same chip [61, 62]. Another way is to have a source that satisfies two phase-matching conditions at the same time [63, 64] or have two sources in series [65]. It is important to note, that "S" and "I", standing for signal and idler, are labels given to 2 output ports, into which the photons can be deterministically separated. For example, with a non-degenerate pair, where signal and idler have non-overlapping spectra, we can separate them using a dichroic beamsplitter, then call one output signal and the other idler. Then having $|\psi\rangle = |H_S, V_I\rangle + |V_S, H_I\rangle$ means, a measurement of the photon in the "S" channel has a 50/50 chance of resulting in either an "H" or a "V" polarization, while doing so fixes the polarization of the photon in the "I" channel to the opposite.

Spatial/path: In an unstructured bulk source, the spatial DOF refers to where the photons can be detected in the continuous propagation plane [49]. In an integrated WG platform, the spatial/path DOF usually refers to which WG and/or which propagation direction a photon is detected in, which is a discrete variable. Path-entanglement [66] is uniquely suited for qubit encoding in integrated optical platforms. It can be easily created and manipulated [67, 68] using coupled waveguides, which are the beamsplitters of an integrated platform, allowing the implementation of complex quantum algorithms [69]. Path-entanglement can also be directly created [70] and manipulated [71] during the pair generation process when coupled waveguide arrays are used as the source, where the WG sources in the array can couple to each other during the pair generation and create complex path-entanglement patterns through the process of a quantum walk [72].

Spectral: As opposed to a classical process like sum-frequency generation (SFG), where the frequency of the input beams add up to fix the frequency of the generated beam, in a spontaneous quantum process, e.g SPDC, one pump photon can split into any combination of the signal and idler frequencies, as long as it satisfies the conservation of energy and the phase-matching condition. There is always a continuous range of ω_S and ω_I that can satisfy these conditions, and the resulting probability amplitude per frequency units of a pair being generated at ω_S and ω_I is expressed by the joint spectral amplitude (JSA) function $JSA(\omega_S, \omega_I)$. The photon-pair state then has the form $|\psi\rangle = \iint d\omega_S d\omega_I JSA(\omega_S, \omega_I) |S, \omega_S\rangle |I, \omega_I\rangle$. The JSA represents the entanglement in the spectral DOF and can be controlled through the group velocities of the modes involved [73, 74, 50].

The above discussion outlines a fundamental advantage of nonlinear sources over the single-emitter sources. Tuning the output of a single-emitter not only requires engineering the optical prop-

erties of the emitter's surrounding, but also needs a control over the electronic band structure of the emitter. With a nonlinear source, it is only the optical modes of the system that determine the properties of the generated photons. Hence, tuning the output of nonlinear sources is less complicated and more versatile compared to the single-emitter sources. Aside from tunability, a main practical advantage of nonlinear sources is their room temperature operation, making their implementation less complicated than many single-emitter sources. Moreover, the mature existing fabrication technology for integrated circuits makes nonlinear sources highly reproducible.

A main disadvantage of nonlinear sources of photon-pairs is, that they do not produce photons on demand, but do it probabilistically, due to the nature of the process. In general, the output of a nonlinear source includes multiple pairs that are created simultaneously [75, 76, 77]. Multiple entangled pairs, although highly desirable when we can have them isolated and in a controlled manner [32], are not desired for cases where only a single pair is expected. To lower the ratio of multiple- to single-pair generation probability, the total generation probability per pump pulse must be lowered to values much smaller than one [75, 76, 77], making the generation process probabilistic. This is the condition at which photon-pair sources are commonly operated at. With a continuous wave (CW) pump beam, it is the generation time of the photon-pair that becomes completely uncertain. Such a source is not on demand, as we do not have any knowledge about when a pair is generated or control over if a pair is to be generated or not. However, since photons are produced in a pair, detection of one photon "heralds" the existence of the other one. This allows us to have heralded single-photon sources [78, 79], in which we know about the existence of a single-photon output whenever we detect its paired photon. It has been shown that even entangled pairs can be heralded at the output of a source, by post-selecting the multiple-pairs that can be generated in the parametric process [80, 81].

However, a heralded single-photon source does not always produce pure single-photon outputs. As explained, the signal and idler photons are in general entangled in the spectral DOF, which means the detection of one photon affects the spectrum of the other one. This makes the output a spectrally mixed state, instead of the desired pure state. This can be avoided by placing narrowband filters at the output of the source, to force the same spectrum for the output photons [68, 82], however, this method severely reduces the brightness of the source and puts fundamental limits on the heralding efficiency [83]. A better solution is to engineer the source to produce spectrally unentangled or factorizable pairs with $JSA(\omega_S, \omega_I) = u(\omega_S)v(\omega_I)$, where upon detection of one photon the other photon always ends up in the same spectral state. This could be done through a proper choice of the group velocities of the modes [73, 74, 50], which requires the source of interest to offer a substantial control over the group velocities of the modes at the point of phase-matching.

Although heralding gives us knowledge of when a pair is produced, it does not give us control over having the pair when wanted. To have photons on demand, multiplexing schemes can be used [84, 85]. We can either use spatial multiplexing [84] with multiple sources, detectors, and switches [86, 87], or time multiplexing [85] with only one source and many delay lines and switches [88], or a combination of the two schemes [51]. This solution however, requires many extra components to supply a truly on-demand output. To reduce the final footprint, photon-pair sources must be miniaturized, while at the same time fast and efficient switches along with low loss and controllable delay lines should be developed for an integrated platform. Finally, although the probability of multiple-pair generation

can be lowered, it is still a finite number that affects the quality of the output state [89]. This could in theory be overcome using a combination of multiplexed sources and photon-number-resolving detectors [90, 91], to result in a near-ideal deterministic source of single photons [89], which again is a solution that needs more components and a larger footprint.

In the last two decades, there has been intense research towards implementing integrated sources of photon-pairs, which resulted in highly efficient probabilistic sources, with a wide range of wavelengths and degrees of entanglement [24, 26, 27, 25, 34]. Today even commercialized probabilistic sources are available [92]. Although the progress is considerable, there is not yet a fully integrated ideal source of quantum light that can generate photons with a high probability, while offering full control over their properties, which as explained should in principle be possible using nonlinear sources. There are recent works on creating integrated on-demand sources using multiplexing [86, 87, 88], but these sources are not yet well-developed due to the complexity of integration of many sources and components on the same chip. At the moment, most of the components for multiplexing are used off-chip. The problem could be mainly categorized as a technical one. Fabrication technologies have yet to advance to be able to create large scale optical circuits with low fabrication disorder to minimize photon losses, and to have the capability to integrate high speed and efficient electronic switches, low loss and controllable delay lines, and photon-number-resolving detectors, along with photon-pair sources of defined properties all on the same chip.

This problem however, can be tackled through a fundamental approach, by choosing more sophisticated optical structures to implement the source with. The improved state of knowledge about the dynamics of light-matter interaction and optical modes in nanostructured elements, along with the improved fabrication technologies, has allowed the design and implementation of complicated nanostructures. Sources made from nanostructured elements can be more efficient and miniaturized, and provide more control over the photon-pair state with fewer pre- or post-processing components needed. With the fabrication technologies advancing and the design of nanostructures getting more sophisticated in a way to reduce the fabrication burden, the two trends will eventually meet in the middle to allow for the implementation of an ideal source of quantum light.

The objective of this thesis is to help the trend in finding sophisticated optical structures as sources. From the previous discussions it is clear that such a structure should be able to strongly control the guided modes, including their wave-vector and group velocity, allowing us to fully shape the properties of the photon-pair state, with as few pre- or post-processing elements as possible. At the same time, it must also be efficient, miniaturized, and compatible with a fully integrated platform. In the next section, I go over the state of the art of implementation of photon-pair sources using different types of integrated structures, with a focus on nonlinear WGs. After comparing them, I identify which type of nonlinear WG can offer the most in controlling the pair generation, which happens to be the least investigated type for this application. This thesis aims to change that.

1.2 State of the art of integrated photon-pair sources

Aside from large-scale and affordable implementation, integration also provides versatility on the design and fabrication of structures. For integrated nonlinear WGs, this provides control over the guided

modes and the phase-matching condition, making WGs especially useful in creating and engineering entanglement in the previously described degrees of freedom [93]. They even allow for creating two or more degrees of entanglement [94] to reach hyper-entanglement [95], which is a valuable resource for quantum communication protocols. In this section, I go over the state of the art of integrated nonlinear WG sources of photon-pairs, categorizing and comparing them based on the WG types. A short overview is also given on integrated nonlinear resonators, which could be thought of as a special category of WGs, for completeness. Given that the operation principle of photon-pair sources are highly dependent on whether they are based on SPDC or SFWM, I first start with a more detailed explanation of the differences between the two spontaneous processes.

SPDC vs. SFWM: SPDC sources can be implemented in non-centrosymmetric crystals, as they possess $\chi^{(2)}$ nonlinearity. Examples of materials with a strong $\chi^{(2)}$ nonlinearity, with which SPDC sources are implemented, are beta-barium borate (BBO) [49], lithium niobate (LN) [96, 65, 82, 59, 67, 87, 70, 71, 51], potassium dihydrogen phosphate (KDP) [50], potassium titanyl phosphate (KTP) [97, 98, 52], and aluminium gallium arsenide/gallium arsenide (AlGaAs/GaAs) [99]. SFWM sources can be implemented in theory in all materials, as $\chi^{(3)}$ nonlinearity is universally available. Examples of materials with a strong $\chi^{(3)}$ nonlinearity, with which SFWM sources are implemented, are silicon [25], silica [54], chalcogenide [100], and silicon nitride [101].

The phase-matching condition is usually easier to satisfy in SFWM, as the frequencies of the modes are close to each other, and hence their wave-vectors are close. In SPDC, the pump has a frequency much different than the signal and idler, and since the material usually has a different refractive index at each frequency, the phase-matching condition is not naturally satisfied. One way of overcoming this is through birefringent phase-matching [58] in anisotropic crystals, such as LN, where modes of different polarization see different refractive indices, which sometimes can counteract the effect of material dispersion and satisfy the phase-matching condition between modes of different polarization. This method however, is limited to crystals with birefringence, certain wavelength ranges, and certain polarization combinations. A more versatile method of phase-matching is called quasi-phase-matching (QPM) [102], where the $\chi^{(2)}$ of the material is periodically modulated along the propagation direction. In LN for example, this can be done by inverting the crystal's domain through applying strong electric fields, called periodic poling, resulting in a $\chi^{(2)}$ that periodically varies between positive and negative values. This in turn creates an extra momentum to compensate the momentum mismatch such that $k_p = k_I + k_S + \frac{2\pi m}{\Lambda}$, where Λ is the poling period and m could be any integer number, although the efficiency of the nonlinear process becomes much lower for higher values of m . Although QPM is more versatile than the birefringent method, it is still limited to materials that allow for modulating the $\chi^{(2)}$ coefficient. The most versatile method with respect to the choice of material, wavelength, and polarization is modal phase-matching. This method relies on using WG structures with strongly dispersive modes, such that the dispersion of the modes can dominate the dispersion of the material and the modal wave-vectors can satisfy the phase-matching condition.

A technical inconvenience with both SPDC and SFWM is the need for filtering the strong pump beam at the output, so it does not interfere with the single-photon detection. This can be done using spectral filters off the chip for both SPDC [70] and SFWM [68], and it is considerably more challenging to do it all on the chip [103, 67]. Pump filtering is fundamentally harder for SFWM, as the

frequencies are close to each other, and hence rejecting the pump beam while transmitting the signal and idler photons with spectral filters will be more challenging compared to SPDC.

When the choice is available between the two processes, SPDC is usually the preferred process due to efficiency, since $\chi^{(2)}$ interactions are overall much stronger than $\chi^{(3)}$ ones. Moreover, SFWM sources often suffer from noise caused by spontaneous Raman scattering [100, 55, 101, 25]. There are also some material dependent sources of noise, for example silicon suffers from two-photon-absorption which would result in the absorption of the generated single photons [25]. Henceforth, SPDC is the more efficient and reliable process for pair generation, and will be the process of choice for the investigations in this thesis. In the review of the state of the art, I go through both SPDC and SFWM sources, especially because the state of the art in integrated sources has been mostly implemented with SFWM in silicon due to its more mature fabrication technology.

1.2.1 Different types of integrated waveguide photon-pair sources

There are many different implementations of integrated WG sources [24, 25, 26, 27, 34]. Based on the type of WGs, they can in general be divided in three main categories.

Low-contrast WGs: The first category is low-contrast WGs, that have a small refractive index contrast of $\Delta n \approx 10^{-4} - 10^{-2}$ between the core of the WG and its surrounding, shown schematically in Fig. 1.1(a). The small change of refractive index is created either through diffusion of different material elements into the substrate [24] or through interaction with strong laser pulses [104]. These WGs have the lowest propagation losses among the presented categories. They also have mode profiles of several microns in size, which is the largest in the presented categories. This allows for efficient in and out coupling to modes of a fiber, which is an advantage for connecting such sources to fiber optical communication lines. However, due to the low core/surrounding permittivity contrast, these WGs do not offer much control over the properties of the guided modes, such as their wave-vector or group velocity, and the dispersion properties of guided modes are often dominated by that of the material. Hence, QPM is often used to phase-match SPDC processes, although birefringent phase-matching is also an option [105]. The most implemented and most reliable of waveguided photon-pair sources are implemented using indiffusion or proton/ion exchanged WGs in periodically poled LN [96, 59] and periodically poled KTP [97, 98] based on SPDC [24]. Given that KTP and LN are ferroelectric materials, periodic poling can be implemented in them, so the phase-matching condition over a wide range of frequencies can be satisfied in these WGs [102]. There are also laser-written WG sources in silica based on SFWM [106], which are easy to fabricate on large scale [104]. All these low-contrast WG sources are usually several centimeters long. Low-contrast WGs have been highly successful in creating path-entangled states through the use of coupled WG arrays and WG couplers [69, 67, 70, 71]. Multiplexing has also been done using them [87], although different integrated elements on separate chips are used to implement the whole multiplexing scheme. They have also been widely used to create polarization-entangled states, but mostly through post-processing using beamsplitters and wave-plates outside the source [59, 60]. Simultaneous phase-matching of two processes to directly generate polarization-entangled pairs has also been reached, using two sources on one chip in series, each having a different poling period [65]. It has also been proposed [63] and implemented [107] that by using a bi-periodic poling pattern, two phase-matching conditions at the same time can be satisfied

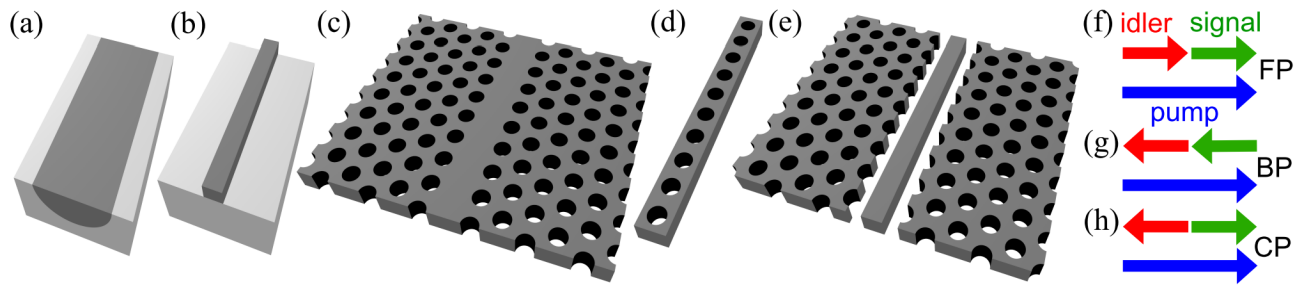


Figure 1.1: (a-e) Schematics of different types of integrated waveguides (WGs). (a) A low-contrast WG, where a small increase of refractive index (the darker region) is created in the substrate for waveguiding; (b) A high-contrast or ridge WG on a lower refractive index substrate; (c) A standard W1 photonic crystal slab waveguide (PCSW); (d) A periodic nanobeam; (e) A double-slot PCSW; (f-h) Schematics of three phase-matching configurations based on the directions of propagation of the signal and idler photons: (f) In the forward-propagating (FP) case, both generated photons propagate in the same direction as the pump; (g) In the backward-propagating (BP) case, both generated photons propagate opposite to the pump; (h) In the counterpropagating (CP) case, signal and idler photons propagate in the opposite direction with respect to each other.

in one WG. Spectrally factorizable pairs have also been generated in low-contrast WGs [97, 98, 106]. However, as the group velocities cannot be controlled strongly, generation of factorizable pairs is limited to certain wavelength ranges that are dictated by the material of choice. A way to overcome this limitation is using the counterpropagating (CP) phase-matching, in which signal and idler photons exit from different ends of the WG, as shown schematically in Fig. 1.1(h). The fact that the group velocity of one of the modes has a negative value in the CP configuration, allows for the factorizability condition to be satisfied easily in a wide range of nonlinear materials and wavelengths, even for low-contrast WGs [108]. However, due to the large phase-mismatch $\Delta k = k_p - k_s - k_i$, satisfying a CP condition is not an easy task, needing either submicron poling periods, which are technologically challenging to implement [102], or to use higher-order poling terms, which result in much lower efficiencies [109]. The commonly used poling periods in LN and KTP WG sources range from several microns to some hundred microns, all to satisfy the forward-propagating (FP) phase-matching condition, schematically shown in Fig. 1.1(f). CP phase-matching can also be satisfied using broad free-space pump beams from above the sample [110, 111, 112, 113, 114], which its use for generation of factorizable pairs has been proposed [115] and implemented [116]. This method, however, is fundamentally non-compatible to a fully integrated platform. Another method only applicable to SFWM uses two CP pump beams from the two ends of the structure [117].

High-contrast WGs: The second category is high-contrast WGs that have a large contrast of Δn in the order of 1 between the core and the surrounding, shown schematically in Fig. 1.1(b), created by physically removing most or all of the surrounding material. These WGs are sometimes called ridge WGs, which is what is used here to refer to them. The loss caused by fabrication disorder in ridge WGs is larger than the low-contrast ones due to the nanostructuring. Ridge WGs can have submicron sized cross-sections, which then allow for enhanced efficiency of the pair generation process [57]. However, submicron cross-sections make coupling from them to fibers more challenging compared to low-contrast WGs. There is active research going on to improve this coupling efficiency through the design of proper couplers [118, 119]. Most importantly, ridge WGs allow for a stronger control over the dispersion properties of modes, which eventually allows for reaching modal phase-matching [120], lifting the need for periodic poling. Ridge WGs are mainly implemented in silicon [121, 61, 62, 68, 122, 88] and AlGaAs/GaAs [99, 64, 123, 114, 124] material platforms. In the Al-

GaAs/GaAs platform, Bragg reflection ridge WGs are created with multilayer Bragg reflectors on top and bottom of the WG, which offer even more freedom in engineering the guided modes. There are also ridge WG implementations for pair generation in silicon nitride [101] and chalcogenide [100]. Enhanced efficiency allows for ridge WG sources to be shorter than low-contrast ones, with lengths usually in the millimeter range. Path-entangled pairs have been created using ridge WG sources and couplers on the same chip [68]. Multiplexing schemes have been implemented using ridge WG sources [88], but most of the processing for the multiplexing is done off-chip. On a nanostructured platform, middle- and post-processing elements are fabricated on the same chip with the ridge WG sources to create polarization-entangled pairs [61, 62, 122]. Through controlling the dispersion relation of guided modes, modal phase-matching of two processes can be satisfied simultaneously in one source, allowing for direct generation of polarization-entangled states [64, 124] without the need for post-processing or complicated poling patterns. CP phase-matching has also been implemented in Bragg reflection ridge WGs to directly generate polarization-entangled pairs [114], where for satisfying two CP phase-matching conditions simultaneously, the WG is pumped from above using two spatially broad free-space beams of different incident angles. Although high-contrast WGs offer more control over the dispersion properties of guided modes compared to low-contrast WGs, modally phase-matching a CP process is still out of reach for them, except by using non-integrated pumping methods. Finally, it has been proposed theoretically, that by using ridge WGs the limitation of low-contrast WGs in reaching factorizability could be overcome to some extent [125, 126], as their modal dispersion can dominate the material one, and hence can better control the group velocity of modes and allow for reaching factorizability at the needed wavelength regardless of the material platform used. However, in these proposals, QPM is still used to phase-match the process, as the ridge WGs were not able to reach modal phase-matching at the same time as factorizability.

Periodic WGs: The third category of integrated WGs are periodic WGs, shown schematically in Figs. 1.1(c) and (d). Fig. 1.1(c) shows a standard W1 photonic crystal slab waveguide (PCSW) suspended in air. It is constituted of a dielectric slab with subwavelength thickness, with a set of holes etched in the slab in a periodic pattern, and then a line defect is created in the pattern by removing one row of holes, hence the name W1. It supports guided Bloch modes [127] confined in the sub-micron-sized line defect. Fig. 1.1(d) shows a simpler periodic WG, known as nanobeam, constituted of a ridge WG with a periodic line of holes in it, which also supports guided Bloch modes. Bloch-modes can have dramatically different dispersion relations compared to that of a bulk material and low-contrast or ridge WGs. Especially in PCSWs, the dispersion relation and group velocity can be engineered, through fine changes in the structure surrounding the line defect [128]. Slow-light modes [129, 130] can then be created and engineered, where propagating modes have a lower group velocity compared to that of modes in a standard WG. The lower group velocity enhances the intensity of light for a constant input optical power and also enhances the nonlinear phase sensitivity of a mode [131]. These in turn enhance the efficiency of nonlinear parametric processes [132], including second-harmonic generation (SHG) [133, 134, 135], third-harmonic generation (THG) [136, 137, 138], four-wave mixing [139, 140], self-phase modulation [141, 142], and electro-optic effect for switching [143]. This makes slow-light PCSWs particularly interesting for integrated platforms, as through enhancing the efficiency it can result in smaller light sources and switches. Another unique property

of Bloch modes is their capability of supporting Umklapp nonlinear processes [144], in which large phase-mismatches can be compensated by the extra momentum introduced by the periodic lattice. This means that backward-propagating (BP) and CP phase-matching conditions, shown schematically in Figs. 1.1(g) and (h) respectively, could in principle be satisfied without the need for periodic poling or non-integrated pumping, through modal phase-matching of Bloch modes. An example is the design of a 2D PC slab, modally phase-matched for a BP SHG process [145].

All these capabilities suggest that PCSWs could be the ultimate structures in controlling the light-matter interaction as a photon-pair source and provide the strongest handle over the biphoton state. However, there have been limited works done towards utilizing them and in general periodic WGs towards this goal. The only implementation of photon-pair sources using PCSWs has been for SFWM, using mainly silicon [146, 86, 147] and less frequently using gallium indium phosphide [148]. In these works, PCSWs were used to enhance the efficiency of the pair generation process using slow-light and consequently miniaturize the sources down to a hundred microns long. This makes PCSWs the most miniaturized WG sources, which has motivated their use in spatial multiplexing schemes [86]. I believe however, that PCSWs are capable of much more than just enhancing the efficiency, especially in controlling the properties of the generated pairs through dispersion engineering the bands and accessing different propagation directions by satisfying CP and BP phase-matching conditions. There were proposals using 1D Bragg structures to facilitate phase-matching for pair generation, in which the change in the dispersion of the Bloch modes is used to overcome the phase-matching limitations in isotropic material systems that do not have birefringence [149, 150]. This however, has been done to only reach a FP phase-matching, not using the full potential of Umklapp processes. There is also a proposal for reaching factorizability in a 1D periodic stack [151], which uses the dispersion relation of Bloch modes to reach group-velocity matching, a condition needed for factorizability, but there has not yet been any proposals toward implementing this effect in a practical integrated structure such as a PCSW. The aim of this thesis is to investigate and hopefully to unleash the full potential of PCSWs as sources of photon-pairs. I discuss this aim in more details in the next section.

It should also be mentioned that PCSWs are more complicated than ridge WGs regarding loss and in/out-coupling. Coupling to PCSWs is harder than ridge WGs, as in addition to the fact that modes are confined to subwavelength sizes, they also have more complicated mode profiles with worse overlap with a focused beam or a fiber output. Coupling gets even harder for slow-light modes, and work has been done to design efficient couplers for PCSWs to overcome these difficulties [152, 153, 154, 155]. On the side of loss, the scattering loss from fabrication disorder has a much stronger effect on slow modes [156, 157], as the low group velocity of modes enhances their interaction with the disorder. This loss enhancement should be taken into account in the analysis and application of slow-light PCSWs, as I will do in this work.

Integrated cavities: For completeness, a short review of integrated nonlinear resonators and cavities as sources of photon-pairs is presented. In an integrated platform, resonators and cavities could be made from WG structures, either by placing mirrors at the end-facets of the WG to create a cavity or by bending the WG and connecting its end-facets together to create a ring resonator. Examples of such integrated resonators used for pair generation are PC cavities [158, 159], ring resonators from ridge WGs [160, 161], and disk resonators with whispering-gallery modes [162,

163]. Another example is in low-contrast WGs, where mirrors are placed at the end-facets by coating multilayered Bragg reflectors creating a resonator for pair generation [164]. In all these structures, the continuous guided mode dispersion relation turns into discretized resonances, and these resonance modes enhance nonlinear efficiencies even further and allow the generation of pairs with extremely narrow spectra [165]. Narrow spectrum is specially of importance for interfacing photon-pair sources with atomic-based systems like quantum memories [166] that have bandwidths in the order of MHz. Narrow spectra also provide the potential for reaching discrete frequency entanglement [167, 168].

1.3 Aim and structure of the thesis and collaborations

The aim of this thesis is investigating SPDC sources of photon-pairs on a PCSW platform. As discussed, PCSWs are the ultimate integrated structures for the control of light-matter interaction on the subwavelength scale [169, 127], and SPDC is the more preferable process for pair generation. Henceforth, one could imagine that PCSWs made from $\chi^{(2)}$ materials could be highly efficient sources of photon-pairs, with a strong control over the output quantum state and its different degrees of entanglement. Another advantage of implementing a source on a $\chi^{(2)}$ platform, is that it includes the electro-optic effect, which allows for the integration of fast switches. Such switches will be more miniaturized if they are implemented using slow-light PCSWs [143]. Moreover, due to the slow-light phenomena, coupled PC cavities could allow for the implementation of small and tunable delay lines [170]. Integrating the switches and the delay lines on the same chip with the source is a vital step towards the implementation of multiplexing schemes, and more generally for reconfigurable quantum optical circuits [171, 67]. Considering the benefits of an SPDC source of photon-pairs implemented using PCSWs, it is surprising that very little research has been done on this topic. The few works done on photon-pair sources in PCSWs were based on SFWM, which I attribute to the fact that reaching phase-matching is more straightforward in SFWM, plus the fact that there also exists a mature silicon nanofabrication technology that allowed the fabrication of PCSWs. However, such a technology also exists for materials with $\chi^{(2)}$ nonlinearity capable of SPDC, like GaAs/AlGaAs, where although its nanofabrication technology is not as mature and commercialized as it is for silicon, it is arguably as accurate when it comes to fabricating PCSWs. Hence, the fact that SPDC sources have not yet been implemented using PCSWs is not due to the technological challenges, but as explained throughout this thesis, was partly due to the complexity of finding a practical phase-matched design and partly due to the complexity of the theoretical analysis. The aim of this thesis is to overcome these challenges and fill the gaps in knowledge for design and analysis of PCSWs as SPDC sources of photon-pairs, as well as to investigate their potential for controlling the properties of the biphoton state, especially for creating and controlling the extent of entanglement in different degrees of freedom.

As for any investigation, a specific material has to be chosen for practical designs. The material of choice for this work will be lithium niobate (LN). LN has many favourable optical, acoustic, and mechanical properties [172], making it a widely used material in telecom technologies and photonic applications [173, 174]. Its strong $\chi^{(2)}$ nonlinearity, wide transparency window, and the possibility for periodic poling, make LN a very efficient material for three-wave mixing (TWM) [175]. Most reliable SPDC sources are made on a LN platform with low-contrast WGs [96]. With high electro-optic

coefficients, LN is the leading material in telecom light modulators and switches [174]. These desirable properties have made LN one of the main platforms of interest in implementation of integrated quantum optical circuits, mostly focused on the use of low-contrast WGs [27]. A nanostructured LN circuit would make an even better platform, combining the desirable properties of LN with the subwavelength confinement and strong control offered by nanostructured elements such as PCSWs.

The realization of such a platform was delayed because of the less developed nanostructuring technology for LN compared to materials like silicon or GaAs. One of the first realizations of a PC pattern on LN was done using focused ion beam milling [176], although the holes were drilled in a bulk LN and there was no slab realized to confine the light in the vertical direction. A major progress has been the realization of submicron-thick LN slabs suspended in air or placed on a lower refractive index substrate. The suspended slab in air has been achieved at our institute [177, 178, 179] through ion beam enhanced etching. A different method is based on ion-slicing a submicron-thick layer of LN and then bonding it onto a lower refractive index substrate [180, 181, 182, 183]. Having submicron slabs allowed the fabrication of functional LN nanostructures in our institute. PCSWs and cavities have been fabricated with this method and tested to demonstrate their linear properties [184, 185] and LN PC cavities have been successfully tested for SHG [186]. In the past few years, the commercial availability of LN on insulator (LNOI) wafers, with the commercial name NANOLN [187], where a submicron-thick layer of LN is bonded to a micron-thick layer of SiO₂ again bonded to a LN substrate, has made the fabrication of LN devices more straightforward and the research on it more widespread [188]. This has resulted in major advances in the implementation of LN nanostructures, including microdisk resonators for SHG and SPDC [189], nanobeam cavities [190], waveguide and microring resonators for electro-optic switches [191], and periodically grooved waveguides [192].

Our institute's capability in nanostructuring LN was also a motivation for its choice for this thesis. Considering the speed of progress in fabrication of LN nanostructures, fabricating PCSWs with the required precision for SPDC applications is not out of reach. Aside from the main part of my thesis, that was centered around theoretical and numerical investigation of such structures, which is the first step in a potential implementation, I also participated in our group's efforts in the development of the nanostructured LN platform for nonlinear optical applications. A major advancement towards this goal, was the experimental demonstration of modally phase-matched SHG in LN ridge WGs [S1], for which I have done its design, analysis, and characterization. This work will be presented in this thesis, as the design and analysis of the experimental results tie closely to the main topic of the thesis.

Structure of this thesis: In chapter 2, the design of modally phase-matched TWM processes in LN PCSWs is investigated, as having practical designs is a vital starting step in investigating the topic. First, I lay the fundamentals needed for understanding TWM in periodic WGs. I then investigate the Bloch modes of a PCSW at the signal/idler and pump frequencies. In PCSWs, there will be complications regarding the pump mode, as it is inherently leaky, which in my opinion was the main reason that hindered investigation of PCSWs for SPDC so far. I will address this issue, and propose the use of a novel type of PCSW called a double-slot PCSW, shown schematically in Fig. 1.1(e), as an ideal structure for SPDC that can reduce this complication with the pump mode. Using the double-slot structure, I present practical designs in LN for reaching and tuning modally phase-matched forward-, backward-, and counterpropagating configurations. I also propose a scheme, along with a practical

design, for satisfying multiple phase-matching conditions simultaneously in a single PCSW.

In chapter 3, I study SHG, which could be thought of as the inverse process to degenerate SPDC. According to the quantum-classical correspondence principle [193, 194, 195, 196], the quantum process and its classical counterpart share many characteristics, and studying one gives much information about the other. Given that doing theoretical and numerical analysis for a classical process is much less complicated than a quantum one, I start by studying the classical process. I develop a theoretical framework for describing SHG in PCSWs, one that is capable of including decaying modes, as the pump is a leaky mode. I use this theory to analyze the experimental results of the LN ridge WG experiment, which is affected by a non-negligible amount of fabrication disorder loss. I then perform direct numerical SHG simulations on one of my PCSW designs and compare the results with the theoretical analysis, to check the validity of my designs and theoretical analysis. At the end, I perform a general study of the effect of loss on SHG interactions involving slow modes, which will be more affected by any type of loss mechanism. These investigations provide the needed insight into TWM processes in PCSWs, on which there has not been much studies done previously.

In chapter 4, I study SPDC in PCSWs. I first develop a formalism for describing the generated biphoton state in a periodic WG, especially such that it can include multiple phase-matching processes of different directions of propagation for the generated signal and idler photons. At this point of the thesis, it would have already been shown that PCSWs are capable of satisfying multiple phase-matching conditions simultaneously, with modes of different propagation direction, while allowing for controlling the group velocities of the modes. Here, I will show how these capabilities translate into controlling various degrees of entanglement of path, mode, and spectrum for the generated photon-pairs in a direct and fully integrated way without the need for any pre- or post-processing steps. I accompany these explanations with two specific examples in a LN double-slot PCSW: First one uses a CP configuration to reach a factorizable photon-pair state, unentangled in the spectral DOF. The other one uses a simultaneous phase-matching configuration to reach a maximally path-entangled photon-pair state, also known as a Bell state. These results fulfill the goal of this thesis in taking the first steps towards establishing PCSWs as highly capable and unique SPDC sources of photon-pairs.

In chapter 5, I introduce the concept of atom-mediated SPDC, which goes beyond the main topic of investigation in this thesis for pair generation, and has emerged from the theoretical investigations in treating SPDC with decaying modes. From the previous discussions, it is evident that single-emitter and nonlinear sources have rather complementary advantages and disadvantages to each other. Hence, it could be imagined that by combining the two systems into a hybrid source, one could benefit from both their advantages. I have found that using PCSWs, one can directly interface a single-emitter source with a SPDC source of photon-pairs, and create new dynamics in the photon generation process. Atom-mediated SPDC could potentially open a path towards realizing truly ideal sources of quantum light, as it combines the fermionic nature of a single-emitter with the bosonic nature of a SPDC source. At the moment, this new topic is at its infancy.

Collaborations that contributed to this thesis: The LN ridge WGs used in this work have been fabricated by Dr. Reinhard Geiss from our group in Jena. The idea of studying evanescent modes for SPDC has been proposed to me by Prof. Andrey A. Sukhorukov of Australian National University, Australia. This study has eventually resulted in the discovery of the atom-mediated SPDC scheme.

Chapter 2

Periodic waveguides for parametric three-wave mixing (TWM)

The first step of the investigation in this thesis is to establish, that there exists the possibility of modally phase-matching a TWM process in a LN PCSW through a practically realizable structure, where the frequency of the pump is about twice that of the signal and idler. In this chapter, all the results regarding the design of phase-matched LN PCSWs along with the foundations needed for understanding the design process are presented. The analysis of the nonlinear interactions in PCSWs is left to the next chapters and the focus here is put on studying the Bloch modes of the system, including their profile, band diagram, and phase-matching capabilities. Most of the developed designs are specifically aimed at a frequency-degenerate SPDC process, with signal and idler photons of equal central frequencies. A few of the designs are aimed at a non-degenerate SPDC process. The classical counterpart of the degenerate and non-degenerate processes are SHG and SFG, respectively. The quantum process and its classical counterpart share the same phase-matching condition and similar matching conditions between the field profiles of the modes. The matching condition between the field profiles is embedded in a quantity that is usually referred to as the overlap integral. Given that the classical process is simpler to formulate and also interpret, it is used in this chapter to present an introductory theory for understanding TWM processes. From this theory, the form of the modal phase-matching condition and the overlap integral will emerge, which will guide our hand in the design process in this chapter. Given that all the structures presented in this chapter are modally phase-matched, from this point on, the "modal" part is dropped when referring to them. There is also a terminology used in this chapter for referring to the modes, that should be mentioned here. When the signal and idler modes are the same and have equal frequencies in a phase-matched structure, they are referred to as the fundamental-harmonic (FH) mode, and the pump mode is referred to as the second-harmonic (SH) mode, similar to the terminology for an SHG process. When that is not the case, the signal, idler, and pump terminology is used.

This chapter starts by presenting a theoretical formulation for describing SHG in lossless and non-periodic WGs, along with some general considerations related to the use of LN as the nonlinear material for TWM interactions, accompanied with an actual design of a phase-matched LN ridge WG. Presenting the WG structure serves as an introduction into understanding the simplest type of design processes, but is also used in the SHG experiment presented in the next chapter. Afterwards,

fundamentals of periodic WGs, including Bloch modes, their band diagrams and symmetries, and how phase-matching can be reached using Bloch modes are explained. These explanations are accompanied with a specific design for reaching FP and BP phase-matching in a LN nanobeam. The nanobeam is used to explain the basics of phase-matching in periodic WGs, as it is a simpler structure with a simpler design approach compared to a PCSW. The nanobeam structure is also used in the next chapter, as a host structure for studying the effect of loss on TWM interactions in periodic WGs. After these fundamentals, we move on to the process of designing phase-matched PCSWs. Formation and engineering of guided modes at the FH frequency are studied for a standard W1 PCSW. Then, modes at the SH frequency are studied, which are leaky due to coupling to the radiative plane-waves of the surrounding, leading to power loss. With the modes understood, a FP phase-matched design and how it can be tuned is presented for a W1 PCSW. This design will be used in the next chapter for the comparison of nonlinear simulations and the analytical formalism. After understanding the limitations of a standard W1 PCSW, the use of a double-slot PCSW is proposed as an ideal structure for TWM, and its guided and leaky modes are studied. Designs for reaching FP, BP, CP, and simultaneous phase-matching in this structure are presented, which will be the center of the proposed SPDC applications in chapter 4 for generating factorizable and path-entangled photon-pair states.

2.1 Fundamentals of waveguided three-wave mixing

In this section, the fundamentals needed for understanding a TWM process will be presented, considering the simple case of a lossless non-periodic WG. First, a theoretical formulation is presented to describe SHG, using the conjugated reciprocity theorem. Afterwards, the relevant material parameters for the use of LN as the nonlinear material are given. Finally, a phase-matched LN ridge WG is presented, to get an understanding of the design process.

2.1.1 Conjugated reciprocity theorem for SHG in lossless non-periodic WGs

In this section, an analytical formulation is presented for describing phase-matched SHG in a lossless non-periodic WG, using the conjugated Lorentz reciprocity theorem [197]. This allows us to understand the significance of the phase-matching condition and the overlap integral for a TWM process. These two concepts are central to the process of design in this chapter, and apply equally to the quantum process of SPDC and its classical counterpart of SHG. In a TWM process, a material with a second-order nonlinear susceptibility $\chi^{(2)}$ mixes three waves of frequencies ω_p , ω_s , and ω_l , such that $\omega_p = \omega_s + \omega_l$, with ω_p being the largest frequency of the three. If the ω_s and ω_l waves are the input to produce ω_p , we have SFG. In the case of SFG with $\omega_s = \omega_l = \omega_{FH} = \omega_{SH}/2$, we have SHG. If ω_p and ω_s waves are input to produce ω_l , we have difference-frequency generation (DFG). If only the ω_p wave is input without any seed waves at ω_l and ω_s and it spontaneously splits into these two frequencies through interacting with the vacuum fluctuations, we have SPDC. All these processes share the same phase-matching condition and similar overlap integrals.

It is the SHG process that is considered here. In the simplest way one can describe SHG as follows: A CW beam of the form $E_{FH}(t) \propto E_0 e^{-i\omega_{FH}t}$ is excited in the structure. The $\chi^{(2)}$ nonlinearity then

generates a nonlinear polarization of the form $P_{\text{NL}} \propto \chi^{(2)} (E_0 e^{-i\omega_{\text{FH}}t})^2$. This nonlinear polarization acts as a source of excitation with a frequency of $2\omega_{\text{FH}} = \omega_{\text{SH}}$, generating a wave at the SH frequency. The objective of the calculation here is to find this generated SH wave. It is clear that the generated SH and the input FH can also interact with each other, and through DFG change the input FH wave. For cases when this change is substantial, one has to calculate its effect on the SHG. Hence, the equations describing SHG and DFG must be solved together. In the analysis here, this effect is neglected, assuming that the generated SH is weak enough so that it cannot cause a substantial DFG that can affect the amplitude of the input FH. This is called the undepleted-pump approximation (UPA) and is a reasonable approximation for experimentally reachable situations in nanostructured WGs.

The above explanation is oversimplified. The nonlinear susceptibility is in reality a rank three tensor, and the vectorial \mathbf{P}_{NL} depends on the different components of the FH field through:

$$P_{\text{NL},\gamma}(\mathbf{r}, \omega_{\text{SH}}) = \varepsilon_0 \sum_{\alpha,\beta} \chi_{\alpha\beta\gamma}^{(2)}(\mathbf{r}) E_{\alpha}(\mathbf{r}, \omega_{\text{FH}}) E_{\beta}(\mathbf{r}, \omega_{\text{FH}}). \quad (2.1)$$

Here, $P_{\text{NL},\gamma}$ is the γ -component of the nonlinear polarization vector \mathbf{P}_{NL} , and E_{α} is the α -component of the electric field vector \mathbf{E} . $\chi_{\alpha\beta\gamma}^{(2)}$ is the second-order nonlinear susceptibility. The α , β , and γ indices run over the x, y, and z indices. It should be mentioned that finding this expression involves the use of approximations and fundamental symmetries of the $\chi^{(2)}$ tensor, namely the Kleinman's symmetry, which can be found in detail elsewhere [58].

The following calculation is based on modal expansion, that describes the dynamics of the field in terms of the individual response of the eigenmodes of the system. For this analysis, a perturbation theory is used, which considers the presence of nonlinearity as a perturbation to the linear (unperturbed) system and assumes that the perturbed system with nonlinearity has the same eigenmodes as the unperturbed linear system. Henceforth, we have to first introduce the modes of the system. A non-periodic WG can be described by an x-invariant relative permittivity profile of $\bar{\varepsilon}(y, z, \omega)$. In the analysis here, $\bar{\varepsilon}(y, z, \omega)$ is assumed to be a real-valued 3×3 symmetric tensor, which means that the material is lossless, reciprocal, and can be anisotropic in general. For a WG structure, $\bar{\varepsilon}(y, z, \omega)$ usually has a region of higher permittivity called the core, that is surrounded by other materials of lower permittivity. Such a system can support guided modes confined to the core through total internal reflection, with an electric field profile of the form $\mathbf{E}(\mathbf{r}, \omega) = \mathbf{e}(y, z, \omega) e^{ik(\omega)x}$, which is a solution to the source-free wave equation $\nabla \times \nabla \times \mathbf{E} = \frac{\omega^2}{c^2} \bar{\varepsilon} \mathbf{E}$. Here, $\mathbf{e}(y, z, \omega)$ is the transverse field profile of the mode, and $k(\omega)$ is the wave-vector of the mode. The wave-vector expressed as a function of frequency, $k(\omega)$, is referred to as the band of the mode. For a fully guided mode in a lossless structure, $k(\omega)$ is a real-valued quantity. We assume only one mode is excited at the FH frequency, with the electric and magnetic field profiles:

$$\{\mathbf{E}_{\text{FH}}, \mathbf{H}_{\text{FH}}\}(\mathbf{r}) = \{\mathbf{e}_{\text{FH}}, \mathbf{h}_{\text{FH}}\}(y, z) e^{ik_{\text{FH}}x}. \quad (2.2)$$

Here, the complex representation for the field is given, assuming a CW excitation with a time dependence of $e^{-i\omega_{\text{FH}}t}$. The FH mode is assumed to be a FP mode, with $k_{\text{FH}} > 0$. In Eq. (2.2), the excited FH field is not separated into a power-dependent amplitude and a power-normalized transverse field

profile, but instead is presented as one quantity in the transverse field profile. By the end of the calculation, a normalization will be done on the final result to make it explicitly dependent on the input FH power. The field profiles for the modes at the SH frequency are:

$$\{\mathbf{E}_{\text{SH}_n}, \mathbf{H}_{\text{SH}_n}\}(\mathbf{r}) = \{\mathbf{e}_{\text{SH}_n}, \mathbf{h}_{\text{SH}_n}\}(y, z)e^{ik_{\text{SH}_n}x}, \quad (2.3)$$

where the index n runs over all the guided modes at ω_{SH} , including FP and BP ones. The SH transverse field profiles are not normalized and a normalization will be done by the end of the calculation to make the final result independent of arbitrary proportionality constants in the SH transverse field profiles. Fields in Eq. (2.3) satisfy the source-free Maxwell's equations at ω_{SH} :

$$\nabla \times \mathbf{E}_{\text{SH}_n} = i\omega_{\text{SH}}\mu_0\mathbf{H}_{\text{SH}_n}, \quad \text{and} \quad \nabla \times \mathbf{H}_{\text{SH}_n} = -i\omega_{\text{SH}}\epsilon_0\bar{\epsilon}_{\text{SH}}\mathbf{E}_{\text{SH}_n}. \quad (2.4)$$

Eq. (2.4) represents the dynamics of the unperturbed system. For the perturbed system with nonlinearity, the equations include the \mathbf{P}_{NL} from Eq. (2.1), giving:

$$\nabla \times \mathbf{E}'_{\text{SH}} = i\omega_{\text{SH}}\mu_0\mathbf{H}'_{\text{SH}}, \quad \text{and} \quad \nabla \times \mathbf{H}'_{\text{SH}} = -i\omega_{\text{SH}}\epsilon_0\bar{\epsilon}_{\text{SH}}\mathbf{E}'_{\text{SH}} - i\omega_{\text{SH}}\mathbf{P}_{\text{NL}}. \quad (2.5)$$

\mathbf{E}'_{SH} and \mathbf{H}'_{SH} are the total generated fields at ω_{SH} , for which the following ansatz is assumed:

$$\{\mathbf{E}'_{\text{SH}}, \mathbf{H}'_{\text{SH}}\}(\mathbf{r}) = \sum_n A_n(x)\{\mathbf{E}_{\text{SH}_n}, \mathbf{H}_{\text{SH}_n}\}(\mathbf{r}). \quad (2.6)$$

This ansatz assumes that the generated SH field is a sum of all the guided modes at the SH frequency, each with an amplitude function $A_n(x)$, to be found. To find $A_n(x)$, the conjugated reciprocity theorem [197] is used, which states that the following relation is true for every mode of index m :

$$\oint_S (\mathbf{E}'_{\text{SH}} \times \mathbf{H}_{\text{SH}_m}^* + \mathbf{E}_{\text{SH}_m}^* \times \mathbf{H}'_{\text{SH}}) \cdot d\mathbf{S} = i\omega_{\text{SH}} \int_V d^3\mathbf{r} \mathbf{P}_{\text{NL}} \cdot \mathbf{E}_{\text{SH}_m}^*. \quad (2.7)$$

Here, V is a volume, S is the closed surface around this volume, and the surface element $d\mathbf{S}$ is pointing outwards on this surface. To use Eq. (2.7) for finding A_n , we need the orthogonality relation between the transverse profiles of the modes at the SH frequency:

$$\iint_{-\infty}^{+\infty} (\mathbf{e}_m^* \times \mathbf{h}_n + \mathbf{e}_n \times \mathbf{h}_m^*) \cdot \mathbf{x} dy dz = \delta_{nm} \mathcal{F}_n, \quad \text{with} \quad \mathcal{F}_n = \iint_{-\infty}^{+\infty} 2\text{Re}[\mathbf{e}_n \times \mathbf{h}_n^*] \cdot \mathbf{x} dy dz. \quad (2.8)$$

To find $A_n(x)$ from Eq. (2.7), a rectangular volume is chosen, starting from $x = x_0$ to $x = x_1$, and infinitely large in the transverse yz -plane. Using Eqs. (2.3) and (2.6) with Eq. (2.7) gives:

$$\sum_n \oint_S A_n(x) (\mathbf{e}_{\text{SH}_n} \times \mathbf{h}_{\text{SH}_m}^* + \mathbf{e}_{\text{SH}_m}^* \times \mathbf{h}_{\text{SH}_n}) \cdot d\mathbf{S} = i\omega_{\text{SH}} \int_V \mathbf{P}_{\text{NL}} \cdot \mathbf{E}_{\text{SH}_m}^* d^3\mathbf{r}. \quad (2.9)$$

The surface integral on the left-hand side of Eq. (2.9) can be simplified. The field profile of the guided modes, being confined in the y - and z -directions, will go to zero on the four surfaces closing

the volume in the transverse directions, and hence not contribute to \oint . As a result, the closed surface integral will turn into two surface integrals over surfaces perpendicular to the x-direction. For these integrals, the orthogonality relation of Eq. (2.8) can be used, simplifying Eq. (2.9) to:

$$A_n(x_1) - A_n(x_0) = \frac{i\omega_{\text{SH}}}{\mathcal{F}_{\text{SH}_n}} \int_V \mathbf{P}_{\text{NL}} \cdot \mathbf{E}_{\text{SH}_n}^* d^3\mathbf{r}. \quad (2.10)$$

Eq. (2.10) gives the change in $A_n(x)$ over the length $x_1 - x_0$. $A_n(x = x_1)$ can be calculated given that we have the initial value at x_0 . We then need to take the integral on the right-hand side of Eq. (2.10) over a volume between x_0 and x_1 . We take this integral by separating $\mathbf{P}_{\text{NL}} \cdot \mathbf{E}_{\text{SH}_n}^*$ into its x- and yz-dependent parts, which give us the phase-matching condition and the overlap integral between the transverse mode profiles, respectively. We first define $\mathbf{p}_{\text{NL}}(y, z)$:

$$\mathbf{p}_{\text{NL},\gamma}(y, z) \equiv \frac{e^{-i2k_{\text{FH}}x}}{2\epsilon_0} \mathbf{P}_{\text{NL},\gamma} = \frac{1}{2} \sum_{\alpha,\beta} \chi_{\alpha\beta\gamma}^{(2)}(y, z) e_{\text{FH},\alpha}(y, z) e_{\text{FH},\beta}(y, z). \quad (2.11)$$

Using this definition we can rewrite Eq. (2.10) as:

$$A_n(x_1) - A_n(x_0) = i2\omega_{\text{SH}}\epsilon_0 \frac{\mathcal{V}_n}{\mathcal{F}_{\text{SH}_n}} \int_{x_0}^{x_1} e^{-i\Delta k_n x} dx, \quad (2.12)$$

where \mathcal{V}_n is the overlap integral that determines the efficiency of the process, defined as:

$$\mathcal{V}_n \equiv \int_{-\infty}^{+\infty} \int_{-\infty}^{+\infty} \mathbf{p}_{\text{NL}} \cdot \mathbf{e}_{\text{SH}_n}^* dydz = \frac{1}{2} \sum_{\alpha,\beta,\gamma} \int_{-\infty}^{+\infty} \int_{-\infty}^{+\infty} \chi_{\alpha\beta\gamma}^{(2)}(y, z) e_{\text{FH},\alpha}(y, z) e_{\text{FH},\beta}(y, z) e_{\text{SH}_n,\gamma}^*(y, z) dydz, \quad (2.13)$$

and $\Delta k_n = k_{\text{SH}_n} - 2k_{\text{FH}}$ is the phase-mismatch. To take the integral along the x-direction, let us assume that we have an infinitely long WG, that has only a finite region of $0 < x < L$ over which $\chi^{(2)} \neq 0$. This means that there will be no reflections from the end-facets of the finite-sized nonlinear region. To find the amplitude of a FP SH mode, we must find the mode's amplitude at the end of the structure. Hence, the boundary condition of $A_n(x = 0) = 0$ is set, which means that there is no additional SH wave inserted into the structure from an external source. This gives:

$$\int_0^L e^{-i\Delta k_n x} dx = \frac{e^{-i\Delta k_n L} - 1}{-i\Delta k_n} = e^{-i\Delta k_n L/2} \frac{2 \sin(\Delta k_n L/2)}{\Delta k_n} = e^{-i\Delta k_n L/2} L \text{sinc}(\Delta k_n L/2).$$

Hence, the amplitude of the n th FP guided mode at the SH frequency, excited through SHG is:

$$A_n(L) = i2\omega_{\text{SH}}\epsilon_0 \frac{\mathcal{V}_n}{\mathcal{F}_{\text{SH}_n}} e^{-i\frac{\Delta k_n L}{2}} L \text{sinc}(\Delta k_n L/2). \quad (2.14)$$

Eq. (2.14) gives the electric field amplitude of the excited SH mode as a function of the input FH electric field, which reside in the overlap integral of Eq. (2.13). Often however, it is desired to have the generated SH power as a function of the input FH power, with an expression that is independent of arbitrary proportionality constants in the field profiles of the modes, so that we can utilize field

profiles found from any numerical method without any type of normalization. For doing so, we need to use an expression that connects the group velocity of a mode v_g to its field profiles [127]:

$$v_g = \frac{c}{n_g} = \frac{1}{dk/d\omega} = \frac{\iint_{-\infty}^{+\infty} \text{Re}[\mathbf{e} \times \mathbf{h}^*] \cdot \mathbf{x} dydz}{\iint_{-\infty}^{+\infty} \mathbf{d} \cdot \mathbf{e}^* dydz}, \quad (2.15)$$

where n_g is the group index and $\mathbf{d} = \epsilon_0 \bar{\epsilon} \mathbf{e}$ is the displacement field profile of the mode, such that $d_i = \sum_j \epsilon_0 \epsilon_{ij} e_j$. Eq. (2.15) neglects the dispersion in the material permittivity around the frequency of interest for calculating v_g , a justified approximation in nanostructured WGs made of transparent dielectric materials, where the modal dispersion induced by the structuring is far stronger than the material dispersion. However, in plasmonic structures the material dispersion must be included [198, 199, 200]. In the following, it is assumed that only one SH mode is phase-matched and generated dominantly, so the index n for the SH mode is dropped. For a CW forward-propagating FH mode, the input power at $x = 0$ and its relation to the group index of the mode is:

$$\mathcal{P}_{\text{FH}} = \frac{1}{2} \iint_{-\infty}^{+\infty} \text{Re}[\mathbf{e}_{\text{FH}} \times \mathbf{h}_{\text{FH}}^*] \cdot \mathbf{x} dydz = \frac{c}{2n_{\text{gFH}}} \iint_{-\infty}^{+\infty} \mathbf{d}_{\text{FH}} \cdot \mathbf{e}_{\text{FH}}^* dydz. \quad (2.16)$$

The generated SH power at the end of the structure is:

$$\mathcal{P}_{\text{SH}} = \frac{1}{2} \iint_{-\infty}^{+\infty} \text{Re}[\mathbf{E}'_{\text{SH}} \times \mathbf{H}'_{\text{SH}}^*] \cdot \mathbf{x} dydz = \frac{1}{2} |A(L)|^2 \iint_{-\infty}^{+\infty} \text{Re}[\mathbf{e}_{\text{SH}} \times \mathbf{h}_{\text{SH}}^*] \cdot \mathbf{x} dydz, \quad (2.17)$$

where Eqs. (2.3) and (2.6) are used for the SH fields. To get the SH power in the form wanted here, $A(L)$ from Eq. (2.14) is substituted into Eq. (2.17). Moreover, a factor of one is inserted in the right-hand side Eq. (2.17) from the equality $1 = (2n_{\text{gFH}} \mathcal{P}_{\text{FH}} / c \iint_{-\infty}^{+\infty} \mathbf{d}_{\text{FH}} \cdot \mathbf{e}_{\text{FH}}^* dydz)^2$, which itself can be verified from Eq. (2.16). Finally, the expression $|A(L)|^2 \iint_{-\infty}^{+\infty} \text{Re}[\mathbf{e}_{\text{SH}} \times \mathbf{h}_{\text{SH}}^*] \cdot \mathbf{x} dydz$ in Eq. (2.17) results in a $1 / \iint_{-\infty}^{+\infty} \text{Re}[\mathbf{e}_{\text{SH}} \times \mathbf{h}_{\text{SH}}^*] \cdot \mathbf{x} dydz$ factor, which is substituted by $n_{\text{gSH}} / c \iint_{-\infty}^{+\infty} \mathbf{d}_{\text{SH}} \cdot \mathbf{e}_{\text{SH}}^* dydz$, using the v_g expression of Eq. (2.15). This turns Eq. (2.17) into:

$$\mathcal{P}_{\text{SH}} = \mathcal{P}_{\text{FH}}^2 L^2 \text{sinc}^2 \left(\frac{\Delta k L}{2} \right) n_{\text{gFH}}^2 n_{\text{gSH}} \frac{\omega_{\text{SH}}^2}{2c^3} \frac{\left| \sum_{\alpha, \beta, \gamma} \iint_{-\infty}^{+\infty} \epsilon_0 \chi_{\alpha\beta\gamma}^{(2)} e_{\text{FH}, \alpha} e_{\text{FH}, \beta} e_{\text{SH}, \gamma}^* dydz \right|^2}{\left(\iint_{-\infty}^{+\infty} \mathbf{d}_{\text{SH}} \cdot \mathbf{e}_{\text{SH}}^* dydz \right) \left(\iint_{-\infty}^{+\infty} \mathbf{d}_{\text{FH}} \cdot \mathbf{e}_{\text{FH}}^* dydz \right)}. \quad (2.18)$$

Eq. (2.18) is the final result of this calculation, describing the generated SH power from a FP SHG process in a non-periodic WG. There are a number of signature dependencies in this equation. Firstly, the generated SH power is quadratically dependent on the input FH power. Secondly, the SH power is dependent on the length of the structure L and phase-mismatch Δk through an $L^2 \text{sinc}^2 \left(\frac{\Delta k L}{2} \right)$ functionality. A sinc-function, $\text{sinc}(x)$, has its absolute maximum at $\text{sinc}(x = 0) = 1$, and it gets smaller for larger x -values, with an embedded periodic variation and a $1/x$ envelope. Henceforth, if we intend to increase the generated SH power by increasing the length of the structure, we have to make sure that the argument of the sinc-function is zero, which means we must satisfy the phase-matching condition

of $\Delta k = 0$. This explains the importance of the phase-matching condition for having an efficient TWM process. If $\Delta k \neq 0$, then the generated SH power will not rise quadratically with L , but rise and fall sinusoidally with a period of $2\pi/\Delta k$ [58].

Aside from having phase-matching, we must also have a substantial overlap integral, defined in Eq. (2.13) that appears in Eq. (2.18), between the arrays of the nonlinear susceptibility tensor and the components of the electric field vectors of the modes. Here, we must consider two aspects for having an efficient interaction. Firstly, the dominant electric field component of the FH mode should use a non-zero array of the nonlinear tensor, preferably the strongest one, to excite the dominant electric field component of the SH mode. Secondly, the transverse profile of the FH and the SH field components and the nonlinear susceptibility must have as much overlap with each other in the yz -plane as possible. These two aspects overall mean, that the chosen modes should not only be phase-matched, but also have dominant components with suitable polarizations and mode profiles. These will be seen in a following design in a LN ridge WG. Before getting to the design process however, a short description of the relevant parameters of LN for TWM is given.

2.1.2 Lithium niobate as the nonlinear material

To design LN structures for TWM, we need to know LN's linear permittivity and nonlinear susceptibility tensors. LN is a uniaxial crystal. At the temperature of 21 °C, its refractive indices for the wavelength of $\lambda = 1550$ nm are $n_e = 2.1376$ and $n_o = 2.2111$, and for the wavelength of $\lambda = 775$ nm are $n_e = 2.1784$ and $n_o = 2.2587$ [201], where indices e and o stand for the extraordinary and ordinary component of the tensor. Because of the crystal symmetry of LN, many of its $\chi^{(2)}$ tensor elements are zero, and many of the non-zero elements are equal. To express the remaining elements, a contracted notation is used here [58], which allows for writing the \mathbf{P}_{NL} of Eq. (2.1) in the following form:

$$\mathbf{P}_{\text{NL}} = \begin{bmatrix} P_{\text{NL},x} \\ P_{\text{NL},y} \\ P_{\text{NL},z} \end{bmatrix} = 2\epsilon_0 \begin{bmatrix} 0 & 0 & 0 & 0 & d_{31} & -d_{22} \\ -d_{22} & d_{22} & 0 & d_{31} & 0 & 0 \\ d_{31} & d_{31} & d_{33} & 0 & 0 & 0 \end{bmatrix} \begin{bmatrix} E_{\text{FH},x}^2 \\ E_{\text{FH},y}^2 \\ E_{\text{FH},z}^2 \\ 2E_{\text{FH},y}E_{\text{FH},z} \\ 2E_{\text{FH},x}E_{\text{FH},z} \\ 2E_{\text{FH},x}E_{\text{FH},y} \end{bmatrix}, \quad (2.19)$$

where here, LN's crystal axis (c-axis) is assumed to be along the z-direction. The elements of the d-tensor are connected to the non-zero elements of the $\chi^{(2)}$ tensor as follows: $2d_{31} = \chi_{xxz}^{(2)} = \chi_{yzy}^{(2)} = \chi_{zxx}^{(2)} = \chi_{zyy}^{(2)} = \chi_{xxz}^{(2)} = \chi_{yyz}^{(2)}$, $2d_{33} = \chi_{zzz}^{(2)}$, and $2d_{22} = \chi_{yyy}^{(2)} = -\chi_{yxx}^{(2)} = -\chi_{xxy}^{(2)} = -\chi_{xyx}^{(2)}$. d_{33} is the dominant component of the d-tensor, with a value around $d_{33} \approx -20.6$ pm/V for $\lambda_{\text{FH}} = 1.52$ μm [202]. The second strongest component is $d_{31} \approx -5$ pm/V and the weakest component is $d_{22} \approx 2$ pm/V, both for $\lambda_{\text{FH}} = 1.064$ μm [203]. The contracted notation provides a more intuitive way of understanding which components of the field take part in the nonlinear interaction, by simply looking at Eq. (2.19). There are two common scenarios used in this thesis: Given that d_{33} is the strongest component of the d-tensor, the interaction will be the strongest when all the three modes involved have their dominant electric field component along the c-axis. If this is not possible in a design, the next best case would

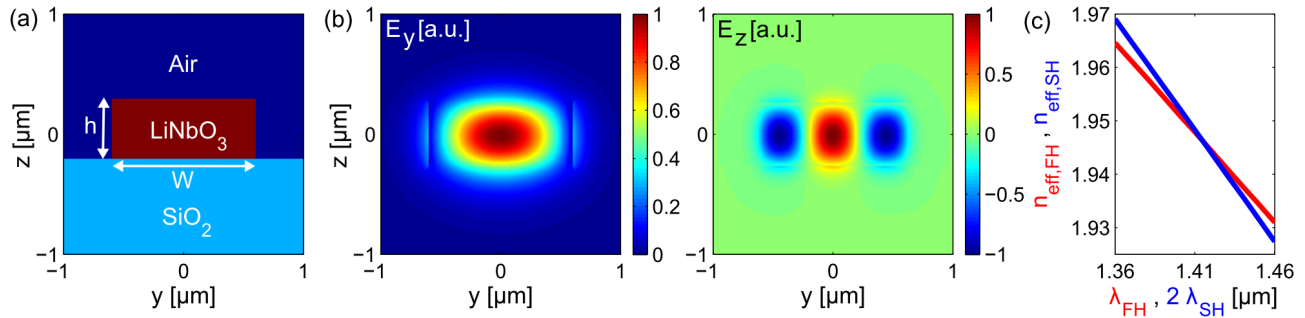


Figure 2.1: (a) The geometry of the LN ridge WG on the SiO₂ substrate. The dimensions here are $W = 1.20 \mu\text{m}$ and $h = 0.53 \mu\text{m}$. The c-axis is along z ; (b) Real-valued field profile of the E_y component of the TE₀₀ mode (left) at the wavelength of phase-matching $\lambda_{\text{FH}} = 1.415 \mu\text{m}$ and the E_z component of the TM₂₀ mode (right) at the wavelength $\lambda_{\text{SH}} = \lambda_{\text{FH}}/2$; (c) The effective refractive indices of the modes: $n_{\text{eff},\text{FH}}$ is for the TE₀₀ mode shown around the FH wavelength, and $n_{\text{eff},\text{SH}}$ is for the TM₂₀ mode shown around the SH wavelength.

be to use d_{31} , e.g. when the SH mode has a dominant electric field component along the c -axis and the FH mode has a dominant component along any other two remaining axes. In the following, such a design is presented in a LN ridge WG, as an introduction to doing practical phase-matched designs.

2.1.3 Phase-matching in a lithium niobate ridge waveguide

FP SHG has been demonstrated in AlGaAs ridge WGs [204], and the design process for modal phase-matching is straightforward. The particular ridge WG design presented here has also been experimentally characterized during this thesis, and the result of this experiment will be presented in the next chapter. The geometry of the LN ridge WG on a SiO₂ substrate is shown in Fig. 2.1(a). SiO₂ has a smaller refractive index of $n \approx 1.44$ compared to LN, which allows the confinement of guided modes. The goal here is to find a pair of modes to satisfy $k_{\text{SH}} = 2k_{\text{FH}}$. This condition could also be written between the effective refractive indices of the modes $n_{\text{eff},\text{SH}} = n_{\text{eff},\text{FH}}$, using the definition $n_{\text{eff}} \equiv \frac{k\lambda}{2\pi}$. Moreover, these modes should have an efficient overlap integral. In the ridge WG of dimensions $h = 0.53 \mu\text{m}$ and $W = 1.20 \mu\text{m}$ with LN's c -axis along z , the pair of modes that satisfy these conditions are the TE₀₀ mode as the FH mode and the TM₂₀ mode as the SH mode. By convention here, a TE mode is one that has a dominant electric component along the y -direction and a TM mode has it along the z -direction. A more standardized definition based on the symmetry of the mode profile will be presented in the next section to categorize Bloch modes. The numbers in the indices refer to the number of nodes that the profile of the dominant electric field component has in the y - and z -directions. The profile of the dominant electric field component for each mode is shown in Fig. 2.1(b). With these modes the SHG process is mediated by the d_{31} component of the d-tensor. The n_{eff} of each mode is shown in Fig. 2.1(c), where the point of phase-matching at $\lambda_{\text{FH}} = 1.415$ can be observed, at which the two curves cross for $n_{\text{eff},\text{SH}} = n_{\text{eff},\text{FH}} = 1.946$. The modal data is numerically found using the Mode Analysis engine of COMSOL, which is based on the finite element method [205].

Some general remarks could be made about the process of design in such structures. Firstly, the choices of modes and dimensions are not unique, and depend on a range of design constraints forced by the practicality of the design. For an SHG experiment, the FH mode best be a TE₀₀ or a TM₀₀ mode with no nodes in the mode profile of its dominant electric field component. Experimentally, this would allow the most efficient in-coupling of light from an objective or a lensed fiber. The SH mode in a modally phase-matched design will usually end up being a higher-order mode. The reason

is, at double the frequency, the refractive index of the material increases, and furthermore the modes become more confined inside the WG, both of which increase the effective refractive index of the modes. Hence, a TE_{00} mode at ω_{FH} cannot phase-match to itself at ω_{SH} . However, as the number of nodes in a mode profile increases, its n_{eff} decreases, which makes the phase-matching between a higher-order SH mode and a first-order FH mode possible. It should be noted, that a higher-order mode will have a smaller overlap integral with a first order mode, compared to if both SH and FH modes were first order modes. Regarding the choice of dimensions, the goal is to confine the mode to as small a transverse area as possible, as the same amount of power confined to a smaller area will result in a larger electric field intensity and hence a more efficient nonlinear interaction. A ridge WG with dimensions around that of the wavelength of the FH mode will usually provide an optimum confinement. If the dimensions are much smaller, the mode profile would be delocalized and have most of its field concentrated in the regions surrounding the WG, rather than inside the WG where the nonlinearity is present. Although the choice of dimensions can be fine tuned to get the best nonlinear efficiency at a target wavelength [206], here I settled with a series of fixed subwavelength dimensions that emerged from the fabrication, and looked for one that had a FH phase-matching wavelength between $1.3 \mu\text{m}$ and $1.6 \mu\text{m}$, for which we had tunable CW lasers in our labs. Finally, in the actual NANOLN substrate used in fabrication of this structure, the SiO_2 substrate is only $1 \mu\text{m}$ thick, and under it is again LN. This theoretically causes leakage, as the evanescent tail of a guided mode's profile can couple to this LN substrate. However, for the modes used here, over the structure length of a millimeter, the leakage is negligible and the $1 \mu\text{m}$ thick SiO_2 substrate can well confine the modes.

2.2 Periodic waveguides: fundamentals and phase-matching

In this section, the fundamentals needed for understanding periodic WGs, their eigenmodes, and their phase-matching mechanism will be presented. A phase-matched design in a LN nanobeam is also presented as an exemplary structure to accompany the fundamental concepts. A detailed explanation of the used numerical methods is left to appendix A.

2.2.1 Bloch modes, Brillouin zone, band diagram, light line, and symmetries

A periodic WG is a structure that is effectively periodic in the propagation direction x , and has some confinement mechanism for its modes in the yz -plane. Assume a structure with a periodic permittivity along the x -direction $\epsilon(\mathbf{r}) = \epsilon(\mathbf{r} + a\mathbf{x})$ and an arbitrary shape in the yz -plane. a is the period, $a\mathbf{x}$ and its integer multiples are referred to as the lattice vectors, and the structure that lies within a period is called a unitcell. The periodic structure can be reproduced by translating a unitcell with all possible combinations of its lattice vectors. This periodic structure can support specific guided modes, called Bloch modes, with the electric field expression $\mathbf{E}(\mathbf{r}, \omega) = \mathbf{e}(\mathbf{r}, \omega)e^{ik(\omega)x}$ in the frequency domain. The two important quantities needed for describing a Bloch mode are its dispersion relation $k(\omega)$, that describes the Bloch wave-vector as a function of frequency, and its periodic Bloch mode profile $\mathbf{e}(\mathbf{r}) = \mathbf{e}(\mathbf{r} + a\mathbf{x})$. The dispersion relation is usually plotted with ω as the vertical axis and k as the horizontal axis, and it is referred to as the band diagram. For a periodic structure, the band diagram

needs not to be sketched for all values of k , as shifting k to $k + \frac{2\pi n}{a}$, where n is an integer, will describe the same Bloch mode only with a new Bloch mode profile described by $\mathbf{e}'(\mathbf{r}) = \mathbf{e}(\mathbf{r})e^{-i\frac{2\pi n}{a}x}$, as $e^{-i\frac{2\pi n}{a}x}$ is also periodic. This can be seen in the following $\mathbf{E}(\mathbf{r}) = \mathbf{e}(\mathbf{r})e^{ikx} = \mathbf{e}(\mathbf{r})e^{i(k+\frac{2\pi n}{a})x}e^{-i\frac{2\pi n}{a}x} = \mathbf{e}'(\mathbf{r})e^{i(k+\frac{2\pi n}{a})x}$. This means that we need to know the band diagram for only one $2\pi/a$ interval of k , the Brillouin zone (BZ). A common choice for it is from $-\pi/a$ to $+\pi/a$, referred to as the first BZ. The $\frac{2\pi}{a}\mathbf{x}$ and its integer multitudes are referred to as the reciprocal lattice vectors. The band diagram for all values of the wave-vector can be reproduced by translating the band diagram in the first BZ with all possible combinations of its reciprocal lattice vectors. The essential part of the first BZ can be reduced even further by having some information about the symmetry of the structure. The simplest one is, as materials used in the optical frequencies are commonly reciprocal, where the permittivity tensor is diagonal, the forward and backward propagation are identical. This means that the band diagram is mirror symmetric ($\mathbf{k} \rightarrow -\mathbf{k}$) with respect to k . For the 1D periodic case, this will give an irreducible BZ from $k = 0$ to $+\pi/a$ that contains all the dispersion information.

A band diagram is calculated for the case of a LN nanobeam using the MPB eigen-solver, explained in detail in appendix A. The permittivity distribution for a LN nanobeam is shown in Fig. 2.2(a) within a unitcell, where the structure is surrounded by vacuum. The band diagram calculated for this structure is shown in Fig. 2.2(b), where the periodic nature of the band diagram can be observed. The first thing to be noticed in Fig. 2.2(b) is that k and ω are given in units of $2\pi/a$ and $2\pi c/a$, respectively. In this work, dimensions, frequencies, and wave-vectors for periodic WGs are expressed in unitless quantities, by choosing the period a as a characteristic length. The scalability of Maxwell's equations [127] will result in the same physics, regardless of what a is. Hence, the band diagram could be found regardless of a , as long as the rest of the geometrical parameters are fixed with respect to a and the permittivities are unchanged. A useful relation in this regard is $\frac{\omega a}{2\pi c} = \frac{a}{\lambda}$, which connects the normalized frequency in units of $\frac{2\pi c}{a}$ to the free-space wavelength λ . In the periodic structure designs with LN in this work, two sets of permittivities are used: one at $\lambda = 1550$ nm for the FH modes and one at $\lambda = 775$ nm for the SH modes. Once a design is reached at the normalized frequency of a/λ_{FH} , a is chosen such that λ_{FH} coincides with 1550 nm. In the band diagram of Fig. 2.2(b), the blue line is the light line, described by $\omega = \frac{c}{n_0}|k|$ in the first BZ, where $n_0 = 1$ is the refractive index of the surrounding vacuum in this case. The light line specifies the boundary of two regions in the band diagram. The region under the light line includes modes that are fully confined to the WG structure through total internal reflection (TIR). The region above the light line includes plane-waves of the surrounding bulk and the leaky modes of the WG that are not fully confined by TIR. In other words, for the frequencies that lie above the light line, the bulk material that surrounds the WG, can support plane-waves with wave-vectors equal or larger than the modes of the WG. This means that the WG modes can couple to these outward-propagating plane-waves and hence become leaky.

Under the light line, there are ranges of frequencies without any guided modes. These regions are known as the bandgap. For example, the first bandgap appears between the frequencies of the first and second modes at the edge of the BZ $k = \pi/a$, where this region is zoomed in and shown in Fig. 2.2(c), with the bandgap shaded gray. In the bandgap region, evanescent modes still exist that carry no power, which are not shown in this plot. Near the bandedge, the group velocity $v_g = d\omega/dk$ of a mode gets lower, goes to zero at the bandedge, and changes sign on the other side of the bandedge, as can be seen

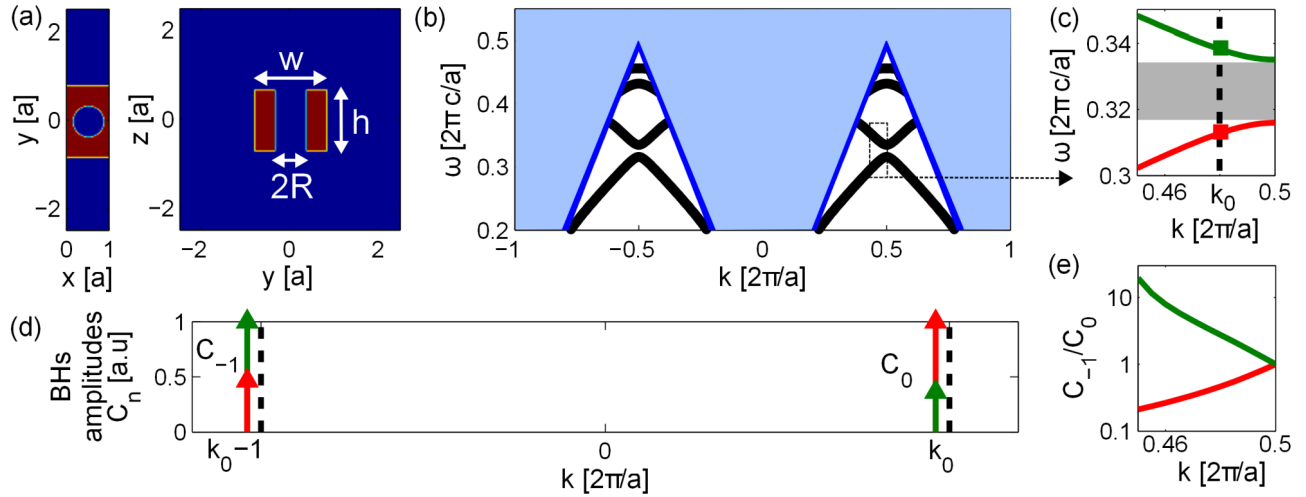


Figure 2.2: (a) The geometry of a nanobeam within a unitcell, shown on the $z = 0$ (left) and $x = 0.5a$ (right) planes. (b) Band diagram of the LN nanobeam (black solid lines), where only modes with the z -odd- y -even symmetry are shown. The blue line is the light line. The blue shaded region is above the light line, where modes are leaky. Design parameters are $h/a = 1.4$, $R/a = 0.35$, and $W/a = 1.65$. The c -axis of LN is along the z -direction. The $\lambda = 775$ nm permittivities are used here; (c) A region of plot (b), zoomed on two bands near the edge of the first Brillouin zone (BZ). The green upper band is BP and the red lower band is FP. The grey shaded region marks the bandgap; (d) The Bloch harmonics (BHs) distribution $C_n = |z \cdot \mathbf{C}_n(y=0, z=0)|$ for the two modes marked in plot (c), both with $k_0 = 0.48 \frac{2\pi}{a}$. The dashed lines mark the edges of the first BZ at $k = \pm\pi/a$; (e) The ratio between the C_{-1} and C_0 BHs for the two bands in plot (c).

from the slope of the bands shown in Figs. 2.2(b) and (c). The sign of the group velocity is related to the direction of propagation of the mode. For example, in Fig. 2.2(c), the lower red band is associated to a forward-propagating (FP) mode, as $v_g > 0$, and the upper green band is associated to a backward-propagating (BP) mode, as $v_g < 0$. The modes exactly at the bandedge $k = \pm\pi/a$ have $v_g = 0$ and hence are stopped. Sometimes instead of group velocity the concept of group index $n_g \equiv c/v_g$ is used, which increases and diverges at the bandedge. It will be seen throughout this work, that a range of interesting phenomena happen near the bandedge. Hence, it is worth taking a closer look at the Bloch modes in that region, to understand the physics behind the formation of bandgaps and lowered group velocities. An argument could be made, that these effects are caused by the periodicity of the structure coupling FP and BP waves together. In a non-periodic WG, the FP and BP modes do not interact with each other. But the introduction of periodicity with the period a , couples modes with wave-vectors that are factors of $\frac{2\pi}{a}$ apart. The coupling is the strongest for modes at the edges of the BZ and causes a frequency splitting in the band diagram. This splitting region is the bandgap frequency range. The band splitting between coupled modes of positive and negative v_g should naturally have a point of zero v_g . At this point, it could be imagined that the power contribution of the FP and BP modes cancel each other, resulting in a standing wave.

A deeper understanding of the above argument can be gained by looking at the field profile of the Bloch modes. Given that the Bloch mode profile is periodic, it can be expanded in a Fourier series $\mathbf{e}(\mathbf{r}) = \mathbf{e}(\mathbf{r} + a\mathbf{x}) = \sum_{n=-\infty}^{+\infty} \mathbf{C}_n(y, z) e^{i\frac{2\pi n}{a}x}$. Henceforth we can write:

$$\mathbf{E}(\mathbf{r}, \omega) = \mathbf{e}(\mathbf{r}, \omega) e^{ik(\omega)x} = \sum_{n=-\infty}^{+\infty} \mathbf{C}_n(y, z, \omega) e^{ik_n(\omega)x}, \quad \text{with } k_n(\omega) \equiv k(\omega) + \frac{2\pi n}{a}. \quad (2.20)$$

This means that a Bloch mode can be expanded into a series of x -invariant modes, called Bloch-

harmonics (BHs) [144], described by a $C_n(y, z)$ profile and a wave-vector k_n . An example for the amplitude of the BHs is plotted in Fig. 2.2(d), for two points marked in the band diagram of Fig. 2.2(c). The two points have the same wave-vector of $k = k_0$ in the first BZ, but the upper band is a BP mode and the lower band a FP mode. Since both modes have a dominant E_z component with a maximum at the center of the nanobeam, the absolute value of the z-component of the BH at the center $C_n = |z \cdot C_n(y = 0, z = 0)|$ is evaluated as a quantity for the plots to appropriately display the strength of each BH. For the index n , the BH that has a k_n within the first BZ, $-\frac{\pi}{a} < k_n < +\frac{\pi}{a}$, is always indexed as C_0 in the convention of this work. For the mode right at the bandedge, the BH at $+\frac{\pi}{a}$ is called C_0 here. Moreover, for each Bloch mode, its BH amplitudes are normalized such that the dominant one stands at the value of 1. There are a number of important observations that can be made from the BHs distribution in Fig. 2.2(d). Firstly, we can see that both of the FP and BP modes are constituted of positive- and negative- k_n BHs. Secondly, these Bloch modes only have two substantial BHs, C_0 and C_{-1} , which are the only ones displayed. Thirdly, we see that the direction of propagation for the FP and BP modes are consistent with the sign of k_n for their dominant BH. That means, the dominant BH for the FP mode (red one) is C_0 at $k_0 > 0$, and for the BP mode (green one) is C_{-1} at $k_0 - \frac{2\pi}{a} < 0$. This intuitively matches with our expectation: C_0 is a positive-k BH and has a FP power and C_{-1} is a negative-k BH and has a BP power. For a mode to be effectively FP, positive-k BHs should have the dominating contribution, and to be effectively BP, negative-k BHs should be dominant. Finally, let us take a look at the ratio of the BP BH to the FP BH, C_{-1}/C_0 , for the two modes as a function of their wave-vector, shown in Fig. 2.2(e). We see that, as expected, across the band of the BP mode this ratio is larger than 1, as C_{-1} stays dominant, and across the band of the FP mode this ratio is smaller than 1, as C_0 stays dominant. More importantly, we see that the ratio approaches 1, as both modes get closer to the bandedge, where their group velocity is getting smaller. The ratio is exactly 1 at the bandedge, where the modes are stopped and have $v_g = 0$. This could be understood, as the second strongest BH propagates power in the opposite direction to the strongest BH, hence canceling some of the strongest BH's contribution. This effectively causes for a lowered v_g when the two BHs have a closer amplitude. At the bandedge, the two BHs exactly cancel each other's contributions, resulting in a standing wave with no power transfer.

At the end, the symmetries of the modes should be discussed, which are used throughout this work for categorizing them. For a structure with a permittivity profile that is invariant in the z-direction, modes of the system that propagate along any direction parallel to the xy-plane can be separated into purely TE modes, with $H_x = H_y = E_z = 0$, and TM modes, with $E_x = E_y = H_z = 0$. In the case of a WG structure that is not invariant in any of the transverse directions of y or z, like a ridge WG or a PCSW, this exact categorization is not possible, as modes generally have all 6 components of the field. However, another categorization based on the symmetry of the mode profiles could be possible. If the structure is symmetric in the z-direction, let us say around the $z = 0$ plane, we can separate its modes into z-even and z-odd, also called TE-like and TM-like, respectively [127]. The z-odd modes have an odd-looking mode profile for $\{E_x, E_y, H_z\}$ and an even-looking profile for $\{H_x, H_y, E_z\}$ with respect to the $z = 0$ plane. The z-even modes are vice versa. This can be verified from an example of the mode profile of a z-odd mode in the nanobeam, shown in Fig. 2.3. One reason for calling z-odd modes TM-like, is that at the $z = 0$ plane the mode profile is exactly like a TM mode, with

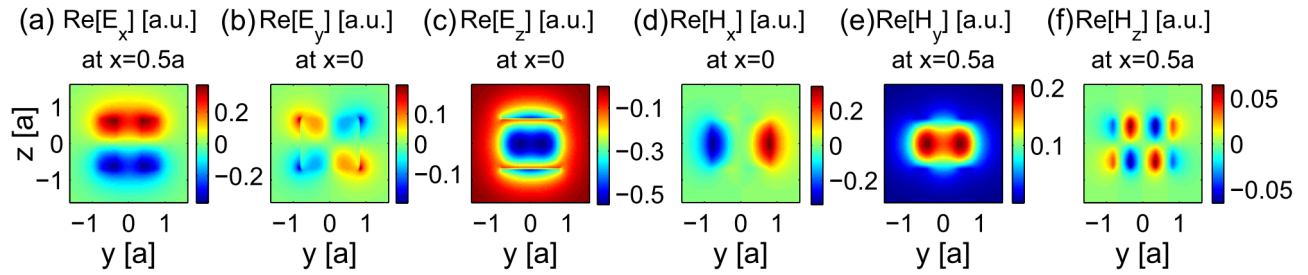


Figure 2.3: (a-f) The real part of the electric and magnetic field profiles for a mode with a z -odd- y -even symmetry, presented over the yz -plane, for the lower band at $k = \pi/a$ in Fig. 2.2(c).

the $\{E_x, E_y, H_z\}$ components being exactly zero. Another reason is that for lower-order modes, the TM-like modes are close to a TM mode, in that $\{H_x, H_y, E_z\}$ are the dominant components and the $\{E_x, E_y, H_z\}$ components are weaker in comparison. The same reasoning is behind naming z -even modes TE-like. The periodic WGs in this work, also have a y -symmetry with respect to the $y = 0$ plane, which can be used to separate the modes into y -even and y -odd modes. The y -even modes have even-looking profiles for $\{E_x, E_z, H_y\}$ and odd-looking profiles for $\{H_x, H_z, E_y\}$. The y -odd modes are vice versa. This can again be verified from Fig. 2.3, where the mode is y -even, in addition to being z -odd. WG modes with z -even- y -odd or z -odd- y -even symmetries commonly appear in this work. A z -even- y -odd mode will have a dominant E_y component with a profile that looks even with respect to both the $y = 0$ and $z = 0$ planes, and a z -odd- y -even mode will have a dominant E_z component with a profile that looks even with respect to both the $y = 0$ and $z = 0$ planes, verifiable from Fig. 2.3(c). In a TWM process, having even-looking mode profiles for the dominant component of the electric field will usually result in a strong overlap integral, enhancing the efficiency of the process.

2.2.2 Phase-matching with Bloch modes

The phase-matching condition for Bloch modes is not as simple as the one found for a non-periodic WG. Here, this condition is found in a general way. The phase-matching condition in a periodic WG can be theoretically derived in a similar way as for the non-periodic WG in section 2.1.1. This calculation will be done comprehensively in chapter 3 for describing SHG and in chapter 4 for describing SPDC in periodic WGs. However, there is also a simpler way of finding the phase-matching condition with our current state of knowledge from section 2.1.1, without performing the whole calculation. This will be done in the following to find the phase-matching condition for periodic WGs and understanding it, which is needed for understanding the process of design in this chapter. The starting point is using the volume integral of $\int_V \mathbf{P}_{\text{NL}} \cdot \mathbf{E}_{\text{SH}}^* d^3\mathbf{r}$, that appears on the right hand side of Eq. (2.7), and goes on to Eq. (2.10) to determine the amplitude of the generated SH mode. Eq. (2.7) is independent from the type of eigenmodes of the system and is a general statement of the conjugated reciprocity theorem, valid for all systems with a real-valued permittivity. Using the expression for the nonlinear polarization in Eq. (2.1), this volume integral takes the form $\int_V \mathbf{P}_{\text{NL}} \cdot \mathbf{E}_{\text{SH}}^* d^3\mathbf{r} \propto \int_V \sum_{\alpha, \beta, \gamma} \chi_{\alpha\beta\gamma}^{(2)} E_{\text{FH}, \alpha} E_{\text{FH}, \beta} E_{\text{SH}, \gamma}^* d^3\mathbf{r}$, which is again independent of the type of eigenmodes. For a TWM process with non-degenerate signal and idler frequencies, this integral takes the form $\int_V \sum_{\alpha, \beta, \gamma} \chi_{\alpha\beta\gamma}^{(2)}(\mathbf{r}) E_{\text{S}, \alpha}(\mathbf{r}) E_{\text{I}, \beta}(\mathbf{r}) E_{\text{P}, \gamma}^*(\mathbf{r}) d^3\mathbf{r}$, with $\omega_{\text{P}} = \omega_{\text{S}} + \omega_{\text{I}}$. To find the phase-matching condition for a periodic WG, we can substitute the electric fields in this volume integral with that of the

Bloch modes of the form $\mathbf{E}(\mathbf{r}, \omega) = \mathbf{e}(\mathbf{r}, \omega)e^{ik(\omega)x}$, where k is the wave-vector in the first BZ. To be able to do a separation of the volume integral into an x -dependent part and a yz -dependent part, we have to expand all the Bloch modes into their BHs, according to Eq. (2.20). Moreover, given that $\chi^{(2)}$ is also periodic, as it is only nonzero where the material exists, it should also be expanded in a Fourier series $\chi_{\alpha\beta\gamma}^{(2)}(\mathbf{r}) = \chi_{\alpha\beta\gamma}^{(2)}F(\mathbf{r}) = \chi_{\alpha\beta\gamma}^{(2)}\sum_{m=-\infty}^{+\infty}F_m(y, z)e^{i\frac{2\pi m}{a}x}$, where $F(\mathbf{r})$ is a periodic function equal to 1 where the nonlinear material exists and is zero otherwise. Using these expansions, the volume integral \mathcal{V} can be written as:

$$\mathcal{V} = \int_V \sum_{\alpha, \beta, \gamma} \chi_{\alpha\beta\gamma}^{(2)}(\mathbf{r}) E_{S, \alpha}(\mathbf{r}) E_{I, \beta}(\mathbf{r}) E_{P, \gamma}^*(\mathbf{r}) d^3\mathbf{r} = \sum_{n_P, n_S, n_I, m} \mathcal{V}_{n_P n_S n_I m} \int_0^L dx e^{-i\Delta k_{n_P n_S n_I m} x}, \quad (2.21)$$

with BHs overlap and phase-mismatch defined as:

$$\mathcal{V}_{n_P n_S n_I m} \equiv \sum_{\alpha, \beta, \gamma} \chi_{\alpha\beta\gamma}^{(2)} \iint_{-\infty}^{+\infty} dy dz F_m(y, z) C_{S, n_S, \alpha}(y, z) C_{I, n_I, \beta}(y, z) C_{P, n_P, \gamma}^*(y, z), \quad (2.22)$$

$$\Delta k_{n_P n_S n_I m} \equiv \left[k_P + \frac{2\pi}{a} n_P \right] - \left[k_S + \frac{2\pi}{a} n_S \right] - \left[k_I + \frac{2\pi}{a} n_I \right] + \frac{2\pi}{a} m. \quad (2.23)$$

Here $C_{S, n_S, \alpha}$ is the α -component of the n_S th Bloch harmonic of the mode at frequency ω_S .

Eqs. (2.21) to (2.23) tell us what we need to know about the phase-matching condition and the overlap integral in TWM processes in periodic WGs. To understand them, let us compare the phase-mismatch of Eq. (2.23) to that of a non-periodic WG, which is $\Delta k = k_P - k_S - k_I$, and the overlap integral of Eq. (2.22) to that of a non-periodic WG, which is $\sum_{\alpha, \beta, \gamma} \iint_{-\infty}^{+\infty} dy dz \chi_{\alpha\beta\gamma}^{(2)}(y, z) e_{S, \alpha}(y, z) e_{I, \beta}(y, z) e_{P, \gamma}^*(y, z)$. This comparison tells us, that the interaction of Bloch modes in a TWM process can be described as a sum of the interaction of all combinations of their BHs with each other, where each combination of BHs interact with each other in the same way that modes of a non-periodic WG do in a TWM process. In other words, $\Delta k_{n_P n_S n_I m}$ is the phase-mismatch between three different BHs of wave-vectors $k_P + \frac{2\pi}{a} n_P$, $k_S + \frac{2\pi}{a} n_S$, and $k_I + \frac{2\pi}{a} n_I$ [144] and $\mathcal{V}_{n_P n_S n_I m}$ is the overlap integral between these three BHs. This makes it clear, that in an efficient TWM process, phase-matching is required between BHs and the efficiency of the process depends on how well the transverse field profiles of these BHs overlap and how strongly each BH contributes to its corresponding Bloch mode. It should be noted, that in the designs throughout this work, $m = 0$ always happens to be the dominant Fourier component of $\chi^{(2)}$ participating in $\mathcal{V}_{n_P n_S n_I m}$. Hence, throughout this work, the phase-mismatch of Eqs. (2.23) is always expressed with $m = 0$. Finally, $\Delta k_{n_P, n_S, n_I} = 0$ is equivalent to:

$$k_P - k_S - k_I = \frac{2\pi}{a} Q, \quad \text{with} \quad Q \equiv n_S + n_I - n_P = 0, \pm 1, \pm 2, \dots \quad (2.24)$$

Henceforth, if phase-matching is satisfied for a particular value of Q , then it is satisfied for infinite combinations of $\{n_P, n_S, n_I\}$ indices, as they are all integers. In other words, if one set of BHs is phase-matched to each other, then there are infinite sets of other BHs that are also phase-matched at the same time. In this work, Bloch modes usually only have at most a handful of non-negligible BHs, similar to what was shown in Fig. 2.2(d). Hence, there is usually only one combination of BHs that produces the dominating contribution to the overlap integral.

The above discussion, allows us to make clear a main advantage of periodic WGs in comparison to non-periodic WGs in satisfying the phase-matching condition. With periodic WGs, we are no longer limited to FP processes. BP and CP processes are in principle possible to reach, because every Bloch mode can have positive- k_n and negative- k_n BHs at the same time, as was shown in Fig. 2.2(d), which are needed for phase-matching such processes. A FP process is usually the most efficient one with the largest overlap integral, compared to a CP or BP process. This is because, as was shown in Fig. 2.2(d), the dominant BH of a Bloch mode commonly has the same propagation direction as the Bloch mode itself. Hence, in a FP process, all the Bloch modes are participating in TWM with their dominant BHs. However, it has also been seen in Fig. 2.2(e), that a mode near the bandedge can have a non-dominant BH of a substantial amplitude with the sign of k_n being opposite to the propagation direction. This means, that by using modes near the bandedge, it is not only possible to phase-match BP and CP processes, but also to do it with a comparable overlap integral to a FP process. These non-dominant BHs will be front and center in all the novel phase-matched structures in this work, and their role can be better understood by looking at an actual design, presented in the following section.

2.2.3 Phase-matched designs in a lithium niobate nanobeam

The previous analytics on phase-matching in periodic WGs becomes clearer through investigating an actual structure. Here, the design of a LN nanobeam phase-matched for a FP and a BP process is presented. A nanobeam offers less dispersion engineering possibilities compared to a PCSW, but its simplicity will facilitate demonstrating how phase-matching can be reached and controlled in a realistic structure. Moreover, the nanobeam designs here will be utilized for the study of the effect of loss on slow-light-enhanced SHG processes, presented in the next chapter. The bands for the z-even-y-odd and z-odd-y-even modes of a nanobeam structure are shown in Fig. 2.4(a). It was explained previously, that these two symmetries are of interest for a TWM process, because of the even-looking profile of their dominant electric field component. For phase-matching, we want to have at least one of the modes near the bandedge, which allows for that mode to have a substantial non-dominant BH to participate in a BP phase-matching configuration. The choice for the FH and SH modes is marked on this band diagram with shaded ellipses, where the red and blue shaded regions mark the frequency and wave-vector region of interest for a FH mode (red dashed line) and a SH mode (blue solid line), respectively. It can be seen, that the blue region has approximately double the frequency and wave-vector compared to the red region, signaling the possibility of phase-matching. With this particular choice, the SH mode is near the bandedge with a small group velocity and the FH mode is away from the bandedge at $k_{\text{FH}} \approx 0.25 \frac{2\pi}{a}$. The FH mode is a z-even-y-odd (TE-like) mode with a dominant even-looking E_y component, shown in Fig. 2.4(b). The SH mode is a z-odd-y-even (TM-like) mode with a dominant even-looking E_z component, shown in Fig. 2.4(c). In this structure, the c-axis of the LN crystal is along the z-direction, hence the process is mediated using the d_{31} coefficient of LN.

An advantage of this design is that phase-matching at different points along the band of the slow SH mode can be reached by just changing the nanobeam width W , allowing us to achieve different values of group index of the SH mode n_{gSH} at the point of phase-matching with small changes in the other properties of the modes. This tuning is possible, because the SH mode is a higher-order mode with two nodes in its field profile along the y-direction, and consequently is more sensitive to

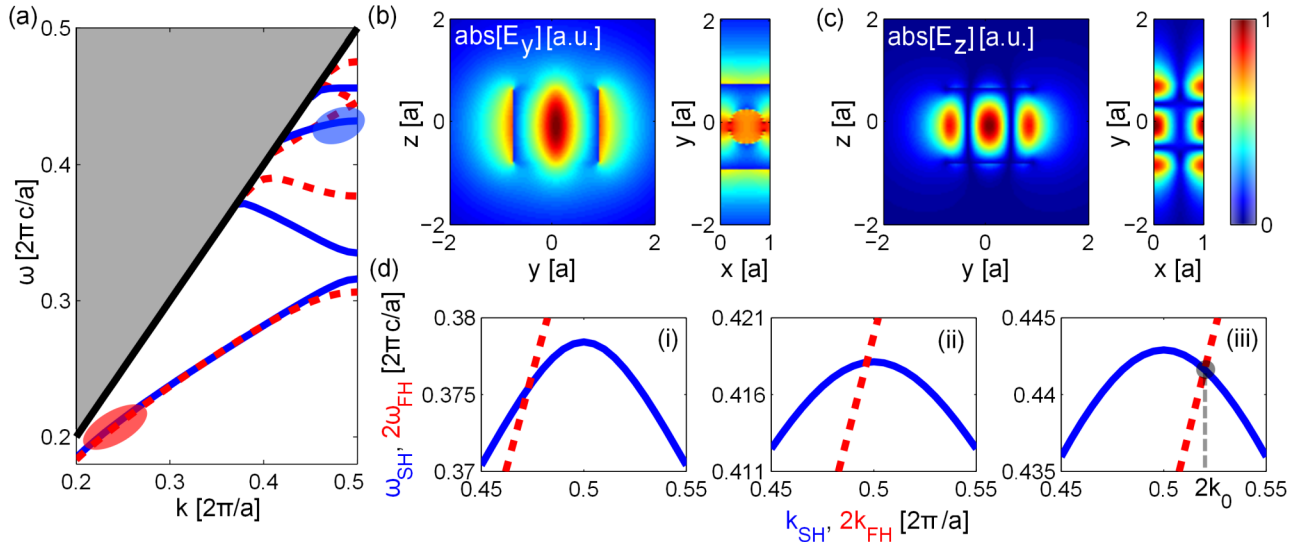


Figure 2.4: (a) Bands of a LN nanobeam under the light line. The red dashed and blue solid lines correspond to modes of z -even- y -odd and z -odd- y -even symmetry, respectively. The red and blue shaded ellipses mark the phase-matched FH and SH modes, respectively; (b,c) Field profile of the phase-matched FH and SH modes. (b) shows the dominant E_y component of the FH mode and (c) shows the dominant E_z component of the SH mode. Left and right figures show the field over the $x = 0$ and $z = 0$ planes, respectively; (d) Bands of the FH and the slow SH mode for three designs, achieving FP and BP phase-matching with different SH group index n_{gSH} at the point of phase-matching: (i) $W/a = 2.1$ gives $n_{\text{gSH}} = 5$, (ii) $W/a = 1.65$ gives $n_{\text{gSH}} = 40$, (iii) $W/a = 1.55$ gives $n_{\text{gSH}} = -8$. All structures have $R/a = 0.35$ and $h/a = 1.4$. LN's c -axis is along the z -direction.

the change of W compared to the FH mode. Hence, by lowering W the SH band shifts faster toward higher frequencies compared to the FH band, which moves the point of phase-matching through the SH band. The phase-matching crossing between the FH and the SH bands for three values of W are shown in Fig. 2.4(d). Here, the frequency and wave-vector of the FH mode is doubled to overlap its band on that of the SH mode to identify the point of phase-matching. Fig. 2.4(d-i), corresponding to $W/a = 2.1$, shows the phase-matching crossing between a FP FH mode and a FP SH mode. We know they are FP, as both the modes at the point of crossing have positive sign of the group velocity. Fig. 2.4(d-ii), corresponding to a lower width of $W/a = 1.65$, also shows a FP case, but with a slower SH mode closer to the bandedge. In Fig. 2.4(d-iii), corresponding to an even lower width of $W/a = 1.55$, the point of phase-matching is pushed past the bandedge into the next BZ, where the SH mode has a negative v_g at the point of phase-matching. Hence here, a FP FH mode is phase-matched to a BP SH mode, giving us a BP configuration.

To understand the BP phase-matching better, the BHs distribution of the modes involved are plotted in Fig. 2.5(a). For the SH mode $C_{n,\text{SH}} = |\mathbf{z} \cdot \mathbf{C}_n(y=0, z=0)|$ is plotted and for the FH mode $C_{n,\text{FH}} = |\mathbf{y} \cdot \mathbf{C}_n(y=0, z=0)|$, in accordance with their dominant electric field component. The FH mode, which has a low group index and is away from the bandedge, has only one strong BH, whereas the slow SH mode with a higher group index and near the bandedge has two strong BHs. Importantly, we can see which BHs of the FH and SH modes coincide in k -value, when we plot the BH of the FH mode on a doubled k -axis. For this BP scenario, it is the dominant BH of the FH mode $C_{0,\text{FH}}$ that is phase-matched to the second strongest BH of the SH mode $C_{1,\text{SH}}$. The profiles of these two BHs are shown in Fig. 2.5(b). We see that they resemble their corresponding Bloch mode profiles in Figs. 2.4(b) and (c), and are concentrated well in the nanobeam, which means they have a good overlap with each other and the WG's nonlinearity profile. It should be mentioned, that in FP processes,

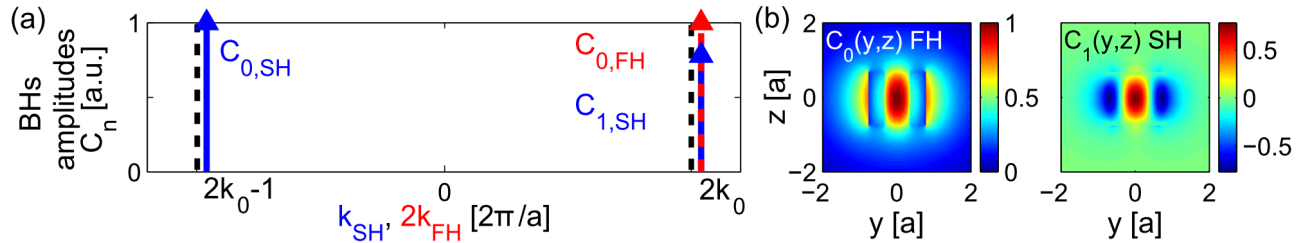


Figure 2.5: (a) Bloch harmonics distribution for the BP phase-matched nanobeam, with the band diagram shown in Fig. 2.4(d-iii), where $2k_0 = 0.52 \frac{2\pi}{a}$ at the point of crossing is marked there. The k -axis for the FH is doubled to show the coinciding BHs. For the SH mode $C_{n,SH} = |z \cdot C_n(y=0, z=0)|$ is plotted and for the FH mode $C_{n,FH} = |y \cdot C_n(y=0, z=0)|$. The dashed black lines mark the edges of the first BZ at $k = \pm\pi/a$; (b) The profile of the main BHs participating in the BP process. For the FP FH mode $y \cdot C_0(y, z)$ is plotted and for the BP SH mode $z \cdot C_1(y, z)$. The profiles are real-valued, done by multiplying each with a constant phase.

shown in Figs. 2.4(d-i) and (d-ii), it is the dominant BHs of both modes, $C_{0,FH}$ and $C_{0,SH}$, that are phase-matched to each other, making the FP process more efficient than the BP one.

2.2.4 The need for leaky SH modes and the troubles that come with it

An example of a practical phase-matched nanobeam structure was presented in the previous section. As said before, the main objective in this work is designing phase-matched PCSW structures, as they can offer strong dispersion engineering possibilities for the signal and idler modes. This task will be undertaken in the following section. However, before getting there, a point regarding the choice of modes should be discussed, that makes the following designs more challenging compared to the simple nanobeam example. In order to benefit from the unique properties of PCSWs for SPDC applications, we want to phase-match a pump mode to signal and idler modes that are close to the edges of the BZ. Near the bandedge is where group velocities vary substantially, so the signal and idler modes can access a wide range of group velocities. Moreover, strong non-dominant BHs are available in the Bloch modes near the bandedge, that are needed for satisfying phase-matching configurations in which the signal and idler photons are not propagating in the same direction as the pump mode. However, having the FH mode near the bandedge results in a leaky SH mode that is above the light line. The reason is as follows: We can see in the nanobeam design, that it is the SH mode that is near the bandedge and the FH mode is away from the bandedge. The lowest place in frequency that we can have a FH mode near the bandedge will be close to the first bandgap, around the frequency of $a/\lambda \approx 0.3$, as can be seen in Fig. 2.4(a). This is not strongly connected to the nanobeam design, but rather to the permittivity of LN. Hence, in any type of LN periodic WG, the lowest normalized frequency near the band edge for a FH mode is around $a/\lambda_{FH} \approx 0.3$. This means the SH frequency will be at least around $a/\lambda_{SH} \approx 0.6$, which is above the light line and results in a leaky SH mode.

This makes things more complicated. Both the numerical and the analytical treatment of a leaky mode, or in general decaying modes with a complex wave-vector, are more challenging compared to guided lossless modes with a real-valued wave-vector. The fact that the second/third-harmonic (TH) mode was a leaky mode seems to be why there were only few further investigations into the topic of studying higher-harmonic generation in PCSWs. There have been some experiments done on SHG [134, 135] and THG [136, 137, 138] in PCSWs. In all cases, the FH mode has been a slow mode near the bandedge for enhanced efficiency, and there has been no attempt in reaching phase-matching. The

PCSW was simply pumped at the FH frequency, and the generated SH or TH was detected from above the sample, due to the strong leakage. There has been an attempt in explaining the phase-matching process for the THG case [207]. The conclusion was that phase-matching cannot manifest itself due to the very short decay length of the TH mode, caused by the leakage of the mode and the material absorption of silicon, that would not allow the TH mode to build up along the propagation direction. However, there are investigations in 2D PC slabs [208, 209] involving leaky modes, that showed there exist leaky modes that have low enough leakage that can demonstrate enhancements in SHG when the phase-matching condition is satisfied. Consequently, for the investigations in this thesis, the challenge is not just satisfying the phase-matching condition, but to do it with a SH/pump mode that has a low enough leakage loss, such that the phase-matching condition can actually manifest itself and result in an efficient interaction. With this understanding, we move on in the next section to the design of PCSWs, with near the band edge FH modes and above the light line SH modes.

2.3 Standard photonic crystal slab waveguides (PCSWs)

The schematic of a W1 PCSW is shown in Fig. 2.6(a), created by removing one row of holes from a PC slab, introducing a line defect in it. A PC slab is a slab of dielectric material of subwavelength thickness, with holes etched in it periodically, where here a 2D periodic hexagonal pattern is chosen. The PC slab is capable of supporting Bloch modes, which are confined in the slab in the z -direction through TIR, and propagate in the xy -plane. The periodicity creates frequency bandgap regions, in which no propagating modes exist in the homogeneous PC slab. The functionality of the PCSW relies on this bandgap region, and the hexagonal pattern provides a large bandgap region suitable for waveguiding applications [127]. A guided mode can propagate in the line defect along the x -direction, confined along the z -direction by TIR and in the y -direction by the bandgap effect. In this section, the focus will be on the W1 PCSW, which is a standard type PCSW, and in the next section, the double-slot structure will be proposed as a better type of PCSW for SPDC applications. First, the formation of the guided FH mode and how its band diagram can be engineered are explained. Afterwards, the leaky SH mode above the light line and its properties are studied. Finally, a FP phase-matched design is presented with a slow FH mode, along with an explanation of how such a design can be tuned.

2.3.1 Guided FH mode and its engineering

Before starting, an important point on the symmetry of the modes in the PC slab must be explained, which restricts the symmetry of the FH mode of choice here. The z -even and z -odd modes have a different response to the bandgap effect. For the case of a LN PC slab with a hexagonal pattern, it is the z -even modes that exhibit a large bandgap region [210], allowing for the formation of fully guided modes over a large frequency and wave-vector bandwidth. On the other hand, the z -odd modes exhibit a small bandgap frequency range, formed in the higher frequencies near the light line, which also limits the range of available wave-vectors for formation of fully guided modes. Hence, z -even is the symmetry of interest for the FH modes in this work. Moreover, it is also desirable to have a symmetric slab in the z -direction. If the z -symmetry is broken, e.g. by having a substrate under the

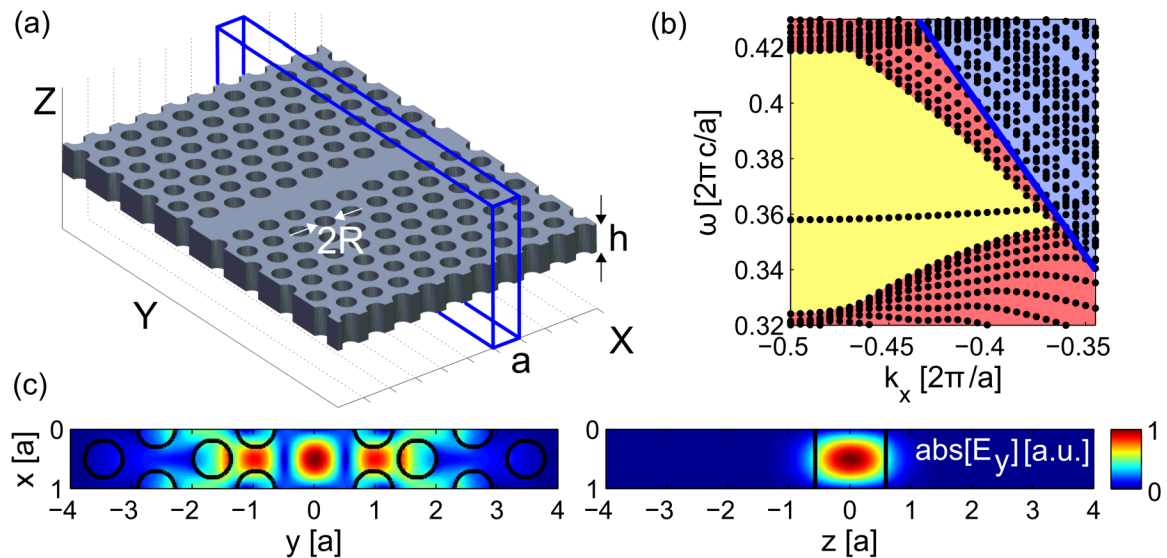


Figure 2.6: (a) Schematic of a W1 PCSW. The extents of a supercell are marked with solid blue lines. The slab thickness is h , the hole radius is R , and a is the distance between the adjacent holes; (b) Band diagram of the modes of the PCSW structure, projected along the propagation direction x . The solid blue line is the light line. The blue shaded region includes the modes above the light line. The red shaded region includes the modes that can propagate in the PC slab. The yellow shaded region is the partial gap, and the dots in it are the band diagram of the fully guided z -even- y -odd FH mode. Design parameters here are $h/a = 1.2$ and $R/a = 0.3$. LN's c -axis is along the y -direction; (c) The absolute value of the dominant electric field component E_y of the FH mode displayed in the $z = 0$ (left) and $y = 0$ (right) planes, at $\omega = 0.35944 \frac{2\pi c}{a}$ and $k = -0.4364 \frac{2\pi}{a}$.

PC slab, there would be coupling between the z -even and z -odd modes, which could be a cause for leakage into the PC slab. The z -even modes, also known as TE-like, have a dominant E_y electric field component. In particular, the z -even- y -odd guided modes are of interest here, because they have an even-looking mode profile of E_y along both the $y = 0$ and $z = 0$ planes. With the FH mode fixed such that it has a dominant E_y component, a good choice will be to have the LN's c -axis oriented along the y -direction in all our PCSW designs, which is the case throughout this work. The reason is that if we manage to find a phase-matched SH mode also with a dominant E_y component, the nonlinear interaction can be most efficiently mediated using the d_{33} coefficient of the d -tensor. If we find a phase-matched SH mode with a dominant E_z component, the d_{31} component can still be used.

A PCSW is effectively a 1D periodic structure, with a unitcell that is of length a along the x -direction and infinitely large in the yz -plane. Such a unitcell is also referred to as a supercell, marked in Fig. 2.6(a). The guided modes of this structure have a wave-vector $\mathbf{k} = k\mathbf{x}$. For a PCSW mode to be fully guided in the line defect, all the modes that can propagate in the PC slab and in the surrounding vacuum at that frequency must have a wave-vector whose projection along the x -direction has a smaller magnitude than k . In this way, the guided mode will not couple to those radiative modes and hence will be confined in the y - and z -directions. This in terms of the band diagram means, that if we find all the modes that can propagate in the PC slab and in vacuum, and plot them in a 1D band diagram called a projected band diagram, where their k -value is projected along the x -direction, there should exist a region in that band diagram that is empty of modes, which can be referred to as a partial gap. If we create a line defect in the PC slab, and with it create a mode whose band falls into this partial gap region, then that mode would be fully guided. Such a band diagram is shown in Fig. 2.6(b), where the MPB tool is used to find all the modes in the supercell of the W1 PCSW. The first thing that can be identified in Fig. 2.6(b), is the dense packing of dots, which represent the projected band

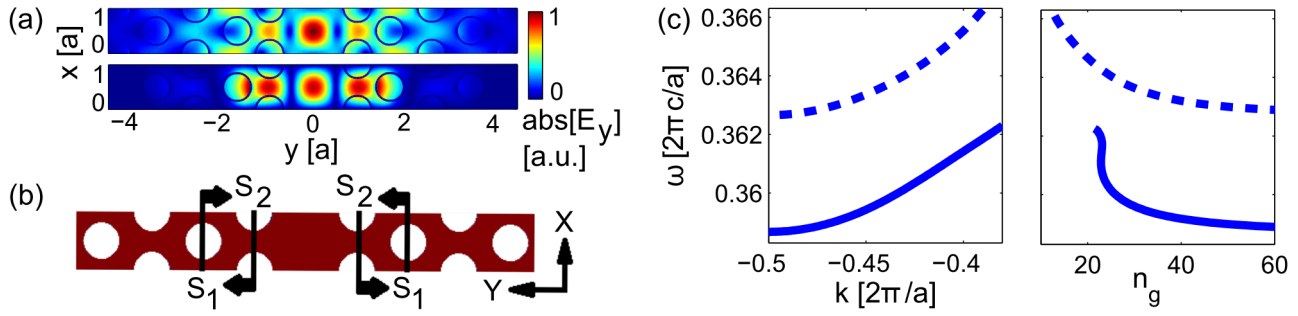


Figure 2.7: (a) Absolute value of E_y at the $z = 0$ plane for the guided mode at the wave-vectors of $k = -0.4 \frac{2\pi}{a}$ (upper) and $k = -0.5 \frac{2\pi}{a}$ (lower); (b) The dispersion engineering design by shifting the first and second rows of holes, out- and in-wards, respectively; (c) Band and group index of the mode without dispersion engineering (dashed line) and with it ($S_1/a = 0.1$, $S_2/a = 0.05$, solid line). $h/a = 1.2$ and $R/a = 0.3$ for both designs.

diagram of the continuum of modes propagating in the PC slab and the surrounding vacuum appearing as discrete points due to the finite yz -size of the supercell used in the simulation. The dots that appear above the light line in the blue shaded region correspond to modes that can propagate in vacuum or couple to vacuum modes. The dots in the red shaded region under the light line correspond to modes that do not couple to vacuum modes but can propagate in the PC slab or couple to the PC slab modes. The yellow shaded region is the partial gap, caused by the PC bandgap effect, in which no slab or vacuum modes appear, and the line of dots that appears in the partial gap is the band diagram of the fully guided FH mode. The band diagram is shown in the negative part of the first BZ, as the FP part of the guided mode happens to be there, apparent from the positive slope of its band. The mode profile of the dominant electric field component of this mode, E_y , is shown in Fig. 2.6(c), showing the modal confinement in the y - and z -directions. It should be noted, that this mode does not cease to exist once its band enters the region of modes of slab and vacuum, but it becomes leaky.

The properties of this guided mode, such as the field profile, the group velocity, and the group velocity dispersion, can be controlled through slight changes in the geometrical parameters of the structure surrounding the line defect. Here, a standard dispersion engineering technique is demonstrated, for achieving low-dispersion slow-light or flat-band slow light, to get a range of frequencies over which the group index of the mode is relatively constant, in other words, the group velocity dispersion is low. A flat band increases the bandwidth of the slow-light region and is also desirable for many pulsed parametric processes [141, 142, 139]. Different designs for achieving low dispersion slow-light in PCSWs exist [211, 128, 212, 213], all based on changing the geometry of the structure near the line defect, as the field profile of the guided mode changes relatively strongly along the band diagram. This is demonstrated in Fig. 2.7(a). Here we see that the field profiles of the mode at the band edge $k = -0.5 \frac{2\pi}{a}$ and away from the band edge at $k = -0.4 \frac{2\pi}{a}$ differ considerably. Hence, by changing the geometry near the line defect, each part of the band diagram could feel this change in dielectric permittivity differently due to their different field profiles. The band diagram at different k -values could shift up and down in frequency differently and consequently reshape the band diagram. For demonstrating dispersion engineering here, transversal shifting of the first and second rows of holes adjacent to the line defect is used [128], as shown in Fig. 2.7(b). This recipe is chosen, as it seems feasible for fabrication. The band diagram and the corresponding group index of the guided mode, with and without dispersion engineering are shown in Fig. 2.7(c). It can be seen that for a mode without engineering, the group index rises monotonically and goes to infinity at the band edge.

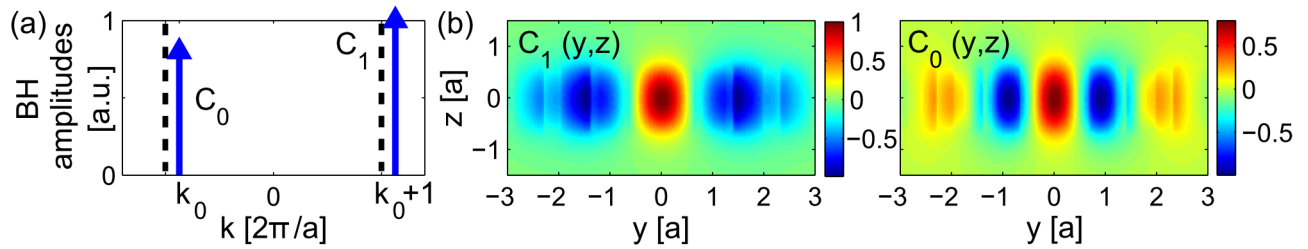


Figure 2.8: (a) The Bloch harmonic distribution of the FH guided mode, at $k_0 = -0.4364 \frac{2\pi}{a}$ in the band of Fig. 2.6(b). The dashed lines mark the edges of the first BZ at $k = \pm\pi/a$; (b) Profiles of the two strongest BHs. The profiles are real-valued, done by multiplying each with a constant phase.

With dispersion engineering, the group index spectrum gets rather flat around $n_g \approx 23$.

Finally, let us take a look at the BH distribution of the FH mode, with the above mentioned dispersion engineering design, to determine the suitable BHs for an efficient TWM process. The BH distribution $C_n = |\mathbf{y} \cdot \mathbf{C}_n(y=0, z=0)|$ is shown in Fig. 2.8(a), for the mode at $k = -0.4364 \frac{2\pi}{a}$. The reason for choosing this point in the band is that soon a phase-matched design will be presented that has a phase-matching crossing point there. The mode is rather slow here with a group index of $n_g = 28$. There are two substantial BHs for this Bloch mode that are shown here, at the negative and positive k -values, with comparable amplitudes, as we would expect for a slow mode. The dominant BH is the positive- k one, as the mode is overall FP. The profiles for both the BHs are shown in Fig. 2.8(b). Both BHs seem to be strongly concentrated in the middle of the line defect, hence making them both appropriate for interaction with any SH mode that is also concentrated in the line defect. We can now move on to find a suitable SH mode for phase-matching.

2.3.2 Leaky second-harmonic mode above the light line

It was explained previously, why leaky SH modes above the light line cannot be avoided for reaching phase-matched designs with a FH mode near the bandedge in a LN periodic WG. We can also see this for the specific W1 PCSW structure presented here, where the FH mode near the bandedge has a frequency around $\omega_{\text{FH}} \approx 0.36 \frac{2\pi c}{a}$, which means the SH mode must be around $\omega_{\text{SH}} \approx 0.72 \frac{2\pi c}{a}$, making it a leaky mode above the light line. In this section, we want to find and study a SH mode in this frequency range suitable for phase-matching. Before that, however, a general point about the design procedure must be explained. A leaky SH mode has a complex-valued wave-vector $k = k' + ik''$, where the imaginary part determines the decay length of the mode $L_{\text{decay}} = 1/k''$. The phase-matching condition $k_{\text{p}} - k_{\text{s}} - k_{\text{l}} = \frac{2\pi}{a} Q$ of Eq. (2.24) was found assuming Bloch modes with real-valued wave-vectors, as the origin of the calculation was based on the conjugated reciprocity theorem, which is only valid for such modes. With modes that have complex-valued wave-vectors, in other words decaying modes, the same phase-matching condition is valid, but with k_{p} , k_{s} , and k_{l} now being complex-valued quantities. This type of complex-valued phase-matching condition will be comprehensively derived in the following chapters, where analytical calculations are done for describing SHG and SPDC with decaying modes. Nonetheless, with complex-valued wave-vectors we have $\Delta k = \Delta k' + i\Delta k''$, where here $\Delta k' = k_{\text{p}}' - k_{\text{s}}' - k_{\text{l}}' - \frac{2\pi}{a} Q$ is called the phase-mismatch and $\Delta k'' = k_{\text{p}}'' - k_{\text{s}}'' - k_{\text{l}}''$ the loss-mismatch. In the design processes that follow in this chapter, the goal is to reach $\Delta k' = 0$ in a phase-matched structure. There is no effort paid in the designs here to make the loss-mismatch zero, as it does not result in an enhanced efficiency in the same way that phase-mismatch does. A $\Delta k'' = 0$ only

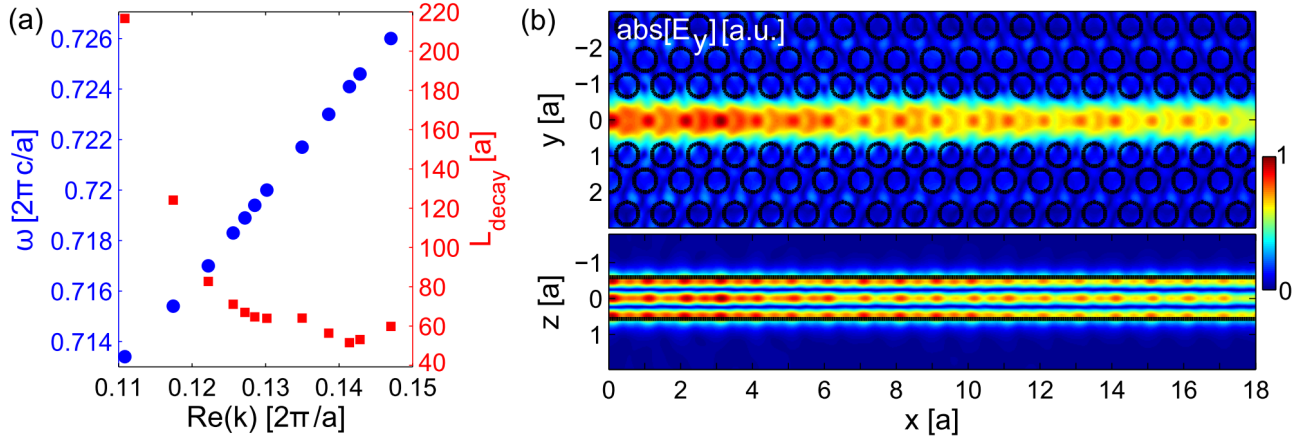


Figure 2.9: (a) Band diagram of the leaky TE_{02} SH mode. The blue circles (left axis) are the frequencies, the red squares (right axis) are the decay lengths; (b) Absolute value of E_y at the $z = 0$ (top) and $y = 0$ (bottom) planes, in a linear FDTD simulation, when the structure is excited from the left side with a CW source at the frequency of $\omega = 0.71889 \frac{2\pi c}{a}$, where the source profile is chosen so that the leaky TE_{02} is dominantly excited (with $k = 0.1272 \frac{2\pi}{a}$). Design parameters are $S_1/a = 0.1$, $S_2/a = 0.05$, $h/a = 1.2$, and $R/a = 0.3$.

serves to preserve the sinc-functionality of the efficiency on $\Delta k'$. To have an efficient process, each one of k_p'' , k_s'' , and k_i'' should be minimized as much as possible. In the case of this work, since we ideally have lossless modes at the FH frequency range, the main effort in controlling loss boils down to minimizing k_p'' , or in other words, minimizing the leakage of the pump mode. In the following discussions in this chapter, whenever k_p/k_{SH} is mentioned, it indicates the real part of the pump/SH mode, and its imaginary part is described through the decay length of the mode.

Let us first determine a range of suitable values for k_p in the first BZ needed for phase-matching. This will let us know in which part of the band diagram we should look for the pump mode. Knowing the range of wave-vectors for the signal/idler modes allows us to find this region, by considering all the possible phase-matching combinations. Having a signal/idler mode near the bandedge means $-0.5 \frac{2\pi}{a} < k_s, k_i < -0.4 \frac{2\pi}{a}$ or $0.4 \frac{2\pi}{a} < k_s, k_i < 0.5 \frac{2\pi}{a}$. Using the phase-matching condition $k_p = k_s + k_i + \frac{2\pi}{a} Q$, we get $-\frac{2\pi}{a} < k_s + k_i < -0.8 \frac{2\pi}{a}$, $0.8 \frac{2\pi}{a} < k_s + k_i < \frac{2\pi}{a}$, or $-0.1 \frac{2\pi}{a} < k_s + k_i < 0.1 \frac{2\pi}{a}$. All these cases can be translated to the first BZ using $Q = 1$, $Q = -1$, and $Q = 0$, respectively, giving us $-0.2 \frac{2\pi}{a} < k_p < 0.2 \frac{2\pi}{a}$ as a range of wave-vectors for the potential phase-matched pump mode. Moreover, this mode should preferably have a dominant E_y component, to use the d_{33} coefficient of the nonlinearity tensor. Having a dominant E_z component is also acceptable, as one can still use d_{31} . Whichever the dominant component is, it has to have an even-looking field profile with respect to both y - and z -directions, so that it can have a nonzero overlap with the nonlinear polarization.

With all this in mind, a suitable z -even- y -odd SH mode was identified, with a dominant E_y component, whose band diagram is shown in Fig. 2.9(a), along with its decay length. Both decay length and frequency are plotted as a function of the real part of the wave-vector. The band is shown in the region $0.11 < \text{Re}(k)a/2\pi < 0.15$, which as will be shown in the next section is around a point that satisfies a FP phase-matching condition with the slow FH mode. The field profile for the E_y component of this mode is shown in Fig. 2.9(b), where the structure is excited from one side to observe the decaying nature of the SH mode along the propagation direction. This mode can be roughly categorized as a TE_{02} mode, as the profile of its dominant electric field component has no nodes in the y -direction and two nodes in the z -direction. The finite-difference time-domain (FDTD) method is used for finding the band diagram and the field profile of this mode, the details of which are given in appendix A.

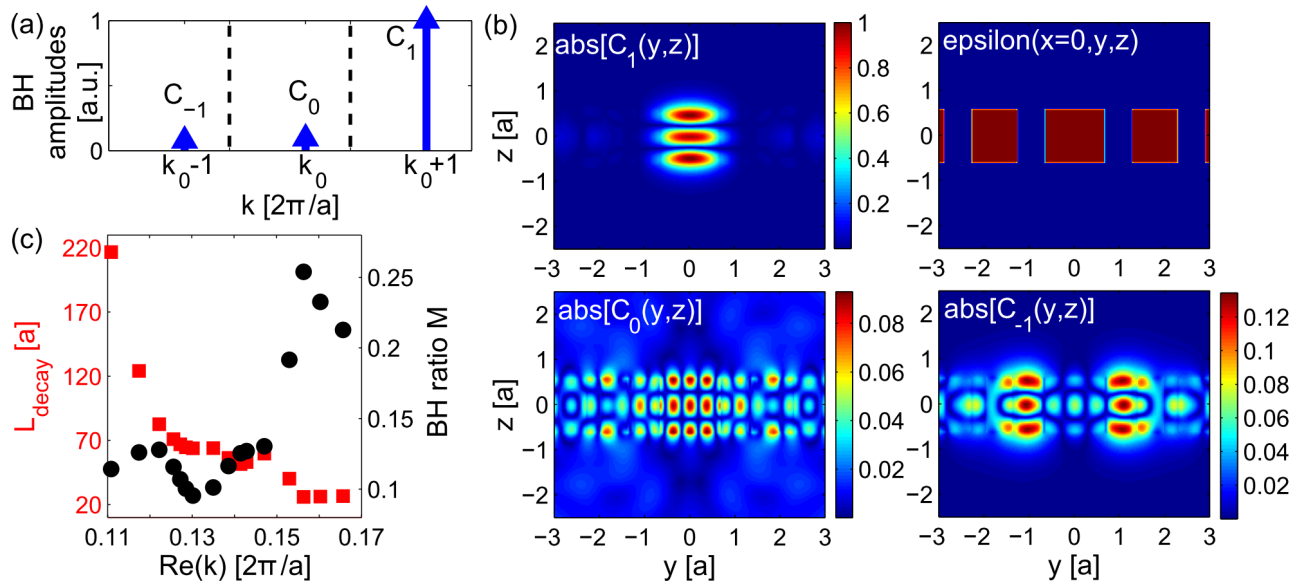


Figure 2.10: (a) BH distribution $C_n = |\mathbf{y} \cdot \mathbf{C}_n(y=0, z=0)|$ for the SH mode at $k_0 = 0.1272 \frac{2\pi}{a}$. The dashed lines mark the edges of the first BZ at $k = \pm\pi/a$; (b) The absolute value of the three strongest BH profiles, along with the dielectric profile in the $x=0$ plane; (c) Comparing the trend of the decay length to the strength of the non-dominant BHs. The red squares (left axis) are L_{decay} and the black circles are the ratio $M \equiv \sqrt{C_0^2 + C_{-1}^2}/C_1$.

To better understand how this mode can efficiently participate in a TWM process, let us take a look at its BHs. For this, the FP SH mode at $k = k_0 = 0.1272 \frac{2\pi}{a}$ in the first BZ is considered here. The BH amplitudes are shown in Fig. 2.10(a), where only the three strongest BHs are shown. The dominant BH is C_1 at $k = k_0 + \frac{2\pi}{a}$. The profiles for the three BHs are shown in Fig. 2.10(b), along with a cut of the dielectric profile of the structure for comparison. We see that the profile of the dominant BH is well concentrated in the line defect region. Henceforth, for an efficient interaction, we want to use the C_1 BH for phase-matching, being the strongest BH with a suitable profile. Looking at the BH profiles for the leaky mode can also give us some information about the leakage mechanism of it, and potentially a way to reduce it. We can see in Fig. 2.10(b), that all three BHs leak in the y -direction into the PC slab, although this is more severe for the two weaker BHs. Moreover, it is only the C_0 BH that leaks in the z -direction into the surrounding vacuum, because it is the only BH whose wave-vector is smaller than the wave-vector of a plane-wave propagating in vacuum at that frequency, which is $k_{vac} = 0.71889 \frac{2\pi}{a}$ at $\omega = 0.71889 \frac{2\pi c}{a}$. From this observation, we can conclude that the two weaker BHs are the ones strongly contributing to the leakage of this mode. We can also investigate if any trend exists in the change of the decay length and the strength of the two weaker BHs over the leaky mode's band. The ratio $M \equiv \sqrt{C_0^2 + C_{-1}^2}/C_1$ is defined, to quantify the strength of the two weaker BHs compared to the dominant BH, and the result is shown in Fig. 2.10(c). We can see that for most regions in the band, an increasing M ratio comes with a decreasing L_{decay} . The dependency is not a simple monotonic one, as the weaker BHs with different wave-vectors along the band could have differing leaking strengths themselves. Nonetheless, around $k = 0.16 \frac{2\pi}{a}$, where L_{decay} is the smallest, the M ratio is much larger than around $k = 0.11 \frac{2\pi}{a}$, where L_{decay} is the largest. From these observations, it is reasonable to conclude that to have a low-leakage SH mode, we need to reduce the contribution of all the non-dominant BHs in the Bloch mode as much as possible. One way of reducing these contributions, is to reduce the interaction of the mode with the periodicity of the surrounding PC slab. This could be understood as follows: Consider the case where there is no PC slab surrounding the line defect and

we just have a ridge WG with a transverse size comparable to the line defect. With $\lambda_{\text{SH}} = 775$ nm and $a/\lambda_{\text{SH}} = 0.71889$, the periodicity must be $a = 0.557$ μm , which gives the height and width of $h = 1.2a = 0.668$ μm and $W = 1.33a = 0.742$ μm for this imaginary ridge WG, respectively. $1.33a$ is the distance between the edge of the two rows of holes surrounding the line defect in this structure. The TE_{02} mode in this ridge WG has an effective refractive index of $n_{\text{eff}} = 1.57$, which gives a normalized wave-vector of $\frac{ka}{2\pi} = \frac{2\pi}{\lambda_{\text{SH}}} n_{\text{eff}} \frac{a}{2\pi} = \frac{a}{\lambda_{\text{SH}}} n_{\text{eff}} \approx 0.71889 \times 1.57 \approx 1.129$ for this imaginary ridge WG. This is very close to the k -value of the C_1 BH of the actual leaky Bloch mode. This means, that one can think of the C_1 BH as the main BH associated with the line defect region when there is no PC slab, and of the two weaker BHs as being created due to the interaction of the mode with the PC slab. Hence, with a SH mode that has less interaction with the PC slab, these two BHs will become weaker, and the mode's leakage will be reduced. This principle will be used later on in this chapter, to propose the use of double-slot PCSWs, that have a SH mode with a much lower leakage loss.

2.3.3 A forward-propagating phase-matched design in a W1 PCSW

Here, a FP phase-matched design in a LN W1 PCSW is presented. The modes at the FH and SH frequencies, along with their field profiles and BHs are already shown in the previous parts of this section, where the design parameters of the structure are $R/a = 0.3$, $h/a = 1.2$, $S_1/a = 0.1$, and $S_2/a = 0.05$. The c -axis is along the y -direction, to make use of the d_{33} coefficient of the nonlinearity tensor, which mediates the nonlinear interaction between the dominant components of the FH and the SH modes, both along the y -direction. The low dispersion slow-light reduces the sensitivity of the group index of the FH mode at the point of phase-matching with respect to the frequency shifts of the band, that could be caused by inaccuracy in a possible fabrication. The band diagrams of the SH and FH modes crossing each other are shown in Fig. 2.11(a). The dashed line here represents the SH band, translated according to the phase-matching condition. For this translation, the frequency of the SH band is divided by 2 and its wave-vector is translated using $(\frac{k_{\text{SH}}a}{2\pi} - 1)/2$, following $k_{\text{SH}} - 2k_{\text{FH}} = \frac{2\pi}{a} Q$ with $Q = 1$. We can see that both of the modes have a positive slope, indicating FP phase-matching. The crossing is at $k_{\text{FH}} = -0.4364 \frac{2\pi}{a}$ and $\omega_{\text{FH}} = 0.35944 \frac{2\pi c}{a}$, which corresponds to $k_{\text{SH}} = 0.1272 \frac{2\pi}{a}$ and $\omega_{\text{SH}} = 0.71889 \frac{2\pi c}{a}$. At the phase-matching point the group indices are $n_{\text{gFH}} = 28$ and $n_{\text{gSH}} = 2.67 + i1.26$. The decay length of the SH mode at the point of phase-matching is about 67 periods. At the end, the lattice constant is set to $a = 0.557$ μm , which fixes the FH wavelength to $\lambda_{\text{FH}} = 1550$ nm and gives us physical dimensions of $h = 0.668$ μm and $R = 0.167$ μm . In Fig. 2.11(b), the BH distribution of the FH and SH modes are shown together, with the k -axis for the SH divided by two to show the overlapping BHs. We see that the dominant BHs of the modes are phase-matched in this FP case. An important capability of this design is its tunability, thanks to the specific choice of the SH mode. The TE_{02} mode has two nodes in its field profile in the z -direction, making it more sensitive than the FH mode to a change in the thickness of the slab. This is of importance in reaching and tuning phase-matching: By increasing (decreasing) the thickness of the slab, the SH band shifts down (up) in frequency with respect to the FH band. Moreover, a change of thickness does not strongly affect the shape of the FH band except for pushing it up and down in frequency, as the group velocity and its dispersion are more dependent on the in-slab parameters. Hence, we get to move the point of phase-matching through the FH band, without affecting its dispersion engineering. This is demonstrated in

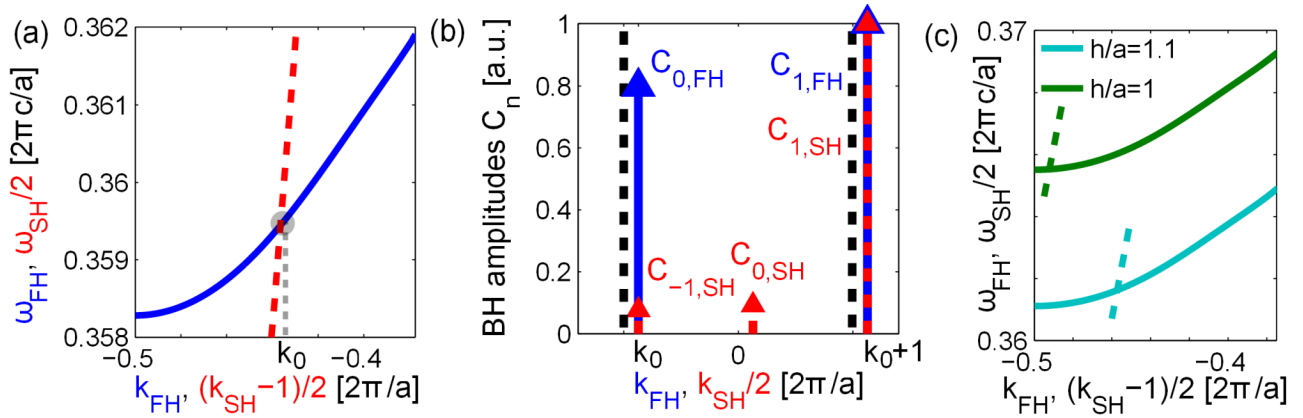


Figure 2.11: (a) Band diagram of the FH mode, together with the SH band translated according to the phase-matching condition. Phase-matching is at $k_0 = -0.4364 \frac{2\pi}{a}$. Design parameters are $R/a = 0.3$, $h/a = 1.2$, $S_1/a = 0.1$, and $S_2/a = 0.05$; (b) The BHs of the FP phase-matched FH and SH modes. The dashed black lines mark the edges of the first BZ at $k = \pm\pi/a$; (c) Tunability of the phase-matched design by changing the thickness of the slab. k_{SH} in all plots represents the real part of the SH's wave-vector.

Fig. 2.11(c), where the phase-matching crossings for two smaller slab thicknesses are displayed.

To summarize, FP phase-matching for a TWM process was reached here in a W1 PCSW, using a FH mode near the bandedge and a leaky SH mode above the light line. However, the leaky SH mode found here in the W1 structure has rather short decay lengths of tens of periods, as shown in Fig. 2.9(a), and it would be highly desirable if the decay length for this leaky mode can be increased. Moreover, as will be seen in the next section, interesting phase-matching configurations could be reached when the SH/pump mode has a wave-vector near the high-symmetry point of $k = 0$ in the first BZ. However, the SH mode becomes very leaky at $k = 0$. This could be understood, as being caused by the stronger interaction of the mode with the PC slab at this high-symmetry point in the band diagram, causing a stronger diffraction effect, and consequently a stronger leakage. This makes the W1 structure rather limited for the purpose of this work. Henceforth, a PCSW structure is needed with a longer decay length for the leaky mode, especially around the $k = 0$ part of its band. As said before, the loss of the leaky mode can be reduced by lowering its interaction with the periodic PC slab, which brings us to the double-slot PCSW proposal.

2.4 A double-slot PCSW: an ideal structure for TWM

In this section, the double-slot PCSW design is proposed, shown in Fig. 2.12(a), as an ideal structure for parametric processes involving a higher-harmonic frequency above the light line. Double-slot structures have been previously used for sensing applications [214], but in this work, they are found to be uniquely useful for SPDC applications. This structure allows for having low leakage pump modes, by reducing the interaction of the pump mode with the PC slab, while still allowing for having dispersion engineered signal and idler modes. Moreover, it allows for low loss pump modes near $k = 0$, which is a key point in the upcoming phase-matching proposals. In this section, the modes in this structure and their engineering are investigated. Afterwards, designs are presented for all three cases of FP, BP, and CP phase-matching, and also for simultaneous phase-matching of multiple processes. These designs will be used in chapter 4 for SPDC applications, to demonstrate the strength of PCSWs in controlling different degrees of entanglement between generated photon

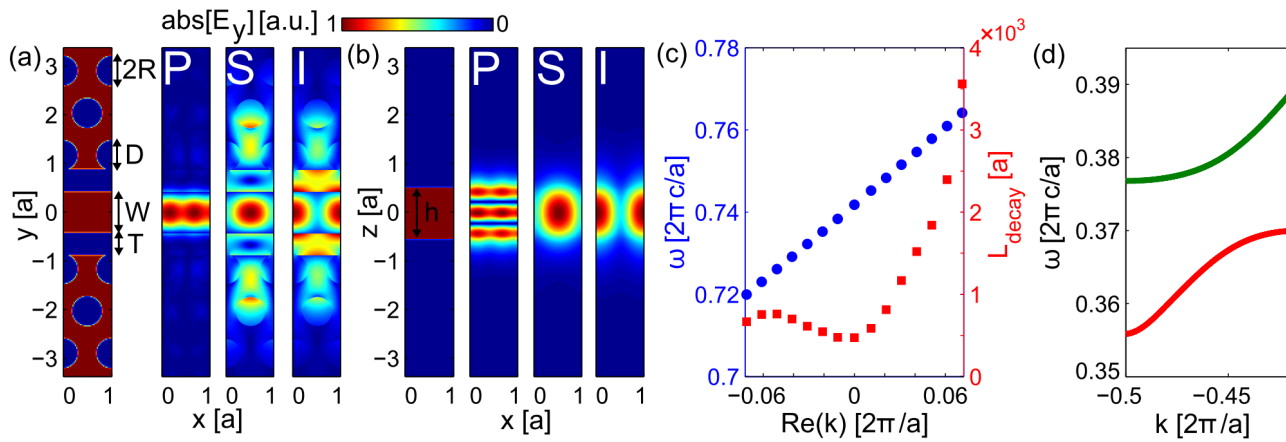


Figure 2.12: The geometry of the double-slot PCSW, with design parameters $R/a = 0.3$, $h/a = 1.07$, $W/a = 0.85$, $T/a = 0.45$, and $D/a = 0.59$, along with the absolute value of the dominant E_y component profile of the modes, shown at planes (a) $z = 0$ and (b) $y = 0$. P stands for pump, S for signal, and I for idler. All modes are of z -even- y -odd symmetry. LN's c -axis is along the y -direction; (c) Band diagram of the leaky pump mode, along with its decay length; (d) Band diagram of the signal mode, the green curve, and the idler mode, the red curve.

pairs. Before proceeding, it should be mentioned that all the modes in the designs in this section are TE-like, with dominant E_y components, and with the LN's c -axis along the y -direction, where all the nonlinear interactions are dominantly mediated by the d_{33} coefficient of the nonlinear tensor.

2.4.1 Leaky mode, guided modes, and band engineering

The slots, visible in Fig. 2.12(a) with width T , reduce the interaction of the pump mode with the PC slab. The slot width T has to be large enough for the pump mode to not interact with the PC slab, and small enough for modes around the FH frequency that are transversally broader, to interact with the PC slab, which allows for the formation of Bloch modes and dispersion engineering. This can be seen in the mode profiles, shown in Figs. 2.12(a) and (b). The pump mode, which has a smaller wavelength, is confined to the central WG and its mode profile is close to that of a ridge WG, not showing strong periodic behavior. The weak interaction of the pump mode with the periodic structure has the wanted effect on its leakage and band diagram. The FP pump mode's band diagram is shown in Fig. 2.12(c). We can see that the decay length of the leaky pump mode in the double-slot structure is hundreds of periods, which is an order of magnitude larger than that of the W1 structure. Moreover, at the high symmetry point of $k = 0$ there is no splitting in the band diagram. A band splitting at a high symmetry point is what one would expect from a Bloch mode. This tells us that the pump mode here is very weakly interacting with the PC slab, and essentially only feels the central ridge WG.

On the other hand, the modes around the FH frequency, that have larger wavelengths, have a transversally broader profile, that is strongly interacting with the PC slab and is showing periodic behavior, as can be seen in their mode profiles in Figs. 2.12(a) and (b). In this case, we have two distinct modes around the FH frequency, whose strongly dispersive bands are shown in Fig. 2.12(d). Here, the upper band in frequency is called signal and the lower band idler. The origin of these two modes is an anticrossing between the bands of an edge state of the PC slab and the guided mode of the central ridge WG. The PC slab supports an edge state, with its field profile shown in Fig. 2.13(a) and its band shown in Fig. 2.13(b). The band of the edge state is rather flat, and its position in frequency could be controlled by the geometry of the edge, where here it is done by the D parameter shown in

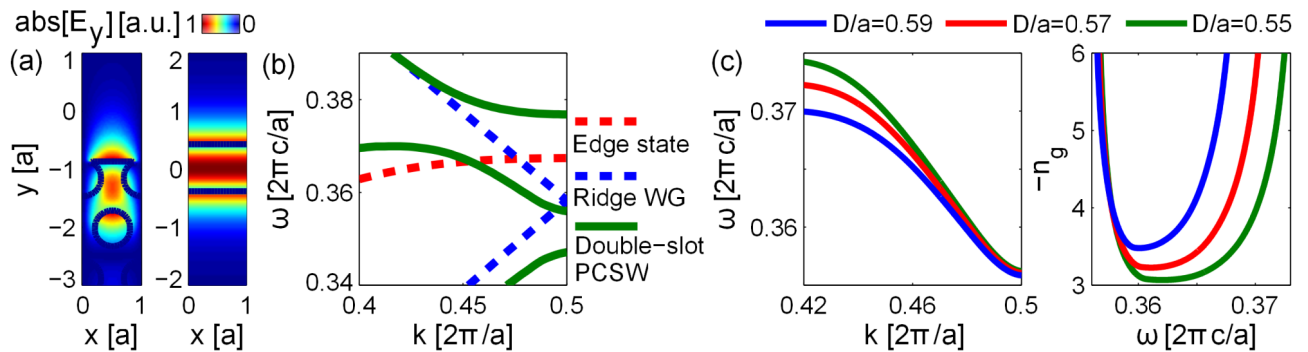


Figure 2.13: (a) Absolute value of E_y for the edge state (left) and the ridge WG mode (right); (b) Bands of the edge state, the ridge WG, and the double slot PCSW, showing the anticrossing; (c) Engineering the idler mode's band and group index by changing the D parameter, marked on Fig. 2.12(a). The other design parameters are fixed to $R/a = 0.3$, $h/a = 1.07$, $W/a = 0.85$, and $T/a = 0.45$.

Fig. 2.12(a). The ridge WG supports a guided mode, with its field profile shown in Fig. 2.13(a) and its band shown in Fig. 2.13(b), where the band is artificially folded at the bandedge. Once we bring the WG close together with the two PC slabs on both its sides, these modes couple with each other, and at the point their bands cross in the band diagram, there will be an anticrossing split in the bands, as can be seen in Fig. 2.13(b). The extent of the splitting in frequency can be controlled through the slot width T . This anticrossing creates the two signal and idler bands. The lowest band of the double-slot PCSW shown in Fig. 2.13(b) is caused by the splitting of the ridge WG band at the bandedge, due to the periodic nature of the interaction with the PC slab. Finally, we can engineer bands of the guided modes in the double-slot structure by changing in-slab parameters like T and D . This can be seen in Fig. 2.13(c), where the band of the idler mode and its group index are shown with a changing D parameter. The D parameter controls the band of the edge state, and as can be seen here, by varying it we can fine tune the n_g of the idler mode.

2.4.2 Forward-, backward-, and counterpropagating phase-matching

All the cases of FP, BP, and CP phase-matching can be reached with the double-slot PCSW. Here the FP and BP cases are reached in one structure, using the same design shown in Fig. 2.12. The overlapped bands, showing the crossings, are displayed in Fig. 2.14(a). In this band diagram, the band of the FP pump mode, translated using $(\frac{k_{pa}}{2\pi} - 1)/2$ and $\omega_p/2$, is crossing the band of the FP signal mode (the green curve), giving us a FP phase-matching, marked with a shaded green circle. Using this configuration for SPDC means, that a FP pump mode can generate a pair of photons, both propagating in the same direction as the pump. In the same plot, the band of the BP pump mode is shown, translated using $(\frac{k_{pa}}{2\pi} - 1)/2$ and $\omega_p/2$, which is crossing the band of the FP idler mode, giving us a BP phase-matching, marked with a shaded red circle. As the material is reciprocal, the configuration with the opposite propagation direction is also phase-matched, which means a FP pump mode is phase-matched to a BP idler mode. Using this configuration for SPDC means, that a FP pump mode can generate a pair of photons, both propagating in the opposite direction to the pump.

Of more interest for the SPDC application, is the CP case, especially for heralded sources of single-photons, as was discussed in chapter 1. In the CP configuration, the generated photons in the pair are propagating in opposite directions to each other. To reach CP phase-matching, a design with a larger slab thickness h is used, that brings the band of the pump mode lower in frequency with

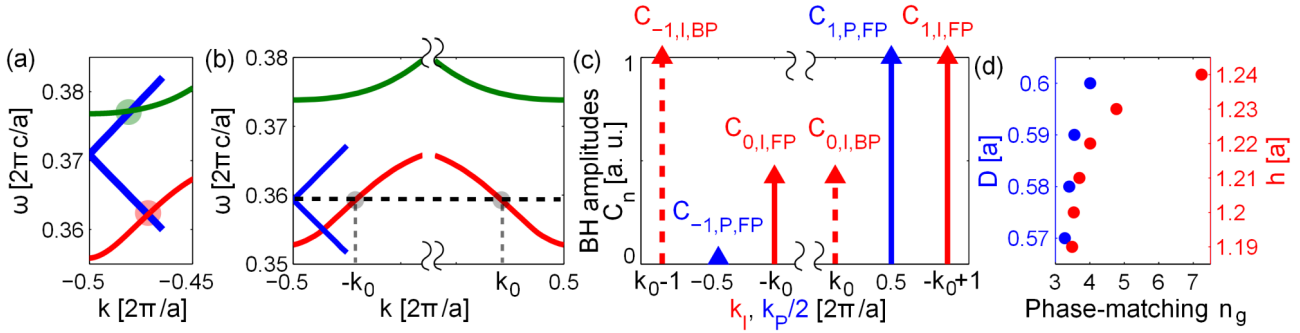


Figure 2.14: (a) Overlapped bands of the design of Fig. 2.12, showing FP and BP phase-matching. The FP signal (green curve) is crossing a FP pump whose band is translated using $(\frac{k_p a}{2\pi} - 1)/2$ and $\omega_p/2$. The FP idler (red curve) is crossing a BP pump whose band is translated using $(\frac{k_p a}{2\pi} - 1)/2$ and $\omega_p/2$. Design parameters are $R/a = 0.3$, $h/a = 1.07$, $W/a = 0.85$, $T/a = 0.45$, and $D/a = 0.59$; (b) Overlapped bands showing the CP phase-matching, where the dashed horizontal line marks the frequency $\omega_p/2$ for the pump mode at $k_p = 0$, with $L_{\text{decay}} \approx 10^3 a$. At this frequency, the pump is phase-matched to a pair of FP and BP idler modes, with $k_0 = 0.471 \frac{2\pi}{a}$. Design parameters are $R/a = 0.3$, $h/a = 1.15$, $W/a = 0.85$, $T/a = 0.45$, and $D/a = 0.59$; (c) BH distribution $C_n = |\mathbf{y} \cdot \mathbf{C}_n(y=0, z=0)|$ for the modes participating in the CP phase-matching shown in (b); (d) Group index of the idler mode at the point of degenerate CP phase-matching, at $k = -k_0$ in plot (b), as a function of design parameters D and h (see Fig. 2.12(a)), demonstrating the tunability of this scheme.

respect to the signal and idler modes, as shown in Fig. 2.14(b). The phase-matching crossing point is determined with a dashed horizontal line, which is between the FP pump mode at $k_p = 0$, the FP idler mode at $k_{\text{FP}} = -k_0$, and the BP idler mode at $k_{\text{BP}} = -k_{\text{FP}} = k_0$, giving $\Delta k = k_p + k_{\text{BP}} + k_{\text{FP}} = 0$. To understand this better, the BH distribution of the modes is shown in Fig. 2.14(c). The BHs contributing dominantly to this interaction are: $C_{1,\text{P,FP}}$ at $k = \frac{2\pi}{a}$ that is the only dominant and non-negligible BH of the FP pump mode, $C_{1,\text{I,FP}}$ at $-k_0 + \frac{2\pi}{a}$ that is the dominant BH of the FP idler mode, and $C_{0,\text{I,BP}}$ at k_0 that is the second strongest BH of the BP idler mode. We can see that the k -values of $C_{1,\text{I,FP}}$ and $C_{0,\text{I,BP}}$ always sum up to $\frac{2\pi}{a}$, satisfying the phase-matching condition to the dominant BH of the pump mode. This tells us, that with a pump mode at frequency ω_p with $k_p = 0$ in the first BZ, CP phase-matching is always satisfied with any mode at frequency $\omega_p/2$, regardless of what the wave-vector of that mode is. The only thing that should be paid attention to in such a configuration, is the strength of the overlap integral of the an interaction, which depends on the strength of the second strongest BH of the Bloch mode at $\omega_p/2$. In this specific case, the idler mode near the bandedge has a relatively strong next-to-dominant BH, with $C_{0,\text{I,BP}}$ having about half the amplitude of the dominant $C_{1,\text{I,FP}}$ BH, which results in an efficient CP interaction compared to a FP one that involves only the dominant BHs.

As was mentioned in chapter 1, to engineer the spectral degree of entanglement in photon-pairs, it is important to have control over the group velocities of the modes at the point of phase-matching. Two different ways can be imagined for doing this in the double-slot PCSW structure. It was shown in Fig. 2.13(c), that by changing the in-slab parameter D (see Fig. 2.12(a)), the band of the guided idler mode and its group index can be changed. On the other hand, the D parameter has a negligible effect on the band of the pump mode. Considering the CP configuration, this means that by changing D the frequency of phase-matching at $\omega_p/2$ will not be moved, as the pump mode is unaffected. Only the n_g of the idler mode at that frequency will be changed. This is demonstrated in Fig. 2.14(d), where the n_g of the idler at the point of CP phase-matching is found for different D values. The second method of tuning is similar to what was shown in Fig. 2.11(c) for the W1 PCSW, which is done through changing the thickness of the slab h . The effectiveness of this method for the double-slot

structure can already be seen by comparing Figs. 2.14(a) and (b), corresponding to two structures with different slab thicknesses. We can see that the pump band is shifted in frequency relative to signal and idler bands. This means that for all the cases of FP, BP, and CP phase-matching, we can move the point of phase-matching through different sections of the signal and idler bands, hence accessing different group indices at the point of phase-matching. This is also shown in Fig. 2.14(d) for the CP phase-matching case, where we can see how changing the slab thickness results in a different n_g at the frequency of CP phase-matching. The stronger n_g increase here is because of the fact, that by increasing h , the $\omega_p/2$ frequency gets lower and very close to the edge of the idler mode. The second tuning method is different than the first method, in that here we are not affecting the dispersion of the signal and idler modes by changing the slab thickness and are simply moving the pump through the band. Whereas in the first method, the phase-matching frequency $\omega_p/2$ was fixed and the dispersion of the lower frequency modes were changed around that frequency. This demonstrated control over the group index in the CP configuration will be used in chapter 4 for the design of heralded sources of single-photons, with pairs that are unentangled in the spectral degree of freedom.

Finally it should be mentioned, that the CP phase-matching is also satisfied for a BP pump. This means that in an SHG scenario, where the FH mode is inserted from both sides of the structure, the SH mode will be excited in both the forward and backward directions.

2.4.3 Simultaneous phase-matching of multiple processes

As discussed in chapter 1, it is of high interest to satisfy multiple phase-matching conditions at the same time in one structure, as it allows for the generation of path- or mode-entangled photon-pairs without the need for pre- or post-processing steps. In this section, it will be shown that this can be done in PCSWs, or in general periodic WGs, using a unique scheme developed in this thesis. This scheme relies on the use of a pump mode at $k_p = 0$ in the first BZ, and signal and idler modes that have $k_s = -k_l$. This type of phase-matching scheme was already used in the previous section to reach a frequency-degenerate CP phase-matching, with the bands shown in Fig. 2.14(b). Interestingly, in satisfying $k_s = -k_l$, the sign of the group velocities of the signal and idler modes are not restricted. Moreover, there is no restriction on the signal and idler to be in the same mode or at the same central frequency. As long as $k_p = k_s + k_l = 0$ and $\omega_p = \omega_s + \omega_l$ conditions are satisfied, we can have a phase-matched process. To explain how this can open our hand in satisfying multiple phase-matching processes simultaneously, a specific double-slot PCSW design will be presented in this section, that can simultaneously phase-match two non-degenerate CP processes. With this understanding, a number of other possibilities for simultaneous phase-matching of multiple processes will be presented schematically, that can be reached with bands that are commonly attainable in periodic WGs.

For reaching two CP phase-matchings simultaneously, a double-slot PCSW is used, whose bands and fields were shown in Fig. 2.12. The overlapped band diagrams for this structure were shown in Fig. 2.14(a), but now they are replotted in Fig. 2.15(a). This plot shows the FP and BP counterparts of the signal (green curve) and idler (red curve) modes, which are all participating in this simultaneous phase-matching configuration. With the pump mode's half-frequency $\omega_p/2$ being exactly between the signal and idler mode's frequencies, such that $\omega_p = \omega_s + \omega_l$, this structure supports two non-degenerate CP processes, marked on the band diagram as \mathcal{A} and \mathcal{B} . In process \mathcal{A} the signal mode is

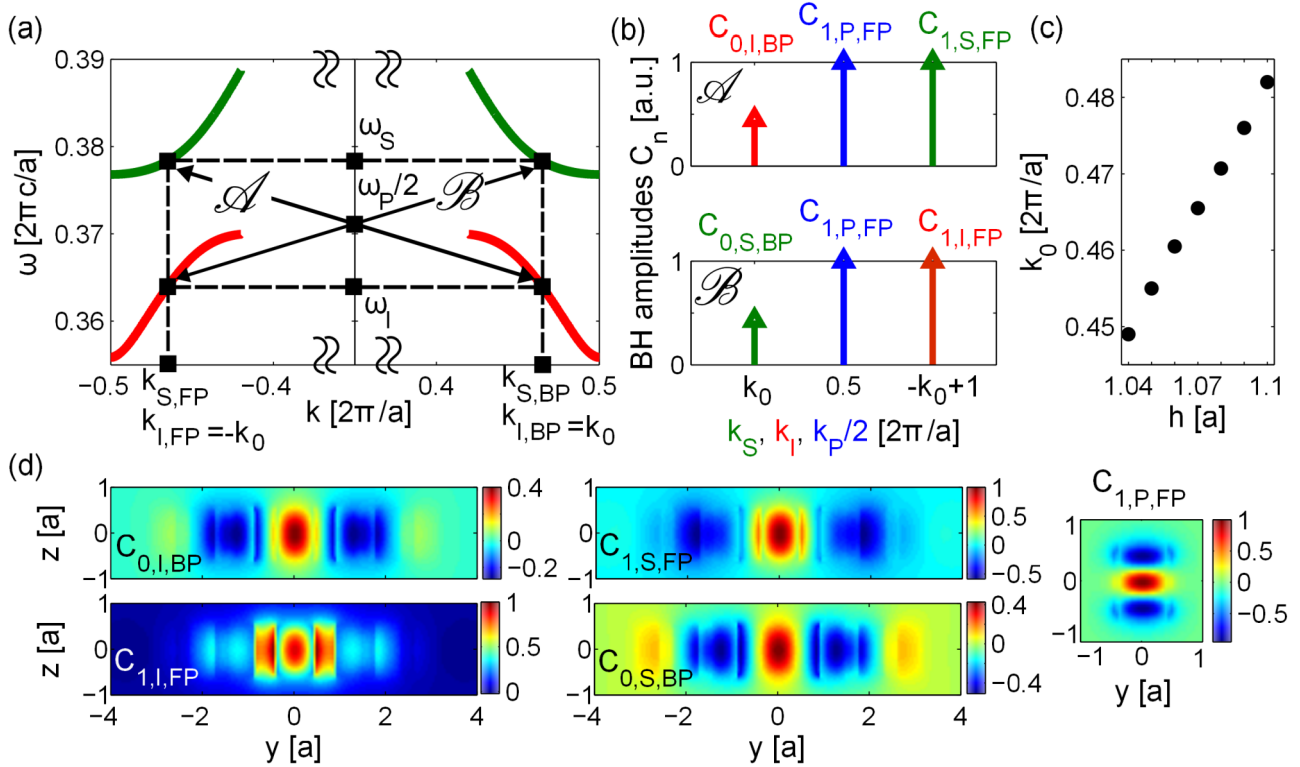


Figure 2.15: (a) Band diagrams of the signal mode (green) and idler mode (red), explaining the condition for simultaneous phase-matching of two non-degenerate CP processes, marked as \mathcal{A} and \mathcal{B} . Design parameters are $R/a = 0.3$, $h/a = 1.07$, $W/a = 0.85$, $T/a = 0.45$, and $D/a = 0.59$; (b) BH distribution $C_n = |\mathbf{y} \cdot \mathbf{C}_n(y=0, z=0)|$ for the main BHs contributing to processes \mathcal{A} (top) and \mathcal{B} (bottom); (c) Tuning the point of simultaneous phase-matching, k_0 from plot (a), by changing the thickness of the slab h . (d) Profiles of the BHs shown in (b).

FP and the idler mode is BP, and in process \mathcal{B} the signal mode is BP and the idler is FP. In process \mathcal{A} , a FP pump at $k_p = 0$ is phase-matched to a FP signal at $k_{S,FP} = -k_0$ and a BP idler at $k_{I,BP} = k_0$, with $k_0 = 0.465 \frac{2\pi}{a}$ for this specific design. The BH distribution for this process is shown in Fig. 2.15(b). The dominant $C_{1,S,FP}$ BH for the FP signal with $k_{1,S,FP} = -k_0 + \frac{2\pi}{a}$ and the next-to-dominant $C_{0,I,BP}$ BH for the BP idler with $k_{0,I,BP} = k_0$ are the main BHs involved in this process, that are phase-matched to the dominant $C_{1,P,FP}$ BH of the pump at $k_{1,P,FP} = \frac{2\pi}{a}$, such that $k_{1,S,FP} + k_{0,I,BP} = k_{1,P,FP} = \frac{2\pi}{a}$. If process \mathcal{A} is phase-matched, process \mathcal{B} should also be phase-matched, given that the band diagram in a reciprocal material is symmetric with respect to $k = 0$. In process \mathcal{B} , a FP pump at $k_p = 0$ is phase-matched to a FP idler at $k_{I,FP} = -k_0$, and a BP signal at $k_{S,BP} = k_0$. The BH distributions for process \mathcal{B} is shown in Fig. 2.15(b). The dominant $C_{1,I,FP}$ BH for the FP idler with $k_{1,I,FP} = -k_0 + \frac{2\pi}{a}$ and the next-to-dominant $C_{0,S,BP}$ BH for the BP signal with $k_{0,S,BP} = k_0$ are phase-matched to the dominant $C_{1,P,FP}$ BH of the pump at $k_{1,P,FP} = \frac{2\pi}{a}$, such that $k_{1,I,FP} + k_{0,S,BP} = k_{1,P,FP} = \frac{2\pi}{a}$. Hence, we have demonstrated that this design simultaneously phase-matches two CP processes.

This structure can also be easily tuned, for example by changing the slab thickness, as was done for the CP case from the previous section. Just like the degenerate CP case from the previous section, it is not important what the actual value of k_0 is in this design. Hence, if we want to have simultaneous phase-matching at a different value of k_0 , we can draw a vertical line from that k_0 and find at which ω_S and ω_I frequencies it intersects with the signal and idler bands, respectively. Then all we need for simultaneous phase-matching, is to have a pump mode at $k_p = 0$ with a $\omega_p/2$ that is exactly between ω_S and ω_I . We can achieve this by changing the slab thickness h , which moves the pump band in frequency with respect to the signal and idler bands. This is demonstrated in Fig. 2.15(c), where the

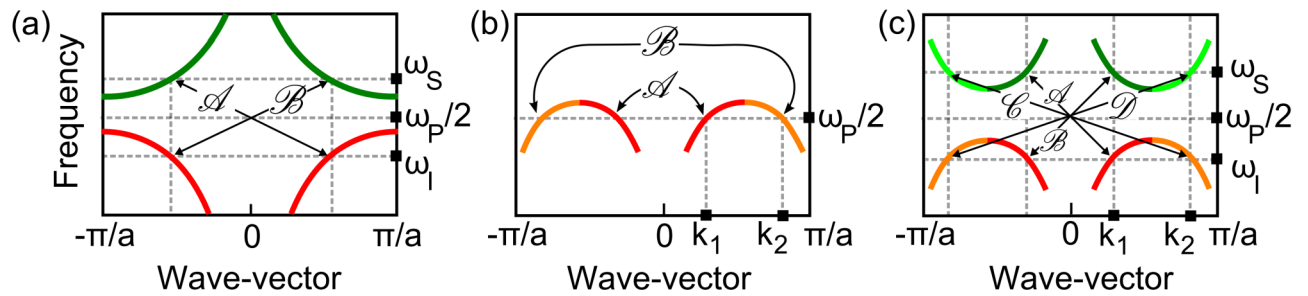


Figure 2.16: (a-c) Different possibilities for satisfying multiple phase-matching conditions simultaneously, shown schematically. Bands or bandlets that are the mirror of one another around $k = 0$ share the same color. (a) Simultaneous phase-matching of two frequency non-degenerate processes: Process \mathcal{A} is between two FP modes and process \mathcal{B} is between two BP modes; (b) Simultaneous phase-matching of two frequency degenerate processes: Both processes \mathcal{A} and \mathcal{B} are between CP modes; (c) Simultaneous phase-matching of four processes: Processes \mathcal{A} and \mathcal{D} are between FP modes and processes \mathcal{B} and \mathcal{C} are between BP modes.

changing k_0 at the point of simultaneous phase-matching is plotted as a function of h . Finally for this particular design, it is important to note, that process \mathcal{B} uses a different set of BHs for phase-matching, $C_{1,I,FP}$ and $C_{0,S,BP}$, compared to process \mathcal{A} , which uses $C_{1,S,FP}$ and $C_{0,I,BP}$. These BHs do not necessarily have the same amplitude or profile, as can be seen in Fig. 2.15(d), where the profiles of the relevant BHs are shown. This means, that processes \mathcal{A} and \mathcal{B} do not necessarily have an equal overlap integral. This point will be important in the design of an SPDC source of Bell states in chapter 4, that makes use of this structure. The specific structure here does actually result in equal efficiencies for processes \mathcal{A} and \mathcal{B} , because the point of phase-matching has been fine tuned by changing the slab thickness to reach that equal efficiency. This will be explained in more details in chapter 4.

The particular scheme explained above is just one of the many different possibilities for simultaneous phase-matching of multiple processes that can be reached in a PCSW. As an example, three other cases are shown schematically in Fig. 2.16, which can be reached using signal and idler bands that are commonly attainable in periodic WGs. All these cases follow the same simultaneous phase-matching principle explained for Fig. 2.15(a), but with different combinations of propagation directions, number of modes, or spectral degeneracy. In Fig. 2.16(a), a schematic band diagram for the signal and idler modes is shown, which is common for modes of periodic WGs at the bandedge. We have seen similar bands in Fig.2.2(c) for the nanobeam structure. With a pump mode half-frequency $\omega_P(k_P = 0)/2$ that is between ω_S and ω_I , we can have simultaneous phase-matching of processes \mathcal{A} and \mathcal{B} . Here, process \mathcal{A} is between FP signal and idler modes (both modes have a positive v_g) and process \mathcal{B} is between BP modes (both modes have a negative v_g). Hence in this case, two frequency non-degenerate processes are phase-matched at the same time, one is FP and the other BP. In Fig. 2.16(b), schematics for simultaneous phase-matching of two frequency-degenerate CP processes are shown. Here I separate the band into two sections at the point where the group velocity changes sign, and each section is called a "bandlet". Bandlet 1 is colored red and bandlet 2 is colored orange. The significance of such a separation of one continuous band into different monotonic sections will become clearer in chapter 4 when SPDC is formulated for periodic WGs. Here it suffices to say, that the two bandlets at points k_1 and k_2 can be distinguished from each other, not by their frequency, but by their different wave-vectors and propagation directions. Moreover, the two bandlets on the two sides of an anticrossing point could have a distinct difference in their mode profiles, caused by the difference in the profiles of the anticrossing modes. With the concept of bandlets introduced, the scheme shown in Fig. 2.16(b)

can be easier explained. Processes \mathcal{A} and \mathcal{B} are both degenerate CP configurations, but \mathcal{A} is involving bandlet 1 and \mathcal{B} is involving bandlet 2, and can be distinguished from each other through the wave-vectors of their bandlets. Such a band diagram shown in this scheme, can be found from the anticrossing of two modes, which was demonstrated for coupled periodic WGs [215], where in this scheme only the lower band of an anticrossing is used. Finally, the simultaneous phase-matching is not restricted to only two processes, but can also be for more than two. To show this, schematics for simultaneous phase-matching of four processes are shown in Fig. 2.16(c). All four processes are frequency non-degenerate. Processes \mathcal{A} and \mathcal{D} are both FP, and processes \mathcal{B} and \mathcal{C} are both BP. Processes \mathcal{A} and \mathcal{D} can be distinguished from each other through the wave-vectors of their bandlets, so can processes \mathcal{B} and \mathcal{C} . The band diagram here is again corresponding to an anticrossing of two modes, where in this case both lower and upper bands are used. It should be pointed out, that reaching this configuration is not as trivial as the ones shown in Figs. 2.16(a) and (b). In Fig. 2.16(c), the lower and upper bands should have some extent of mirror symmetry around the frequency of $\omega_p/2$, where a path towards achieving it could be through careful dispersion engineering.

All the above schematics for reaching multiple simultaneous phase-matchings with a variety of signal and idler propagation directions and modes have a specific meaning in the context of photon-pair generation. It means that SPDC processes with a wide variety of path- and modal-entanglements can be realized in such a PCSW platform. This idea will be the subject of investigation in chapter 4.

2.5 Summary of the results and related publications

In this chapter, I have presented practical designs for reaching different manners of phase-matching configurations in LN PCSWs. Initial designs have been done in standard PCSWs, but then designs were improved by using double-slot PCSWs. FP, BP, and CP phase-matchings were satisfied modally in the double-slot structure, without the need for periodic poling or non-integrated pump illuminations. A design has also been proposed for reaching simultaneous phase-matching of two CP processes. These results fulfill the first goal of this thesis, in establishing that PCSWs are capable of fully controlling the phase-matching condition, far more than what can be done with conventional non-periodic WGs. The importance of these designs for SPDC applications will become clear in chapter 4. However, even for classical nonlinear applications, these novel configurations are of high interest. Examples are the application of the CP configuration for realizing mirror-less optical parametric oscillators [216], and the BP configuration for pulse shaping [217] and self-pulsation [218]. Finally, the designs presented in this chapter have been used in several publications, that include the result of this thesis. The LN ridge WG design was used in an SHG experiment [S1], the W1 PCSW design was used for the theoretical and numerical analysis of the SHG process in PCSWs [S2], the nanobeam design was used in a general study of the effect of loss on slow-light-enhanced SHG [S3], and the double-slot PCSW design has been used to design a source of path-entangled Bell states [S4]. These results will be presented in detail in chapters 3 and 4.

Chapter 3

Second-harmonic generation (SHG) in the presence of loss

In the previous chapter, PCSWs phase-matched for TWM were presented, with lossless guided FH modes near the bandedge and a leaky SH mode. With phase-matched designs at hand, it is time to analyze the dynamics of the nonlinear process. The ultimate goal of analysis for this work is the SPDC process in a phase-matched PCSW, as such an investigation has not yet been done before. But similarly, there has not been much more investigation on the classical counterpart process of SHG in this system either. For this work, it is beneficial to start the formulation for the classical process rather than the quantum one for a number of reasons. The benefits have a theoretical and a practical side to them, both of which are related to the fact that loss is an unavoidable part of this system.

The value in formulating the classical nonlinear process from the theoretical standpoint is twofold. Firstly, it provides a path to understanding the response of a nonlinear PCSW with decaying modes, and doing so for the first time will be an easier task for the classical process compared to the quantum one. More importantly, the classical process allows for direct numerical simulations of the nonlinear response of the system, e.g. by using the FDTD method [133], which allows for verifying the validity of the formulation. Doing such direct nonlinear simulations is not possible for the quantum process, as the spontaneous quantum process relies on the concept of quantum vacuum, which in a TWM analogy could be thought of as a seed wave for TWM, and this cannot be imitated rigorously in a simulation. In checking the validity of the formulation with a direct nonlinear simulation, there are a number of things that can be verified, which are shared between the quantum and the classical process. One thing is to check if the phase-matching condition is satisfied for the structures designed in chapter 2, although the arguments in chapter 2 in the design process guarantee a phase-matched structure and a nonlinear simulation would simply be a double-checking with more direct visuals. The more important thing to be verified is the basis for the modal expansion, which is used in this chapter and all the following chapters. Lossless guided Bloch modes with real-valued wave-vectors have been used extensively as a basis for modal expansion to describe nonlinear interactions in periodic structures [219, 133, 220]. Here however, we have to use quasi-normal Bloch modes (QNBM) with complex-valued wave-vectors as the basis [221], where the propagation of the mode along the propagation direction is governed by the Floquet-Bloch boundary condition with a complex-valued wave-vector in general and in the transverse direction to the WG there are open boundary conditions. This basis

has not been used so often for describing nonlinear interactions [222], especially not in PCSWs. In particular, it should be checked that the field profile and the band diagram of the QNBMs, that are found using linear simulations, when used with the analytical formulations predict the same result as the nonlinear simulation. This verifies that the QNBMs found numerically are correctly found and hence can also be used to describe the quantum process. Finally, both the analytical and numerical studies done in this chapter allow for gaining more understanding about lossy TWM in PCSWs.

From the practical side, studying the classical process is of value to the experiment. It is much easier to characterize the nonlinear structure using SHG or SFG compared to SPDC, due to the higher levels of powers involved. As said before, according to the quantum-classical correspondence principle [193, 194, 195, 196], the quantum process and its classical counterpart share many similarities, such as similar overlap integrals between the mode profiles and the same phase-matching condition. Hence, by testing the classical process, we can determine if the structure that was designed for the quantum process has been fabricated correctly and accurately. For nanostructures, it is usually the case that they suffer from fabrication disorders, which cause scattering losses. Consequently, the phase-matching spectrum and the efficiency of the interaction will differ from the ideal structure. By characterizing the structure for the classical nonlinear process, these additional scattering losses could be determined, through comparing the experimental results with the predictions of an analytical formulation in the presence of loss. Overall, the quality of the fabricated sample for a TWM process can be assessed using a classical experiment that is much more feasible than a quantum one.

In this chapter, an analytical method is developed to describe SHG in periodic WGs, with lossy or in general decaying modes. This formulation is used to analyze the result of an SHG experiment on a LN ridge WG, which suffers from scattering losses. Afterwards, the formulation is used to make an analytical prediction of the generated SH power in the W1 PCSW design of chapter 2, and the result is compared to a rigorous nonlinear FDTD simulation. Finally, a general study is performed on the effect of loss on SHG processes involving slow-light modes. The result of this study is not directly applicable for SPDC. Nonetheless, the effect of loss on slow-light-enhanced nonlinear interactions has been an unresolved issue, even though much work has been done on using slow-light for enhancing nonlinear effects. The developed formulation here allows us to investigate this interesting topic.

3.1 Unconjugated reciprocity theorem for SHG in PCSWs

In this section, an analytical formulation is presented for describing phase-matched SHG in a periodic WG with in general decaying modes, which means that the FH and SH modes could be lossless, lossy/leaky, or even evanescent. To describe a nonlinear process involving only lossless guided Bloch modes with real-valued wave-vectors, one can use the conjugated Lorentz reciprocity theorem [219, 133, 220], similar to what was done in chapter 2 for a lossless non-periodic WG. However, a decaying mode no longer exhibits orthogonality with its conjugate, similar to Eq. (2.8), preventing us from using the conjugated reciprocity theorem. Hence, a reciprocity theorem based on a more general orthogonality relation is needed. All modes, may they be lossy, lossless, or evanescent, are orthogonal to a set of adjoint modes [223, 224, 200, 225], so that modes and their adjoints form a biorthogonal set. For a system made of reciprocal materials, the adjoint of a mode is its BP counterpart, which is

a mode with the opposite sign of the complex-valued wave-vector [221]. Consequently, the biorthogonality condition will simplify to an unconjugated orthogonality relation between the QNBMs of the structure [221], which only gives a non-zero value when a mode is mixed with its BP counterpart. The unconjugated (or adjoint) reciprocity theorem [221, 197, 226] has been used recently to develop a nonlinear coupled mode theory for lossy periodic structures [222]. In the following, this formalism will be used and adapted to describe phase-matched SHG with a modal expansion based on QNBMs.

We start by defining the input QNBM at the FH frequency and all the possible QNBMs at the SH frequency in the complex representation, which assumes we have a CW FH. We then have:

$$\{\mathbf{E}_{\text{FH}}, \mathbf{H}_{\text{FH}}\}(\mathbf{r}) = \{\mathbf{e}_{\text{FH}}, \mathbf{h}_{\text{FH}}\}(\mathbf{r})e^{ik_{\text{FH}}x}, \text{ with } k_{\text{FH}} = k'_{\text{FH}} + ik''_{\text{FH}}, \quad (3.1a)$$

$$\{\mathbf{E}_{\text{SH}_n}, \mathbf{H}_{\text{SH}_n}\}(\mathbf{r}) = \{\mathbf{e}_{\text{SH}_n}, \mathbf{h}_{\text{SH}_n}\}(\mathbf{r})e^{ik_{\text{SH}_n}x}, \text{ with } k_{\text{SH}_n} = k'_{\text{SH}_n} + ik''_{\text{SH}_n}, \quad (3.1b)$$

$$\{\mathbf{e}_{\text{FH}, \text{SH}_n}, \mathbf{h}_{\text{FH}, \text{SH}_n}\}(\mathbf{r}) = \{\mathbf{e}_{\text{FH}, \text{SH}_n}, \mathbf{h}_{\text{FH}, \text{SH}_n}\}(\mathbf{r} + a\mathbf{x}). \quad (3.1c)$$

The indices FH and SH correspond to the time-harmonic fields (time-dependence of $e^{-i\omega t}$) at the FH frequency ω_{FH} and the SH frequency $\omega_{\text{SH}} = 2\omega_{\text{FH}}$. A single mode is assumed for the FH and the integer n runs over the QNBMs present at the SH frequency. The following convention is used to separate FP and BP modes: $n > 0$ refers to a mode propagating forward along the $+x$ direction with wave-vector k , and $n < 0$ refers to its backward counterpart with wave-vector $-k$. If k is real-valued, a mode is FP when $v_g > 0$ and BP when $v_g < 0$. If k is complex-valued, a mode is FP when $k'' > 0$ and BP when $k'' < 0$. The electric and magnetic field profiles of the modes of the unperturbed system at the SH frequency are related by the source-free Maxwell's equations:

$$\nabla \times \mathbf{E}_{\text{SH}_n} = i\omega_{\text{SH}}\mu_0\mathbf{H}_{\text{SH}_n}, \quad \text{and} \quad \nabla \times \mathbf{H}_{\text{SH}_n} = -i\omega_{\text{SH}}\epsilon_0\bar{\epsilon}_{\text{SH}}\mathbf{E}_{\text{SH}_n}. \quad (3.2)$$

Here $\bar{\epsilon}_{\text{SH}}(\mathbf{r}) = \bar{\epsilon}_{\text{SH}}(\mathbf{r} + a\mathbf{x})$ is the relative permittivity tensor of the structure at the SH frequency. This is a symmetric tensor that could be complex valued, meaning that the material is reciprocal but could be anisotropic and/or lossy. Assuming the UPA in the perturbed case, the FH mode feels negligible back-action from the SH field, and hence its amplitude stays the same as in the unperturbed case of Eq. (3.1a). The FH can still decay from any loss mechanism that is present at ω_{FH} . The UPA is no longer valid when the FH field has decayed to powers comparable with the generated SH. However, as in this case no longer a substantial SH is generated, this does not affect the results. To go beyond the UPA, coupled nonlinear equations at both the FH and SH frequencies must be considered [227, 228, 133]. With the UPA, we just need the fields at the SH frequency in the perturbed system, which are governed by the Maxwell's equations including the nonlinear polarization \mathbf{P}_{NL} :

$$\nabla \times \mathbf{E}'_{\text{SH}} = i\omega_{\text{SH}}\mu_0\mathbf{H}'_{\text{SH}}, \quad \text{and} \quad \nabla \times \mathbf{H}'_{\text{SH}} = -i\omega_{\text{SH}}\epsilon_0\bar{\epsilon}_{\text{SH}}\mathbf{E}'_{\text{SH}} - i\omega_{\text{SH}}\mathbf{P}_{\text{NL}}, \quad (3.3)$$

where \mathbf{P}_{NL} for a SHG process is formulated in the same way as Eq. (2.1). The periodicity of Bloch modes can be used to introduce the periodic variable $\mathbf{p}_{\text{NL}}(\mathbf{r}) = \mathbf{p}_{\text{NL}}(\mathbf{r} + a\mathbf{x})$:

$$\mathbf{p}_{\text{NL}, \gamma}(\mathbf{r}) \equiv \frac{e^{-i2k_{\text{FH}}x}}{2\epsilon_0} P_{\text{NL}, \gamma} = \frac{1}{2} \sum_{\alpha, \beta} \chi_{\alpha\beta\gamma}^{(2)}(\mathbf{r}) e_{\text{FH}, \alpha}(\mathbf{r}) e_{\text{FH}, \beta}(\mathbf{r}), \quad (3.4)$$

which will prove to be useful in simplifying the results. For the perturbed SH field the following ansatz is considered, where the total SH field consists of all the QNBMs present at the SH frequency, each with an amplitude $A_n(x)$ to be found:

$$\{\mathbf{E}'_{\text{SH}}, \mathbf{H}'_{\text{SH}}\}(\mathbf{r}) \approx \sum_n A_n(x) \{\mathbf{E}_{\text{SH}_n}, \mathbf{H}_{\text{SH}_n}\}(\mathbf{r}). \quad (3.5)$$

Eq. (3.5) is an approximation. To be exact, in addition to the sum over the QNBMs, the right hand side of Eq. (3.5) should also include an integral over the continuum of the radiation modes. Since we are mainly interested in FH and SH modes that are concentrated in the WG region, Eq. (3.5) is a good approximation for the SH field in and around the WG region. This approximation is made following a similar one for the quasi-normal modes (QNMs) of a resonant structure, where QNMs are modes of a cavity structure with complex-valued eigenfrequencies [229] and the QNM expansion without the radiation modes is a good approximation for describing the field dynamics in regions inside and close to the cavity [198, 199]. To find $A_n(x)$ for each QNBM, we need the unconjugated reciprocity theorem at the SH frequency, which states:

$$\oint_S (\mathbf{E}'_{\text{SH}} \times \mathbf{H}_{\text{SH}_m} - \mathbf{E}_{\text{SH}_m} \times \mathbf{H}'_{\text{SH}}) \cdot d\mathbf{S} = -i\omega_{\text{SH}} \int_V d^3\mathbf{r} \mathbf{P}_{\text{NL}} \cdot \mathbf{E}_{\text{SH}_m}, \quad (3.6)$$

where V is a volume, S is the closed surface around this volume, and the surface element $d\mathbf{S}$ is pointing outwards on this surface. We also need the biorthogonality relation between each QNBM and its backward counterpart [221] at the SH frequency:

$$\iint_{-\infty}^{+\infty} (\mathbf{e}_m \times \mathbf{h}_n - \mathbf{e}_n \times \mathbf{h}_m) \cdot \mathbf{x} dy dz = \delta_{n(-m)} \mathcal{F}_n. \quad (3.7)$$

The left-hand side of Eq. (3.7) is nonzero for $m = -n$. $\mathcal{F}_n = -\mathcal{F}_{-n}$ is referred to as the adjoint flux of a mode and is a finite x -independent quantity [200]. To find $A_n(x)$ from Eq. (3.6), a rectangular volume is chosen, from $x = x_0$ to x_1 . Using Eqs. (3.1b), (3.4), and (3.5) with Eq. (3.6) gives:

$$\sum_n \oint_S A_n(x) (\mathbf{e}_{\text{SH}_n} \times \mathbf{h}_{\text{SH}_m} - \mathbf{e}_{\text{SH}_m} \times \mathbf{h}_{\text{SH}_n}) \cdot d\mathbf{S} = -i2\omega_{\text{SH}} \epsilon_0 \int_V e^{i(2k_{\text{FH}} + k_{\text{SH}_m})x} \mathbf{p}_{\text{NL}} \cdot \mathbf{e}_{\text{SH}_m} d^3\mathbf{r}. \quad (3.8)$$

With an open boundary around the structure, the four surfaces closing the volume on the transversal directions will not contribute to the surface integral on the left-hand side of Eq. (3.8) [221]. As a result, the closed surface integral turns into two integrals over surfaces perpendicular to the propagation direction, for which the biorthogonality relation of Eq. (3.7) can be used. This simplifies Eq. (3.8) to:

$$A_n(x_1) - A_n(x_0) = \frac{i2\omega_{\text{SH}} \epsilon_0}{\mathcal{F}_{\text{SH}_n}} \int_V e^{i(2k_{\text{FH}} - k_{\text{SH}_n})x} \mathbf{p}_{\text{NL}} \cdot \mathbf{e}_{\text{SH}_{-n}} d^3\mathbf{r}, \quad (3.9)$$

where $\mathcal{F}_{\text{SH}_n}$ is the adjoint flux of the n th SH mode. Here we used the fact that $k_{-n} = -k_n$. $A_n(x = x_1)$ can be calculated from Eq. (3.9), given that we have its initial value at x_0 . Then we only need to take the integral on the right-hand side of Eq. (3.9) over a volume between x_0 and x_1 .

Still, a more closed-form expression for $A_n(x)$ is desired. For doing this, the volume integral of Eq. (3.9) could be separated into x -dependent and yz -dependent parts, by expanding the Bloch mode

profiles into their BHs, which similarly was done in chapter 2 and has resulted in Eq. (2.21). In this way however, we have to keep track of all the possible combinations of BHs and their corresponding phase-matching conditions. A more compact expression is desired here, with only the one phase-matching condition of Eq. (2.24), which was $k_P - k_S - k_I = \frac{2\pi}{a}Q$, so that we can only consider one Q value that satisfies or is close to satisfying the phase-matching condition. So we write:

$$\int e^{i(2k_{\text{FH}} - k_{\text{SH}_n})x} \mathbf{p}_{\text{NL}} \cdot \mathbf{e}_{\text{SH}_{-n}} d^3\mathbf{r} = \int e^{-i\Delta k_n x} e^{-i\frac{2\pi Q_n}{a}x} \mathbf{p}_{\text{NL}} \cdot \mathbf{e}_{\text{SH}_{-n}} d^3\mathbf{r}, \quad (3.10)$$

where the complex-valued Δk_n is defined as:

$$\Delta k_n \equiv k_{\text{SH}_n} - 2k_{\text{FH}} - \frac{2\pi Q_n}{a} = \Delta k'_n + i\Delta k''_n = \left[k'_{\text{SH}_n} - 2k'_{\text{FH}} - \frac{2\pi Q_n}{a} \right] + i \left[k''_{\text{SH}_n} - 2k''_{\text{FH}} \right], \quad (3.11)$$

where $Q_n = 0, \pm 1, \pm 2, \dots$ corresponds to phase-matching to the n th SH mode. As explained in the previous chapter, we can separate the complex-valued Δk_n into a phase-mismatch $\Delta k'_n$ and a loss-mismatch $\Delta k''_n$. Now $e^{-i\frac{2\pi Q_n}{a}x} \mathbf{p}_{\text{NL}} \cdot \mathbf{e}_{\text{SH}_{-n}}$ is still an x -dependent quantity, that cannot be exactly separated from $e^{-i\Delta k_n x}$, but an approximation can be made to do another type of separation to simplify the expression. This can be done when modes are close to satisfying the phase-matching condition, which anyway is the desired state of the system for us. To do this, a specific volume of $V = \Omega$ is chosen, where Ω is the volume of one supercell. If the system is close to satisfying the phase-matching condition with the n th SH mode such that $|\Delta k_n| \ll 1/a$, $e^{-i\Delta k_n x}$ can be approximated as a constant over the length of one supercell and can be pulled out of the volume integral on the right-hand side of Eq. (3.10). After this, only $e^{-i\frac{2\pi Q_n}{a}x} \mathbf{p}_{\text{NL}} \cdot \mathbf{e}_{\text{SH}_{-n}}$ remains in the integral, which is a periodic function that repeats itself in every supercell. Being close to the point of phase-matching, we can also assume that $A_n(x)$ varies slowly over a period, such that $A_n(x+a) - A_n(x) \approx a\partial A_n/\partial x$. Eq. (3.9) can now be turned into the following form:

$$\frac{\partial A_n}{\partial x} = \frac{i2\omega_{\text{SH}}\epsilon_0}{a} e^{-i\Delta k_n x} \frac{\mathcal{V}_n}{\mathcal{F}_{\text{SH}_n}}, \quad (3.12)$$

where \mathcal{V}_n is the overlap integral that determines the efficiency of the process, defined as:

$$\mathcal{V}_n \equiv \int_{\Omega} e^{-i\frac{2\pi Q_n}{a}x} \mathbf{p}_{\text{NL}} \cdot \mathbf{e}_{\text{SH}_{-n}} d^3\mathbf{r}. \quad (3.13)$$

This integral is over one supercell, and only depends on the periodic Bloch mode profiles, the periodic $\chi^{(2)}(\mathbf{r})$ profile, and the value of the integer Q_n . The difference between the more compact expression of Eq. (3.12), that has only one overlap integral and phase-matching condition, and that of Eq. (2.21), that has a sum over all possible combinations of BHs, is that here we are essentially only taking into account the contributions from the phase-matched BHs with $n_S + n_I - n_P = Q$, and neglect the effect of all the other out-of-phase combinations. The neglected combinations of BHs have a phase-mismatch of at least $\frac{2\pi}{a}$ or larger factors of it, hence their contribution is negligible.

Eq. (3.12) is a first-order differential equation, which can be solved with an initial condition for $A_n(x)$. Let us assume, that we have an infinite periodic WG with a finite region of $0 < x < L$ over which nonlinearity exists. With no additional SH input into the structure from an external source, there are

two types of initial conditions we can have: If n corresponds to a FP SH mode, then $A_n(x=0) = 0$, and if n corresponds to a BP SH mode, then $A_n(x=L) = 0$. Hence, to find $A_n(x)$, for $n > 0$ we take the integral $\int_0^x dx$ over Eq. (3.12), and for $n < 0$ we take the integral $\int_x^L dx$. This gives:

$$A_n(x) = \frac{2\omega_{\text{SH}}\epsilon_0}{a\Delta k_n} \frac{\mathcal{V}_n}{\mathcal{F}_{\text{SH}_n}} \begin{cases} 1 - e^{-i\Delta k_n x}, & \text{for } n > 0 \quad (\text{FP SHG}) \\ e^{-i\Delta k_n x} - e^{-i\Delta k_n L}, & \text{for } n < 0 \quad (\text{BP SHG}) \end{cases}. \quad (3.14)$$

Eq. (3.14) gives the amplitude of any QNBM at the SH frequency, excited through SHG. However, it is often the generated SH power as a function of the input FH power that is of interest. Moreover, an expression is desired that is independent of arbitrary proportionality constants in the field profiles, as was done for the non-periodic WG in chapter 2. For doing this, we have to make an extra assumption compared to a case with lossless modes. For having an expression for the generated SH power in each lossy SH mode, we have to assume that only one SH mode satisfies the phase-matching condition and is dominantly excited. The reason is, that in a system with decaying modes, modes are not power-orthogonal to each other, which means that the total power is no longer the sum of the power in each of the modes, but there exist crossterms between the modal powers [230]. This is a very important point, which will also affect our ability in defining photons later on in chapter 5, when we deal with a quantum theory involving decaying signal and idler modes. Hence, here the assumption is made that only the n th SH mode is dominantly excited. In the first step, we want to make $A_n(x)$ dependent on the input FH power, instead of the amplitude of the FH mode, which resides in the variable \mathcal{V}_n in Eq. (3.14). To do this, we need to make use of the expression for the complex-valued group velocity v_g of the FH mode. For a decaying Bloch mode, v_g is no longer equal to the energy velocity, and its relation only connects the complex-valued derivative $d\omega/dk$ to the field profile of the mode [200]. This relation for the complex v_g and n_g of the n th mode is [221, 200]:

$$v_{g_n} = \frac{c}{n_{g_n}} = \frac{a \iint_{-\infty}^{+\infty} (\mathbf{e}_{-n} \times \mathbf{h}_n - \mathbf{e}_n \times \mathbf{h}_{-n}) \cdot \mathbf{x} dy dz}{2 \int_{\Omega} \mathbf{d}_n \cdot \mathbf{e}_{-n} d^3\mathbf{r}} = \frac{a\mathcal{F}_n}{2 \int_{\Omega} \mathbf{d}_n \cdot \mathbf{e}_{-n} d^3\mathbf{r}}, \quad (3.15)$$

where $\mathbf{d} = \epsilon_0 \bar{\epsilon} \mathbf{e}$ is the displacement field profile of the Bloch mode, such that $d_i = \sum_j \epsilon_0 \epsilon_{ij} e_j$. For a CW forward-propagating FH mode, the input power at $x = 0$ is:

$$\mathcal{P}_{\text{FH}} = \frac{1}{2} \iint_{-\infty}^{+\infty} \text{Re}[\mathbf{e}_{\text{FH}_+} \times \mathbf{h}_{\text{FH}_+}^*] \cdot \mathbf{x} dy dz = \mathcal{R}_{\text{FH}} \frac{c}{2a|n_{\text{gFH}_+}|} \left| \int_{\Omega} \mathbf{d}_{\text{FH}_+} \cdot \mathbf{e}_{\text{FH}_-} d^3\mathbf{r} \right|, \quad (3.16)$$

where the equation for the complex group velocity of the FH mode was used for the last equality. The $+$ subscript refers to a FP mode. The variable \mathcal{R} for the FH mode is defined as:

$$\mathcal{R}_{\text{FH}} \equiv 2 \iint_{-\infty}^{+\infty} \text{Re}[\mathbf{e}_{\text{FH}_+} \times \mathbf{h}_{\text{FH}_+}^*] \cdot \mathbf{x} dy dz \left/ \left| \iint_{-\infty}^{+\infty} (\mathbf{e}_{\text{FH}_-} \times \mathbf{h}_{\text{FH}_+} - \mathbf{e}_{\text{FH}_+} \times \mathbf{h}_{\text{FH}_-}) \cdot \mathbf{x} dy dz \right| \right. \quad (3.17)$$

\mathcal{R} is a dimensionless parameter, defined for organizing the final expression of this calculation. For a lossless guided mode, \mathcal{R} is equal to $+1$ for a FP mode and -1 for a BP mode, as for a lossless guided mode we can substitute $\mathbf{e}_{-n}(\mathbf{r}) = \mathbf{e}_n^*(\mathbf{r})$ and $\mathbf{h}_{-n}(\mathbf{r}) = -\mathbf{h}_n^*(\mathbf{r})$ [221, 200]. For a lossy mode, \mathcal{R} will have an absolute value close to 1. For a purely evanescent mode, \mathcal{R} will be zero,

as the evanescent mode carries no power, meaning that with purely evanescent modes we cannot work with the power quantity but can only work with the amplitude of the modes, as they appear in Eq. (3.14). We can now insert a factor of one into the right-hand side of Eq. (3.14), from the equality $1 = \frac{4a^2}{c^2} \left| n_{\text{gFH}_+} \right|^2 \frac{\mathcal{P}_{\text{FH}}^2}{\mathcal{R}_{\text{FH}}^2} \left/ \left| \int_{\Omega} \mathbf{d}_{\text{FH}_+} \cdot \mathbf{e}_{\text{FH}_-} d^3\mathbf{r} \right|^2 \right.$, which is derived from Eq. (3.16). This substitution makes the right-hand side of Eq. (3.14) independent of the amplitude of the Bloch mode profile of the FH mode, and instead makes it dependent on the input FH power \mathcal{P}_{FH} .

With the above substitution in Eq. (3.14), we now want to use the amplitude $A_n(x)$ to find the generated SH power. Assuming the n th SH mode is dominantly generated, we have:

$$\mathcal{P}_{\text{SH}}(x) = \frac{1}{2} \iint_{-\infty}^{+\infty} \text{Re}[\mathbf{E}'_{\text{SH}} \times \mathbf{H}'_{\text{SH}}^*] \cdot \mathbf{x} dy dz \approx \frac{1}{2} \left| e^{-k''_{\text{SH}_n} x} A_n(x) \right|^2 \iint_{-\infty}^{+\infty} \text{Re}[\mathbf{e}_{\text{SH}_n} \times \mathbf{h}_{\text{SH}_n}^*] \cdot \mathbf{x} dy dz, \quad (3.18)$$

where Eqs. (3.1b) and (3.5) are used to get the last expression. It is important to note, that it is only for a lossless Bloch mode that the quantity $\iint \text{Re}[\mathbf{e} \times \mathbf{h}^*] \cdot \mathbf{x} dy dz$ is x -independent. For a QNBM, it is only the adjoint flux \mathcal{F} that is x -independent, but $\iint \text{Re}[\mathbf{e} \times \mathbf{h}^*] \cdot \mathbf{x} dy dz$ is in general periodically x -dependent. This means that the definition of the power flux in Eq. (3.18) has a dependence on the x -point in the supercell, $0 < x < a$, which is chosen to calculate $\iint \text{Re}[\mathbf{e} \times \mathbf{h}^*] \cdot \mathbf{x} dy dz$ at. This can be taken care of by being consistent in that choice. Nonetheless, such changes in $\iint \text{Re}[\mathbf{e} \times \mathbf{h}^*] \cdot \mathbf{x} dy dz$ across one period cannot be bigger than a factor of $e^{2k''a}$, as $e^{-2k''x} \iint \text{Re}[\mathbf{e} \times \mathbf{h}^*] \cdot \mathbf{x} dy dz$, which is proportional to the power flux of a mode excited linearly from an end-facet, must still be a monotonically decaying function of x . With a SH mode of a decay length much larger than a period, $a \ll L_{\text{decay}} = 1/k''$, the $e^{2k''a}$ factor will be very close to 1, such that even not being consistent in our choice will not introduce a big inaccuracy in calculating the power flux. We now substitute Eq. (3.14), with the extra factor of 1 as mentioned, into Eq. (3.18) to find the SH power. We also substitute $\iint \text{Re}[\mathbf{e}_{\text{SH}_n} \times \mathbf{h}_{\text{SH}_n}^*] \cdot \mathbf{x} dy dz / |\mathcal{F}_{\text{SH}_n}|^2$, which appears in the final formula, with $|n_{\text{gSH}_n}| \mathcal{R}_{\text{SH}} \frac{a}{4c} / \left| \int_{\Omega} \mathbf{d}_{\text{SH}_n} \cdot \mathbf{e}_{\text{SH}_{-n}} d^3\mathbf{r} \right|$, which can be shown to be true from the complex-valued v_{g} expression of the SH mode. The \mathcal{R} factor for the SH mode is defined similar to the FH mode as:

$$\mathcal{R}_{\text{SH}} \equiv 2 \iint_{-\infty}^{+\infty} \text{Re}[\mathbf{e}_{\text{SH}_n} \times \mathbf{h}_{\text{SH}_n}^*] \cdot \mathbf{x} dy dz \left/ \left| \iint_{-\infty}^{+\infty} (\mathbf{e}_{\text{SH}_{-n}} \times \mathbf{h}_{\text{SH}_n} - \mathbf{e}_{\text{SH}_n} \times \mathbf{h}_{\text{SH}_{-n}}) \cdot \mathbf{x} dy dz \right| \right. \quad (3.19)$$

The purpose of this substitution is to incorporate the magnetic field dependency of the SH mode into the \mathcal{R} factor. The final expression for the generated SH power is:

$$\mathcal{P}_{\text{SH}}(x) = \frac{\mathcal{P}_{\text{FH}}^2}{\mathcal{P}_{\text{eff}}} \frac{\mathcal{R}_{\text{SH}}}{\mathcal{R}_{\text{FH}}^2} \frac{|n_{\text{gSH}_n} n_{\text{gFH}_+}^2|}{|a \Delta k_n|^2} \begin{cases} \left| e^{i \Delta k'_n x} e^{-k''_{\text{SH}_n} x} - e^{-2k''_{\text{FH}_+} x} \right|^2, & n > 0 \\ \left| e^{i \Delta k'_n (L-x)} e^{-2k''_{\text{FH}_+} x} - e^{-2k''_{\text{FH}_+} L} e^{k''_{\text{SH}_n} (L-x)} \right|^2, & n < 0 \end{cases}, \quad (3.20)$$

$$\frac{1}{\mathcal{P}_{\text{eff}}} \equiv \frac{2\omega_{\text{SH}}^2 a^3}{c^3} \frac{\left| \int_{\Omega} e^{-i \frac{2\pi Q_n}{a} x} \boldsymbol{\varepsilon}_0 \mathbf{p}_{\text{NL}} \cdot \mathbf{e}_{\text{SH}_{-n}} d^3\mathbf{r} \right|^2}{\left| \int_{\Omega} \mathbf{d}_{\text{SH}_n} \cdot \mathbf{e}_{\text{SH}_{-n}} d^3\mathbf{r} \right| \left| \int_{\Omega} \mathbf{d}_{\text{FH}_+} \cdot \mathbf{e}_{\text{FH}_-} d^3\mathbf{r} \right|^2}. \quad (3.21)$$

where we have defined \mathcal{P}_{eff} as an effective power. The nominator of Eq. (3.21) includes the overlap integral between the backward counterpart of the SH mode and the nonlinear polarization. To have

an efficient nonlinear interaction, this overlap has to be maximized by the proper choice of the crystal orientation and the symmetry of the dominant components of the electric field profile of the modes. The denominator includes the adjoint density integral for the modes, which will turn into energy density for lossless guided modes. They serve as a normalization for \mathcal{P}_{eff} , so it is independent of arbitrary proportionality constants in the Bloch mode profiles.

Eq. (3.20) is the main result of this calculation and represents the generated power in the n th SH mode, if only that mode is dominantly excited. There are a number of things that distinguish this result from a conjugated-reciprocity-based calculation with lossless guided modes. With only lossless modes, it has been shown that the SHG efficiency enhances quadratically and linearly with respect to real-valued n_{gFH} and n_{gSH} , respectively [133]. However, with a lossy mode that has a complex-valued group index [200], Eq. (3.20) shows a dependency on the absolute value of the group indices. Eq. (3.20) also reproduces the length dependency, that is expected from a lossy SHG process [204]. With a lossless FH mode and a lossy SH mode, or vice versa, the generated SH power approaches a constant value or saturates for structure lengths L much larger than the decay length of the lossy mode. For FP SHG this happens towards the end of the structure and for BP SHG towards its beginning. As an example, consider the case of the FP phase-matched PCSW design with $\Delta k' = 0$, which has a leaky SH mode. The length dependency of the SH power in this case is $\mathcal{P}_{\text{SH}}(L) \propto \left| \left(e^{-k''_{\text{SH}}L} - 1 \right) / k''_{\text{SH}} \right|^2$, which in the limit of $1/k''_{\text{SH}} \ll L$ approaches $\mathcal{P}_{\text{SH}}(L) \propto |1/k''_{\text{SH}}|^2$. The saturation here is the result of the generated SH power gradually balancing with the radiating SH power. If both modes are lossless, there will be a quadratic length dependency, as was derived in chapter 2. It should be noted, that the quadratic dependence here is found assuming a periodic WG with no reflections at its end-facets. For a finite periodic structure with strong reflections at its end-facets, the length dependency is different, due to the presence of Fabry-Perot resonances [231, 232]. Finally, if both modes are lossy, there exists an optimum length [226] at which the maximum generated power is attainable.

At the end, the phase-matching spectrum for this process should be investigated in more details, as it is no longer a sinc-function, which was derived for the lossless process. Let us consider the FP case. A dimensionless phase-matching function can be defined as:

$$\text{PM}(\omega_{\text{FH}}, L) \equiv \left| \frac{e^{i\Delta k' L} e^{-k''_{\text{SH}}L} - e^{-2k''_{\text{FH}}L}}{a(\Delta k' + i\Delta k'')} \right|^2, \quad (3.22)$$

which is a part of Eq. (3.20). All the wave-vectors are a function of ω_{FH} . This PM function usually carries the main information about the dependency of the generated SH at the end of the structure on the frequency of the input FH. That is unless the field profile or group indices of the modes have an even stronger frequency dependence, which could happen at a bandedge for n_{g} or at a splitting in the bands for the field profiles. But for most practical cases, the strongest spectral changes occur in the PM function, and it would suffice to just study PM for the spectral dependency of the process. With lossless modes, the phase-matching function in the limit of $\{k''_{\text{FH}}, k''_{\text{SH}}\} \rightarrow 0$ turns into $(L/a)^2 \text{sinc}^2(\Delta k' L/2)$, which has the well-known sinc-dependency [58] and gets spectrally narrower as L is increased. This is shown in Fig.3.1(a), where a simple linear dependency of the wave-vector on frequency is assumed for both FH and SH modes, which is a good approximation over small spectral ranges. In this approximation we can write $k_{\text{FH}} = k_{\text{FH},0} + \frac{n_{\text{gFH}}}{c}(\omega_{\text{FH}} - \omega_{\text{FH},0})$ and $k_{\text{SH}} = k_{\text{SH},0} + \frac{n_{\text{gSH}}}{c}(2\omega_{\text{FH}} - \omega_{\text{SH},0})$,

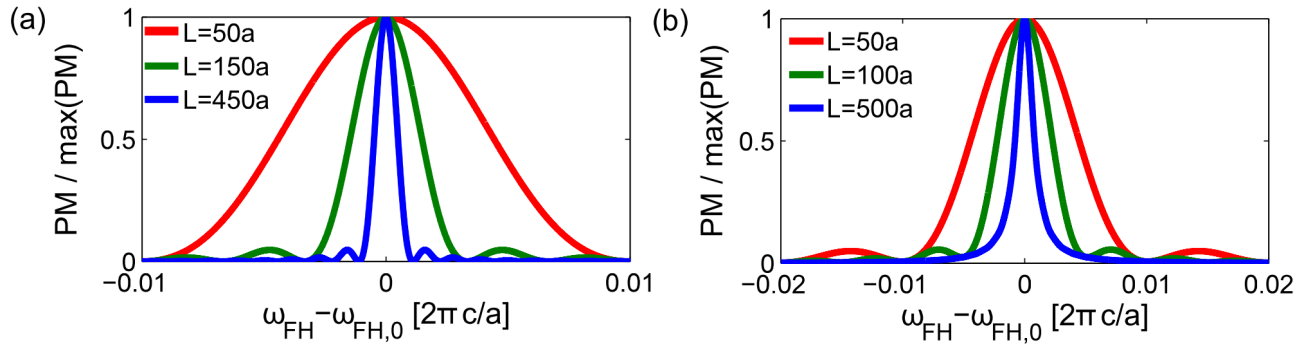


Figure 3.1: (a) Normalized PM function for lossless FH and SH modes, $\text{PM}/\max(\text{PM}) = \text{sinc}^2(\Delta k' L/2)$, plotted for different structure lengths L ; (b) Normalized PM function plotted for the case of a lossless FH and a lossy SH mode with $L_{\text{decay,SH}} = 1/k''_{\text{SH}} = 100a$, for different structure lengths L . For both plots linear bands for the FH and SH modes are assumed, with $\text{Re}[n_{\text{gSH}} - n_{\text{gFH}}] = 1$.

where variables $k_{\text{SH},0} = 2k_{\text{FH},0}$ and $\omega_{\text{SH},0} = 2\omega_{\text{FH},0}$ correspond to the point of phase-matching. This results in $\frac{\Delta k' L}{2} = \frac{n_{\text{gSH}} - n_{\text{gFH}}}{c} (\omega_{\text{FH}} - \omega_{\text{FH},0}) L$. It is evident from this formula, that increasing $n_{\text{gSH}} - n_{\text{gFH}}$ has the same effect that increasing L has on narrowing the spectral bandwidth of the phase-matching function. This means that having FH and SH modes that have a large group index difference, is an alternative solution to having a long structure for getting narrow phase-matching spectrum.

Now let's consider a case where the generated SH saturates as a function of L with a lossy SH and a lossless FH. In this case, for $1 \ll k''_{\text{SH}} L$, the PM function approaches $1/a^2(\Delta k'^2 + k''_{\text{SH}}{}^2)$. Usually k'' has a weaker frequency dependence compared to $\Delta k'$, so we only investigate the $\Delta k'$ dependence of the PM function. In this limit, the PM function is a Lorentzian function of $\Delta k'$, as can be seen in Fig.3.1(b), for the case of $k''_{\text{SH}} L = L/L_{\text{decay,SH}} = 5$ (blue curve). In the saturation limit, increasing the length of the structure no longer has any effect on its spectral bandwidth, and the lowest achievable bandwidth is proportional to k''_{SH} . For the case where one or both of the modes are lossy and L is not too large, the PM function is something between a sinc and a Lorentzian shape. This can be seen in Fig.3.1(b), where the PM-function is displayed for three different values of L . This plot shows how increasing the structure length from below the decay length of the lossy mode to the saturation limit, changes the shape of the PM function from a sinc to a Lorentzian.

3.2 SHG experiment in a lithium niobate ridge waveguide

In the previous section, a theory for describing SHG in lossy periodic WGs was developed. Such a theory allows us to interpret the results of the SHG characterization of a fabricated sample, especially to determine the losses of its modes. As mentioned before, part of my time during this thesis has been devoted to the experimental development of the integrated LN platform for nonlinear optical applications, which involved the SHG characterization of LN ridge WGs on a NANOLN substrate, fabricated successfully at our institute. I have constructed an optical setup for this purpose and measured phase-matched SHG in a LN ridge WG, the design of which was presented in chapter 2. This experiment was an important progress in the development of integrated nanostructured LN platforms. In analyzing the measurements in comparison with theory, it became clear that there exists a non-negligible loss in the modes, caused by fabrication imperfections. This loss needs to be measured and taken into account to compare the measured SHG efficiency and phase-matching spectrum to the

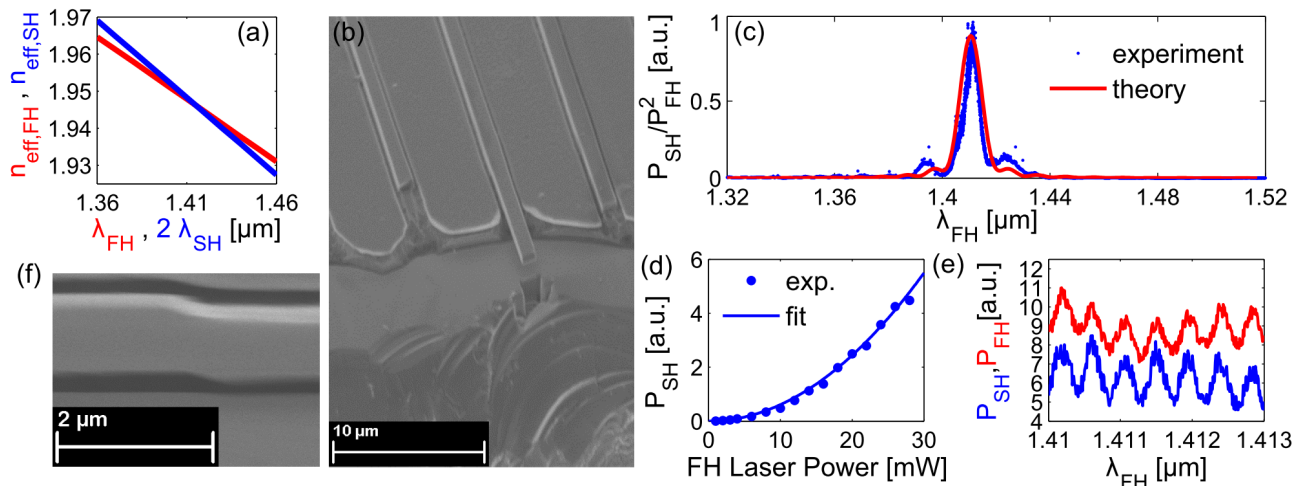


Figure 3.2: (a) The effective refractive indices of the TE_{00} FH and the TM_{20} SH modes, showing the crossing point corresponding to phase-matching. (b) SEM image of the fabricated ridge WGs; (c) Plot of the SHG efficiency, experimental and theoretical, as a function of the FH wavelength; (d) Measured quadratic dependence of the generated SH power as a function of the input FH power; (e) Measured FH and SH spectra displaying the Fabry-Perot fringes; (f) SEM image of a stitching error in the fabricated WG sample.

theoretical ones. For this comparison, the developed formalism for lossy periodic WGs can be used, with small variations to make it suitable for a non-periodic WG. In this section, the results of this SHG experiment will be presented and analyzed using the theory developed in the previous section.

A LN ridge WG with an approximate thickness of $h = 0.53 \mu\text{m}$, width of $W = 1.2 \mu\text{m}$, and length of $L = 0.9 \text{ mm}$ is characterized. The phase-matched bands for this LN ridge WG was shown previously in Fig. 2.1(c) and for convenience it is shown again in Fig. 3.2(a). The WGs have been fabricated using the ion-beam-enhanced etching method [233], and their scanning electron microscope (SEM) image is shown in Fig. 3.2(b). For the experiment, a butt-coupling setup is used. The sample is placed on a piezo stage, and FH light coming from a tunable CW laser is coupled into the WG at the front-facet using a lensed fiber. A fiber polarizer is used to control the polarization of the excitation. To ensure efficient incoupling of the FH, the butt-coupling process is controlled using a microscope that looks from above at the lensed fiber and the front-facet of the WG. The output light from the WG is collected with a 100X microscope objective of $NA = 0.7$. The emitted SH and FH are separated using a dichroic beamsplitter and then imaged onto two CCD cameras. The relative SH and FH powers are determined by integrating over the images obtained. These powers are used to construct a normalized SHG efficiency curve, where the power of the generated SH is divided by the squared power of the input FH. The measured normalized SH power can be seen in Fig. 3.2(c) as a function of the FH wavelength. This so-called tuning curve, or the phase-matching curve, was measured in the interval of $1.32 \mu\text{m}$ to $1.52 \mu\text{m}$ of the FH wavelength. The data is renormalized to take into account the wavelength dependent response of the optical elements in the setup and the quantum efficiencies of the cameras. We can see that the wavelength of maximum efficiency $\lambda_{\text{FH}} = 1.411 \mu\text{m}$ from this experiment is very close to what is theoretically predicted from Fig. 3.2(a), which shows a crossing at $\lambda_{\text{FH}} = 1.415 \mu\text{m}$ for $n_{\text{eff,SH}} = n_{\text{eff,FH}} = 1.946$. The fabricated structure here is slightly different than the theoretical schematic shown previously in Fig. 2.1(a), in that the SiO_2 substrate is under-etched slightly under the ridge WG. Taking that into account in the simulation results in the shift of the phase-matching wavelength to $\lambda_{\text{FH}} = 1.413 \mu\text{m}$ and the effective refractive indices to $n_{\text{eff,SH}} = n_{\text{eff,FH}} = 1.944$. Henceforth, experiment and theory are in good agreement in predicting the

phase-matching wavelength. Moreover, to confirm that the measured SH power is indeed the result of an SHG process, it is shown experimentally that the SH power is proportional to the square of the FH power. For this, the FH laser is set to the wavelength of maximum SHG efficiency ($\lambda_{\text{FH}} = 1.411 \mu\text{m}$) and the laser power is changed from 1 mW to 28 mW. The resulting SH power is shown in Fig. 3.2(d), along with a quadratic curve showing a good fit to the measurement and confirming SHG.

Importantly, we can notice that the phase-matching curve in Fig. 3.2(c) does not exactly resemble the sinc-function we expect from a lossless structure, as one of the minimum points around the central maximum does not hit zero, and the curve is rather between a sinc and a Lorentzian function, as was shown in Fig.3.1(b). This tells us that we must have non-negligible losses on this length scale, most probably caused by scattering from fabrication imperfections. To determine the loss of the FH mode, the contrast of the Fabry-Perot fringes can be used, that can be observed in transmission, induced by reflections from the end-facets [234]. The lossier a WG gets the smaller the contrast of its Fabry-Perot fringes becomes. By calculating what the reflection should be from a WG-air interface, one can predict the contrast of these fringes based on the loss of the WG. In Fig. 3.2(e), the measured power of the FH and the SH without normalization is shown, zoomed in a wavelength interval of 3 nm around the phase-matching wavelength. The Fabry-Perot fringes of the FH, which also cause fringes in the measured SH, are clearly visible. From the contrast of these fringes, the loss of the FH mode is found to be around 61 dB/cm, corresponding to a decay length of about $1/2k''_{\text{FH}} = 0.7 \text{ mm}$ for the power. Determining the loss of the SH mode is a more complicated task that requires comparison with the analytical results, as the Fabry-Perot fringes for the SH mode cannot be clearly observed, given that this higher-order mode cannot be excited dominantly using a focused beam. However, an indirect way can be used [204], where first the SHG efficiency is found experimentally and then is compared to an analytical prediction that uses the loss of the SH mode as the unknown variable. By equating the efficiencies, the loss of the SH mode can be determined. To make the analytical prediction, Eq. (3.20) is used with some adaptations. Firstly, Eq. (3.20) was derived for Bloch modes, whereas here we have simpler modes. If the WG mode profile $\mathbf{e}(y, z)$ is substituted instead of the Bloch mode profile, any integral over the volume of a supercell $\int_{\Omega} d^3\mathbf{r}$ turns into $a \iint dydz$. Secondly, for determining the field profile and band diagram of the lossy WG modes, a perturbative approach is used. It is assumed, that the scattering loss is not strong enough to change any property of the lossless mode considerably, except for an added imaginary part to the wave-vector. For a lossless mode profile, one can substitute $\mathbf{e}_{\text{FH}\pm}(y, z)$ with $\mathbf{e}_{\text{FH}\pm}^*(y, z)$. This also means, that the \mathcal{R} factors from Eqs. (3.17) and (3.19) are both equal to 1. Taking into account these changes in Eq. (3.20) will result in:

$$\mathcal{P}_{\text{SH}}(L) = \mathcal{P}_{\text{FH}}^2 \left| \frac{e^{i\Delta k' L} e^{-k''_{\text{SH}} L} - e^{-2k''_{\text{FH}} L}}{\Delta k' + i(k''_{\text{SH}} - 2k''_{\text{FH}})} \right|^2 \frac{n_{\text{gSH}} n_{\text{gFH}}^2 \frac{2\omega_{\text{SH}}^2}{c^3} \left| \iint \epsilon_0 \mathbf{p}_{\text{NL}} \cdot \mathbf{e}_{\text{SH}}^* dydz \right|^2}{\left| \iint \mathbf{d}_{\text{SH}} \cdot \mathbf{e}_{\text{SH}}^* dydz \right| \left| \iint \mathbf{d}_{\text{FH}} \cdot \mathbf{e}_{\text{FH}}^* dydz \right|^2}, \quad (3.23)$$

with \mathbf{p}_{NL} defined in Eq. (2.11) and $\Delta k' = k'_{\text{SH}} - 2k'_{\text{FH}}$. The same result as Eq. (3.23) can also be found using the conjugated reciprocity theorem under the perturbative approximation, where coupled mode equations similar to Eq. (3.12) are found for lossless modes and then loss is added phenomenologically to them [204]. Although the conjugated reciprocity theorem in the presence of small perturbative losses is a good approximation for this specific case, it will not be accurate for cases when large losses alter the modes, like modes near the bandedge, or when decay is an inherent property of the mode,

like a leaky or an evanescent mode. Then the unconjugated reciprocity theorem is needed.

Eq. (3.23) allows us to find the efficiency of the process as a function of the loss of the SH mode. The next step is to determine the efficiency of the SHG process from the experiment. For this, the powers of the FH mode and the generated SH mode at the phase-matching wavelength are measured at the output of the WG using a standard power-meter. By tracing back the effect of the optical elements, the light cone of the microscope objective, the transmission through the WG end-facet, and the loss of the FH mode, the FH power at the front-facet in the WG is approximated to be around $737 \mu\text{W}$ and the generated SH power inside the WG at its end-facet to be around 305 pW . Using these powers an SHG efficiency of about $6.9\% \text{ W}^{-1}\text{cm}^{-2}$ is found. This is almost 44 times smaller than the theoretical prediction for the case if the WG was completely lossless. For Eq. (3.23) to predict the same efficiency with the measured FH loss, the SH mode has to have a loss of 256 dB/cm , which corresponds to a decay length of about $1/2k''_{\text{SH}} = 0.17 \text{ mm}$ for the power. Using all the determined losses, the theoretical phase-matching function $\left| \frac{e^{i\Delta k' L} e^{-k''_{\text{SH}} L} - e^{-2k''_{\text{FH}} L}}{\Delta k' + i(k''_{\text{SH}} - 2k''_{\text{FH}})} \right|^2$ can be found for this structure. This is plotted in Fig. 3.2(c), overlapped with the experimental measurement. The theoretical curve is spectrally shifted by -3 nm to overlap with the experimental one, so the features of both curves can be compared easier. A good overall agreement can be seen between the theoretical and the experimental phase-matching curves. A point of discrepancy, is the fact that the theoretical curve has a wider spectral full-width-at-half-maximum (FWHM) of around 10 nm compared to the measured FWHM of around 6 nm . An explanation could be that we have overestimated the loss of the structure, used in evaluating the theoretical curve, that resulted in a widened spectrum. However, this cannot be the correct explanation, as even without loss the theory predicts a FWHM of around 9 nm for this WG. If the theory predicts a larger bandwidth than the experiment, it could be that the group index difference between the FH and SH modes found numerically does not match that of the experimental structure. This also cannot be a correct explanation, as this group index difference determines the wavelength distance between the two minor peaks around the main peak in Fig. 3.2(c), which for both cases of experiment and theory are around 30 nm apart. A remaining explanation could be connected to the fact that the fabricated WG sample suffers from stitching errors, an example of which is shown in the SEM image of Fig. 3.2(f). This happens at certain places along the WG sample, and its effect cannot be accurately taken into account in the current theory as a continuous out-of-structure scattering loss. This could cause internal reflections in the structure that in turn can modulate the phase-matching spectrum. This same effect could be why the measured spectrum does not look exactly symmetric with respect to the phase-matching wavelength. Nonetheless, these are still small discrepancies, and the main properties of this SHG experiment had been well described by the theoretical calculations.

Finally, these results can be compared with AlGaAs ridge WGs [204]. In reference [204], the measured efficiency is $13.8\% \text{ W}^{-1}\text{cm}^{-2}$, where the loss of the FH mode is measured to be 18.3 dB/cm and the loss of the SH mode is predicted to be 525 dB/cm . All numbers are comparable to the LN experiment here. Finally, it has to be mentioned, that knowing the decay lengths of the modes, one can predict the optimal structure length for getting maximum SHG, which analytically is $L_{\text{max}} = \ln(2k''_{\text{FH}}/k''_{\text{SH}})/(2k''_{\text{FH}} - k''_{\text{SH}})$ [226], and for the LN WG here gives a length of about 0.48 mm . If the experimental structure here was 0.48 mm long, instead of the 0.9 mm that it is, with an input FH power of $737 \mu\text{W}$ it would have generated 483 pW of SH power, instead of the 305 pW that it has.

3.3 SHG in a PCSW: nonlinear simulation and analysis

In the previous section, the analytical formulation for lossy SHG was put to use to analyze the results of an SHG experiment that suffered from fabrication disorder losses. In this section, the formulation will be used to theoretically analyze the SHG response of a phase-matched PCSW, where the SH mode suffers from leakage losses. As was discussed, given that phase-matched TWM processes, quantum or classical, have not yet been properly studied in PCSWs, performing such a study for the classical counterpart process of SHG will give us some needed insight on the quantum process of SPDC in this system. Moreover, as will be outlined in this section, it is possible to perform a nonlinear simulation using the FDTD method, to directly find the SHG response of the system. The results of this nonlinear simulation are then compared with the analytical predictions. This comparison will indirectly benefit the formulation of the SPDC process that appears in the next two chapters. The formulations for both the classical and quantum processes in this work rely on the QNBM expansion. Hence, the band diagram and the field profile of the QNBMs must be found numerically, and then inserted into the formulas. The details of the numerical methods in finding the lossless and leaky QNBMs are outlined in appendix A. By comparing the analytical predictions for SHG and the results of a direct nonlinear simulation, we are essentially testing the accuracy of the QNBM expansion and the numerical methods used in finding their modal information. More precisely, the focus of this comparison is verifying that we are correctly finding and using the leaky QNBM at the SH frequency, which is a type of mode that is not commonly used. Verifying the correct use of the leaky QNBMs for the classical process justifies their use equally in the quantum formulation. The lossless guided Bloch modes are already well studied and the numerical tools for finding them well established [169, 127].

For this study, the FP phase-matched design in the LN W1 PCSW is used, the band diagram of which was shown previously in Fig. 2.11(a), and is shown again in Fig. 3.4(a) for convenience. In this structure, a lossless slow FH mode is phase-matched to a leaky SH mode. A slow FH mode has advantages for both the classical and quantum nonlinear processes. As discussed before, slow light at the FH frequency can be used to enhance the efficiency of SHG [133, 134, 135], evident in Eq. (3.20) from the quadratic dependence of the generated SH power on the group index of the FH mode. Slow-light also has an advantage very important for the SPDC application, and that is the phase-matching spectrum of a TWM process involving slow modes can be much narrower than a process with regular modes. Hence, with slow modes, one can reach a narrow-spectrum interaction using shorter structure lengths, compared to the case with non-slow modes. This effect will be shown in this section.

First, we evaluate the generated SH power through Eq. (3.20), for which we need to use the linear properties of the Bloch modes involved in the interaction. This includes the Bloch mode profiles, group indices, and the real- or complex-valued wave-vectors, all of which have been found previously in chapter 2. However, before using these numerical data in Eq. (3.20), there is an important point that needs to be considered, regarding the field profile of a leaky QNBM at the SH frequency. Although the leaky mode of a WG is mainly concentrated in the WG region, it has an exponentially rising radiation tail in the transverse direction, which can be observed sufficiently far away from the WG [197]. We can observe this phenomena, by finding the field profile of the leaky mode in a supercell with a large transverse dimension of $160a$ in the y -direction, as shown in Fig. 3.3. The details of how this field profile is found with FDTD is explained in appendix A. The rising tail of the field is clearly visible

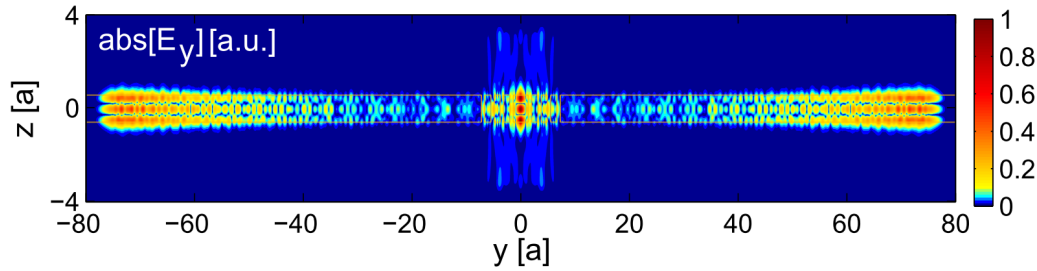


Figure 3.3: The absolute value of the E_y field component of the SH mode on the $x = 0.5a$ plane, in a supercell with a large y -dimension, showing the rising tail of the field.

at the left and right side of the simulation domain. This is the direction in which the mode is leaking into the PC slab due to the lack of a bandgap at this frequency range. A similar rising field should be observable in the z -direction, where the mode leaks into the surrounding air, if we choose a supercell that is large enough in the z -direction. An intuitive explanation is given in appendix A on the origin of this rising tail, by making an analogy between the leaky QNBMs and the more investigated leaky QNMs of a cavity [229, 235, 198, 199, 236, 237]. In numerical evaluation of integrals over infinite transversal dimensions with leaky modes, such as the adjoint flux and adjoint density integrals that also appear in Eq. (3.20), one has to be aware of this rising tail to avoid potentially non-converging or even diverging results. The finiteness of such integrals was mathematically proven for specific geometries [238, 229] by performing a complex coordinate transformation that causes the exponential tails of the leaky mode to decay, but preserves the total value of the integral. This was later generalized [221, 198] through the use of the PML boundary condition, which acts as a numerical equivalent of a complex coordinate transformation for any structure with an open boundary condition. In this way, the fields inside the PMLs can be used for the integration, and because the fields in the PMLs go to zero, the integrals are convergent. This property of the PMLs are used here for a correct evaluation of the integrals for the leaky mode in Eq. (3.20). More details of this procedure are given in appendix A.

An adjustment should also be made to Eq. (3.20), regarding this rising field profile of the leaky SH mode. For the leaky SH mode, we must use a finite transverse size, let us say a rectangle of width W and height H , in the definition of the power flux of Eq. (3.18), to avoid the infinite value of the Poynting vector integral of a leaky QNBM. Realistically, we will not be able to create the steady state field profile of the leaky mode over an infinite transversal dimension, which theoretically carries infinite power, as we need an infinite propagation direction to reach that steady state profile. Moreover, in a practical scenario, we only care for the power that is carried in the line defect region, as we usually couple the light out from that region. Henceforth in this case, $W = H = 2a$ is chosen to correspond to regions close to the line defect, where the QNBM expansion is also a good approximation, as was discussed before. Then the definition for \mathcal{R}_{SH} would be changed to $\mathcal{R}_{\text{SH}} \equiv 2 \int_{-H/2}^{+H/2} \int_{-W/2}^{+W/2} \text{Re}[\mathbf{e}_{\text{SH}_n} \times \mathbf{h}_{\text{SH}_n}^*] \cdot \mathbf{x} dy dz / |\mathcal{F}_{\text{SH}_n}|$. We must also calculate the power from the nonlinear FDTD simulation in the same region, to keep it comparable to this analytical calculation.

With these considerations, we can move on to calculate the generated SH power from Eq. (3.20). The input power into the FH mode is chosen to be 1 mW. Only the d_{33} coefficient of the d -tensor is considered in the calculation, as it later on simplifies the rigorous nonlinear simulation. It is also a good approximation, as the LN crystal has its c -axis in the y -direction, and both FH and SH modes are TE-like. The analytically calculated $\mathcal{P}_{\text{SH}}(x)$ is shown in Fig. 3.4(b) (the red curve). The SH power rises quadratically as a function of length at the beginning of the structure, then saturates for

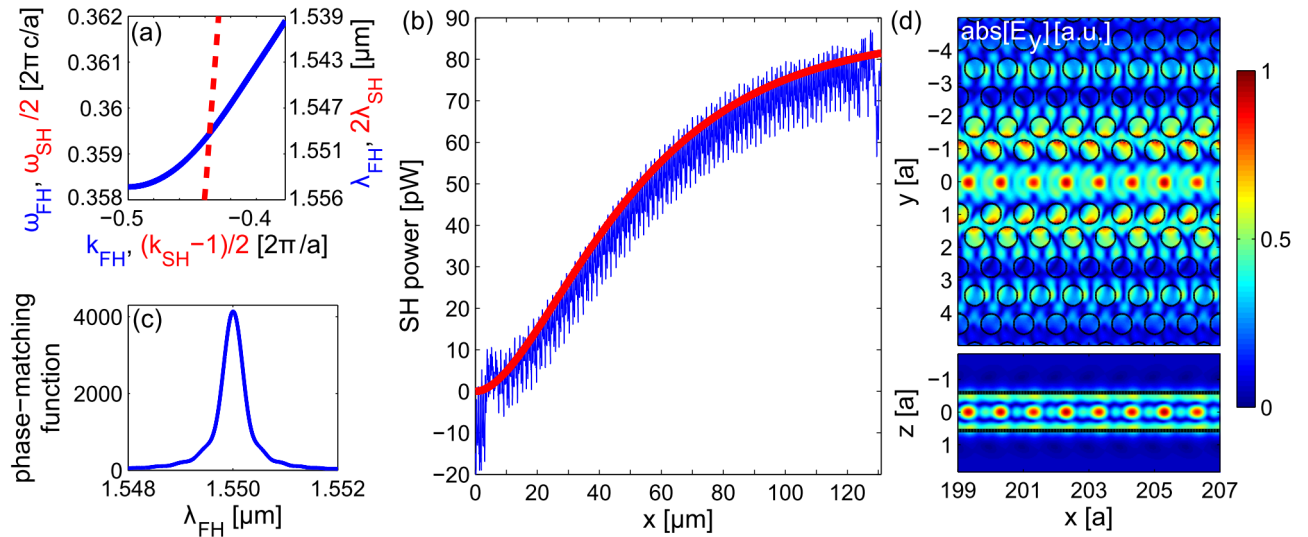


Figure 3.4: (a) Bands of the FH and SH modes (translated according to the phase-matching condition) corresponding to the dispersion engineered W1 PCSW presented in chapter 2 with design parameters $R/a = 0.3$, $h/a = 1.2$, $S_1/a = 0.1$, and $S_2/a = 0.05$ (see Figs. 2.6(a) and 2.7(b) for schematics of geometries), with $a = 0.557 \mu\text{m}$; (b) The generated SH power $\mathcal{P}_{SH}(x)$ for this FP phase-matched structure calculated from Eq. (3.20) (red curve) and from the nonlinear FDTD simulation (blue curve). Both cases are assuming an input FH power of 1 mW; (c) The phase-matching function calculated from Eq. (3.22), for $L = 120 \mu\text{m}$, as a function of the FH wavelength; (d) The absolute value of the E_y component of the generated SH field from the nonlinear FDTD simulation at the end region of the structure, at $z = 0$ (top) and $y = 0$ (bottom) planes.

propagation lengths greater than $120 \mu\text{m}$. This is the signature of an SHG process with a lossy SH mode, as was discussed before. This also means that structure lengths more than about $120 \mu\text{m}$ are not of much benefit for enhanced efficiency in this structure. At this length, the generated SH is about 80 pW. This limits the total efficiency of this specific design to about $8 \times 10^{-5} \text{W}^{-1}$. One can also give the efficiency in the units of $\text{W}^{-1}\text{cm}^{-2}$ by dividing the W^{-1} number with the square of the structure length, which will give an efficiency of $55\% \text{W}^{-1}\text{cm}^{-2}$. It should be kept in mind, that the efficiency of this PCSW will not rise for lengths larger than $120 \mu\text{m}$, so the $55\% \text{W}^{-1}\text{cm}^{-2}$ number is rather misleading, and $8 \times 10^{-5} \text{W}^{-1}$ gives a more accurate picture.

The phase-matching function of Eq. (3.22) can also be calculated using the band diagram of the modes and $L = 120 \mu\text{m}$. This is shown in Fig. 3.4(c), expressed as a function of the FH wavelength, showing an almost Lorentzian function. The Lorentzian shape is expected, as the structure length is more than the decay length of the SH mode. The FWHM bandwidth of the phase-matching function is around 0.5 nm, which is a very narrow spectral bandwidth compared to the length of this structure. We can compare this to the ridge WG from the previous section, which ideally without loss has a FWHM bandwidth of around 9 nm for a longer structure of 0.9 mm length. Hence, the PCSW is capable of delivering a narrower spectrum with a much shorter structure compared to a ridge WG. This is caused by the large difference between the group indices of the FH and the SH modes, due to the slow FH mode of group index 28, which results in a large $\text{Re}[n_{gSH} - n_{gFH}] \approx 25$. This quantity for the ridge WG is around 0.1. Consequently, with a slow mode involved in a parametric process, narrow spectral bandwidths can be achieved with shorter structures, compared to the cases involving non-slow modes. This illustrates a main benefit of using slow modes for SPDC applications when narrow spectra is needed for the generated photons. It is important to mention, that the spectrum does not get any narrower for structure lengths much longer than the decay length of the SH mode, as was

discussed before. Hence, the spectral-narrowing benefit of such PCSW designs only manifests itself over structure lengths comparable to or shorter than the decay length of its lossy modes.

To test the validity of the analytical model, a nonlinear FDTD simulation is performed in the UPA and the result for the generated SH power is compared with the theory. The method behind the nonlinear FDTD simulation is as follows: the FH field creates the nonlinear polarization, which acts as a source to excite the SH mode, as it is evident from Eq. (3.3). In the UPA, this source term does not get affected by the SH field. The source of nonlinear polarization in the simulation is created by using the Bloch mode profile of the FH mode and reproducing a FP FH mode in a structure with a length of 235 periods. This corresponds to $131 \mu\text{m}$, which is long enough to exhibit the saturation effect. Afterwards, the complex-valued E_y component of the FH field over the whole domain is squared and then multiplied by a spatial function that represents $d_{33}(\mathbf{r})$. Multiplying this by $2\epsilon_0$ generates the nonlinear polarization \mathbf{P}_{NL} . With this \mathbf{P}_{NL} , the current source $\mathbf{J}_{\text{NL}} = -i\omega_{\text{SH}}\mathbf{P}_{\text{NL}}$ can be generated, which according to Eq. (3.3) is the current source that is driving the field at the SH frequency. For the SHG simulation, \mathbf{J}_{NL} is used as a complex-valued source in the same geometry to drive the FDTD simulation at the SH frequency. The results of this simulation are shown in Figs. 3.4(b) and (d). In Fig. 3.4(d), the absolute value of the E_y component of the generated SH field can be seen around the region where the spatial nonlinear source ends. For finding the generated SH power, the SH Poynting vector is integrated over the same rectangular cross-section used for the analytical calculation. The result for the generated SH power is shown in Fig. 3.4(b), overlapped with the analytical prediction.

First, let us investigate the field profile of the generated SH, shown in Fig. 3.4(d). We see, that the generated field resembles that of the TE_{02} mode at the SH frequency, which is the target of the phase-matching design (see Fig. 2.9(b)). This resemblance is only in the line defect region, in which the QNBM expansion is a good approximation for modal expansion. Outside the line defect, especially around the first and second rows of holes, we see a strong field that corresponds to the part of the nonlinear polarization that is not concentrated in the line defect and overlaps best with the radiation modes of the PC slab, which are not of interest for guided and phase-matched SHG. The more important comparison is between the generated SH powers in Fig. 3.4(b). Overall, the analytical result agrees well with that of the nonlinear FDTD simulation. A distortion in the power can be observed for the nonlinear FDTD at the beginning and the end of the simulation domain, which could be caused by the abrupt starting and ending of the source of nonlinear polarization. Furthermore, the generated power in the nonlinear simulation has an additional oscillation of about $\pm 8 \text{ pW}$, whereas the analytical result is a smooth curve. This extra oscillation is caused by the out-of-phase generation of the SH power in the other QNBMs present at the SH frequency, including FP and BP ones. This is why the generated SH field in the line defect is not exactly the same as the field profile of the TE_{02} mode, but only resembles it, as the TE_{02} is the dominant mode contributing to the SHG process, but not the only one. In this case, out of all of the out-of-phase SH modes, the ones with the largest overlap integral with the nonlinear polarization are the FP and BP TE_{00} modes at the SH frequency, contributing dominantly to this power oscillation. Nonetheless, the TE_{02} mode, that is considered in the analytical evaluation, remains the dominant contributor to the SH power. This comparison not only verifies the validity of this particular phase-matched design, but more importantly verifies the analytical description of the SHG based on the QNBM expansion. At the same time, this comparison

makes clear the source of small differences between the results of a direct nonlinear simulation and an analytical calculation, that can arise from certain approximations made in the analytical formalism.

Before ending this section, it is interesting to compare the theoretical SHG efficiency found here for the W1 PCSW with that measured for the LN ridge WG in the previous section. The ridge WG experiment had a SHG efficiency of $6.9\% \text{ W}^{-1}\text{cm}^{-2}$, and the theoretical prediction for it without the scattering loss was 44 times larger, giving $304\% \text{ W}^{-1}\text{cm}^{-2}$. This tells us that in theory, the ridge WG has a better efficiency than the W1 PCSW, which has $55\% \text{ W}^{-1}\text{cm}^{-2}$. We have to keep in mind, that the efficiency for the PCSW was measured at a length where the SH power was already saturated because of the SH mode's loss. If we measure the efficiency for the PCSW at a much shorter length of $20 \mu\text{m}$ before the SH power saturates, we get $375\% \text{ W}^{-1}\text{cm}^{-2}$, which is now larger than what the lossless ridge WG can do. This tells us, that the PCSW with a slow FH mode could be beneficial for SHG compared to a ridge WG, but only on length scales shorter than the decay length of the leaky SH mode. In other words, the benefit of slow-light for enhancing SHG is an effect dependent not only on the group indices of the modes, but on their decay lengths and the length of the structure. At the same time, it is known that in the presence of any loss mechanism, the decay length of a mode has a strong dependence on its group index, such that a higher group index commonly results in a shorter decay length [156, 157]. This intertwined dependency of loss and group index on the efficiency of a nonlinear process demands an investigation to make clear the effect of loss on the usefulness of such slow-light-enhanced nonlinear processes, which has not yet been done before. This will be done in a general way in the next section, using the developed formulation for lossy SHG.

3.4 Effect of loss on slow-light-enhanced SHG

The dependence of P_{SH} on the group indices of the modes, expressed in Eq. (3.20), is the main motivation for using slow-modes for enhancing the efficiency of SHG. However, it has been shown that the decay length of a slow mode is shorter than that of a regular mode in the presence of any loss mechanism [156, 157]. This means the k'' of the modes in Eq. (3.20) increases with an increasing n_g . Hence, in the presence of loss, having a slow-light mode can have a positive and negative effect at the same time on the SHG efficiency, creating a trade-off. To make matters more complex, the presence of loss also puts a fundamental limit on how large the n_g of a slow-mode can get [239, 240]. Although the FH modes in all the designs in this work are ideally lossless, in practice, loss will always be present in nanostructured devices. If not in the form of material absorption or through some inherent leakage mechanism, loss will definitely exist in the form of scattering from fabrication imperfections, as was seen in the LN ridge WG experiment. Consequently, in enhancing a nonlinear parametric process using slow-light, the mentioned trade-off should be taken into account. Especially in the design process, it would be of interest to know if there exists an optimum regime of operation in using slow-modes, depending on the existing loss. In this section, this problem is investigated analytically in its general form for slow-light-enhanced SHG processes. The analytical method developed for lossy SHG is used to study the dependence of the SHG efficiency on the group indices of the lossy modes and to investigate different possible scenarios of using slow-light to enhance the efficiency of SHG. The results are corroborated by nonlinear FDTD simulations in the nanobeam designs of chapter 2.

To simplify the investigation using Eq. (3.20), it is assumed here that we are always at the point of phase-matching $\Delta k' = 0$ of a FP SHG process. Moreover, only parts of the formula that contain the information about the band diagram are kept. Hence, the equation used here for the analysis is:

$$P_{\text{SH}} \propto P_{\text{FH}}^2 |n_{\text{gFH}}^2 n_{\text{gSH}}| \left| \left(e^{-k''_{\text{SH}}L} - e^{-2k''_{\text{FH}}L} \right) / (k''_{\text{SH}} - 2k''_{\text{FH}}) \right|^2. \quad (3.24)$$

Here, the variables \mathcal{R}_{SH} , \mathcal{R}_{FH} , and \mathcal{P}_{eff} from Eq. (3.20) are disregarded, which are dependent on the profile of the modes, assuming that they are not a strong function of frequency compared to the group indices and losses at the bandedge. This is a reasonable approximation, as long as we are dealing only with the guided part of the modes and not their evanescent part into the bandgap. This is because lossy evanescent modes carry very little power, and purely evanescent modes carry no power. So the \mathcal{R} variables that have a power-flux integral in their nominator, will be much lower for the evanescent part of a band compared to its guided part. Consequently, for the SH powers calculated from Eq. (3.24), the values in the bandgap are not actually meaningful without adding the \mathcal{R} variables.

To get numbers from Eq. (3.24), a specific band diagram has to be chosen. For this, a generic quadratic band of a lossless Bloch mode near the bandedge $\omega(k) = \omega_0 + B(k - k_0)^2$ is used, where $2B$ is a parameter similar to the group velocity dispersion, but defined as $\partial^2\omega/\partial k^2 = \partial v_g/\partial k$. Other shapes of bands can be achieved as well in realistic structures [241, 242] and can be treated analytically with the same formalism as used here. However, the results are not expected to differ qualitatively. To find the complex- k band of the corresponding lossy system, a perturbative approach is used [239, 240], where the effect of loss is equivalent to an imaginary shift of $i\Delta\omega$ in the frequency. By changing $\omega_0 \rightarrow \omega_0 + i\Delta\omega$ and inverting the quadratic equation, we get:

$$k(\omega) \approx k_0 - \sqrt{(\omega - \omega_0 - i\Delta\omega)/B}. \quad (3.25)$$

This is only applicable for losses that follow the exponential decay of the Beer-Lambert law, like material loss [239, 240] or out-of-structure scattering caused by fabrication disorder [243]. $\Delta\omega$ can be calculated, in the case of material absorption from the field profile of a mode [239, 240], and in the general case it can be evaluated numerically, as done for the leaky SH modes in appendix A. $\Delta\omega a/2\pi c = 0.0002$ is set as a comparable number to what is found for the leaky SH modes. The real and imaginary parts of $k = k' + ik''$ are plotted from Eq. (3.25) in Figs. 3.5(a) and (b), for a lossless mode with $\Delta\omega = 0$ and a lossy mode with $\Delta\omega a/2\pi c = 0.0002$, respectively. The absolute value of the group index $|n_g|$ for both cases and the decay length $L_{\text{decay}} = 1/k''$ for the lossy case are shown in Figs. 3.5(c) and (d), respectively. As can be seen in Fig. 3.5(a) for the lossless case, we have a propagating mode with a purely real-valued k below ω_0 and an evanescent mode with a complex-valued k and a constant-valued $k' = \pi/a$ above ω_0 , where ω_0 denotes the bandedge frequency. The quadratic shape of k' results in a diverging n_g for the guided mode at the bandedge, as shown in Fig. 3.5(c). A purely imaginary-valued n_g can also be calculated for the evanescent mode in the bandgap of the lossless structure, but it is not displayed in this plot. In the presence of loss, this distinct jump between the purely guiding and purely evanescent character of the mode is obscured, as shown in Fig. 3.5(b). The band below ω_0 now has a k'' that increases towards the bandedge, resulting in an ever decreasing L_{decay} plotted in Fig. 3.5(d). The k' above the bandedge is no longer constant.

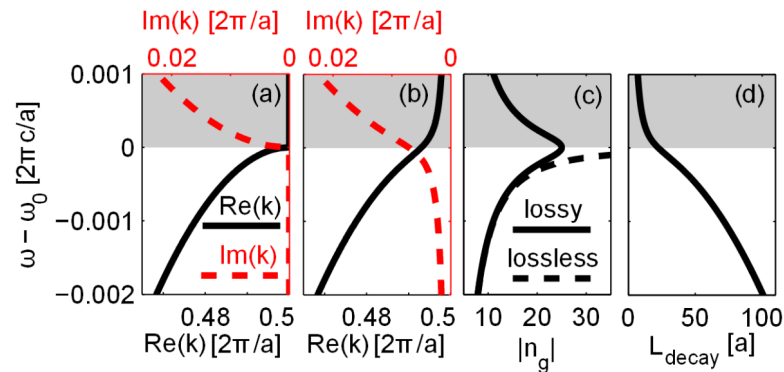


Figure 3.5: The real and imaginary part of k near the bandedge from Eq. (3.25) for (a) a lossless and (b) a lossy Bloch mode with $\Delta\omega a/2\pi c = 0.0002$. For both cases $B = -5\omega_0(a/2\pi)^2$ and $\omega_0 a/2\pi c = 0.4$ are fixed; (c) Absolute value of the group index $|n_g|$ of the lossy and the lossless modes; (d) Decay length of the lossy mode. The gray-shaded area is the bandgap region.

More importantly, k' at the bandedge is no longer quadratic, but flips upward. Hence, n_g no longer diverges, but its absolute value now reaches a finite maximum at ω_0 , as can be seen in Fig. 3.5(c). This maximum value for $|n_g|$ will be smaller for larger losses.

To investigate the trade-off in using slow-light for enhancing SHG in the presence of loss, let us consider two different cases, leading to different effects. In realistic scenarios, usually only one of the modes, FH or SH, is in a slow-light regime and it is phase-matched to a non-slow mode propagating with a group index close to that of a non-periodic structure. For example, in the nanobeam design of chapter 2 the SH mode was slow, whereas in the W1 PCSW it was the FH mode that was a slow mode. For the lossy slow mode in this analysis, the n_g and k'' of the band shown in Fig. 3.5(b) are used. These n_g and k'' are inserted into Eq. (3.24) as that of either a slow FH mode or a slow SH mode, while assigning a frequency-independent value to the k'' of the other non-slow mode. A frequency-independent n_g for the non-slow mode is just a multiplying factor and is not of interest. The assumption here is, that phase-matching can be achieved at any point along the band of the slow mode. As a result, the generated SH power $P_{\text{SH}}(L, \omega)$ can be calculated as a function of structure length and frequency of phase-matching in the slow mode. It is known for a lossy SHG process, that there exists an optimum structure length $L = L_{\text{max}}$ at which the generated SH power is maximal [226]. For a longer L the power decreases. L_{max} can be found by setting $\partial P_{\text{SH}}(L, \omega)/\partial L = 0$, which gives $L_{\text{max}} = \ln(2k''_{\text{FH}}/k''_{\text{SH}})/(2k''_{\text{FH}} - k''_{\text{SH}})$. The maximum power that can be generated in a structure phase-matched to the frequency ω in the slow band, can now be analytically evaluated by $P_{\text{SH}}(L_{\text{max}}, \omega)$.

$P_{\text{SH}}(L_{\text{max}}, \omega)$ and L_{max} are plotted for different cases in Fig. 3.6, where P_{FH}^2 is kept constant, meaning that the SH power in these plots is proportional to the SHG efficiency. Figs. 3.6(a) and (b) correspond to the case with a slow FH mode, and Figs. 3.6(c) and (d) to the case with a slow SH mode. Each case itself is studied under 3 different conditions: For the case with a slow FH (SH) mode, the loss for the non-slow SH (FH) mode is considered to be either much lower, comparable, or much higher than the slow FH (SH) mode. These relations between the losses have an important impact on the optimal group index at the point of phase-matching. In a realistic structure, such differences in the loss can be caused by differing loss mechanisms, e.g. material loss ϵ'' , scattering due to surface roughness, or leakage by coupling to radiating substrate modes. The losses caused by such mechanisms depend intricately on the frequency and profile of the specific modes and hence each of the scenarios investigated here could in principle take place. In this analysis, all the different possibilities

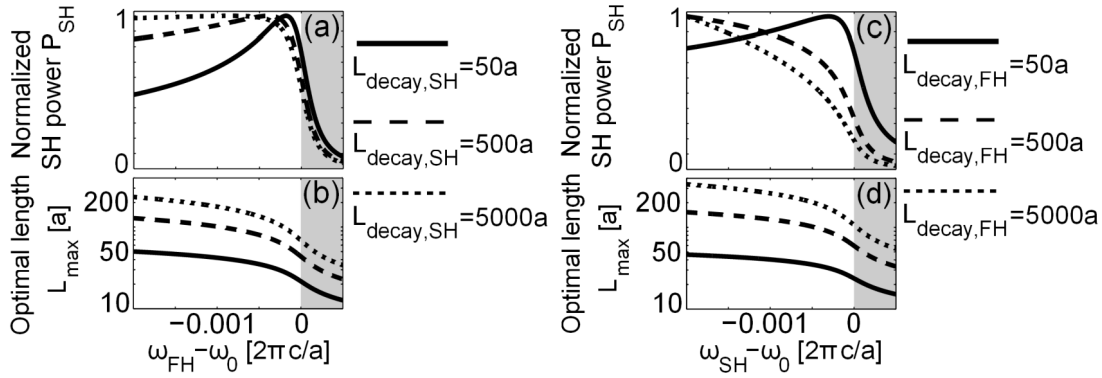


Figure 3.6: The normalized SH power $P_{SH}(L_{max}, \omega)$ and the optimal length $L_{max}(\omega)$, with ω being the phase-matching frequency. (a) and (b) use a slow FH mode with $\omega = \omega_{FH}$; (c) and (d) use a slow SH mode with $\omega = \omega_{SH}$. In each case, three different frequency-independent decay lengths L_{decay} are assigned to the non-slow mode. The gray-shaded area is the bandgap region.

are taken into account in the most abstract way by assigning different frequency-independent values to L_{decay} of the non-slow mode. The L_{decay} of the slow mode is the same as shown in Fig. 3.5(d). P_{SH} in each case is normalized to its maximum, as only the frequency dependence is of interest here.

As can be seen in Fig. 3.6, in some cases there exists a maximum in the SH power, corresponding to the maximum achievable SHG efficiency. Hence, in a device with a given amount of loss, there exists an absolute maximum efficiency for the SHG process, which is achieved at a certain length of the device L_{max} and for a certain group index n_g at the frequency of phase-matching. Notably, this maximum in the efficiency does not necessarily coincide with the maximum of $|n_g|$. Hence, when the loss of a slow mode is known, one can determine this optimum group index, and hence determine the frequency in the band of the slow mode that it is most efficient to phase-match to. The optimum length of the structure can also be determined, and in this way, the absolute maximum SHG efficiency achievable for that device will be reached. A maximum in efficiency near the bandedge is exhibited in all three cases with a slow FH mode in Fig. 3.6(a), but only in one of the cases with the slow SH mode in Fig. 3.6(c). This shows that the quadratic n_{gFH} dependency in Eq. (3.24) overcomes the increased losses for the slow FH mode and hence the maximum efficiency appears near the bandedge. The loss of the SH mode determines where exactly this maximum appears in Fig. 3.6(a). When the SH mode becomes lossier, L_{max} decreases and a slower FH mode is needed to have the power rise faster before reaching the length L_{max} . Hence, the maximum appears closer to the bandedge. Surprisingly, for a low loss SH mode the effect of the FH group index on the achievable efficiency is minute and all phase-matching frequencies will lead to approximately the same SH output powers, as can be seen in the rather flat curve in Fig. 3.6(a) for the $L_{decay,SH} = 5000a$ case. However, a slower FH mode allows reaching the maximal power at a shorter length L_{max} , as can be seen in Fig. 3.6(b).

In the case of a slow SH mode shown in Figs. 3.6(c) and (d), the behavior is different. Because of the linear n_{gSH} dependency of Eq. (3.24), having a slow SH mode is not always advantageous. In fact, when the FH mode loss is smaller or comparable to the SH mode loss, there is no maximum appearing near the bandedge, and the efficiency decreases with a slower SH mode. It is only for the case of a very lossy FH mode, that a slow SH mode can be advantageous, because SH power can be quickly generated along the propagation direction before the input FH completely decays. In all cases, the SH power decreases rapidly if the point of phase-matching is shifted beyond the frequency of maximum efficiency closer to the bandedge. This is because very close to the bandedge, the decay length is

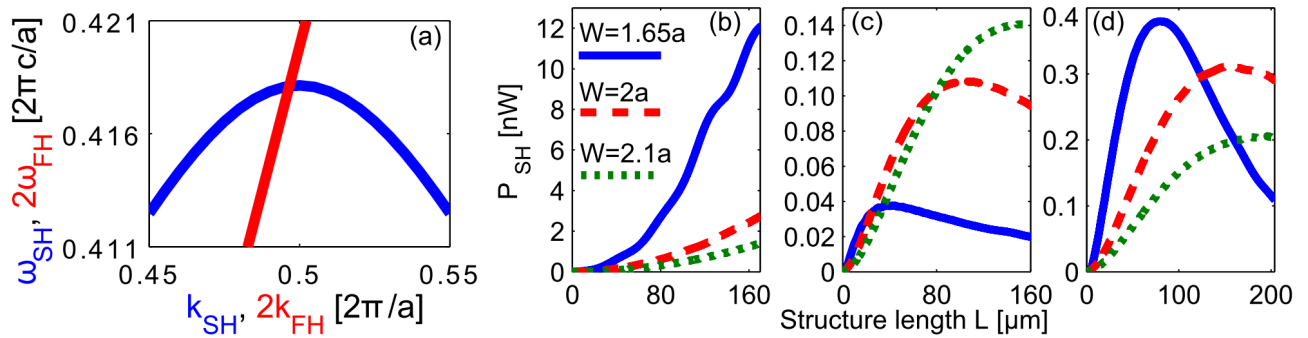


Figure 3.7: (a) The band diagram of the FH and the slow SH mode for the nanobeam design with $W/a = 1.65$, showing the phase-matching for a FP case; (b-d) The SH power along the propagation direction found from nonlinear FDTD simulations for 3 different nanobeam designs for the lossless and the lossy cases. The different nanobeam widths of $W/a = 2.1$, $W/a = 2$, and $W/a = 1.65$ result in the SH group index of $n_{\text{gSH}} = 5$, $n_{\text{gSH}} = 10$, and $n_{\text{gSH}} = 40$ at the point of phase-matching, respectively. FH pump power is 1mW: (b) The lossless structure; (c) The lossy case with $\epsilon''_{\text{FH}} = \epsilon''_{\text{SH}} = 0.003$; (d) The lossy case with $\epsilon''_{\text{FH}} = 0.01$ and $\epsilon''_{\text{SH}} = 0.0005$.

rapidly decreasing, which cannot be counteracted by an increasing group index, as $|n_{\text{g}}|$ is reaching its upper limit. This means that if the point of phase-matching for an optimally designed structure is frequency shifted towards the bandedge through fabrication inaccuracies, the structure will have a much lower SHG efficiency, compared to a frequency shift away from the bandedge.

To rigorously verify parts of the above analysis, the case of SHG with a slow SH mode is investigated by nonlinear FDTD in the presence of different levels of loss, using the nanobeam design of chapter 2. The bands and mode profiles for the phase-matched modes of this structure were previously presented in Fig. 2.4, and here we show the crossing bands of Fig. 2.4(d-ii) again in Fig. 3.7(a) for convenience. Fig. 3.7(a) shows the FP phase-matching crossing between a non-slow FH mode and a slow SH mode. As was presented in chapter 2, we are able to move the point of phase-matching through the SH band by changing the width W of the nanobeam. This allows us to have phase-matching at different n_{gSH} values along the SH band. The nonlinear FDTD simulation is performed for 3 different designs, all with the same $R/a = 0.35$ and $h/a = 1.4$, and different widths of $W/a = 2.1$, $W/a = 2$, and $W/a = 1.65$, which result in the group indices of $n_{\text{gSH}} = 5$, $n_{\text{gSH}} = 10$, and $n_{\text{gSH}} = 40$ at the point of phase-matching, respectively. The bands shown in Fig. 3.7(a) correspond to the $n_{\text{gSH}} = 40$ case. The FH mode is excited from one side of the structure and the generated SH power is measured along the propagation direction. The SHG process in this case is mediated dominantly by the d_{31} coefficient of the d-tensor. Loss is introduced by the imaginary part of the relative permittivity ϵ'' , which can be chosen independently in the FDTD simulation for the FH and the SH frequencies.

The nonlinear FDTD result for the lossless case is shown in Fig. 3.7(b). As expected from Eq. (3.24), an almost linear enhancement of P_{SH} with respect to n_{gSH} can be observed. The design with $n_{\text{gSH}} = 40$ produces about 4 times higher power than the one with $n_{\text{gSH}} = 10$, which itself produces about 2 times higher power compared to the $n_{\text{gSH}} = 5$ design. The oscillation in the power for the $n_{\text{gSH}} = 40$ case is caused by the out-of-phase generation of the backward SH mode. This out-of-phase generation is more pronounced in this case, because as can be seen in the band diagram corresponding to this design in Fig. 3.7(a), the point of phase-matching is very close to the bandedge. Hence, the FH mode is very close to satisfying the phase-matching condition with the BP SH mode on the other side of the bandedge, and consequently the out-of-phase BP SHG is stronger in this case compared to the other two designs. To investigate the effect of loss, two different scenarios are considered. In one, an

equal $\epsilon''_{\text{FH}} = \epsilon''_{\text{SH}} = 0.003$ is assigned to the relative permittivities of the dielectric. Because of the mode structure, the FH mode, which has less field concentrated in the dielectric, experiences lower losses compared to the SH mode. Hence, this scenario resembles the two cases in Fig. 3.6(c), where slow-light is not beneficial. Simulation results for this case are shown in Fig. 3.7(c). To study the case where the FH mode has a much higher loss compared to the SH mode, two different $\epsilon''_{\text{FH}} = 0.01$ and $\epsilon''_{\text{SH}} = 0.0005$ are assigned. This resembles the conditions of the only case in Fig. 3.6(c) where slow-light is beneficial. The result of the corresponding simulation is shown in Fig. 3.7(d). It can be seen that in both lossy configurations, a design with a higher n_{gSH} reaches its maximum SH power at a shorter length, as was predicted analytically. More importantly, the behavior of the maximum achievable SH power matches the analytical predictions. In Fig. 3.7(c), where the FH mode has lower losses than the SH mode, the design with the largest n_{gSH} produces the smallest maximum power, although it rises faster along the propagation direction compared to the other two designs. In Fig. 3.7(d), where the damping of the FH mode exceeds that of the SH mode, the design with the largest n_{gSH} produces the largest maximum SH power. Here, because the FH pump is decaying quickly, the SH mode with the largest group index can make the best use of the FH pump before it decays. These numerical results consolidate the insight from the theoretical analysis.

The analysis in this section shows, that for enhancing SHG in a lossy structure using slow-light, an optimum regime of operation exists, that can analytically be determined. It was also shown, that in some cases, using slow-light could be detrimental to the maximum achievable SHG efficiency. Although this analysis was restricted to SHG, these results can be generalized to any other parametric process, giving us intuition about the use of slow modes in the presence of loss in a TWM process.

3.5 Summary of the results and related publications

In this chapter, I have used analytical methods in combination with direct nonlinear FDTD simulations, to investigate and understand SHG in PCSWs, especially in the presence of loss, as a needed step before approaching the analysis of SPDC in PCSWs. This investigation also allowed for verifying some of the phase-matched designs for periodic WGs in a LN platform, which were presented in chapter 2. Moreover, results of an SHG experiment with a LN ridge WG were presented and analyzed, which I have performed during my thesis as part of our group's collective effort in developing an integrated LN platform for nonlinear optical applications. The result of the SHG experiment in the LN ridge WG is published in Optics Letters [S1]. The results for analyzing phase-matched SHG in PCSWs, based on the W1 design, including the analytical formulation of lossy SHG in periodic WGs and the comparison with the nonlinear FDTD simulation is published in Physical Review A [S2]. The results of the slow-light-enhanced loss study is published in Optics Letter [S3]. Finally, the nonlinear FDTD method that I developed during my thesis, was also used for simulating SHG in GaAs nanodisks, in a collaboration with the group of Igal Brener in Sandia National Laboratories, who have fabricated and characterized the nanodisks. The resulting work is published in Nano Letters [S4]. SHG experiments on GaAs nanodisks have also been performed in our group, again in collaboration with the Sandia group, where my nonlinear simulations again assisted in understanding the measurements, the result of which is published in ACS Photonics [S7].

Chapter 4

Spontaneous parametric down-conversion (SPDC)

In the previous chapters, it was shown that modally phase-matched designs for TWM processes can be reached in PCSWs, and classical TWM was numerically and analytically studied in these structures. It was in particular demonstrated, that PCSWs can offer a strong control over the phase-matching configurations. This includes reaching phase-matching between modes of different propagation directions, reaching simultaneous phase-matching between multiple processes, and controlling the group index of the modes at the point of phase-matching. In this chapter, I show how these capabilities of PCSWs allow us to control the different degrees of entanglement of spectrum, path, and mode, in an SPDC source of photon-pairs. For each case, the explanation will first be given in a general way regardless of the underlying periodic WG. Afterwards as particular examples, the double-slot LN PCSW designs presented in chapter 2 will be used to show how these capabilities can be implemented in a practical structure. The presentation of these results will conclude the main objective of this thesis, in demonstrating that PCSWs are highly versatile and compact sources of photon-pairs, capable of creating and controlling multiple degrees of entanglement at the generation stage, all in an integrated manner and without the need for pre- or post-processing steps.

I start this chapter by developing the theoretical framework needed for describing SPDC in periodic WGs. I will keep to a simpler and more standard theory in this chapter, involving lossless quantized signal and idler modes, as the focus in this chapter is on demonstrating SPDC applications. A more general SPDC theory is presented in the next chapter. After presenting the analytical method, I will first address the spectral entanglement. We have seen that a phase-matched PCSW provides control over the amplitude and sign of the group indices of the signal and idler modes. Here I explain how this control over group indices allows us to engineer spectral entanglement, especially for getting spectrally unentangled or factorizable pairs. This explanation is accompanied by a specific example of a double-slot PCSW from chapter 2. After spectral entanglement, I will address the path and modal entanglements. My proposal for creating these entanglements relies on the concept of simultaneous phase-matching introduced in chapter 2, where I presented a specific example of the simultaneous phase-matching of two CP processes and then presented schematically how different bands in a PCSW can give us various configurations of simultaneous processes involving different modes of different propagation directions. Here I explain how this idea translates into creating vari-

ous types of path and modal entanglements. I also use the double-slot PCSW with two CP processes as an example to show how such a structure can be tuned to produce maximally-entangled states, in this particular case, a path-entangled Bell state.

4.1 SPDC theory for lossless and guided signal and idler modes

In this section, a formalism is developed for describing the generated biphoton state $|\psi\rangle$ from SPDC in a periodic WG. A semi-classical approximation is used, in which the strong and leaky pump beam is treated classically and only the lossless signal and idler modes are quantized. The signal and idler modes in all the designs in this work are ideally lossless, assuming no fabrication disorder, and here they are treated in this ideal condition. The UPA is used for the pump, which assumes that the pair-generation does not have any effect on the amplitude of the strong classical pump mode, which is a reasonable approximation. It is also assumed, that the nonlinear interaction is weak enough, or equivalently the pump power is low enough, that the probability of generating higher-order pairs is negligible. This is the desired regime for photon-pair sources to operate in, to avoid multiple pair emission, that reduces the purity of such sources [89]. This also has an analytical convenience, in that the first-order perturbation theory can be used for the calculation, which finds the probability of generating one pair of photons at a time. The framework for this type of calculation is already well-developed for non-periodic WGs [244]. This framework has also been applied to periodic structures [150], by expanding the Bloch modes into their BHs and quantizing the plane-wave-like BHs. Here, a more simplified version of such a calculation is used, by using a quantization scheme for Bloch modes [245] that makes the calculations more compact and easier to use. The calculation starts from the Schrödinger equation in the interaction picture [246]:

$$i\hbar \frac{\partial |\psi(t)\rangle}{\partial t} = \hat{H}_{\text{int}}(t) |\psi(t)\rangle, \quad (4.1)$$

where $\hat{H}_{\text{int}}(t)$ is the nonlinear Hamiltonian of the SPDC process [245, 244]:

$$\hat{H}_{\text{int}}(t) = -\mathcal{D}\epsilon_0 \int d^3\mathbf{r} \sum_{\alpha,\beta,\gamma} \chi_{\alpha\beta\gamma}^{(2)}(\mathbf{r}) E_{\text{P},\gamma}(\mathbf{r},t) \hat{E}_{\text{S},\alpha}^-(\mathbf{r},t) \hat{E}_{\text{I},\beta}^-(\mathbf{r},t) + \text{H.c.} \quad (4.2)$$

Here H.c. stands for Hermitian conjugate and the volume integral is over the nonlinear medium. \mathcal{D} is a constant factor referring to the modal degeneracy of the process. When signal and idler modes are both in the same band, where a band is defined as a dispersion relation described by a continuous $k(\omega)$ expression, then $\mathcal{D} = 1$. When signal and idler are in two different bands we have $\mathcal{D} = 2$. $E_{\text{P},\gamma}(\mathbf{r},t)$ is the γ -component of the positive-frequency part of the electric field of the classical pump pulse:

$$\mathbf{E}_{\text{P}}(\mathbf{r},t) = \int_0^{+\infty} d\omega_{\text{P}} A_{\text{P}}(\omega_{\text{P}}) \mathbf{E}_{\text{P}}(\mathbf{r},\omega_{\text{P}}) e^{-i\omega_{\text{P}}t}, \text{ with } \mathbf{E}_{\text{P}}(\mathbf{r},\omega_{\text{P}}) = \mathbf{e}_{\text{P}}(\mathbf{r},\omega_{\text{P}}) e^{ik_{\text{P}}(\omega_{\text{P}})x - \alpha_{\text{P}}(\omega_{\text{P}})x}, \quad (4.3)$$

where A_{P} is the spectrum of the pump pulse, k_{P} is the real part of pump's wave-vector and α_{P} its imaginary part, $1/\alpha_{\text{P}}$ is the decay length of the pump mode, and \mathbf{e} is the electric field profile of the Bloch mode. The real-valued pump pulse can be found by adding $\mathbf{E}_{\text{P}}(\mathbf{r},t)$ to its complex conjugate.

$\hat{E}_{S,\alpha}^-(\mathbf{r},t)$ in Eq. (4.2) is the α -component of the negative-frequency part of the electric field operator in the interaction picture for the quantized signal mode. The total electric field operator is $\hat{\mathbf{E}} = \hat{\mathbf{E}}^- + \hat{\mathbf{E}}^+$, where $\hat{\mathbf{E}}^+ = (\hat{\mathbf{E}}^-)^\dagger$. The negative-frequency part of the electric field operator is [245, 244]:

$$\hat{\mathbf{E}}_m^-(\mathbf{r},t) = \int_{-\pi/a}^{+\pi/a} dk_m \sqrt{\frac{\hbar \omega_m(k_m)}{2}} e^{i\omega_m t} \mathbf{E}_m^*(\mathbf{r},k_m) \hat{a}_{m,k_m}^\dagger, \text{ with } \mathbf{E}_m(\mathbf{r},k) = \mathbf{e}_m(\mathbf{r},k) \frac{e^{ikx}}{\sqrt{2\pi}}, \quad (4.4)$$

with $m = S, I$ for the signal and idler modes. The band diagram for each mode covers the first BZ. This means, that the integral $\int_{-\pi/a}^{+\pi/a}$ includes both the FP and the BP parts of a mode. It should be mentioned, that for every band in a periodic WG there always exists a part of the band that is above the light line and leaky. These regions are not considered in the calculations here, as the used quantization method is strictly for fully guided signal and idler modes. So the assumption is that the phase-matching condition is set to dominantly create the pair in the fully guided parts of the signal and idler bands. $\hat{a}_{m,k}^\dagger$ is the creation operator corresponding to the creation of a photon in mode m at the wave-vector k . The commutation relations for these creation and annihilation operators are:

$$[\hat{a}_{m,k}, \hat{a}_{m',k'}] = 0, \quad [\hat{a}_{m,k}, \hat{a}_{m',k'}^\dagger] = \delta_{mm'} \delta(k - k'). \quad (4.5)$$

To use a Bloch mode profile in Eq. (4.4), it has to be normalized such that [245]:

$$\int_{\Omega} d^3\mathbf{r} \mathbf{d}_m(\mathbf{r},k) \cdot \mathbf{e}_m^*(\mathbf{r},k) = \int_{\Omega} d^3\mathbf{r} \epsilon_0 \bar{\epsilon} \mathbf{e}_m(\mathbf{r},k) \cdot \mathbf{e}_m^*(\mathbf{r},k) = a, \quad (4.6)$$

where \mathbf{d} is the displacement field profile of the Bloch mode and Ω is the volume of a supercell. Solving the time evolution of Eq. (4.1) at times much longer than the extent of the nonlinear interaction using the first-order perturbation theory results in:

$$|\psi(t \rightarrow +\infty)\rangle \approx |\psi(t \rightarrow -\infty)\rangle - \frac{i}{\hbar} \int_{-\infty}^{+\infty} \hat{H}_{\text{int}}(t) |\psi(t \rightarrow -\infty)\rangle dt. \quad (4.7)$$

Substituting $\hat{H}_{\text{int}}(t)$ from Eq. (4.2) and assuming a vacuum initial state $|\psi(t \rightarrow -\infty)\rangle = |0\rangle$ gives:

$$|\psi\rangle = \mathcal{D} \frac{i\epsilon_0}{\hbar} \int_{-\infty}^{+\infty} dt \int d^3\mathbf{r} \sum_{\alpha,\beta,\gamma} \chi_{\alpha\beta\gamma}^{(2)}(\mathbf{r}) E_{P,\gamma}(\mathbf{r},t) \hat{E}_{S,\alpha}^-(\mathbf{r},t) \hat{E}_{I,\beta}^-(\mathbf{r},t) |0\rangle, \quad (4.8)$$

where the dominant contribution of the existing vacuum is disregarded. Substituting the frequency and the wave-vector domain expansion of the fields from Eqs. (4.3) and (4.4) into Eq. (4.8) allows us to take the time integral of $\int_{-\infty}^{+\infty} e^{-i(\omega_P - \omega_S - \omega_I)t} dt = 2\pi \delta(\omega_P - \omega_S - \omega_I)$. This consequently allows us to take the $\int d\omega_P$ integral, which fixes ω_P to $\omega_S + \omega_I$, indicating that conservation of frequency must be held after an infinite interaction time. It should be reminded that all the frequency variables defined above are positive valued, such that $\{\omega_P, \omega_S, \omega_I\} > 0$. This gives:

$$|\psi\rangle = \mathcal{D} \frac{i\epsilon_0}{2} \iint_{-\pi/a}^{+\pi/a} dk_S dk_I \sqrt{\omega_S(k_S) \omega_I(k_I)} A_P(\omega_S + \omega_I) \int d^3\mathbf{r} \sum_{\alpha,\beta,\gamma} \chi_{\alpha\beta\gamma}^{(2)}(\mathbf{r}) \times e^{i\Delta kx - \alpha_P(\omega_S + \omega_I)x} e^{i\frac{2\pi Q}{a}x} e_{P,\gamma}(\mathbf{r}, \omega_S + \omega_I) e_{S,\alpha}^*(\mathbf{r}, k_S) e_{I,\beta}^*(\mathbf{r}, k_I) \hat{a}_{S,k_S}^\dagger \hat{a}_{I,k_I}^\dagger |0\rangle, \quad (4.9)$$

with $\Delta k = k_P(\omega_S + \omega_I) - k_S - k_I - \frac{2\pi Q}{a}$, $Q = 0, \pm 1, \pm 2, \dots$, where the integrand was multiplied by a $e^{-i\frac{2\pi Q}{a}x} e^{i\frac{2\pi Q}{a}x} = 1$ factor. The volume integral is over the nonlinear volume of a periodic waveguide of length L , meaning $\int d^3\mathbf{r} = \int_0^L dx \int_{-\infty}^{+\infty} dy dz$. Let us evaluate this volume integral, assuming that at least one or more phase-matching conditions ($\Delta k = 0$) are satisfied around certain regions in the $k_S k_I$ -space, and hence these regions have the main contribution to the $\int_{-\pi/a}^{+\pi/a} dk_S dk_I$ integrals. Around the phase-matching conditions we have $\Delta k \ll 1/a$, which means the function $e^{i\Delta k x}$ has a slow variation over the length of a period. Let us also assume that the pump has a low enough leakage loss such that $\alpha_P \ll 1/a$, which makes $e^{-\alpha_P x}$ also slowly varying over a period. The above two assumptions are valid for any useful SPDC design. With these slowly varying functions, and the fact that Bloch mode profiles and $e^{i\frac{2\pi Q}{a}x}$ are periodic functions over the length a , we can make the approximation $\int_0^L dx \int_{-\infty}^{+\infty} dy dz e^{i(\Delta k - \alpha_P)x} f(\mathbf{r}) \approx \frac{\int_0^L dx e^{(i\Delta k - \alpha_P)x}}{a} \int_{\Omega} d^3\mathbf{r} f(\mathbf{r})$, where $f(\mathbf{r}) \equiv \sum_{\alpha, \beta, \gamma} \chi_{\alpha\beta\gamma}^{(2)} e^{i\frac{2\pi Q}{a}x} e_{P,\gamma} e_{S,\alpha}^* e_{I,\beta}^*$ is a periodic function. Evaluating $\int_0^L dx e^{(i\Delta k - \alpha_P)x}$ gives:

$$|\psi\rangle = \mathcal{D} \frac{i\epsilon_0}{2} \iint_{-\pi/a}^{+\pi/a} dk_S dk_I \sqrt{\omega_S \omega_I} A_P \frac{e^{(i\Delta k - \alpha_P)L} - 1}{(i\Delta k - \alpha_P)a} \int_{\Omega} d^3\mathbf{r} f(\mathbf{r}, k_S, k_I) \hat{a}_{S,k_S}^\dagger \hat{a}_{I,k_I}^\dagger |0\rangle. \quad (4.10)$$

Although Eq. (4.10) is a simplified expression, it has integrals in the k -domain, whereas usually it is desired to have frequency-dependent expressions. Hence, a change of variables will be performed to go from modes quantized in the k -domain to the frequency domain. To be able to do this, there should exist a monotonic relation between the wave-vector of a mode and its frequency. This means that we have to separate the $\int_{-\pi/a}^{+\pi/a} dk_S dk_I$ integrals into k -regions, in which the signal and idler bands are monotonic. Hence, each band over the first BZ is separated into regions where the sign of $d\omega/dk$ does not change. This is exactly the same as what was done in chapter 2, when the concept of a bandlet was introduced. An example of separating a band into its bandlets was shown in Fig. 2.16(b). Here, the bandlets in the signal and idler bands are indexed with $n = \pm 1, \pm 2, \dots$ and $m = \pm 1, \pm 2, \dots$, respectively, up to as many bandlets that exist. The positive and negative indexes correspond to the FP and BP bandlets, as every FP bandlet has a BP counterpart. This separates the $k_S k_I$ -space into k -regions over which the modes do not change their propagation directions. In each such region, we can then use the following relations to transform k -quantized modes to ω -quantized ones: $dk = d\omega \frac{dk}{d\omega} = d\omega \frac{n_g(\omega)}{c}$, with the new operators in the ω -domain given by $\hat{a}_{m,\omega} = \hat{a}_{m,k} \sqrt{\frac{dk}{d\omega}}$, with commutation relations:

$$[\hat{a}_{m,\omega}, \hat{a}_{m',\omega'}] = 0, \quad [\hat{a}_{m,\omega}, \hat{a}_{m',\omega'}^\dagger] = \delta_{mm'} \delta(\omega - \omega'). \quad (4.11)$$

We can now write $dk \hat{a}_k^\dagger = d\omega \frac{dk}{d\omega} \hat{a}_\omega^\dagger \left(\sqrt{\frac{d\omega}{dk}} \right)^*$. n_g of the lossless quantized modes is a real number, but could be positive or negative based on the propagation direction. Hence, we can simplify $\frac{dk}{d\omega} \left(\sqrt{\frac{d\omega}{dk}} \right)^* = \frac{1}{\sqrt{c}} \frac{\text{sign}(n_g) |n_g|}{(\sqrt{n_g})^*} = \text{sign}(n_g) \sqrt{\frac{n_g}{c}}$. Implementing these in Eq. (4.10) results in:

$$|\psi\rangle = \mathcal{D} \frac{i\epsilon_0}{2} \sum_{n,m} \iint d\omega_S d\omega_I \text{sign}(n_{gS,n} n_{gI,m}) \sqrt{n_{gS,n} n_{gI,m}} \sqrt{\frac{\omega_S}{c} \frac{\omega_I}{c}} \times A_P \frac{e^{(i\Delta k - \alpha_P)L} - 1}{(i\Delta k - \alpha_P)a} \int_{\Omega} d^3\mathbf{r} f(\mathbf{r}, k_S(\omega_S), k_I(\omega_I)) \hat{a}_{S,n,\omega_S}^\dagger \hat{a}_{I,m,\omega_I}^\dagger |0\rangle. \quad (4.12)$$

The final result can be made independent of arbitrary proportionality factors in the electric field profile of the modes, by dividing $|\psi\rangle$ by $\sqrt{\int_{\Omega} d^3\mathbf{r} d\mathbf{s} \cdot \mathbf{e}_S^* \int_{\Omega} d^3\mathbf{r} d\mathbf{l} \cdot \mathbf{e}_I^*} / a = 1$, where equality to 1 is according to the normalization condition of Eq. (4.6). This results in:

$$|\psi\rangle = \sum_{n,m} \iint d\omega_S d\omega_I \text{JSA}_{n,m}(\omega_S, \omega_I) |S, n, \omega_S\rangle |I, m, \omega_I\rangle, \quad (4.13)$$

where $|S, n, \omega_S\rangle |I, m, \omega_I\rangle$ is another way of writing $\hat{a}_{S,n,\omega_S}^\dagger \hat{a}_{I,m,\omega_I}^\dagger |0\rangle$. The joint spectral amplitude (JSA) of the SPDC process corresponding to every pair of signal and idler bandlets is defined as:

$$\text{JSA}_{n,m}(\omega_S, \omega_I) \equiv A_P(\omega_S + \omega_I) \text{Ov}_{n,m}(\omega_S, \omega_I) \text{JPS}_{n,m}(\omega_S, \omega_I), \quad (4.14)$$

where the joint phase-matching spectrum JPS and the overlap integral Ov are defined as:

$$\text{JPS}_{n,m}(\omega_S, \omega_I) \equiv \frac{e^{[i\Delta k_{n,m}(\omega_S, \omega_I) - \alpha_P(\omega_S + \omega_I)]L} - 1}{[i\Delta k_{n,m}(\omega_S, \omega_I) - \alpha_P(\omega_S + \omega_I)]a}, \quad (4.15)$$

$$\begin{aligned} \text{Ov}_{n,m}(\omega_S, \omega_I) &\equiv \mathcal{D} \frac{i}{2} \text{sign}(n_{gS,n} n_{gI,m}) \sqrt{n_{gS,n} n_{gI,m}} \sqrt{\frac{\omega_S a}{c} \frac{\omega_I a}{c}} \\ &\times \frac{\int_{\Omega} d^3\mathbf{r} \sum_{\alpha,\beta,\gamma} \chi_{\alpha\beta\gamma}^{(2)}(\mathbf{r}) e^{i\frac{2\pi Q}{a}x} e_{P,\gamma}(\mathbf{r}, \omega_S + \omega_I) e_{S,n,\alpha}^*(\mathbf{r}, \omega_S) e_{I,m,\beta}^*(\mathbf{r}, \omega_I)}{\sqrt{\int_{\Omega} d^3\mathbf{r} \bar{\epsilon}(\omega_S) \mathbf{e}_{S,n}(\mathbf{r}, \omega_S) \cdot \mathbf{e}_{S,n}^*(\mathbf{r}, \omega_S) \int_{\Omega} d^3\mathbf{r} \bar{\epsilon}(\omega_I) \mathbf{e}_{I,m}(\mathbf{r}, \omega_I) \cdot \mathbf{e}_{I,m}^*(\mathbf{r}, \omega_I)}}, \end{aligned} \quad (4.16)$$

with the phase-mismatch being $\Delta k_{n,m}(\omega_S, \omega_I) \equiv k_P(\omega_S + \omega_I) - k_{S,n}(\omega_S) - k_{I,m}(\omega_I) - \frac{2\pi Q}{a}$.

Eqs. (4.13) to (4.16) are the final results of this calculation. The biphoton state in Eq. (4.13) has a sum over different combinations of signal and idler bandlets that could be phase-matched to the pump. This represents an entanglement in the modal DOF or more accurately in the bandlet DOF. Since the bandlets could have different directions of propagation, the sum in Eq. (4.13) also represents an entanglement in the path DOF. With what probability each pair of bandlets are contributing to the sum in Eq. (4.13), is determined by its JSA function. The JSA also describes the entanglement in the spectral DOF. The JSA in Eq. (4.14) is separated into three parts. A_P determines the pump pulse's spectrum and strength, and can be chosen in an experiment according to what is needed. It should be noted, that there is also e_P appearing in the overlap integral that could determine pump pulse's strength. In the definition of pump in Eq. (4.3), the amplitude of e_P was not restricted, henceforth, whatever the strength of the pump pulse is, it can be arbitrarily divided between A_P and e_P . The JPS function depends on the phase-mismatch Δk . The Ov function is dependent on the overlap integral of the modes, telling us how efficiently the electric field profiles of the modes and the nonlinearity tensor of the material are coming together to mediate the interaction. The spectral functionality of the JSA can usually be determined only by A_P and JPS, as Ov is a weaker function of frequency, except if the modes are very close to the bandedge, where group indices change rapidly, or near a band splitting, where mode profiles change strongly. Finally, by looking at the group index dependencies in Eq. (4.16), one could draw the conclusion that the efficiency of a process could be strongly enhanced with slow signal and idler modes, but that is not a correct conclusion. The larger n_g gets, the smaller

the frequency bandwidth for it becomes, such that the integral $\int d\omega n_g(\omega)$ stays finite. This is more evident, when the generation probability of a single photon-pair $\langle \psi | \psi \rangle$ is calculated. From Eq. (4.13) and using Eq. (4.11), we find $\langle \psi | \psi \rangle = \sum_{n,m} \iint d\omega_S d\omega_I |JSA_{n,m}(\omega_S, \omega_I)|^2$. The group index functionality in $|JSA_{n,m}(\omega_S, \omega_I)|^2$ is $|n_{gS,n} n_{gI,m}|$, which means we have $\langle \psi | \psi \rangle = \iint d\omega_S d\omega_I |n_{gS,n} n_{gI,m}| \dots$. Looking back at how the group index originally appeared in the formulation, we remember that it originated from the k-space integral with $dk \propto d\omega n_g$. Consequently, the larger n_g gets, the smaller its frequency bandwidth $d\omega$ becomes, in a way to produce the same dk . This means, that slow-light for signal and idler modes does not enhance the total probability of pair-generation, but instead narrows the spectral bandwidth of the interaction.

4.2 Controlling spectral entanglement: counterpropagating factorizable pair example

The signal and idler photons in a pair are spectrally entangled to each other, as described by the JSA function in $|\psi\rangle = \iint d\omega_S d\omega_I JSA(\omega_S, \omega_I) |S, \omega_S\rangle |I, \omega_I\rangle$. To simplify things here, it is assumed that we have only one phase-matched process. To understand spectral entanglement, a Schmidt decomposition [247, 73] can be done on the JSA to decompose it into a biorthogonal set of functions $\{u_n(\omega_S)\}$ and $\{v_n(\omega_I)\}$, such that $JSA(\omega_S, \omega_I) = \sum_n \sqrt{\Lambda_n} u_n(\omega_S) v_n(\omega_I)$, with the probabilities summing up to one, $\sum_n \Lambda_n = 1$. Hence, the biphoton state can be decomposed into $|\psi\rangle = \sum_n \sqrt{\Lambda_n} |\psi_S^n\rangle \otimes |\psi_I^n\rangle$, with the Schmidt modes defined as $|\psi_S^n\rangle \equiv \int d\omega_S u_n(\omega_S) |S, \omega_S\rangle$ and $|\psi_I^n\rangle \equiv \int d\omega_I v_n(\omega_I) |I, \omega_I\rangle$, and \otimes being a direct product. This expansion makes the meaning of spectral entanglement clearer: Upon detection, there is a probability Λ_n that we detect a signal photon with the $u_n(\omega_S)$ spectrum and an idler photon with the $v_n(\omega_I)$ spectrum. A photon-pair state is unentangled in the spectral DOF, if there exists only one non-zero probability, e.g. $\Lambda_0 = 1$, in the Schmidt decomposition. This is referred to as a factorizable state, because the JSA can be separated or factorized into its signal and idler spectra, such that $JSA(\omega_S, \omega_I) = u(\omega_S)v(\omega_I)$, which results in $|\psi\rangle = |\psi_S\rangle \otimes |\psi_I\rangle$. Such JSAs are shown schematically in Fig. 4.1(a), where $JSA(\omega_S, \omega_I)$ is shown as a function of the signal and idler frequencies. A visual clue in recognizing a factorizable JSA is for it to look either like a horizontal ellipse, a vertical ellipse, or an intermediate case of a circle. Spectrally unentangled pairs are highly desired for sources of heralded single-photons, and a common effort in the design of photon-pair sources is centered around producing factorizable JSAs [73, 74, 151, 50, 108, 125, 97, 98, 106, 126]. Hence, the explanation here on engineering the spectral DOF using PCSWs will be focused on achieving this goal. A specific example using a double-slot LN PCSW in a CP phase-matching configuration will accompany the explanations to demonstrate the practicality of the ideas.

The important parameters for reaching a factorizable JSA are the spectral bandwidth of the pump pulse $\Delta\omega_P$, length of the structure L , and the group indices of the modes [73, 74, 50]. The effect of these parameters will be explained in the following, with the help of the schematic plots shown in Figs. 4.1(b) and (c). As was shown in Eq. (4.14) and discussed in the previous section, the main spectral functionality of the JSA comes from the pump pulse's spectrum A_P and the join phase-matching spectrum JPS, such that $JSA(\omega_S, \omega_I) \propto A_P(\omega_S + \omega_I) JPS(\omega_S, \omega_I)$. A_P is shown schematically in Figs. 4.1(b-i) and (c-i), where the A_P in plot (c-i) corresponds to a larger $\Delta\omega_P$. The -45 degrees

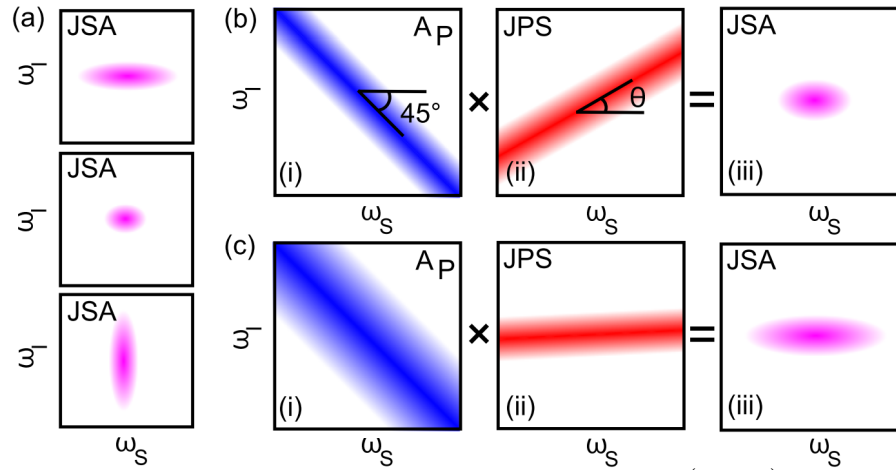


Figure 4.1: (a) Examples of a factorizable joint spectral amplitude, $JSA(\omega_S, \omega_I)$, shown schematically. Respectively from above, a horizontal ellipse, a circle, and a vertical ellipse shaped JSAs are shown; (b) and (c) schematically show two different cases where a factorizable JSA is produced from the multiplication of the pump pulse's spectrum $A_P(\omega_S + \omega_I)$ and the joint phase-matching spectrum $JPS(\omega_S, \omega_I)$. θ is the angle that the line of the maximum-JPS makes with the ω_S -axis.

angle that the A_P function exhibits in these plots, where the angle is with respect to the ω_S axis, is fixed due to the conservation of energy. The main control parameter here is $\Delta\omega_P$, that changes the width of A_P . JPS is shown schematically in Figs. 4.1(b-ii) and (c-ii), corresponding to two different sets of L and n_g of the modes. The width of JPS depends on L and also on the difference between the group indices of the modes. If a certain combination of group indices are already fixed by the design, then L can be used to control this width, where a larger L results in a narrower JPS. Although with a lossy pump, there is a limit to how narrow JPS can get for lengths much longer than the pump's decay length. But more importantly, the angle θ of the JPS, marked on Fig. 4.1(b-ii), can be controlled through the group indices with the dependency of $\theta = -\tan^{-1}(n_{gp} - n_{gs}/n_{gp} - n_{gl})$ [108]. To have the multiplication of A_P and JPS to produce any of the shapes in Fig. 4.1(a), given that the A_P angle is a negative number at -45 degrees, we need as a necessary condition to have the JPS angle such that $0 < \theta < 90$. This is only a necessary but not sufficient condition. To get factorizability, $\Delta\omega_P$ and L must also be set correctly with respect to each other, as both parameters control the width of their corresponding functions. There exists an approximate relation between all the involved parameters to get a factorizable state, which is estimated assuming a Gaussian pulse in a lossless pump mode, and that is [73]:

$$\gamma L^2 (n_{gp} - n_{gs})(n_{gp} - n_{gl}) = -c^2 / \Delta\omega_P^2, \quad (4.17)$$

with $\gamma = 0.04822$. We can see for the above equation to be satisfied, a necessary condition is $(n_{gp} - n_{gs})(n_{gp} - n_{gl}) < 0$, which is equivalent to having $0 < \theta < 90$. This necessary condition for factorizability means that we require either $n_{gs} < n_{gp} < n_{gl}$ or $n_{gl} < n_{gp} < n_{gs}$. Hence in a design, we should first be able to satisfy this condition, and then we get to the choice of L and $\Delta\omega_P$, where one of them has to be chosen first so that the other one can be found from Eq. (4.17). Either choice of L or $\Delta\omega_P$ has to do with the bandwidth that is desired for the generated signal and idler, and the narrower we want the spectra, the smaller $\Delta\omega_P$ or the larger L has to be. The last point to be mentioned, is that the angle θ also controls the spectral bandwidths of the factorizable signal and idler photons with respect to each other. We can see this for the two factorizable JSAs shown schematically in Figs. 4.1(b-iii) and (c-iii). In the case of Fig. 4.1(b), the JPS function has a θ close to $+45$ degrees,

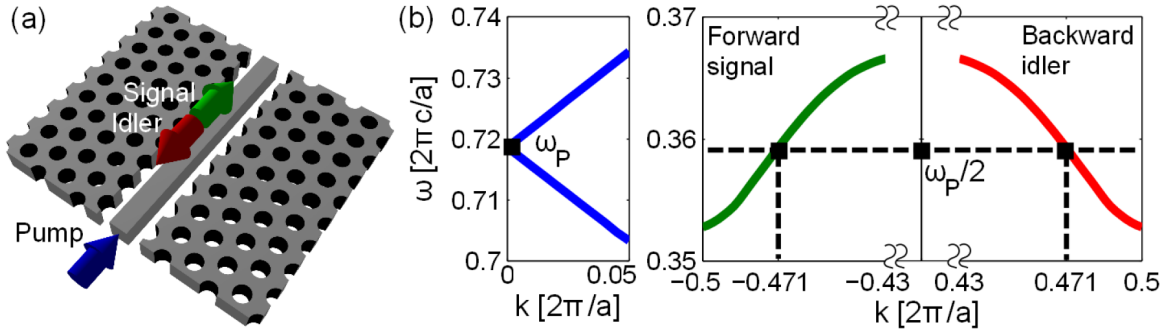


Figure 4.2: (a) Schematics of CP SPDC in a double-slot PCSW; (b) Bands of the pump (left) and signal/idler (right) modes. The dashed horizontal line marks the frequency of CP phase-matching. The design parameters are $R/a = 0.3$, $h/a = 1.15$, $W/a = 0.85$, $T/a = 0.45$, and $D/a = 0.59$.

and hence the factorizable JSA will look close to a circle, which means that the resulting signal and idler photons have comparable spectral widths. In the case of Fig. 4.1(c), the JPS function has a θ close to zero, and hence the factorizable JSA will look like a horizontal ellipse, which means that the resulting idler photon has a much narrower spectral width compared to the signal photon.

The above discussion makes clear the importance of group index control in producing factorizable pairs. PCSWs offer this control through dispersion engineering and different phase-matching configurations, as was shown in chapter 2, which allows for not only controlling the amplitude but also the sign of the group indices of the phase-matched signal and idler modes. To demonstrate this capability of PCSWs, a double-slot structure from chapter 2 is used, that is phase-matched for a degenerate CP SPDC process, as shown schematically in Fig. 4.2(a). The band diagram of the pump, signal, and idler modes for this structure were shown in Fig. 2.14(b), and here we show these bands again in Fig. 4.2(b) for convenience. These bands show that the pump mode at $k_P(\omega_P) = 0$ is phase-matched to a pair of FP and BP modes at the $\omega_P/2$ frequency. In such a phase-matching configuration, we have a pump mode and a signal mode with positive group indices and an idler mode with a negative group index. This means that by satisfying a CP phase-matching condition we are already halfway through in satisfying the necessary factorizability condition of $n_{g_I} < n_{g_P} < n_{g_S}$, which in this case turns into $-|n_{g_I}| < n_{g_P} < n_{g_S}$. Hence, we just need to have a signal mode with a group index larger than the pump mode. The group index engineering here is less cumbersome than a FP phase-matching configuration, where all group indices are positive and we have to choose two different signal and idler modes and tune the design such that the pump group index falls inbetween that of the signal and idler [125, 126]. As a matter of fact, if the group indices of the pump and the signal modes in the CP configuration are close to each other, such that $|n_{g_P} - n_{g_S}| \ll n_{g_P} + |n_{g_I}|$, we do not even need to exactly satisfy $n_{g_P} < n_{g_S}$. This is because the angle θ of the JPS function will be close to zero in such a CP case, as we have $\theta = -\tan^{-1}(n_{g_P} - n_{g_S}/n_{g_P} - n_{g_I}) = -\tan^{-1}(n_{g_P} - n_{g_S}/n_{g_P} + |n_{g_I}|) \approx 0$. It could be understood by looking at Fig. 4.1(c), that no matter the sign of θ , as long as it is close to zero, we will be able to approximately get a horizontally-shaped JSA ellipse, giving us a near-factorizable pair. This is exactly why the CP configuration was proposed initially as a way of overcoming the limits of low-contrast WGs in n_g -engineering for the generation of factorizable pairs [108]. However, as mentioned before, satisfying the CP phase-matching condition in non-periodic WGs is not easy, requiring either a technologically challenging submicron poling period [108] or a non-integrated free-space pump [110, 111, 112, 113, 114, 116]. With the PCSW structures presented in this thesis, we are able to reach the CP configuration without poling and in a fully integrated way. Not only we can

satisfy the CP phase-matching condition with a PCSW, but we can also control the group index of the signal mode at the point of phase-matching, as was shown in Fig. 2.14(d). This means that we can choose any of the designs that has $n_{\text{gp}} < n_{\text{gs}}$. The design chosen for the demonstration in this section, with its bands shown in Fig. 4.2(b), has the group indices $n_{\text{gs}} = -n_{\text{gi}} = 3.5$ and $n_{\text{gp}} = 3.2$ at the point of degenerate CP phase-matching, which satisfies $n_{\text{gi}} < n_{\text{gp}} < n_{\text{gs}}$ and results in a $\theta \approx 3$ degrees for the JPS function at the degenerate phase-matching point.

Let us now look at the JSA of this CP process quantitatively. In the CP configuration shown in Fig. 4.2(b), we want to use the pump at the normalized frequency of $\frac{\omega_{\text{p}_0} a}{2\pi c} = 0.7187 = a/\lambda_{\text{p}_0}$. To have the central wavelength of the pump at $\lambda_{\text{p}_0} = 775$ nm, and hence the signal and idler photons at 1550 nm, the periodicity must be set to $a = 557$ nm. We then choose an arbitrary structure length of $L = 300a \approx 167$ μm , which then from Eq. (4.17) gives a pump spectral bandwidth of $\Delta\omega_{\text{p}} = 1.58 \times 10^{-3} \frac{2\pi c}{a}$ for reaching factorizability. This corresponds to an intensity FWHM of about 2 nm. It should be noted, that Eq. (4.17) is only a good approximation for the case of a lossless pump mode. Here, we have a lossy pump mode and Eq. (4.17) is only a good approximation when the structure length $L = 300a$ is smaller than the decay length of the pump mode, which is about 10^3 periods in this case. The trend of JPS getting narrower slows down for cases where the structure length is longer than the decay length of the pump, and hence in that limit, Eq. (4.17) is no longer a good approximation, and one has to numerically look for the best value of $\Delta\omega_{\text{p}}$ that results in the highest degree of factorizability. The pump pulse has a Gaussian spectrum $A_{\text{p}}(\omega_{\text{S}} + \omega_{\text{I}}) = \exp\left[-\left(\frac{\omega_{\text{S}} + \omega_{\text{I}} - \omega_{\text{p}_0}}{\Delta\omega_{\text{p}}}\right)^2\right]$, and is shown in Fig. 4.3(a), plotted as a function of ω_{S} and ω_{I} . The absolute value of the JPS function of this process, found from Eq. (4.15), is shown in Fig. 4.3(b), where the solid white line marks the maximum of the pump spectrum from Fig. 4.3(a). We see that at the place the JPS and A_{p} cross, the JPS function has a close to zero θ , which is in fact the $\theta \approx 3$ degrees that was predicted from the group indices.

Multiplying the JPS and A_{p} from Figs. 4.3(a) and (b) results in the JSA function, shown in Fig. 4.3(c-i). It should be reminded again, that the displayed JSA does not include the overlap integral Ov , which has much weaker spectral variations compared to A_{p} and JPS. The resulting JSA has a desirable horizontal ellipse shape, and hence offers a high degree of factorizability. To quantify the degree of factorizability, a Schmidt decomposition is performed on this JSA, which gives the probability of each Schmidt pair, shown in Fig. 4.3(c-ii), where the indexing starts with the strongest Schmidt pair. This strongest pair has $\Lambda_0 = 0.96$, and the second strongest pair has a much lower weight of $\Lambda_1 = 0.02$. There is also a way of quantifying the degree of factorizability with one quantity, through the Schmidt number $K = 1/\sum_n \Lambda_n^2$. $1/K$ is associated to the purity of the heralded single-photon state [50]. The ideal case of a completely unentangled pair has $K = 1$. In this case we have $K = 1.09$, which is a comparably close-to-one number to other types of designs [125, 97, 98, 106, 126]. Finally, let us take a look at the spectra of the signal and idler photons corresponding to the strongest pair of Schmidt modes, shown in Fig. 4.3(c-iii). Here we can see, that the spectral bandwidth of the BP idler photon, with a intensity FWHM of $\Delta\lambda_{\text{I}} \approx 2$ nm, is smaller than the bandwidth of the FP signal with $\Delta\lambda_{\text{S}} \approx 8$ nm. This is due to the fact that the group index difference $n_{\text{gs}} - n_{\text{gp}}$ is much smaller than $n_{\text{gp}} - n_{\text{gi}}$, which also manifests itself in a close-to-zero θ .

As was explained with the schematics shown in Figs. 4.1(b) and (c), the ratio between the spectral bandwidths of the factorizable signal and idler photons can be controlled with the angle θ of the JPS.

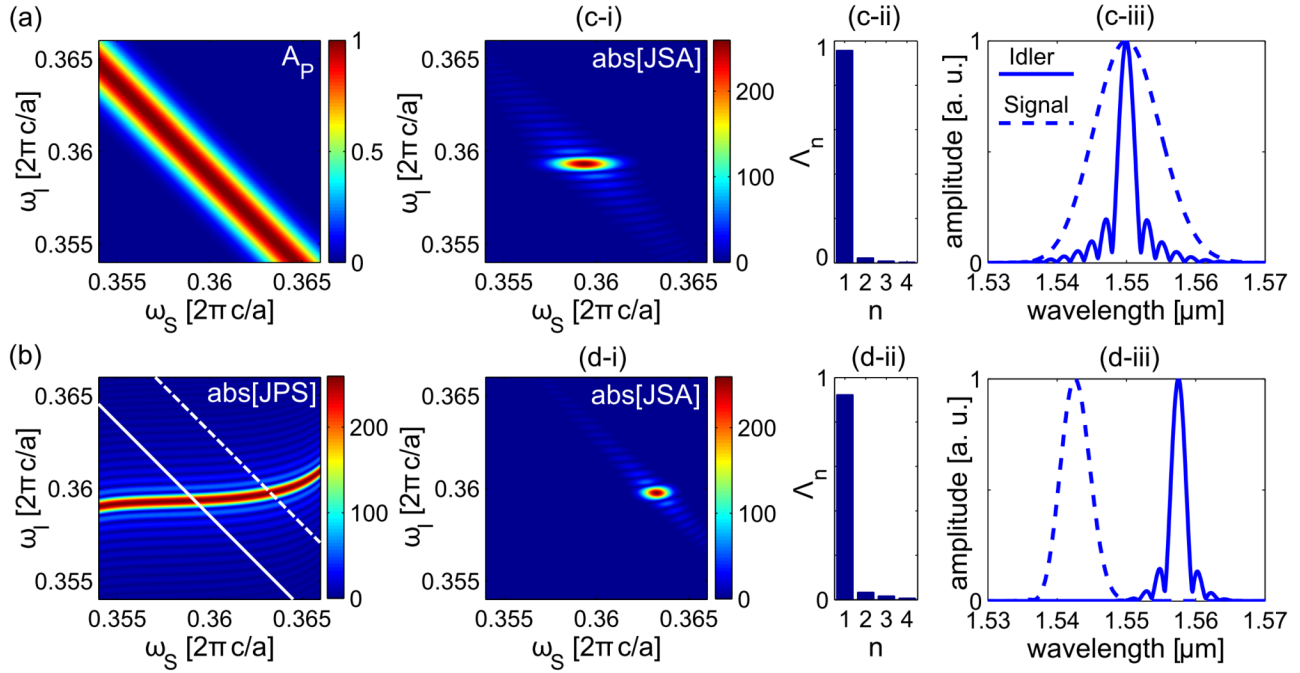


Figure 4.3: Achieving factorizability using the CP phase-matching configuration in a double-slot PCSW, the band diagram of which is shown in Fig. 4.2(b). (a) Pump spectrum $A_p(\omega_s + \omega_i)$; (b) The absolute value of the JPS function. The solid white line corresponds to the maximum of the pump spectrum shown in plot (a). The dashed white line corresponds to the maximum of another pump pulse of different central frequency and bandwidth; (c) and (d) correspond to two different JSA functions, resulting from multiplying the JPS function by these two pump pulses, represented by the solid and dashed white lines, respectively. (c) gives a factorizable pair with degenerate central wavelengths and (d) gives a factorizable pair with non-degenerate central wavelengths. Each of the cases in (c) and (d) include three plots: (i) The absolute value of the JSA function, excluding the overlap integral; (ii) The probabilities of Schmidt mode pairs Λ_n , corresponding to the JSA in graph (i); (iii) The spectra of the Schmidt modes for the signal and idler photons corresponding to the dominant Schmidt pair of graph (ii), shown as a function of wavelength.

If we have control over the group indices of the signal and idler modes, we can achieve different values of θ , and hence control the spectral bandwidths of our factorizable pair. As mentioned before, with the PCSWs we can also control the group index at the point of phase-matching by changing the design parameters, as was shown in Fig. 2.14(d). Here we demonstrate this control using the same structure that was just used, but instead with a different pump pulse that gives us a frequency-non-degenerate factorizable pair. This pump pulse has a central frequency of $\omega_p = 0.723 \frac{2\pi c}{a}$ and bandwidth of $\Delta\omega_p = 7.76 \times 10^{-4} \frac{2\pi c}{a}$. By setting the periodicity to $a = 560$ nm, we get a pump at $\lambda_{p0} = 775$ nm and an intensity FWHM of about 1 nm. The maximum of this pump pulse's spectrum is shown in Fig. 4.3(b) as a dashed white line, which is crossing the JPS function at a point where it has an angle of $\theta \approx 12$ degrees. At this point, the signal frequency is larger, and due to the fact that the band diagram of a Bloch mode near the bandedge is highly dispersive, a small shift in the frequency results in a substantially larger group index of $n_{gs} = 4.6$, compared to what it was with the frequency-degenerate case with $n_{gs} = 3.5$. In this case the idler frequency does not change much, which results in the idler group index to change only slightly to $n_{gi} = 3.6$. This brings the group index differences $n_{gs} - n_{gp}$ and $n_{gp} - n_{gi}$ closer to each other, resulting in a larger θ . The fact that the bands of the signal and idler modes in such a design in a PCSW are highly dispersive, is the reason that the JPS in Fig. 4.3(b) shows a strong change in its angle over such a small wavelength range of about 50 nm. The resulting JSA is shown in Fig. 4.3(d-i), which is still a horizontal ellipse, but now closer

to a circle compared to Fig. 4.3(c-i). This JSA also exhibits a high degree of factorizability, as can be seen from its Schmidt decomposition shown in Fig. 4.3(d-ii), with $\Lambda_0 = 0.92$, and $\Lambda_1 = 0.03$. The Schmidt number in this case is $K = 1.17$. The spectrum of the frequency-non-degenerate signal and idler photons, corresponding to the dominant Schmidt pair, are shown in Fig. 4.3(d-iii). Here we see that the larger θ has resulted in a closer spectral bandwidth for the pair, which are now $\Delta\lambda_I \approx 2$ nm for the idler and $\Delta\lambda_S \approx 4$ nm for the signal photon.

The discussions in this section establish the capability of PCSWs in controlling the spectral entanglement, resulting in reaching and tuning the generation of factorizable photon-pairs, which can be generated in a CP configuration. Such a PCSW source is ideal as a heralded single-photon source. Aside from producing spectrally unentangled pairs, that are essential for efficient heralding [83], this source allows the separation of photon-pairs into different channels directly at the source, without the need for any extra components. Another advantage of a CP configuration is, that it results in a much narrower spectrum [110, 111, 248] compared to the more common FP one, due to the large difference between the positive and negative group indices of the modes involved. This means that narrow spectra can be reached using shorter structures, resulting in more miniaturized sources. The spectrum of the idler photon in Fig. 4.3(c-iii), shows a FWHM of about 2 nm, which is achieved in a PCSW of length $L = 167$ μm . Proposals for reaching factorizability with ridge WGs in a FP configuration can achieve such a narrow bandwidth with a several millimetres long structure [126]. Hence, the CP configuration is reducing the length requirement to get narrow spectra by at least an order of magnitude. Involving slow-light modes can make the spectrum even narrower, as the difference between the group indices will be increased more, as was shown in chapter 3 with SHG in a W1 PCSW.

4.3 Controlling modal and path entanglement: path-entangled Bell state example

Eq. (4.13), found in this chapter, expresses the general biphoton state in a periodic WG as $|\psi\rangle = \sum_{n,m} \iint d\omega_S d\omega_I \text{JSA}_{n,m}(\omega_S, \omega_I) |S, n, \omega_S\rangle |I, m, \omega_I\rangle$, which is a sum over all possible combinations of phase-matched bandlets, indexed by n and m in bands S and I, respectively. As discussed, this means that if there exists more than one pair of bandlets that are phase-matched, we will have entanglement in the bandlet DOF. Since bandlets are essentially different modes that can be FP or BP, this is equivalent to entanglement in the path or/and modal degree/s of freedom. As was demonstrated in chapter 2, PCSWs are capable of satisfying multiple phase-matching conditions simultaneously, between processes that involve different modes of different propagation directions. This means, that with a PCSW source of photon-pairs, we can produce pairs entangled in the path or modal DOF, directly at the source, and do it without the need for any pre- or post-processing steps. This makes the source much more compact and suitable for integration. In this section, this capability of PCSWs will be explained generally, using some of the simultaneous phase-matching configurations that were proposed in chapter 2. It is important to note, that it is not just creating entanglement that is of interest in a photon-pair source, but also controlling the extent of it, specially for reaching a maximally entangled state, also known as a Bell state. Hence, after the general explanation, a specific design for creating a path-entangled Bell state in a double-slot LN PCSW will be presented, to show how in

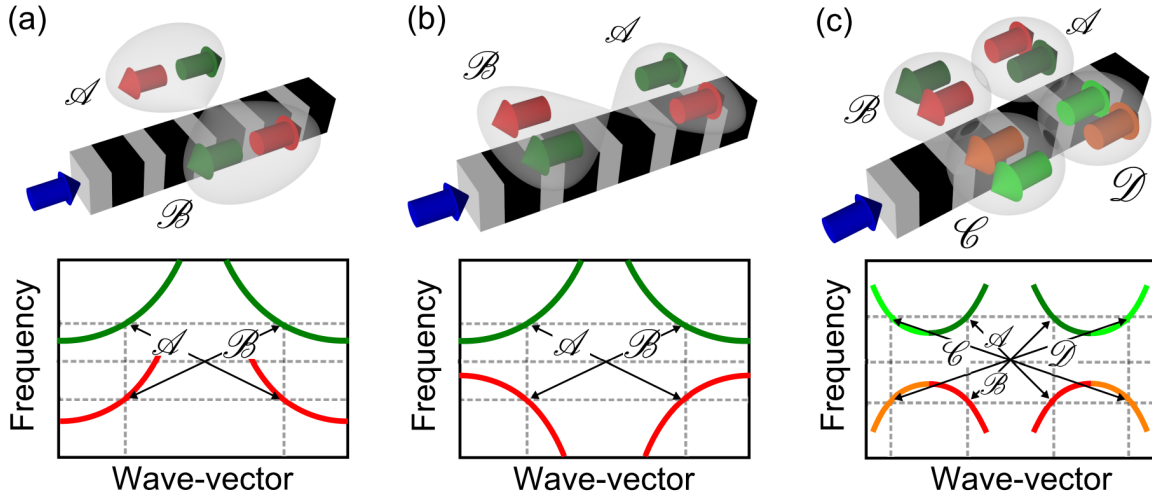


Figure 4.4: Schematics of path- and/or modally-entangled photon-pairs from a periodic WG source, based on different simultaneous phase-matching configurations. (a) A path-entangled pair, where by detecting the signal on one side of the source we know of the existence of the idler on the opposite side. The corresponding band diagram shows the simultaneous phase-matching of two CP processes. (b) A path-entangled pair, where by detecting the signal on one side of the source we know of the existence of the idler on the same side. The corresponding band diagram shows the simultaneous phase-matching of a FP and a BP process. (c) A path- and modally-entangled pair, where the signal photon can be on either side of the source and in either of the two modes/bandlets. By detecting the signal in any of the four possible combinations of path and mode we know of the path and mode of the idler. The corresponding band diagram shows the simultaneous phase-matching of four processes.

practice the extent of entanglement can be controlled in such structures.

In Fig.4.4, three different cases of creating path and modal entanglement are shown schematically, corresponding to three configurations for reaching simultaneous phase-matching that were presented in chapter 2. Fig.4.4(a) shows a path-entangled state, produced by simultaneous phase-matching of two CP processes. In process \mathcal{A} , the signal photon is FP and the idler photon is BP, and in process \mathcal{B} vice versa. Hence, Eq. (4.13) predicts a biphoton state in such a structure of the form:

$$|\psi\rangle = \iint d\omega_S d\omega_I \{ \mathcal{A}(\omega_S, \omega_I) |S, FP, \omega_S\rangle |I, BP, \omega_I\rangle + \mathcal{B}(\omega_S, \omega_I) |S, BP, \omega_S\rangle |I, FP, \omega_I\rangle \}, \quad (4.18)$$

where $\mathcal{A}(\omega_S, \omega_I)$ and $\mathcal{B}(\omega_S, \omega_I)$ are the corresponding JSAs for each process. In this state, detecting a signal photon on one side of the source tells us of the existence of the idler photon on the opposite side. It should be pointed out, that the labels signal and idler here correspond to photons from the upper and lower bands in frequency, respectively. This means that for detecting entanglement, we can separate the signal and idler into two channels using a dichroic beamsplitter. The second case in Fig.4.4(b), shows a different path-entangled state, produced by simultaneous phase-matching of a FP and a BP process. In process \mathcal{A} , both of the signal and idler photons are FP and in process \mathcal{B} both are BP. The generated biphoton state is:

$$|\psi\rangle = \iint d\omega_S d\omega_I \{ \mathcal{A}(\omega_S, \omega_I) |S, FP, \omega_S\rangle |I, FP, \omega_I\rangle + \mathcal{B}(\omega_S, \omega_I) |S, BP, \omega_S\rangle |I, BP, \omega_I\rangle \}. \quad (4.19)$$

In this state, detecting a signal photon on one side of the source tells us of the existence of the idler photon on the same side. The third case in Fig.4.4(c), shows a state entangled in both the path and modal degrees of freedom, produced by simultaneous phase-matching of four process. Processes \mathcal{A}

and \mathcal{D} are between FP modes and processes \mathcal{B} and \mathcal{C} are between BP modes. Here, each of the signal and idler bands are constituted of two bandlets. The bandlets further from the bandedge (dark green for the signal and red for the idler) are indexed 1, and the bandlets closer to the bandedge (light green for the signal and orange for the idler) are indexed 2. Hence, processes \mathcal{A} and \mathcal{B} are between bandlets of index 1, and \mathcal{C} and \mathcal{D} are between bandlets of index 2. The generated state is:

$$|\psi\rangle = \iint d\omega_S d\omega_I \{ \mathcal{A}(\omega_S, \omega_I) |S, 1, FP, \omega_S\rangle |I, 1, FP, \omega_I\rangle + \mathcal{B}(\omega_S, \omega_I) |S, 1, BP, \omega_S\rangle |I, 1, BP, \omega_I\rangle \\ + \mathcal{C}(\omega_S, \omega_I) |S, 2, BP, \omega_S\rangle |I, 2, BP, \omega_I\rangle + \mathcal{D}(\omega_S, \omega_I) |S, 2, FP, \omega_S\rangle |I, 2, FP, \omega_I\rangle \}. \quad (4.20)$$

In this state, the signal photon can be on either side of the source and in either of the two modes/bandlets. By detecting the signal photon in any of the four possible combinations of path and mode we know of the path and mode of the idler photon.

The above discussion shows how simultaneous phase-matching of multiple processes can result in the creation of path- and/or modally-entangled photon-pairs. However, it does not tell us about the extent of the entanglement in those degrees of freedom and how it could be controlled in practice. As a quantitative example, a double-slot PCSW design is used in the following to calculate the extent of entanglement and show that the PCSW can be designed to result in a maximally entangled photon-pair state. The design of this double-slot structure is shown in Fig. 2.12. This structure supports the simultaneous phase-matching of two CP processes, the bands of which were shown previously in Fig. 2.15(a), and are repeated here in Fig. 4.5(a) for convenience. The satisfied phase-matching condition in process \mathcal{A} is $\Delta k_{\mathcal{A}} = k_P - k_{S,FP} - k_{I,BP} = 0$, and in process \mathcal{B} is $\Delta k_{\mathcal{B}} = k_P - k_{S,BP} - k_{I,FP} = 0$. A similar configuration has been realized in a ridge WG structure [114], using two free-space pump beams from above the sample. The advantage of the PCSW, is that there is only one and a fully integrated pump illumination. Using this structure for pair generation will produce the path-entangled state of the type shown in Fig.4.4(a) and described by Eq. (4.18). The schematic for this entangled state is repeated in Fig. 4.5(b) for convenience. The state described in Eq. (4.18) is entangled in the three degrees of freedom mode, frequency, and path, although in this case the mode DOF is a binary subspace of the frequency DOF. To generate a maximally entangled state in the path DOF, there must be modal and spectral indistinguishability between processes \mathcal{A} and \mathcal{B} . Moreover, the nonlinear efficiencies for the two processes must be equal. Modal indistinguishability is assured, as the FP and BP counterparts of a mode in a reciprocal material are identical. For equal nonlinear efficiencies of processes \mathcal{A} and \mathcal{B} , we must have $\alpha_{\mathcal{A}} = \alpha_{\mathcal{B}}$, with $\alpha_{\mathcal{A}} \equiv \int d\omega_S \int d\omega_I |\mathcal{A}(\omega_S, \omega_I)|^2$ and $\alpha_{\mathcal{B}} \equiv \int d\omega_S \int d\omega_I |\mathcal{B}(\omega_S, \omega_I)|^2$, which strongly depends on the overlap integral of Eq. (4.16). For having spectral indistinguishability, we must have $\alpha_{\mathcal{B}} = |\alpha_{\mathcal{A}\mathcal{B}}|$, with $\alpha_{\mathcal{A}\mathcal{B}} \equiv \int d\omega_S \int d\omega_I \mathcal{A}(\omega_S, \omega_I) \mathcal{B}^*(\omega_S, \omega_I)$, which ensures that the two JSAs have a perfect spectral overlap. In the following, these quantities are investigated numerically.

The periodicity of $a = 575$ nm is chosen to set the pump wavelength to $0.775 \mu\text{m}$. The pump mode has a decay length of about 450 periods or $260 \mu\text{m}$ at $k_P = 0$. The structure length is chosen to be $L = 1000a = 575 \mu\text{m}$. Although both the efficiency and the spectral bandwidth of the process tend to saturate for structure lengths larger than the decay length of the pump mode, the phase-matching spectrum approaches a Lorentzian function in this limit, in contrast to the sinc-function of a lossless

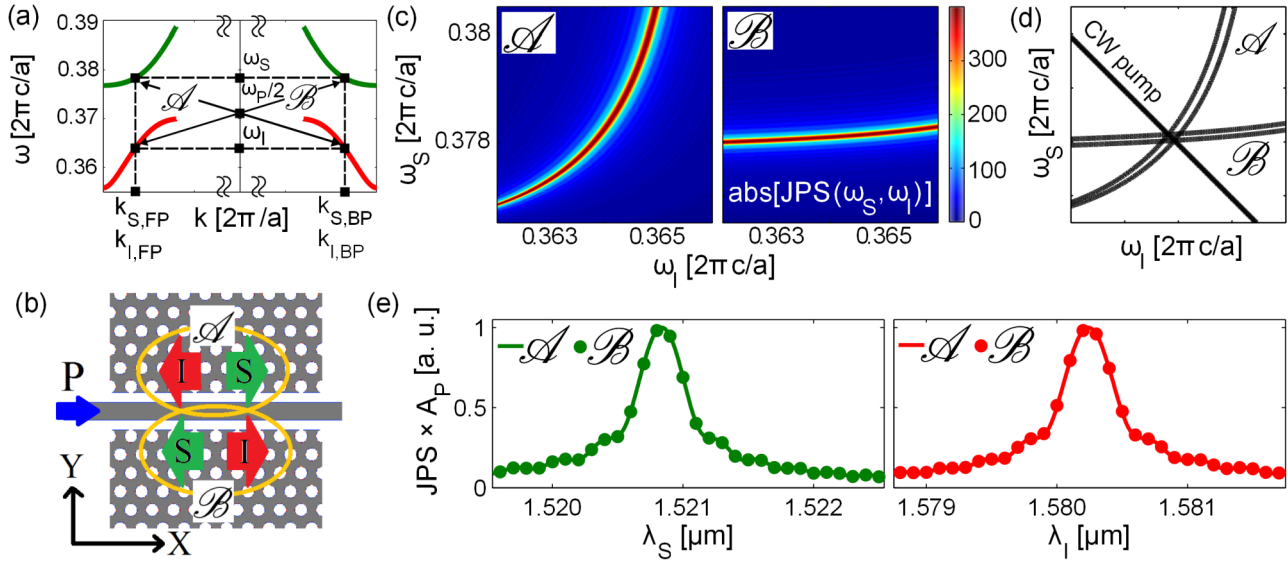


Figure 4.5: (a) Bands of the signal (green) and idler (red) modes, reaching simultaneous phase-matching of two non-degenerate CP processes, marked as \mathcal{A} and \mathcal{B} , in a double-slot PCSW. ω_P is the frequency of the pump mode at which $k_P = 0$. The design parameters are $R/a = 0.3$, $h/a = 1.07$, $W/a = 0.85$, $T/a = 0.45$, and $D/a = 0.59$; (b) Schematics of a path-entangled Bell state in a double-slot PCSW. (c) Joint phase-matching spectrum (JPS) of processes \mathcal{A} and \mathcal{B} ; (d) Overlap of JPSs with the CW pump line; (e) Projected spectra of the signal and idler photons from both processes.

case, which is advantageous in increasing the similarity between the produced JSAs of both processes. The JPSs of processes \mathcal{A} and \mathcal{B} are calculated from Eq. (4.15) and shown in Fig. 4.5(c). To achieve similar JSAs a CW pump at $\omega_P = 0.742 \frac{2\pi c}{a}$ ($k_P = 0$) is used, corresponding to the vacuum wavelength of 775 nm. The pump spectrum $A_P(\omega_S + \omega_I = 0.742 \frac{2\pi c}{a})$ for this CW pump is shown in Fig. 4.5(d), which is a line overlapped with the two JPSs. The fact that this line passes the JPSs exactly at their crossing point is a direct consequence of the simultaneous phase-matching design. This results in an almost perfect spectral overlap of $\mathcal{A}(\omega_S, \omega_I)$ and $\mathcal{B}(\omega_S, \omega_I)$. This overlap can be more clearly seen in Fig. 4.5(e), by plotting $\mathcal{A}(\omega_S, \omega_I)$ and $\mathcal{B}(\omega_S, \omega_I)$ projected onto each of the ω_S and ω_I axis, here presented as a function of wavelength.

For processes \mathcal{A} and \mathcal{B} to have equal nonlinear efficiencies, they should have the same overlap integral, calculated from Eq. (4.16). As was previously mentioned, since the BHs involved in the two processes are different, shown in Figs. 2.15(b) and (d), the two processes do not necessarily have the same overlap integral. However, the point of phase-matching can be carefully tuned to get there: The distributions of BHs of the signal and idler modes strongly depend on their wave-vectors. As was shown in chapter 2, by changing the thickness of the slab h , we can control the wave-vectors $k_{I,BP} = k_{S,BP}$ (see Fig. 4.5(a)) at which phase-matching is achieved, and hence control the overlap integral of the two processes. The advantage of changing h in this design is that the shape of the bands mostly depend on in-slab parameters and are not affected. Changing h will only shift these bands up and down in frequency, with stronger shifts for the pump mode, which is a higher-order mode in the z -direction. The change in the phase-matching wave-vector as a function of h was shown previously in Fig. 2.15(c), and is repeated here in Fig. 4.6(a) for convenience. For each case, the overlap integrals of processes \mathcal{A} and \mathcal{B} can be calculated, and compared to each other. The ratio of both overlap integrals $\text{Ov}_{\mathcal{A}}/\text{Ov}_{\mathcal{B}}$ as a function of the slab thickness of the design is shown in Fig. 4.6(b). It can be seen, that equal efficiencies are reached for $h = 1.07 a \approx 615$ nm.

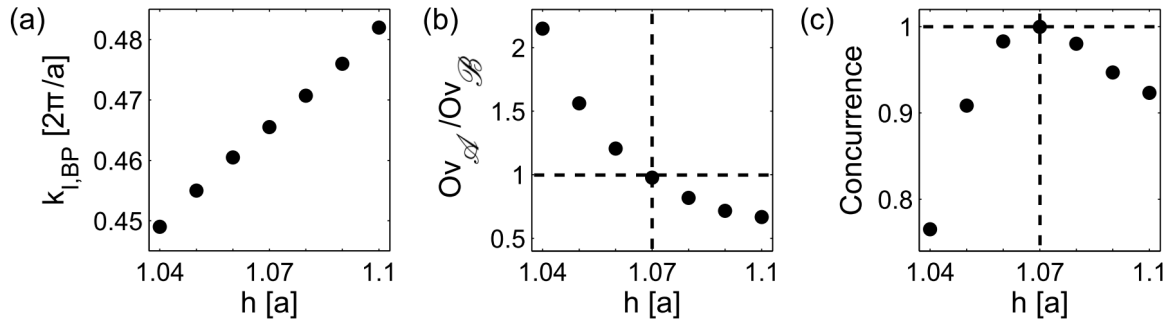


Figure 4.6: Changes in design properties as a function of slab thickness h : (a) Wave-vector $k_{I,BP}$ (see Fig. 4.5(a)) at the central point of phase-matching; (b) Ratio between the overlap integrals of processes \mathcal{A} and \mathcal{B} ; (c) Concurrence of the path-entangled state.

The above analysis shows that the presented double-slot design satisfies the required conditions for reaching maximal entanglement in the path DOF. We can also quantify the extent of this entanglement, by calculating the concurrence parameter $\mathcal{C} \equiv 2|\alpha_{\mathcal{A}\mathcal{B}}|/(\alpha_{\mathcal{A}} + \alpha_{\mathcal{B}})$ [114]. A Bell state, or a maximally entangled state should have $\mathcal{C} = 1$. Here, the concurrence is calculated as a function of h and is shown in Fig. 4.6(c), to show the effect of having equal nonlinear efficiencies in the design. As expected, the concurrence of 1 is reached for $h = 1.07a$, indicating the generation of a path-entangled Bell state. It is also clear from the variation of concurrence in Fig. 4.6(c), that this design is capable of producing nonmaximally entangled states [249] and control the extent of the entanglement by varying h , without compromising the state's purity. This concludes the analysis in this section.

4.4 Summary of the results and related publications

In this chapter, I have shown that PCSWs used as SPDC sources of photon-pairs are capable of creating and controlling entanglement in the spectral, path, and modal degrees of freedom, with specific designs presented in LN double-slot PCSWs. All this was reached in a single PCSW with a single integrated pump mode, without the need for periodic poling, non-integrated pump illumination, or any other extra components for post-processing. This reaches the objective of this thesis, in showing the potential of PCSWs as highly versatile and suitable for integration sources of quantum light that offer a strong control over the properties of the generated photon-pairs, and do it without the need for extra pre- or post-processing steps. The results for the design and analysis of the maximally path-entangled source of photon-pairs using the double-slot PCSW has been published in Physical Review Letters [S5]. This publication is the most important result of this work, in that my efforts in the design and analysis of SPDC sources of photon-pairs in PCSWs converge in this work, where I also show the unique strength of PCSWs for SPDC applications, as was the aim of this thesis.

Chapter 5

Atom-mediated SPDC

In the previous chapter, I have presented the theory for describing SPDC with guided and lossless signal and idler modes in a periodic WG. Given that in a PCSW design the signal and idler modes are usually chosen such that they are ideally guided and lossless, that theory suffices for the description of the SPDC designs. However, that will not always be the case, as there could be a non-negligible amount of scattering loss present after the fabrication, or the modes could end up having inherent losses due to material absorption or some unavoidable leakage mechanism. For a quantum process, the existence of loss is more detrimental than for a classical one. In the classical case it is only the efficiency that is affected by loss, but in the quantum process there is also the correlation between the pairs that is affected. For example, when a signal photon is detected, we cannot be sure that the idler photon will reach its destination, as it could have been lost along the way, creating an extra source of uncertainty. To take this into account, perturbative approaches have been used for treating SPDC in structures that suffer from scattering losses or material absorption [250, 251, 193, 252], in which, lossless modes are assumed initially, and their loss is then treated as a weak coupling to a reservoir.

In this work however, a more general method is desired, that can take into account any type or amount of loss, to correspond to the needs of any complex nanostructured system, such as PCSWs. A general method should be able to take care of any type of non-power-orthogonal mode in the calculation, the same way that the classical calculation using unconjugated reciprocity theorem could incorporate any QNBM, without needing special treatment for the quantization of different types of modes. The main obstacle in developing such a formalism is the definition of photons [253, 230]. Photons are quanta of energy associated to modes of a lossless system. It is often convenient to expand the state of the quantized electromagnetic field into photons, as the orthogonality relation between the mode profiles results in a simplified Hamiltonian for the field in terms of the creation and annihilation operators of photons. Moreover, when the field is expressed in terms of such a physically intuitive object, it is easier to interpret the state. However, when we have a lossy WG system, modes are non-power-orthogonal, and this means that even in the classical formulation the total power in the WG cannot be expanded into a sum of the powers from every individual mode. In a quantum picture, this results in a Hamiltonian of the system that has cross-terms between creation and annihilation operators of different modes [253, 230], which means that if we assign a certain number of photons to every mode, to describe how much power each mode is carrying, then the total power in the system will no longer correspond to the sum of photons from all the modes. This completely jeopardizes the

usefulness of the definition in terms of the feasibility of the calculation and interpretation. It should be mentioned, that for weakly absorbing material, effective photons can be defined that are associated to the modes of the system [254]. However, such an approach is applicable only to systems with low levels of loss. The problem of photon definition is not only specific to lossy systems, but can also exist in lossless systems, if we try to treat a specific class of non-power-orthogonal modes: the evanescent modes. Here the problem is even more fundamental, as purely evanescent modes do not carry power, hence assigning photons to them as a quanta of power is not possible.

Luckily, a suitable solution is available in the Green's function (GF) quantization method [255, 256, 257, 258, 259]. This method is not based on photons associated to modes, but describes the field in terms of the classical GF of the system and local bosonic excitations in the medium-assisted field, which is the system of material coupled to the field. The classical GF can be either found numerically or expressed in terms of the QNBMs of the system. Hence, changes in the type of the system or its loss mechanism is only affecting the GF and will not affect the quantization scheme. The trade-off is that the local bosonic excitation is a rather unintuitive object and the quantum state described with it is not easy to interpret. The solution is to make a measurement of the state, e.g. calculate the expectation value of some observable or calculate the probability of an event. The result will no longer include the local bosonic operator and will only depend on the GF of the system. Such a GF-based calculation for SPDC has been done recently [194], where 2-level atoms have been introduced as detectors. The atoms are exposed to the generated state of light from the SPDC process, and the properties of the generated pair are measured by looking at the excitation probabilities of the atoms.

Studying this method however, reveals an interesting physical effect. The pair-generation response of a system with and without the involvement of the atomic detectors exhibits very different GF-functionalities. This tells us that by controlling the GF of the system, a photon-pair source can show a very different response in the presence of an atomic detector, which is essentially a resonant 2-level system. PCSWs are the ideal platform for the investigation of such an effect, as they allow for a strong control of the modes of the system and equivalently of its GF. In particular, I have discovered that this contrast of pair-generation behavior with and without a 2-level system manifests itself in its most extreme way in the presence of evanescent modes in the bandgap of the periodic WG. Relying on these bandgap modes, a new effect emerges, in which photon-pair generation can only take place in the presence of a single 2-level emitter. More specifically, using a guided signal mode and an evanescent idler mode, I have found that the pair-generation process is completely prohibited due to the zero DOS of the evanescent mode, but it could be mediated by embedding an atom-like emitter with the idler's transition frequency in the structure. In this system, the spontaneous generation of the signal photon becomes conditional on the absorption of the idler by the atom. This creates a heralded excitation mechanism, where the detection of a signal photon outside the structure heralds the excitation of the embedded emitter. I call this process atom-mediated SPDC, and the calculations that resulted in identifying this process will be the main topic of this chapter.

In the following, first the GF quantization method is introduced and then used to find the pair-generation probability without atoms as detectors. Afterwards, the calculation method in Ref. [194] with atoms as detectors is reviewed. Going through the main parts of the calculations with and without atoms is important for understanding the effect of the atom's mediation in the SPDC process. The

intermediate steps of the calculations, which are rather lengthy and are not needed for understanding the main physics, are left to appendix B. Before introducing the atom-mediated SPDC, the result for coincidence detection with two atomic detectors are used to gain some understanding about SPDC with decaying modes, where the result is interpreted and compared to the biphoton state formula that was found in chapter 4 for lossless signal and idler modes. Finally, the concept of atom-mediated SPDC using evanescent modes is introduced, where the atoms, which were previously introduced just as detectors, are now an essential part of the process themselves.

5.1 Green's function method for SPDC

In this section, the GF quantization method [255, 256, 257, 258, 259] will be introduced and used to calculate the probability of generating a pair of bosonic excitations through SPDC, without the presence of atomic detectors. In this calculation, the expression for the nonlinear Hamiltonian stays the same as introduced previously in Eq. (4.2), so does the final state of the system expressed in Eqs. (4.7) and (4.8), calculated with the first-order perturbation theory. The important difference between this calculation and the previous one is in how the electric field operator is expressed. In Eq. (4.4), the electric field operator was expanded into photons associated to the modes of the system. In the GF method, this expansion is in terms of the GF of the system and the local bosonic excitation in the medium-assisted field, with vectorial annihilation (creation) operator $\hat{\mathbf{f}}(\mathbf{r}, \omega)$ ($\hat{\mathbf{f}}^\dagger(\mathbf{r}, \omega)$), giving:

$$\hat{\mathbf{E}}(\mathbf{r}, t) = \hat{\mathbf{E}}^+(\mathbf{r}, t) + \hat{\mathbf{E}}^-(\mathbf{r}, t) = \int_0^{+\infty} d\omega \hat{\mathbf{E}}(\mathbf{r}, \omega) e^{-i\omega t} + \text{H.c.}, \quad (5.1)$$

$$\hat{\mathbf{E}}_\alpha(\mathbf{r}, \omega) = i \sqrt{\frac{\hbar}{\pi \epsilon_0}} \frac{\omega^2}{c^2} \sum_\beta \int d^3s \sqrt{\epsilon''(s, \omega)} G_{\alpha\beta}(\mathbf{r}, s, \omega) \hat{f}_\beta(s, \omega). \quad (5.2)$$

ϵ'' is the imaginary part of the relative permittivity. s is the spatial coordinate. $G_{\alpha\beta}$ is an array of the 3×3 GF tensor \bar{G} , also called dyadic GF, with $\alpha, \beta \in \{x, y, z\}$. The GF satisfies the wave equation:

$$\left[(\nabla \times \nabla \times) - \frac{\omega^2}{c^2} \epsilon \right] \bar{G}(\mathbf{r}, \mathbf{r}', \omega) = \bar{I} \delta(\mathbf{r} - \mathbf{r}'), \quad (5.3)$$

where \bar{I} is the identity tensor. This tensorial equation can also be written as three separate vectorial equations $\left[(\nabla \times \nabla \times) - \frac{\omega^2}{c^2} \epsilon \right] (G_x \mathbf{x} + G_y \mathbf{y} + G_z \mathbf{z}) = \mathbf{j} \delta(\mathbf{r} - \mathbf{r}')$, with $j = x, y, z$. In addition to the wave equation, the GF should also satisfy the proper boundary conditions of the system. The components of the bosonic operator $\hat{\mathbf{f}}(\mathbf{r}, \omega)$ satisfy the canonical commutation relations:

$$\left[\hat{f}_\alpha(\mathbf{r}, \omega), \hat{f}_\beta^\dagger(\mathbf{r}', \omega') \right] = \delta_{\alpha\beta} \delta(\mathbf{r} - \mathbf{r}') \delta(\omega - \omega'), \quad [\hat{f}_\alpha(\mathbf{r}, \omega), \hat{f}_\beta(\mathbf{r}', \omega')] = 0. \quad (5.4)$$

The linear Hamiltonian of the free electromagnetic field is $\hat{H}_{\text{Lin}} = \int d^3\mathbf{r} \int_0^\infty d\omega \hbar \omega \hat{\mathbf{f}}^\dagger(\mathbf{r}, \omega) \cdot \hat{\mathbf{f}}(\mathbf{r}, \omega)$. It should be mentioned, that the expansion in Eq. (5.2) is made for a non-magnetic material, which encompasses materials in the optical frequency, with an isotropic ϵ'' , which is not necessarily always the case. For the case of an anisotropic loss, the quantization scheme has to be written in a more generalized way [260]. Here, the calculations are done assuming an isotropic ϵ'' to keep the notation from

getting over-complicated. Moreover, the final results always end up having no explicit appearance of ε'' in them, and they are only a function of the GF of the system. Hence, even if an anisotropic ε'' is considered for the middle steps of the calculation, it is acceptable to think that the final result will end up the same, and all the details about the form of ε'' will be embedded in the GF of the system. Substituting the electric field operator of Eq. (5.2) into the nonlinear Hamiltonian or directly into Eq. (4.8) gives the final state of the system $|\psi\rangle$, calculated using the first-order perturbation theory. The nonlinear Hamiltonian looks similar to Eq. (4.2):

$$\hat{H}_{\text{NL}}(t) = -\varepsilon_0 \int d^3\mathbf{r} \sum_{\alpha,\beta,\gamma} \chi_{\alpha\beta\gamma}^{(2)}(\mathbf{r}) E_{\text{P},\gamma}(\mathbf{r},t) \hat{E}_{\alpha}^{-}(\mathbf{r},t) \hat{E}_{\beta}^{-}(\mathbf{r},t) + \text{H.c.}, \quad (5.5)$$

except that here, there is no modal dependency on the field operators, and hence the degeneracy parameter \mathcal{D} is always equal to 1. $E_{\text{P}}(\mathbf{r},t) = \int_0^{+\infty} d\omega_{\text{P}} E_{\text{P}}(\mathbf{r},\omega_{\text{P}}) e^{-i\omega_{\text{P}}t}$ is the positive-frequency part of the classical pump pulse, treated in the UPA assuming a weak interaction. Doing this however, will not result in an answer like Eq. (4.9), where the biphoton state was expanded in photon operators associated to the modes of the system. Here the answer will be in terms of the local bosonic operator $\hat{f}^{\dagger}(\mathbf{r},\omega)$, which does not allow a straightforward interpretation of the result, other than telling us that a pair of bosons have been generated in the medium-assisted field. To get more information about this state, $P = \langle \psi | \psi \rangle$ is calculated, which is the probability of a pair of bosons being generated through SPDC, per input pump pulse. Instead of using the expression $\langle \psi | \psi \rangle$ to calculate P , an equivalent way is used, that is more inline with the formulations used in the next section. P is calculated through:

$$P = \sum_{\sigma_i, \sigma_s} \int d^3\mathbf{r}_s \int_0^{\infty} d\omega_s \int d^3\mathbf{r}_i \int_0^{\infty} d\omega_i \left| \langle f | V^{(1)} | i \rangle \right|^2, \text{ with } V^{(1)} = \frac{-i}{\hbar} \int_{-\infty}^{+\infty} dt \hat{H}_{\text{NL}}(t), \quad (5.6)$$

with $\sigma_i, \sigma_s \in \{x, y, z\}$. Eq. (5.6) gives the probability of the system at the initial quantum state $|i\rangle = |0\rangle$ to end up at the final state of $|f\rangle = \hat{f}_{\sigma_s}^{\dagger}(\mathbf{r}_s, \omega_s) \hat{f}_{\sigma_i}^{\dagger}(\mathbf{r}_i, \omega_i) |0\rangle$, at times much longer than it takes for the interaction to take place. Here, $\sum_{\sigma_i, \sigma_s} \int d^3\mathbf{r}_s \int_0^{\infty} d\omega_s \int d^3\mathbf{r}_i \int_0^{\infty} d\omega_i$ takes into account all the spatial, spectral, and polarization possibilities for the generated bosonic pair. In Eq. (5.6), the final state is written just as $|f\rangle$ without all its spatial, spectral, and polarization dependencies, to keep the formula compact. The small letter indices i and s do not refer to any particular signal or idler modes or frequency ranges, and are just labels here. Calculating P from Eq. (5.6), using the GF expansion of the electric field operators from Eq. (5.2), results in:

$$P = 16 \int_0^{\infty} d\omega_s \int_0^{\infty} d\omega_i \frac{\omega_s^2}{c^2} \frac{\omega_i^2}{c^2} \sum_{\alpha,\beta,\gamma,\alpha',\beta',\gamma'} \int d^3\mathbf{r} \int d^3\mathbf{r}' \chi_{\alpha\beta\gamma}^{(2)}(\mathbf{r}) \chi_{\alpha'\beta'\gamma'}^{(2)}(\mathbf{r}') \\ \times E_{\text{P},\gamma}(\mathbf{r}, \omega_i + \omega_s) E_{\text{P},\gamma'}^*(\mathbf{r}', \omega_i + \omega_s) \text{Im} [G_{\beta'\beta}(\mathbf{r}', \mathbf{r}, \omega_s)] \text{Im} [G_{\alpha'\alpha}(\mathbf{r}, \mathbf{r}', \omega_i)]. \quad (5.7)$$

The calculation steps for getting from Eq. (5.6) to Eq. (5.7) are detailed in appendix B. The result in Eq. (5.7) achieves the objective of the calculation, in having measured a meaningful physical quantity that does not include the local bosonic operators. The calculated probability depends on the spectrum of the classical pump pulse, the $\chi^{(2)}$ profile of the structure, and the classical GF of the system. To be more specific, P is dependent on the imaginary part of the GF, which determines DOS. In this

case, $\text{Im}[G(\mathbf{r}', \mathbf{r})]$ is more accurately described as the cross DOS [199], instead of the local DOS $\text{Im}[G(\mathbf{r}, \mathbf{r})]$. P gives us the probability per input pump pulse of generating a pair of bosons, taking into account all the spectral, spatial, and polarization possibilities. This probability is close in physical interpretation to the number of photon-pairs generated from a lossless SPDC process. One could also deduce the spectral dependency of the generated pair from the integrand of the $\int_0^\infty d\omega_s \int_0^\infty d\omega_i$ integrals in Eq. (5.7), as it carries a type of joint spectral information.

5.2 Atoms as detectors

The probability calculated in the previous section, although it tells us the overall pair-generation probability, does not tell us the detection probabilities at different spatial coordinates, specially single-photon and coincidence detection probabilities that are commonly of interest. To access this information, a pair of 2-level atoms can be introduced as the simplest kind of detectors, and the excitation of these atoms can be interpreted as the clicks of the detectors. This calculation has already been done in Ref. [194] and will be reviewed in this section, with some of its details presented in Appendix B. Afterwards, the GF expression of a periodic WG based on its QNBMs is inserted into the resulting expression for the coincidence detection probability, to gain some insight about the modal dependencies of the result. Two quantities are calculated here: $P_{\text{is}}(\mathbf{r}_s, \mathbf{r}_i, \omega_s, \omega_i)$ is the probability of two atoms of transition frequencies ω_s and ω_i placed at \mathbf{r}_s and \mathbf{r}_i , referred to as the signal and idler atoms, being excited through SPDC with no excitation remaining in the field. This event could be thought of as detectors registering a coincidence. The other quantity is the single-photon detection event, that is the probability of one of the atoms being excited regardless of what happens to the other atom. From here onward, the term "photon" is used rather loosely to refer to what is essentially a local bosonic excitation. If we want to measure this probability for the signal atom, we do not care if the idler boson has been absorbed by the idler atom or remains in the field. For this, we calculate $P_s(\mathbf{r}_s, \omega_s)$, the probability of the signal atom at position \mathbf{r}_s being excited through SPDC with the idler photon remaining in the field and not being absorbed by the idler atom. Then $P_s + P_{\text{is}}$ is the single photon detection probability for the signal atom, as it sums the probabilities of both cases of signal detection with the idler atom being excited and not being excited. These calculation are already done in Ref. [194]. Here I slightly modify the calculation by using a pulsed pump instead of the original calculation with a CW pump, and instead of the rate of an atomic transition I find the probability of an atomic transition per pump pulse, which will also be required in the next section. To calculate P_{is} , the third-order perturbation theory [246] is used, as it involves three events happening: the generation of a pair of bosons, the excitation of the signal atom, and the excitation of the idler atom. This gives:

$$P_{\text{is}} = |\langle f | V^{(3)} | i \rangle|^2, \quad \text{with } V^{(3)} = \left(\frac{-i}{\hbar}\right)^3 \int_{-\infty}^{+\infty} dt_1 \int_{-\infty}^{t_1} dt_2 \int_{-\infty}^{t_2} dt_3 \hat{H}_{\text{int}}(t_1) \hat{H}_{\text{int}}(t_2) \hat{H}_{\text{int}}(t_3), \quad (5.8)$$

where the total interaction Hamiltonian of the system in the interaction picture is $\hat{H}_{\text{int}} = \hat{H}_{\text{NL}} + \hat{H}_i + \hat{H}_s$, with the vacuum initial state $|i\rangle = |0\rangle$ and the final state $|f\rangle = \hat{b}_i^\dagger \hat{b}_s^\dagger |0\rangle$ where both atoms are excited and there is no quantum of excitation remaining in the field. Here $\hat{H}_{i,s}(t) = -\hat{\mathbf{d}}_{i,s}(t) \cdot \hat{\mathbf{E}}(\mathbf{r}_{i,s}, t)$ is the interaction Hamiltonian between the atoms and the field, with $\hat{\mathbf{d}}_{i,s}(t) = \hat{b}_{i,s} \mathbf{d}_{i,s} e^{-i\omega_{i,s}t} + \hat{b}_{i,s}^\dagger \mathbf{d}_{i,s}^* e^{i\omega_{i,s}t}$

being the dipole moment operator of the atoms, \mathbf{d} the vectorial dipole moment, and \hat{b}^\dagger the atomic raising operator with $[\hat{b}_m, \hat{b}_q^\dagger] = \delta_{mq}$. The calculation steps for evaluating this quantity are detailed in appendix B, which results in:

$$P_{\text{is}} = \left| \frac{4\pi}{\hbar\epsilon_0} \frac{\omega_s^2 \omega_i^2}{c^4} \sum_{\alpha, \beta, \gamma} \sum_{\sigma_i, \sigma_s} d_{i, \sigma_i}^* d_{s, \sigma_s}^* \int d^3 \mathbf{r} \chi_{\alpha\beta\gamma}^{(2)}(\mathbf{r}) E_{\text{P}, \gamma}(\mathbf{r}, \omega_i + \omega_s) G_{\sigma_i \beta}(\mathbf{r}_i, \mathbf{r}, \omega_i) G_{\sigma_s \alpha}(\mathbf{r}_s, \mathbf{r}, \omega_s) \right|^2. \quad (5.9)$$

For calculating P_s , the second-order perturbation theory is used, as it involves two events happening: the generation of a pair of bosons and the excitation of the signal atom. This gives:

$$P_s = \sum_{\sigma_i} \int d^3 \mathbf{r}_i \int_0^\infty d\omega_i |\langle f | V^{(2)} | i \rangle|^2, \quad \text{with } V^{(2)} = \left(\frac{-\mathbf{i}}{\hbar} \right)^2 \int_{-\infty}^{+\infty} dt_1 \int_{-\infty}^{t_1} dt_2 \hat{H}_{\text{int}}(t_1) \hat{H}_{\text{int}}(t_2), \quad (5.10)$$

where the total interaction Hamiltonian of the system in the interaction picture is $\hat{H}_{\text{int}} = \hat{H}_{\text{NL}} + \hat{H}_s$, with the vacuum initial state $|i\rangle = |0\rangle$ and the final state $|f\rangle = \hat{f}_{\sigma_i}^\dagger(\mathbf{r}_i, \omega_i) \hat{b}_s^\dagger |0\rangle$ at which the signal atom is excited and there is one quantum of excitation remaining in the field at the idler frequency. All the spatial, spectral, and polarization possibilities for the generated idler boson are taken into account. The calculation steps for evaluating P_s from Eq. (5.10) is a combination of what was done for finding P_{is} and P in appendix B, which results in:

$$P_s = \frac{16\pi}{\hbar\epsilon_0} \frac{\omega_s^4}{c^4} \sum_{\sigma_s, \sigma_{s'}} d_{s, \sigma_s} d_{s, \sigma_{s'}}^* \int_0^\infty d\omega_i \frac{\omega_i^2}{c^2} \sum_{\alpha, \beta, \gamma} \sum_{\alpha', \beta', \gamma'} \int d^3 \mathbf{r} \int d^3 \mathbf{r}' \chi_{\alpha\beta\gamma}^{(2)}(\mathbf{r}) \chi_{\alpha'\beta'\gamma'}^{(2)}(\mathbf{r}') \\ \times E_{\text{P}, \gamma}(\mathbf{r}, \omega_i + \omega_s) E_{\text{P}, \gamma'}^*(\mathbf{r}', \omega_i + \omega_s) \text{Im} [G_{\beta\beta'}(\mathbf{r}, \mathbf{r}', \omega_i)] G_{\sigma_s \alpha}(\mathbf{r}_s, \mathbf{r}, \omega_s) G_{\sigma_{s'} \alpha'}^*(\mathbf{r}_s, \mathbf{r}', \omega_s). \quad (5.11)$$

Both P_{is} and P_s can be evaluated numerically for any system for which the classical GF is known. This will be done in the next section for describing atom-mediated SPDC.

Before getting to the atom-mediated proposal, let us get some modal-based understanding of the results here. We can reveal the modal dependencies in P_{is} by inserting the GF of a periodic WG, expressed in terms of its QNBMs, into Eq. (5.9). The GF for an infinite periodic WG can be found using the unconjugated reciprocity theorem, as detailed in appendix C, which gives:

$$G_{\alpha\beta}(\mathbf{r}, \mathbf{r}', \omega) = [e_\alpha^+(\mathbf{r}, \omega) e_\beta^-(\mathbf{r}', \omega) e^{ik^+(\omega)(x-x')} \Theta(x-x') \\ + e_\alpha^-(\mathbf{r}, \omega) e_\beta^+(\mathbf{r}', \omega) e^{ik^+(\omega)(x'-x)} \Theta(x'-x)] \frac{iac}{2\omega} \frac{n_g^+(\omega)}{\int_\Omega d^3 \mathbf{r} \boldsymbol{\epsilon}^+ \cdot \mathbf{e}^-}. \quad (5.12)$$

Here only a single mode is assumed to be present at each frequency, to simplify the notation. The + and - refer to the FP and BP counterparts of the mode, respectively, with complex-valued wavevectors $k^+ = -k^-$. Let us use this GF expression in Eq. (5.9) to find P_{is} . There are two GFs in Eq. (5.9), $G_{\sigma_i \beta}(\mathbf{r}_i, \mathbf{r}, \omega_i)$ and $G_{\sigma_s \alpha}(\mathbf{r}_s, \mathbf{r}, \omega_s)$. $G_{\sigma_i \beta}(\mathbf{r}_i, \mathbf{r}, \omega_i)$ is a sum of two terms, one with $\Theta(x_i - x)$ and the other with $\Theta(x - x_i)$, where x_i is the x-position of the idler atom. $G_{\sigma_s \alpha}(\mathbf{r}_s, \mathbf{r}, \omega_s)$ is also a sum of two terms, one with $\Theta(x_s - x)$ and the other with $\Theta(x - x_s)$, where x_s is the x-position of the signal atom. Hence $G_{\sigma_i \beta}(\mathbf{r}_i, \mathbf{r}, \omega_i) G_{\sigma_s \alpha}(\mathbf{r}_s, \mathbf{r}, \omega_s)$ will be a sum of four terms. Assuming that at the ω_s and ω_i frequencies we have signal and idler modes indexed by S and I , respectively, these four terms

correspond to the four different possibilities for the propagation directions of these modes: (1) Both signal and idler are FP with the term $\Theta(x_i - x)\Theta(x_s - x)$, which tells us the spatial integral is only nonzero for nonlinear area that is before both the detectors. (2) Both signal and idler are BP with $\Theta(x - x_i)\Theta(x - x_s)$, which tells us the spatial integral is only nonzero for nonlinear area that is after both the detectors. (3,4) We have a FP signal and a BP idler with the term $\Theta(x - x_i)\Theta(x_s - x)$, or a BP signal and a FP idler with the term $\Theta(x_i - x)\Theta(x - x_s)$, which in both cases tell us that the spatial integral is only nonzero for nonlinear area that is between the two detectors. To simplify the result, we consider a case where the nonlinearity profile $\chi^{(2)}$ is only non-zero in a finite space of $0 < x < L$, although the linear permittivity is infinite, and we assume that the two detectors are placed somewhere after this area such that $L \leq x_i, x_s$. In this way, we only need to consider the case where both signal and idler are FP. The resulting P_{is} shares much similarity with the JSA function of Eq. (4.14), but also has some extra parts in it that needs understanding. Hence, we regroup the terms in it to put together the parts it shares with Eqs. (4.14) to (4.16). This results in:

$$P_{\text{is}} = \left| A_{\text{P}} \frac{e^{(i\Delta k' - k''_{\text{P}})L} - e^{-(k''_{\text{S}} + k''_{\text{I}})L}}{(i\Delta k' - \Delta k'')a} \frac{\sqrt{n_{\text{gs}}^+ n_{\text{gl}}^+} \sum_{\alpha, \beta, \gamma} \int_{\Omega} d^3 \mathbf{r} \chi_{\alpha\beta\gamma}^{(2)}(\mathbf{r}) e^{i\frac{2\pi Q}{a}x} e_{\text{P},\gamma}(\mathbf{r}) e_{\text{S},\alpha}^-(\mathbf{r}) e_{\text{I},\beta}^-(\mathbf{r})}}{\sqrt{\int_{\Omega} d^3 \mathbf{r} \epsilon_{\text{S}}(\mathbf{r}) \mathbf{e}_{\text{S}}^+(\mathbf{r}) \cdot \mathbf{e}_{\text{S}}^-(\mathbf{r})} \int_{\Omega} d^3 \mathbf{r} \epsilon_{\text{I}}(\mathbf{r}) \mathbf{e}_{\text{I}}^+(\mathbf{r}) \cdot \mathbf{e}_{\text{I}}^-(\mathbf{r})}} \right|^2 \times \left(\frac{\pi}{\hbar \epsilon_0} \frac{\omega_{\text{S}} \omega_{\text{I}} a^2}{c^2} \right)^2 \left| \frac{\sum_{\sigma_i, \sigma_s} d_{i, \sigma_i}^* d_{s, \sigma_s}^* e_{\text{S}, \sigma_s}^+(\mathbf{r}_s) e_{\text{I}, \sigma_i}^+(\mathbf{r}_i)}{\sqrt{\int_{\Omega} d^3 \mathbf{r} \epsilon_{\text{S}}(\mathbf{r}) \mathbf{e}_{\text{S}}^+(\mathbf{r}) \cdot \mathbf{e}_{\text{S}}^-(\mathbf{r})} \int_{\Omega} d^3 \mathbf{r} \epsilon_{\text{I}}(\mathbf{r}) \mathbf{e}_{\text{I}}^+(\mathbf{r}) \cdot \mathbf{e}_{\text{I}}^-(\mathbf{r})}} \right|^2 |n_{\text{gs}}^+ n_{\text{gl}}^+|. \quad (5.13)$$

Here the capital letter indices I, S, and P are corresponding to variables at frequencies ω_i , ω_s , and $\omega_i + \omega_s$, respectively, and the small letter indices s and i are labels for signal and idler, respectively. We have substituted $\mathbf{E}_{\text{P}} = A_{\text{P}} \mathbf{e}_{\text{P}} e^{ik_{\text{P}}x}$ for this result. We have also written $k = k' + ik''$, with the phase-mismatch defined as $\Delta k' = k'_{\text{P}} - k'_{\text{S}} - k'_{\text{I}} - \frac{2\pi Q}{a}$ and loss-mismatch defined as $\Delta k'' = k''_{\text{P}} - k''_{\text{S}} - k''_{\text{I}}$. We also set the detectors at the end of the nonlinear region $x_i = x_s = L$. We have also taken the integral over the length of the structure, assuming that we are close to the point of phase-matching and all modes have decay lengths much longer than a period. The first line of Eq. (5.13) has all the terms similar to the JSA of the lossless structure, from the group index dependence to the overlap integral of the process. Although there are differences which are associated with the fact that signal and idler here are not lossless, so the overlap integral instead of the conjugate of the signal and idler mode profiles now has the backward mode profiles. The JPS now is affected by the decay of the signal and idler modes through k''_{S} and k''_{I} , so this method of detection reveals to us the effect of the decay lengths of the signal and the idler modes on the efficiency of the process. The second line of Eq. (5.13) however, includes more terms, which I interpret to be associated with the method of detection. There are three components to this part that are important: The first one is the dipole moments of the atoms, d_{i, σ_i}^* and d_{s, σ_s}^* , which affect the strength of the detection. The second is the local electric fields at the point of detection, $e_{\text{S}, \sigma_s}^+(\mathbf{r}_s)$ and $e_{\text{I}, \sigma_i}^+(\mathbf{r}_i)$, which are normalized with volume integrals of the Bloch mode profiles under a square root, making the dependency irrespective of any arbitrary proportionality constant in the Bloch mode profiles. This is understandable, as the atoms' response is electric field dependent, so naturally there should be a local dependency on the Bloch mode profile of the signal and idler modes. The third term is the group indices $|n_{\text{gs}}^+ n_{\text{gl}}^+|$, which allows for the enhancement of P_{is}

with slow signal and idler modes. This is the same effect as the Purcell enhancement [41], where the rate of the spontaneous emission of an emitter is enhanced in an environment of higher local DOS, as the DOS of a slow mode enhances proportional to its group index n_g [41]. Such a calculation for finding the Purcell enhancement factor is done assuming lossless guided modes with a real-valued n_g [41]. The above calculation hints that in a lossy WG this dependency is on the absolute value of the complex-valued n_g . This could be the topic of a future investigation. Overall, it is important to take note of these detection effects, which tell us that the detection scheme with atoms not only gives us information about the pair-generation, but also includes extra modal effects.

5.3 Atom-mediated SPDC with evanescent modes

By comparing Eqs. (5.7), (5.9), and (5.11), which refer to three different measured probabilities in an SPDC process, we can understand how the measurement has an impact on the result. In Eq. (5.7), we have P , the probability of SPDC happening while no atoms are present and both bosonic excitations remain in the field. In Eq. (5.9), we have P_{is} , the probability of SPDC happening and both generated bosonic excitations end up exciting the present 2-level atoms. In Eq. (5.11), we measure P_s , the probability of SPDC happening and one of the bosonic excitations exciting the signal atom, while the other bosonic excitation remains in the field. By looking at these equations we can deduce, that every time a generated bosonic excitation remains in the field we have the imaginary part of GF corresponding to that frequency in the expression, but when the bosonic excitation is absorbed by an atom, we have the total GF for that frequency appearing in the expression. The fact that measurement has an impact on the system is an obvious statement in quantum mechanics. In this case, this impact is something we could engineer through the GF of the system. If we use modes that have a very different real and imaginary parts of GF, like evanescent modes that have $\text{Im}[G] = 0$ corresponding to their zero DOS, we will get very different SPDC responses with and without the presence of 2-level emitters. Consequently, if we make the detection apparatus, here the 2-level atoms, part of the system, we can create a hybrid source with new functionalities that can be controlled through the GF of the system. This is the basis of the proposed atom-mediated SPDC scheme using evanescent modes. In most applications with an emitter in a PC, it is the PC that is used to alter the DOS of the medium surrounding the emitter [261], which enables the engineering of the emission of emitters and their interactions with each other [262, 263, 264, 41, 42, 16, 40]. However, when the emitter's transition frequency is within the bandgap of the PC, where evanescent modes have zero DOS [265], it is the emitter that alters the PC, making the DOS non-zero by adding a free state to the system. Such a state is referred to as an atom-photon bound state [266, 261] or an atom-induced cavity [263], which allows engineering of atom-atom and atom-photon interactions [263, 264]. Here, a new possibility in tailoring quantum light-matter interactions is suggested through a combination of nonlinear parametric processes and atom-induced states.

The proposed scheme for atom-mediated SPDC is as follows: consider an infinite periodic WG, in which the phase-matching condition for the SPDC process is set to be satisfied between a propagating pump, a propagating signal, and a bandgap idler mode, with a 2-level atom with the idler's transition frequency placed near or inside the nonlinear WG structure, similar to what is shown in Fig. 5.1(a).

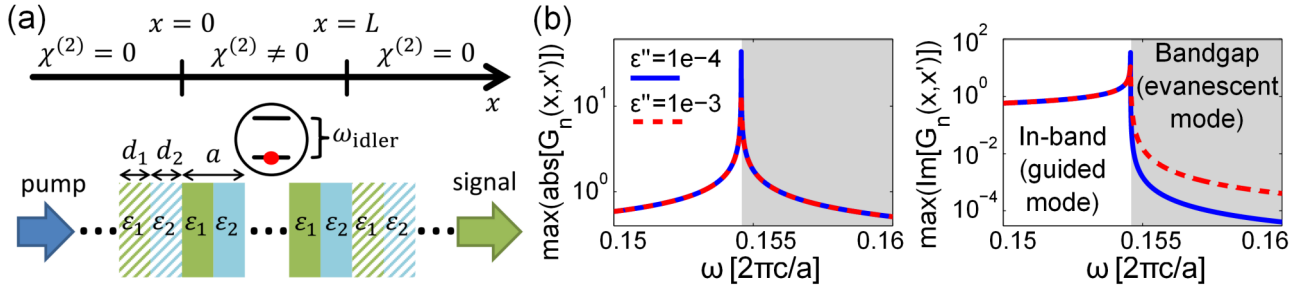


Figure 5.1: (a) Schematic of atom-mediated SPDC. The atom with idler's transition frequency is placed near a nonlinear periodic WG, where idler frequency falls within its bandgap frequency range; (b) The absolute value and imaginary part of the normalized GF $G_n(x, x', \omega)$, where maximum values are taken over spatial coordinates x and x' , for $\varepsilon'' = 0.001$ and 0.0001 . A periodic WG with $\varepsilon_1 = 3 + i\varepsilon''$, $\varepsilon_2 = 12 + i\varepsilon''$, and $d_1 = d_2 = 0.5a$ is assumed. The gray shaded area is the bandgap region.

To investigate SPDC with and without the mediation of the idler atom, we formally introduce a signal atom to model a single-photon detector. We then compare $P_{is}(\mathbf{r}_s, \mathbf{r}_i, \omega_s, \omega_i)$ in Eq. (5.9) and $P_s(\mathbf{r}_s, \omega_s)$ in Eq. (5.11). By comparing P_{is} and P_s , we can determine the effect of the idler atom in the SPDC process, as in both cases the signal photon has been detected, or absorbed by the signal atom, but in P_s the idler photon remains in the field and in P_{is} it excites the idler atom. We see from Eq. (5.11) that P_s is exactly zero with an evanescent idler mode, as $\text{Im}[G(\mathbf{r}, \mathbf{r}', \omega_i)] = 0$ when ω_i is within the bandgap of an infinitely extended periodic structure. This means that SPDC with an idler photon remaining in the field of a purely evanescent mode is completely prohibited, as a mode with zero DOS is incapable of accepting a photon. On the other hand, according to Eq. (5.9), P_{is} is dependent on the total GF and henceforth is not zero, as the evanescent mode still has a purely real-valued GF. In other words, the presence of the idler atom provides a free state for the quantum of excitation to be generated into, exciting the idler atom and mediating the previously prohibited SPDC process. An important implication is, that in the event of a signal photon detection, we know with certainty that an idler atom has been present and excited through SPDC. This creates a unique heralding mechanism, where the detection of the signal photon heralds the excitation of the idler atom.

In a realistic structure, however, we do not have purely evanescent modes, as loss is ever present due to either material absorption or fabrication imperfections. This means that the heralded excitation mechanism will be deteriorated in the presence of loss. In the following, the effect of loss on this heralding efficiency will be numerically quantified and in the process also more insight will be gained about the atom-mediated SPDC process. Consider the simplified model shown in Fig. 5.1(a), with an infinite 1D periodic WG. To simplify the notations, a scalar scenario is considered, where the system is invariant in the yz -plane, the only non-zero element of the $\chi^{(2)}$ tensor is $\chi_{zzz}^{(2)} = \chi^{(2)}$, and the dipole moments for the atoms are $\mathbf{d}_{i,s} = d_{i,s}\mathbf{z}$. Consequently, only the z -components of vectors ($\mathbf{E} = \mathbf{E} \cdot \mathbf{z}$) participate in the interactions. To numerically evaluate P_{is} and P_s , we need to evaluate the GF of the system at the signal and idler frequencies. The GF of an infinite periodic WG expressed in terms of its QNBMs was found in appendix C. Rewriting the expression for a 1D scalar scenario gives:

$$G(x, x', \omega) = [e^+(x, \omega)e^-(x', \omega)e^{ik^+(\omega)(x-x')} \Theta(x-x') + e^-(x, \omega)e^+(x', \omega)e^{ik^+(\omega)(x'-x)} \Theta(x'-x)] \times \frac{iac}{2\omega} \frac{n_g^+(\omega)}{\mathcal{S} \int_0^a dx \varepsilon(x) e^+(x) e^-(x)} \equiv \frac{a}{\mathcal{S}} G_n(x, x', \omega), \quad (5.14)$$

where we have only a single mode present at each frequency. \mathcal{S} is some transverse normalization area perpendicular to the x -direction in the yz -plane, where any volume integral can be written as $\int d^3\mathbf{r} = \mathcal{S} \int dx$. We define the normalized Green's function G_n as a unitless quantity that is independent of \mathcal{S} , and can be constructed with periodicity-normalized dimensions and frequencies, which are common variables to use for a periodic structure. The $+$ and $-$ indices refer to FP and BP modes, respectively. With decaying modes, FP is equivalent to decaying in the $+x$ -direction, and BP vice versa. A 1D periodic WG with parameters $\varepsilon_1 = 3 + i\varepsilon''$, $\varepsilon_2 = 12 + i\varepsilon''$, and $d_1 = d_2 = 0.5a$ is assumed, where the $\chi^{(2)}$ nonlinearity only exists within the finite region $0 < x < L$. The GF of this periodic WG is evaluated numerically, the details of which are explained in appendix C. To visualize the main physics, we take the spatial maximum of $\text{abs}[G_n(x, x')]$ and $\text{Im}[G_n(x, x')]$, and plot them in Fig. 5.1(b) as a function of ω and for two different values of ε'' . This is done for a range of frequencies around the first bandgap of this structure. We take the signal and idler frequencies to be around this frequency range. There are a number of important observations to make here. As expected, we see that in the presence of a finite amount of loss we no longer have a purely evanescent mode in the bandgap with $\text{Im}[G] = 0$. This means that with a finite loss, SPDC is no longer completely prohibited for the bandgap mode. $\text{Im}[G]$ of the bandgap mode is still much smaller than its $\text{abs}[G]$, which means that we still expect SPDC without the mediation of the idler atom to be much weaker compared to SPDC with the idler atom. Furthermore, $\text{Im}[G]$ in the bandgap decreases with decreasing ε'' , which as expected shows that decreasing loss brings the bandgap mode closer to the case of a purely evanescent mode. The sharp increase in $\text{abs}[G]$ and $\text{Im}[G]$ at the bandedge correspond to the slow-light mode.

We can now evaluate P_{is} and P_s using this GF. Here the main goal is to study the underlying GF-dependent physics of the process, regardless of the strength and profile of the nonlinearity, the strength of the pump beam or its spectrum, or the strength of the atomic dipole moments. For this purpose, some assumptions are made to simplify the 1D problem which eventually allows us to define quantities for this study that are independent of these factors, but still include all the GF-related physics. Firstly, we only consider the phase-matched pump Bloch harmonic $E_P(\mathbf{r}, \omega_P) = E_P(\omega_P)e^{ik_P(\omega_P)x}$ participating in the process. We also assume a constant nonlinearity profile $\chi^{(2)}(\mathbf{r}) = \chi^{(2)}$. With these assumptions, we can reorganize the generation probabilities into $P_{\text{is}} = \left| d_i d_s \chi^{(2)} E_P / a \mathcal{S} \hbar \varepsilon_0 \right|^2 W_{\text{is}}$ and $P_s = \left| d_s^2 / a \mathcal{S} \hbar \varepsilon_0 \int_0^\infty d\omega_i \left| \chi^{(2)} E_P \right|^2 \right| W_s$, and define the normalized efficiencies W_{is} and W_s as:

$$W_{\text{is}} \equiv 16\pi^2 \frac{a^8 \omega_s^4 \omega_i^4}{c^8} \left| \int \frac{dx}{a} e^{ik_P x} G_n(x_i, x, \omega_i) G_n(x_s, x, \omega_s) \right|^2, \quad (5.15)$$

$$W_s \equiv 16\pi \frac{a^6 \omega_s^4 \omega_i^2}{c^6} \int \frac{dx}{a} \int \frac{dx'}{a} e^{ik_P(x-x')} \text{Im} [G_n(x, x', \omega_i)] G_n(x_s, x, \omega_s) G_n^*(x_s, x', \omega_s). \quad (5.16)$$

The defined normalized pair-generation efficiencies W_{is} and W_s only include the physics associated with the GF. We insert the numerically evaluated $G_n(x, x')$ into Eqs. (5.15) and (5.16) to evaluate W_{is} and W_s . To proceed with the numerical analysis, it is assumed that for every frequency combination $\omega_P = \omega_s + \omega_i$, the phase-matching condition $k_P = \text{Re}[k_s + k_i]$ is satisfied. As was shown in this thesis, such modal phase-matchings for a TWM process can be reached for realistic periodic WG structures. The results are plotted in Fig. 5.2 as a function of the position of the atoms, x_i and x_s . Plots (a-d) are averaged over every unitcell to give better visibility to slower variations. A non-averaged plot is

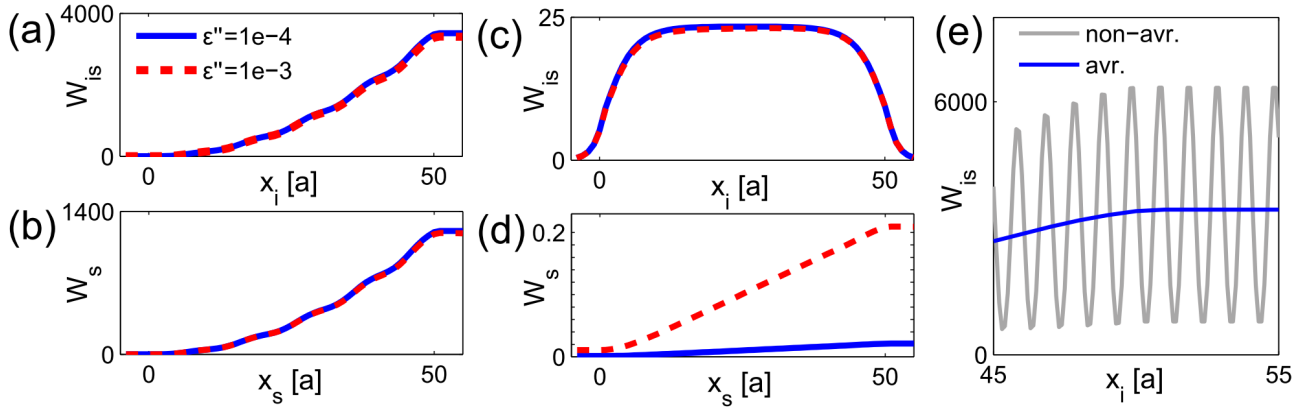


Figure 5.2: The normalized pair-generation efficiencies with the idler photon (a,c) absorbed by the idler atom at position x_i , $W_{is}(x_s = 55a, x_i)$, and (b,d) not absorbed by the idler atom, $W_s(x_s)$. Parameters are (a,b) $\omega_s = \omega_i = 0.15 \frac{2\pi c}{a}$ (both propagating) and (c,d) $\omega_i = 0.16 \frac{2\pi c}{a}$ (evanescent) and $\omega_s = 0.15 \frac{2\pi c}{a}$ (propagating). Plots in (a-d) are averaged over every unitcell, and (e) shows the non-averaged (a) near the edge of the nonlinear region. $\chi^{(2)} \neq 0$ for $0 < x < 50a$. Blue solid and red dashed curves correspond to $\epsilon'' = 10^{-4}$ and $\epsilon'' = 10^{-3}$, respectively.

shown in Fig. 5.2(e) as a sample, displaying periodic variations. To focus on the dependence of W_{is} on x_i , we fixed $x_s = 55a$ to outside of the nonlinear region, as the detection probability of the guided signal photon only decays slowly further away from the nonlinear region. In Figs. 5.2(a) and (b) we consider the case where both signal and idler are guided modes. The efficiency of an idler photon to be absorbed by an atom, W_{is} , shows a quadratic rise as a function of x_i , similar to the quadratically rising intensity of a guided mode that is pumped with a lossless and phase-matched source of nonlinear polarization [267]. The efficiency of the idler photon to be generated but not absorbed by an atom, W_s , shows the same behavior as W_{is} , which means that having the photon of a guided mode absorbed by the atom or remaining in the field does not qualitatively affect the SPDC process, as G and $\text{Im}[G]$ are comparable for a guided mode, as shown in Fig. 5.1(b). The small periodic modulations of the graphs are due to the out-of-phase backward process. The considered losses have negligible effect on the process on this length scale.

In Figs. 5.2(c) and (d), the idler mode is evanescent and the signal mode is guided. W_{is} increases from both ends of the nonlinear region inwards, and saturates after about twice the decay length of the evanescent mode. The saturation causes the overall SPDC efficiency to be much smaller compared to the case of both guided modes, as can be seen by comparison to Figs. 5.2(a) and (b). Importantly, we see that the efficiency of signal detection without idler atom's excitation W_s is now much smaller than with idler atom's excitation W_{is} , due to the effect of the evanescent mode, but it is not exactly zero due to the presence of the finite loss. We see that for an order of magnitude larger ϵ'' , W_s also increases by an order of magnitude, clearly showing how loss can degrade our heralding mechanism. Finally, W_{is} is bound to the region inside and near $\chi^{(2)} \neq 0$, because the evanescent field cannot propagate beyond the generation region. Hence, the idler atom can only be excited near $\chi^{(2)} \neq 0$ regions, whereas the generated guided signal photon can escape the nonlinear structure.

Finally, we can define a heralding efficiency $H \equiv P_{is}/(P_{is} + P_s)$, which is the probability of the idler atom's excitation, in the event of a signal photon's detection (signal atom being excited). With a purely evanescent idler mode $P_s = 0$ and $H = 1$, and with loss $P_s \neq 0$ and $H < 1$. Let us assume a narrow rectangular spectrum for the pump, centered at $\omega_s + \omega_i$ with bandwidth $\Delta\omega_p$, over which the

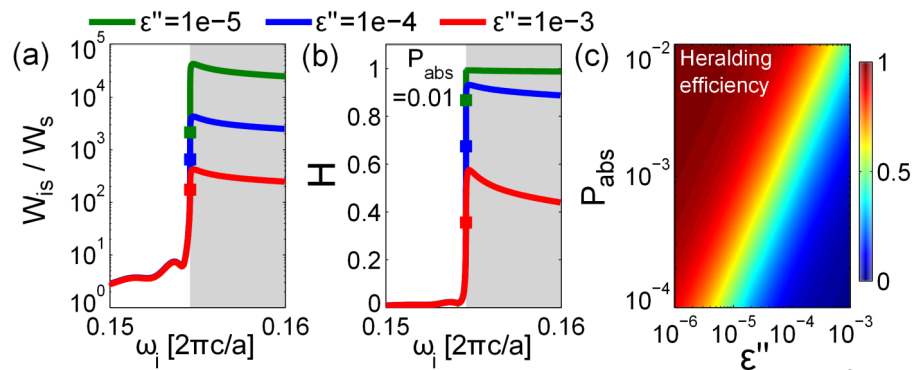


Figure 5.3: (a) The W_{is}/W_s ratio for three different values of ϵ'' . We fix $\omega_s = 0.15 \frac{2\pi c}{a}$ and vary ω_i . The solid squares mark where each plot passes the bandedge. The gray shaded area is the bandgap region; (b) The heralding efficiency H for idler-atom's vacuum absorption probability $P_{abs} = 0.01$; (c) H for $\omega_i = 0.16 \frac{2\pi c}{a}$ (evanescent) and $\omega_s = 0.15 \frac{2\pi c}{a}$ (guided) as a function of ϵ'' and P_{abs} . For all plots $L = 50a$, $x_s = 50a$ and $x_i = 25a$.

GF does not change considerably. Then we can put $\int_0^\infty d\omega_i \approx \Delta\omega_i = \Delta\omega_p$, where $\Delta\omega_i$ is the bandwidth of the generated idler photon remaining in the field, and get:

$$H = P_{is}/(P_{is} + P_s) \approx 1/(1 + \frac{2\pi^2 a/\lambda_i}{P_{abs}} \frac{W_s}{W_{is}}), \quad (5.17)$$

where $P_{abs} = 2\pi^2 |d_i|^2 / (\hbar\epsilon_0\Delta\omega_i\lambda_i\mathcal{S}) \ll 1$ is the probability of the idler atom in vacuum (in 1D) absorbing a single-photon wave-packet of central wavelength λ_i and with a rectangular spectrum of bandwidth $\Delta\omega_i$, which can be calculated using the first-order perturbation theory [259]. As can be seen in Eq. (5.17), the W_{is}/W_s ratio plays a key role in determining the heralding efficiency. We evaluate and plot W_{is}/W_s in Fig. 5.3(a) for three different values of loss. Here we fixed ω_s to a guided mode, and varied ω_i over the whole frequency range to see the difference between having a guided idler mode and an evanescent one. The signal detector is fixed to the end of the nonlinear structure and the idler atom is placed in the middle of the nonlinear structure. We can see that W_{is}/W_s is much larger in the bandgap region, showing the effect of an evanescent idler mode in suppressing W_s . We also see that lowering the loss by an order of magnitude increases this ratio in the bandgap by an order of magnitude, improving the effect.

We now plot H , the probability of the idler atom's excitation in the event of a signal photon's detection, in Fig. 5.3(b) for a particular value of $P_{abs} = 0.01$. We see that H is much closer to 1 in the bandgap region compared to the in-band region, showing that with a bandgap idler mode we can be almost certain of the idler atom's excitation in the event of a signal detection, whereas with a guided idler mode the pair-generation will happen with almost no interaction with the idler atom. Moreover, we see how this high probability in the bandgap gets degraded with increasing losses. It is important here to notice, that if the idler atom was placed in vacuum outside of the source and we wanted it to absorb a single idler photon produced from this SPDC source, its absorption probability would be the very small number of $P_{abs} = 0.01$. Even if we placed this idler atom inside the source with a guided idler mode, the probability of the idler atom getting excited is still much smaller than the probability of the generated idler photon just passing by the atom and not interacting with it. This is described by the close to zero H in Fig. 5.3(b) when the idler frequency is in-band. It is only when the idler frequency is in the bandgap region, that we can be almost certain that the idler atom

is going to be excited through SPDC, as the probability of SPDC happening without the idler atom's participation is very small in comparison. This is described by the close to 1 H . This discussion shows that by using evanescent modes, we can interface a photon-pair source with a single-emitter source with high certainty, even though the absorption probability of the emitter itself is very low when a photon is passing through it. Finally, we plot H for a fixed frequency pair of a guided signal and an evanescent idler as a function of P_{abs} and ϵ'' in Fig. 5.3(c). We see that a smaller P_{abs} , meaning either a shorter pump pulse in time or a weaker dipole moment of the atom, lowers H , but this could always be amended in a less lossy system. This result shows the robustness of this heralded excitation mechanism against loss.

In order to assess the practical feasibility of emitter-mediated SPDC, we consider a PCSW made of GaAs, a material with $\chi^{(2)}$ nonlinearity, which can be fabricated with a layer of quantum dots (QDs) embedded in it [16]. The bandgap region in GaAs PCSWs is around $a/\lambda \approx 0.3$, hence for covering a QD's central wavelength of $\lambda_i = 940$ nm, we need a periodicity of $a \approx 280$ nm. GaAs itself is transparent at 940 nm. However, an equivalent $\epsilon'' \approx c\epsilon'/(n_g\omega L_{\text{decay}})$ [241] must be assigned to the structure, where L_{decay} is the scattering losses' decay length caused by fabrication imperfections. For $L_{\text{decay}} \approx 1$ cm [268], we get $\epsilon''(\omega_i) \approx 10^{-4}$. We rewrite $P_{\text{abs}} = 3\lambda_i^2\Gamma_0/(4\mathcal{S}\Delta\omega_i\sqrt{\epsilon'})$, where $\Gamma_0 = \omega_i^3|d|^2\sqrt{\epsilon'}/(3\pi\hbar\epsilon_0c^3)$ is the spontaneous emission rate of the emitter placed in bulk [41]. The cross-section \mathcal{S} of such PCSWs is roughly around $(\lambda_i/\sqrt{\epsilon'})^2$, giving us $P_{\text{abs}} \approx \frac{\Gamma_0\sqrt{\epsilon'}}{\Delta\omega_i}$. For a QD with $\Gamma_0/2\pi = 0.1$ GHz [16], using a pump bandwidth of $\Delta\omega_p/2\pi = 30$ GHz gives us $P_{\text{abs}} \approx 0.01$, which according to Fig. 5.3(c) gives a heralding efficiency larger than 0.98. To get a signal photon at the telecom wavelength of $\lambda_s = 1550$ nm, one can use a pump central wavelength $\lambda_p = 585$ nm. This λ_p is outside the transparency window of GaAs, resulting in a very short decay length for the pump, but this could be solved using a pump-from-above scheme [114]. Considering the remarkable experimental advances made in interfacing PCs with emitters, an implementation of this proposal is within reach.

Finally, it is clear from Fig. 5.2(d), where W_s rises almost linearly with the length L while W_{is} saturates after a short length, that reducing L should increase W_{is}/W_s and result in $H \rightarrow 1$. However, a realistic structure is finite, causing a reflection of evanescent modes from its ends, which creates DOS at those ends that decay exponentially towards the inside of the structure [269, 270]. Hence, L has to be still large enough so that the idler atom can be placed inside the structure far enough from the ends to not get affected by this created DOS. This means that an optimum length should exist in a practical design, based on the amount of loss, to maximize the heralding efficiency.

5.4 Summary of the results and related publications

The main result of this chapter was the proposal of the atom-mediated SPDC process, in which I showed analytically and numerically in a 1D periodic structure, that SPDC involving an evanescent idler mode is prohibited, but it can be mediated by embedding a 2-level emitter near the nonlinear structure, giving rise to a unique heralded excitation mechanism. This type of light-matter interaction can result in the development of new types of nonlinear sensing schemes and hybrid sources of quantum light. The work on the atom-mediated SPDC proposal has been published in Optics Letters [S6].

Chapter 6

Conclusion and outlook

In this thesis, I have taken the first theoretical and numerical steps in establishing photonic crystal slab waveguides (PCSWs) as highly capable SPDC sources of photon-pairs with unique abilities in engineering the biphoton quantum state, and paved the way for practical implementation of such sources. I have reached the main goals of my thesis, in laying the foundations and filling the holes in the knowledge on the design and analysis of PCSWs for pair-generation through SPDC, while proposing practical structures for SPDC applications with unique capabilities in creating and controlling the extent of entanglement in various degrees of freedom. Now SPDC applications can benefit from the PCSW platform, especially when there is a need for engineering more complex photon-pair states.

PCSWs can strongly control light-matter interactions at the subwavelength scale, but surprisingly, this control was never put to use toward shaping the quantum state of photon-pairs generated through SPDC. The main reason hindering research in this promising direction was the lack of practical modally phase-matched PCSW designs to begin with, made more complicated by the fact that modes at the pump frequency are inherently leaky. As the first step in my thesis, I solved this problem. I have shown, that not only phase-matched designs for three-wave mixing (TWM) processes can be reached in PCSWs, but I also proposed a new type of double-slot PCSW to reduce the leakage of the pump mode, making PCSWs a viable option for SPDC applications. I have then used this structure to find practical phase-matched designs in lithium niobate (LN) PCSWs. I have demonstrated that PCSWs can offer a strong control over the phase-matching configuration. This includes reaching phase-matching between modes of different propagation directions, reaching simultaneous phase-matching between multiple processes, and controlling the group index of the modes at the point of phase-matching. These capabilities proved to be the keys to enabling a PCSW source of photon-pairs to create and control the extent of entanglement in the spectral, path, and modal degrees of freedom.

Before proceeding to investigate PCSWs for SPDC, I have first committed to studying classical phase-matched TWM processes in PCSWs, specifically the process of SHG, as SHG and degenerate SPDC share much similarities according to the quantum-classical correspondence principle. With the classical studies, I have gained understanding of signature behaviors of TWM processes in periodic waveguides (WGs) involving lossy modes, and I also managed to double-check my phase-matched designs using direct nonlinear simulations. More importantly, I have verified the use of a decaying Bloch mode basis, known as quasi-normal Bloch modes (QNBMs), for analytical treatment of TWM in PCSWs. This was done through comparing the analytical results with that of direct nonlinear

simulations done with FDTD. The verification from the classical analysis meant that I can use the QNBM basis also for describing the quantum processes in this system.

Studying phase-matched SHG in PCSWs, aside from being of benefit for understanding SPDC in PCSWs, was itself a new result in the category of classical nonlinear interactions in periodic nanostructured WGs. This classical study also had some extra benefits on the side. First was the development of a method for performing nonlinear FDTD simulations in nanostructured systems. This method was not just used in my work with PCSWs, but also contributed to works on studying SHG in dielectric nanoresonators, which is an active field of research. Second was developing a formulation for treating SHG in periodic WGs in the presence of loss. I used this formulation not just to describe SHG in my PCSW designs, but also to perform a general study on the effect of loss on the efficiency of nonlinear interactions in periodic WGs, identifying optimum regimes for the use of such structures in the presence of loss.

With the designs and understanding of phase-matched TWM processes in PCSWs, I moved on to studying SPDC. I first developed a formalism for describing the biphoton state generated from a periodic WG source. Then I demonstrated, with general explanations and specific examples, how a PCSW source can control the entanglement in different degrees of freedom. Engineering spectral entanglement requires control over the group velocities of the modes involved. In this thesis, I have shown that a PCSW allows for controlling not only the amplitude, but also the sign of the group velocities of the signal and idler modes at the point of phase-matching. This is an ability that regular non-periodic WGs lack, or can gain partially through unintegrated pumping schemes or submicron poling periods, but a PCSW possesses it naturally. Such a source can avoid extra pre- or post-processing steps, like filtering, to prepare the photon-pair in the desired spectral state. Of particular interest is reaching spectrally unentangled pairs, needed for heralded sources of single-photons. As an example, I presented the design and analysis for a LN double-slot PCSW capable of generating such factorizable pairs in a counterpropagating configuration. I also demonstrated this source's capability in tuning the output factorizable state. Another important capability of PCSWs discovered in this work, is that they can phase-match multiple processes simultaneously, where each process can be between different modes of different propagation directions. I showed how this unique capability can result in creating path- and/or modal-entanglement in the biphoton state, and importantly doing it directly at the source and without the need for poling, unintegrated pumping, or any other pre- or post-processing steps. I then presented an example with a LN double-slot PCSW, capable of simultaneously phase-matching two counterpropagating processes, and showed how such a design can in practice be tuned to produce a maximally-entangled state, specifically, a path-entangled Bell state. The results in this thesis, show the unique power of PCSWs in creating and tuning the extent of entanglement in different degrees of freedom on an integrated platform, with minimum processing steps and on a short length scale, making them ideal optical structures for large-scale implementation of photon-pair sources.

Naturally, the future step in this research would be to fabricate and characterize the designed and analyzed photon-pair sources. The material platform chosen for the PCSWs throughout this thesis was LN, and for them to be implemented with this material, the nanostructuring technology in LN has to be developed enough for the fabrication of such integrated WGs for nonlinear applications. During my thesis project, I have also participated in our group's activities toward this goal. I have

designed LN ridge WGs phase-matched for SHG, which were successfully fabricated in our institute. I have characterized these WGs in an SHG experiment, showing modally phase-matched SHG, which was a major advancement in our efforts. With the progress taking place in the past few years in nanostructuring integrated optical elements in LN, the successful fabrication of LN PCSWs is within reach in the near future. However, one does not have to wait for this advancement in the LN platform. The ideas and designs presented in this work are general and can easily be adapted to other $\chi^{(2)}$ materials with a nanostructuring capability, like GaAs or gallium phosphide. As a matter of fact, I have successfully done double-slot PCSW designs on a GaAs platform. In the future, whether in LN or in GaAs, I will be actively pursuing the implementation of SPDC sources of photon-pairs using PCSWs, so that I can materialize my ideas developed during this thesis.

Aside from the investigated applications in this thesis, there are also a number of other applications in the realm of photon-pair sources that PCSWs can potentially make an impactful contribution to, and these could be the topic of future investigations. For example, I have shown that a backward-propagating phase-matching configuration can be reached in a double-slot PCSW. In such a source, both the signal and idler photons will be propagating in the opposite direction to the pump mode, which could naturally act as a pump filtering scheme. This falls in the same category of another proposal for spatially filtering the pump beam, which is based on adiabatically coupled WGs [271] that combine the generation and filtering stages together. It would be interesting to investigate, if an SPDC source in the backward-propagating configuration could in practice provide the needed pump rejection in the backward direction, to not require any extra pump filtering. Another investigation could be towards reaching extremely narrow spectra, which are specially important for interfacing photon-pair sources with quantum memories [166] that have bandwidths in the order of MHz, which can nowadays only be reached in resonators of very high quality factors [165]. In this thesis, I have shown that using a counterpropagating configuration results in much narrower spectra compared to non-periodic WGs of similar lengths that operate in a forward-propagating configuration. It would be interesting to investigate, given a certain quality of fabrication, if such narrow spectra compatible to quantum memories can be reached in practice using PCSWs. Finally, given the capabilities the PCSWs have shown in this work in controlling different degrees of entanglement, it would be interesting to investigate their potential for creating entanglement in multiple degrees of freedom, to reach what is called hyper-entanglement [95], which is a valuable resource for quantum communication.

The final result of this thesis to be discussed here is the atom-mediated SPDC proposal. In my investigations toward formulating SPDC in periodic WGs with decaying modes, I have discovered that under certain conditions, 2-level emitters can have a strong effect on the photon-pair generation process. The core idea of atom-mediated SPDC can be expressed as follows: one can combine a nonlinear source of photon-pairs, which has bosonic properties, with a single-emitter, which has fermionic properties, and make these fermionic properties more pronounced by using evanescent modes that have zero density of bosonic states. I have used this idea to propose and investigate a new type of heralded excitation mechanism, where a photon-pair source and a single-emitter source are interfaced with each other directly at the pair-generation stage. In general, interfacing matter-based and photonic qubits is of vital importance for the implementation of quantum repeaters [166], and I believe that the atom-mediated SPDC proposal can bring about new possibilities for the engineering

of such components, eventually needed for constructing a quantum network [272].

Aside from the heralded excitation effect, I envision a range of applications that can be investigated in the future for this new type of light-matter interaction. As the 2-level emitter is only capable of accepting one quantum of excitation, a hybrid atom-mediated source naturally suppresses multiple-pair generation, a constant hurdle for heralded single-photon sources that creates a trade-off between the generation rate and the fidelity of the heralded state [89]. This proposal could offer a path to lifting this fundamental trade-off, because if the source no longer has a problem with multiple-pair generation, then there is no need to operate in low generation probabilities that is the cause for probabilistic pair-generation, and instead one can potentially get an on-demand generation of tunable photons using strong pump pulses. Another interesting application is regarding a multiplexing scheme, in which one of the photons in the pair at the output of an array of photon-pair sources is coupled into an array of quantum memories, which would allow for the control of the statistics of the output single-photons and also reaching multiphoton entanglement [273]. Atom-mediated SPDC could be a compact realization of this multiplexing scheme, if we can use the embedded emitter as a quantum memory. In this way, one of the photons in a pair is directly generated into the quantum memory and could be released when needed. Another application is in the realm of sensing. In the atom-mediated configuration, the increase in the counts of the signal photon is essentially a sign of the presence of an idler atom near the nonlinear structure. This offers a new scheme for nonlinear quantum spectroscopy [274], where the presence of the 2-level atoms, e.g. a gas that has a resonant absorption line at the idler's frequency, can be sensed by observing an increase in the counts of the photons at the signal frequency. In this sensing scheme, the close to 1 heralding efficiency essentially means a high signal to noise ratio, where P_s is the probability of the background or noise that is detected without the presence of the atoms, and P_{is} is the "signal" that is detected in the presence of the atoms. As a final example, it would be interesting to investigate what will happen if more than one single-emitter are present in an atom-mediated interaction. Would there be any type of entanglement created between the excitation of these single-emitters, caused by the spontaneous nonlinear process?

Aside from all these theoretical proposals emerging from the field of atom-mediated SPDC, which I am planning to actively pursue in the near future, there is also the important question of how to do a practical implementation of them, which I also plan to find an answer for. Firstly, it is important to note that the atom-mediated nonlinear effect is not specific to SPDC and can equally be applied to SFWM in a $\chi^{(3)}$ material. The important part of the effect is having a pair-generation process with an idler frequency, at which the system has zero density of states of optical modes, and then add a 2-level system at that frequency to the system. Henceforth, for implementing the hybrid source idea one can choose any material system capable of SPDC or SFWM, creating a nonlinear periodic WG, and hosting 2-level emitters, or bringing the emitter to the vicinity of the nonlinear periodic WG. A good candidate for this could be the diamond platform with vacancy centers or the GaAs platform with quantum dots. The sensing idea could offer an easier path to implementation. One can use Bragg grating silica fibers as the periodic system for pair-generation through SFWM, and then use them for sensing materials that could be surrounding the fiber core, e.g. a gas with a resonant absorption line at the idler frequency, at which we also have the bandgap of the Bragg fiber. The fiber system at the moment is a near future candidate for me, for investigating the nonlinear sensing idea.

Deutschsprachige Zusammenfassung

Das Ziel dieser Arbeit war Entwicklung von Photonenpaarquellen auf der Basis des spontanen parametrischen Zerfalls von Photonen (SPDC – spontaneous parametric down-conversion) in photonischen Kristallwellenleitern (PCSW – photonic crystal slab waveguide). Dabei sollten theoretische Werkzeuge zur Beschreibung und zum Design derartiger Photonenpaarquellen entwickelt als auch die Eigenschaften der Photonenpaarquellen im Hinblick auf eine möglichst weitreichende Beeinflussung des erzeugten Photonpaarzustands optimiert werden.

Diese Ziele habe ich in der vorliegenden Arbeit erreicht. Ich habe einen theoretischen Formalismus zur Analyse von sowohl dem quantenmechanisch zu beschreibenden SPDC-Prozess als auch dessen klassischen Umkehrprozess der Generation der zweiten Harmonischen (SHG – second-harmonic generation) entwickelt. Dieser wurde durch Vergleich seiner Vorhersagen mit rigorosen numerischen Simulationen verifiziert. Spezielles Augenmerk wurde bei der theoretischen Beschreibung auf eine korrekte Behandlung optischer Verluste gelegt, welche eine inhärente Eigenschaft realistischer photonischer Strukturen darstellen. Diese analytischen und numerischen Studien ermöglichten eine präzise Beschreibung der untersuchten nichtlinearen Konversionsprozesse.

Auf Basis der durch die theoretischen Untersuchungen gewonnenen Erkenntnisse wurden verschiedene praktisch realisierbare Strukturgeometrien auf der Basis von PCSWs entwickelt, welche unterschiedliche Phasenanpasskonfigurationen und damit unterschiedliche nichtlineare Konversionsprozesse ermöglichen. Dabei habe ich unter anderem Phasenanpassung zwischen propagierenden Moden gegensätzlicher Ausbreitungsrichtung, gleichzeitige Phasenanpassung zwischen unterschiedlichen Modenpaaren sowie die gleichzeitige Kontrolle von Phasenanpassung und Gruppengeschwindigkeit nachweisen können. Diese Variabilität ist ein entscheidender Faktor für den Einsatz von PCSW als Photonenpaarquelle mit breitem Einsatzspektrum. Ich konnte zeigen, dass kompakte Photonenpaarquelle auf der Basis von SPDC in PCSWs die Erzeugung von Photonenpaaren mit kontrollierbarer Verschränkung in Propagationsrichtung und Spektrum erlauben.

Mit meiner Arbeit habe ich Wege zur Nutzung von PCSWs als Photonenpaarquellen für quantenoptische Anwendungen eröffnet. Davon können insbesondere Anwendungen profitieren, die hochintegrierte und ultrakompakte Photonenpaarquellen mit in weiten Bereichen einstellbaren Eigenschaften benötigen.

Als ersten Schritt zur experimentellen Realisierung habe ich außerdem nichtlineare Frequenzkonversion in nanoskaligen Wellenleitern aus dem Material Lithiumniobat demonstriert, welches auch SPDC ermöglicht. Ausgehend von diesen experimentellen Arbeiten werde ich die theoretisch entwickelten Konzepte zur Photonenpaarerzeugung in PCSWs nach Abschluß meiner Promotion auch experimentell demonstrieren.

Daneben habe ich in meiner Arbeit auch die Kopplung von Wellenleitern zur Photonenerzeugung mit Einzelphotonenemittern untersucht. Dabei habe ich einen neuartigen Mechanismus, die durch Atome vermittelte SPDC entdeckt und theoretisch untersucht. Die Ausnutzung dieses Effekts kann die Eigenschaften von Photonenerzeugern weiter verbessern und diversifizieren.

List of own contributions

Peer reviewed journal papers

- [S1] R. Geiss, S. Saravi, A. Sergeyev, S. Diziain, F. Setzpfandt, F. Schrepel, R. Grange, E.-B. Kley, A. Tünnermann, and T. Pertsch, “Fabrication of nanoscale lithium niobate waveguides for second-harmonic generation,” *Optics Letters* **40**, 2715–2718 (2015).
- [S2] S. Saravi, S. Diziain, M. Zilk, F. Setzpfandt, and T. Pertsch, “Phase-matched second-harmonic generation in slow-light photonic crystal waveguides,” *Physical Review A* **92**, 063821 (2015).
- [S3] S. Saravi, R. Quintero-Bermudez, F. Setzpfandt, N. A. Mortensen, and T. Pertsch, “Effect of loss on slow-light-enhanced second-harmonic generation in periodic nanostructures,” *Optics Letters* **41**, 3110–3113 (2016).
- [S4] S. Liu, M. B. Sinclair, S. Saravi, G. A. Keeler, Y. Yang, J. Reno, G. M. Peake, F. Setzpfandt, I. Staude, T. Pertsch, and I. Brener, “Resonantly enhanced second-harmonic generation using III–V semiconductor all-dielectric metasurfaces,” *Nano Letters* **16**, 5426–5432 (2016).
- [S5] S. Saravi, T. Pertsch, and F. Setzpfandt, “Generation of counterpropagating path-entangled photon pairs in a single periodic waveguide,” *Physical Review Letters* **118**, 183603 (2017).
- [S6] S. Saravi, A. N. Poddubny, T. Pertsch, F. Setzpfandt, and A. A. Sukhorukov, “Atom-mediated spontaneous parametric down-conversion in periodic waveguides,” *Optics Letters* **42**, 4724–4727 (2017).
- [S7] F. Löchner, A. N. Fedotova, S. Liu, G. A. Keeler, G. M. Peake, S. Saravi, M. R. Shcherbakov, S. Burger, A. A. Fedyanin, I. Brener, T. Pertsch, F. Setzpfandt, and I. Staude, “Polarization-dependent second harmonic diffraction from resonant GaAs metasurfaces,” *ACS Photonics* **5**, 1786–1793 (2018).

Conference talks

- [S8] S. Saravi, S. Diziain, M. Zilk, F. Setzpfandt, and T. Pertsch, “Phase-matched Second Harmonic Generation in Lithium Niobate Slow Light Photonic Crystal Slab Waveguides,” *CLEO Europe*, Munich, Germany (2015).

- [S9] S. Saravi, F. Setzpfandt, and T. Pertsch, “Counter-propagating factorizable photon pairs in slow light lithium niobate photonic crystal slab waveguides,” 2nd EOS Topical Meeting on Optics at the Nanoscale, Capri, Italy (2015).
- [S10] S. Saravi, R. Quintero-Bermudez, F. Setzpfandt, N. A. Mortensen, and T. Pertsch, “How Useful Is Slow Light in Enhancing Nonlinear Interactions in Lossy Periodic Nanostructures?,” Nonlinear Photonics, Sydney, Australia (2016).
- [S11] S. Saravi, F. Setzpfandt, and T. Pertsch, “Periodic Waveguides for Generation of Engineered Photon-pair States,” Nonlinear Photonics, Sydney, Australia (2016).
- [S12] F. J. F. Löchner, A. Fedotova, S. Liu, S. Saravi, T. Pertsch, I. Brener, F. Setzpfandt, and I. Staude, “Polarization dependence of second-harmonic generation in GaAs metasurfaces,” CLEO Europe, Munich, Germany (2017).
- [S13] S. Saravi, A. N. Poddubny, T. Pertsch, F. Setzpfandt, and A. A. Sukhorukov, “Atom-mediated Spontaneous Parametric Down-conversion Using Evanescent Modes in Nonlinear Periodic Waveguides,” CLEO USA, San Jose, USA (2018).
- [S14] S. Saravi, T. Pertsch, and F. Setzpfandt, “Photonic Crystal Waveguides As Integrated Sources of Counterpropagating Factorizable Photon Pairs,” CLEO USA, San Jose, USA (2018).
- [S15] S. Saravi, A. N. Poddubny, T. Pertsch, F. Setzpfandt, and A. A. Sukhorukov, “Atom-mediated Spontaneous Parametric Down-conversion Using Bandgap Modes in Nonlinear Periodic Waveguides,” Nonlinear Photonics, Zürich, Switzerland (2018).
- [S16] S. Saravi, T. Pertsch, and F. Setzpfandt, “Generation of Spectrally Factorizable Counterpropagating Photon Pairs in Photonic Crystal Waveguides,” Nonlinear Photonics, Zürich, Switzerland (2018).

Conference posters

- [S17] R. Quintero-Bermudez, S. Saravi, F. Setzpfandt, and T. Pertsch, “Slow-Light Enhanced Second-Harmonic Generation in Periodic Nanobeam Waveguides,” CLEO Europe, Munich, Germany (2015).
- [S18] S. Saravi, R. Quintero-Bermudez, F. Setzpfandt, N. A. Mortensen, and T. Pertsch, “Effect of Loss on Slow-light-enhanced Second Harmonic Generation in Periodic Nanostructures,” CLEO USA, San Jose, USA (2016).
- [S19] S. Saravi, F. Setzpfandt, and T. Pertsch, “Counter-propagating Spatially Entangled Bell-states Generation in Photonic Crystal Waveguides,” CLEO USA, San Jose, USA (2016).

Bibliography

- [1] M. A. Nielsen and I. L. Chuang, *Quantum Computation and Quantum Information* (Cambridge University Press, 2011).
- [2] D. Deutsch, “Quantum theory, the Church–Turing principle and the universal quantum computer,” *Proceedings of the Royal Society of London A: Mathematical, Physical and Engineering Sciences* **400**, 97–117 (1985).
- [3] P. W. Shor, “Algorithms for quantum computation: discrete logarithms and factoring,” in “Proceedings of the 35th Annual Symposium on Foundations of Computer Science,” (IEEE, 1994), pp. 124–134.
- [4] C. H. Bennett and G. Brassard, “Quantum cryptography: Public key distribution and coin tossing,” in “Proceedings of the International Conference on Computers, Systems and Signal Processing,” (1984), p. 175–179.
- [5] C. H. Bennett and S. J. Wiesner, “Communication via one-and two-particle operators on Einstein-Podolsky-Rosen states,” *Physical Review Letters* **69**, 2881–2884 (1992).
- [6] T. B. Pittman, Y. H. Shih, D. V. Strekalov, and A. V. Sergienko, “Optical imaging by means of two-photon quantum entanglement,” *Physical Review A* **52**, R3429–R3432 (1995).
- [7] D. S. Simon, G. Jaeger, and A. V. Sergienko, *Quantum Metrology, Imaging, and Communication* (Springer, 2017).
- [8] I. Bloch, J. Dalibard, and S. Nascimbene, “Quantum simulations with ultracold quantum gases,” *Nature Physics* **8**, 267–276 (2012).
- [9] A. Reiserer and G. Rempe, “Cavity-based quantum networks with single atoms and optical photons,” *Reviews of Modern Physics* **87**, 1379–1418 (2015).
- [10] R. Blatt and C. F. Roos, “Quantum simulations with trapped ions,” *Nature Physics* **8**, 277–284 (2012).
- [11] A. A. Houck, H. E. Türeci, and J. Koch, “On-chip quantum simulation with superconducting circuits,” *Nature Physics* **8**, 292–299 (2012).
- [12] A. Aspuru-Guzik and P. Walther, “Photonic quantum simulators,” *Nature Physics* **8**, 285–291 (2012).

- [13] I. A. Walmsley, “Quantum optics: Science and technology in a new light,” *Science* **348**, 525–530 (2015).
- [14] J. J. L. Morton and B. W. Lovett, “Hybrid solid-state qubits: the powerful role of electron spins,” *Annual Review of Condensed Matter Physics* **2**, 189–212 (2011).
- [15] J. J. Pla, K. Y. Tan, J. P. Dehollain, W. H. Lim, J. J. L. Morton, F. A. Zwanenburg, D. N. Jamieson, A. S. Dzurak, and A. Morello, “High-fidelity readout and control of a nuclear spin qubit in silicon,” *Nature* **496**, 334–338 (2013).
- [16] A. Faraon, A. Majumdar, D. Englund, E. Kim, M. Bajcsy, and J. Vučković, “Integrated quantum optical networks based on quantum dots and photonic crystals,” *New Journal of Physics* **13**, 055025 (2011).
- [17] A. Sipahigil, R. E. Evans, D. D. Sukachev, M. J. Burek, J. Borregaard, M. K. Bhaskar, C. T. Nguyen, J. L. Pacheco, H. A. Atikian, C. Meuwly, R. M. Camacho, F. Jelezko, E. Bielejec, H. Park, M. Lončar, and M. D. Lukin, “An integrated diamond nanophotonics platform for quantum-optical networks,” *Science* **354**, 847–850 (2016).
- [18] M. Aspelmeyer, T. J. Kippenberg, and F. Marquardt, “Cavity optomechanics,” *Reviews of Modern Physics* **86**, 1391–1452 (2014).
- [19] G. Kurizki, P. Bertet, Y. Kubo, K. Mølmer, D. Petrosyan, P. Rabl, and J. Schmiedmayer, “Quantum technologies with hybrid systems,” *Proceedings of the National Academy of Sciences* **112**, 3866–3873 (2015).
- [20] R. Horodecki, P. Horodecki, M. Horodecki, and K. Horodecki, “Quantum entanglement,” *Reviews of Modern Physics* **81**, 865–942 (2009).
- [21] J. L. O’Brien, A. Furusawa, and J. Vučković, “Photonic quantum technologies,” *Nature Photonics* **3**, 687–695 (2009).
- [22] H.-K. Lo, M. Curty, and K. Tamaki, “Secure quantum key distribution,” *Nature Photonics* **8**, 595–604 (2014).
- [23] M. J. Padgett and R. W. Boyd, “An introduction to ghost imaging: quantum and classical,” *Philosophical Transactions of the Royal Society of London A: Mathematical, Physical and Engineering Sciences* **375**, 20160233 (2017).
- [24] S. Tanzilli, A. Martin, F. Kaiser, M. P. De Micheli, O. Alibart, and D. B. Ostrowsky, “On the genesis and evolution of integrated quantum optics,” *Laser & Photonics Reviews* **6**, 115–143 (2012).
- [25] J. W. Silverstone, D. Bonneau, J. L. O’Brien, and M. G. Thompson, “Silicon quantum photonics,” *IEEE Journal of Selected Topics in Quantum Electronics* **22**, 390–402 (2016).
- [26] A. Orioux and E. Diamanti, “Recent advances on integrated quantum communications,” *Journal of Optics* **18**, 083002 (2016).

- [27] O. Alibart, V. D'Auria, M. De Micheli, F. Doutre, F. Kaiser, L. Labonté, T. Lunghi, É. Picholle, and S. Tanzilli, "Quantum photonics at telecom wavelengths based on lithium niobate waveguides," *Journal of Optics* **18**, 104001 (2016).
- [28] P. Kok, W. J. Munro, K. Nemoto, T. C. Ralph, J. P. Dowling, and G. J. Milburn, "Linear optical quantum computing with photonic qubits," *Reviews of Modern Physics* **79**, 135–174 (2007).
- [29] N. Gisin, G. Ribordy, W. Tittel, and H. Zbinden, "Quantum cryptography," *Reviews of Modern Physics* **74**, 145–195 (2002).
- [30] N. Gisin and R. Thew, "Quantum communication," *Nature Photonics* **1**, 165–171 (2007).
- [31] A. Zeilinger, M. A. Horne, H. Weinfurter, and M. Żukowski, "Three-particle entanglements from two entangled pairs," *Physical Review Letters* **78**, 3031–3034 (1997).
- [32] J.-W. Pan, Z.-B. Chen, C.-Y. Lu, H. Weinfurter, A. Zeilinger, and M. Żukowski, "Multiphoton entanglement and interferometry," *Reviews of Modern Physics* **84**, 777–838 (2012).
- [33] M. D. Eisaman, J. Fan, A. Migdall, and S. V. Polyakov, "Invited review article: Single-photon sources and detectors," *Review of Scientific Instruments* **82**, 071101 (2011).
- [34] L. Caspani, C. Xiong, B. J. Eggleton, D. Bajoni, M. Liscidini, M. Galli, R. Morandotti, and D. J. Moss, "Integrated sources of photon quantum states based on nonlinear optics," *Light: Science & Applications* **6**, e17100 (2017).
- [35] B. Lounis and M. Orrit, "Single-photon sources," *Reports on Progress in Physics* **68**, 1129–1179 (2005).
- [36] A. Kuhn, M. Hennrich, and G. Rempe, "Deterministic single-photon source for distributed quantum networking," *Physical Review Letters* **89**, 067901 (2002).
- [37] I. Aharonovich, D. Englund, and M. Toth, "Solid-state single-photon emitters," *Nature Photonics* **10**, 631–641 (2016).
- [38] M. Müller, S. Bounouar, K. D. Jöns, M. Glässl, and P. Michler, "On-demand generation of indistinguishable polarization-entangled photon pairs," *Nature Photonics* **8**, 224–228 (2014).
- [39] X. Ding, Y. He, Z.-C. Duan, N. Gregersen, M.-C. Chen, S. Unsleber, S. Maier, C. Schneider, M. Kamp, S. Höfling, C.-Y. Lu, and J.-W. Pan, "On-demand single photons with high extraction efficiency and near-unity indistinguishability from a resonantly driven quantum dot in a micropillar," *Physical Review Letters* **116**, 020401 (2016).
- [40] P. Lodahl, S. Mahmoodian, and S. Stobbe, "Interfacing single photons and single quantum dots with photonic nanostructures," *Reviews of Modern Physics* **87**, 347–400 (2015).
- [41] V. S. C. Manga Rao and S. Hughes, "Single quantum-dot purcell factor and β factor in a photonic crystal waveguide," *Physical Review B* **75**, 205437 (2007).

- [42] S. Noda, M. Fujita, and T. Asano, “Spontaneous-emission control by photonic crystals and nanocavities,” *Nature Photonics* **1**, 449–458 (2007).
- [43] V. Loo, L. Lanco, A. Lemaître, I. Sagnes, O. Krebs, P. Voisin, and P. Senellart, “Quantum dot-cavity strong-coupling regime measured through coherent reflection spectroscopy in a very high-q micropillar,” *Applied Physics Letters* **97**, 241110 (2010).
- [44] R. Ohta, Y. Ota, M. Nomura, N. Kumagai, S. Ishida, S. Iwamoto, and Y. Arakawa, “Strong coupling between a photonic crystal nanobeam cavity and a single quantum dot,” *Applied Physics Letters* **98**, 173104 (2011).
- [45] R. B. Patel, A. J. Bennett, I. Farrer, C. A. Nicoll, D. A. Ritchie, and A. J. Shields, “Two-photon interference of the emission from electrically tunable remote quantum dots,” *Nature Photonics* **4**, 632–635 (2010).
- [46] A. Sipahigil, K. D. Jahnke, L. J. Rogers, T. Teraji, J. Isoya, A. S. Zibrov, F. Jelezko, and M. D. Lukin, “Indistinguishable photons from separated silicon-vacancy centers in diamond,” *Physical Review Letters* **113**, 113602 (2014).
- [47] D. C. Burnham and D. L. Weinberg, “Observation of simultaneity in parametric production of optical photon pairs,” *Physical Review Letters* **25**, 84–87 (1970).
- [48] M. Fiorentino, P. L. Voss, J. E. Sharping, and P. Kumar, “All-fiber photon-pair source for quantum communications,” *IEEE Photonics Technology Letters* **14**, 983–985 (2002).
- [49] P. G. Kwiat, K. Mattle, H. Weinfurter, A. Zeilinger, A. V. Sergienko, and Y. Shih, “New high-intensity source of polarization-entangled photon pairs,” *Physical Review Letters* **75**, 4337–4341 (1995).
- [50] P. J. Mosley, J. S. Lundeen, B. J. Smith, P. Wasylczyk, A. B. U’Ren, C. Silberhorn, and I. A. Walmsley, “Heralded generation of ultrafast single photons in pure quantum states,” *Physical Review Letters* **100**, 133601 (2008).
- [51] G. J. Mendoza, R. Santagati, J. Munns, E. Hemsley, M. Piekarek, E. Martín-López, G. D. Marshall, D. Bonneau, M. G. Thompson, and J. L. O’Brien, “Active temporal and spatial multiplexing of photons,” *Optica* **3**, 127–132 (2016).
- [52] F. Kaneda, K. Garay-Palmett, A. B. U’Ren, and P. G. Kwiat, “Heralded single-photon source utilizing highly nondegenerate, spectrally factorable spontaneous parametric downconversion,” *Optics Express* **24**, 10733–10747 (2016).
- [53] H. Takesue and K. Inoue, “Generation of polarization-entangled photon pairs and violation of Bell’s inequality using spontaneous four-wave mixing in a fiber loop,” *Physical Review A* **70**, 031802 (2004).
- [54] X. Li, P. L. Voss, J. E. Sharping, and P. Kumar, “Optical-fiber source of polarization-entangled photons in the 1550 nm telecom band,” *Physical Review Letters* **94**, 053601 (2005).

- [55] A. S. Clark, M. J. Collins, A. C. Judge, E. C. Mägi, C. Xiong, and B. J. Eggleton, “Raman scattering effects on correlated photon-pair generation in chalcogenide,” *Optics Express* **20**, 16807–16814 (2012).
- [56] M. Fiorentino, S. M. Spillane, R. G. Beausoleil, T. D. Roberts, P. Battle, and M. W. Munro, “Spontaneous parametric down-conversion in periodically poled KTP waveguides and bulk crystals,” *Optics Express* **15**, 7479–7488 (2007).
- [57] S. M. Spillane, M. Fiorentino, and R. G. Beausoleil, “Spontaneous parametric down conversion in a nanophotonic waveguide,” *Optics Express* **15**, 8770–8780 (2007).
- [58] R. W. Boyd, *Nonlinear Optics, Third Edition* (Academic Press, 2008).
- [59] A. Martin, A. Issautier, H. Herrmann, W. Sohler, D. B. Ostrowsky, O. Alibart, and S. Tanzilli, “A polarization entangled photon-pair source based on a type-II PPLN waveguide emitting at a telecom wavelength,” *New Journal of Physics* **12**, 103005 (2010).
- [60] F. Kaiser, A. Issautier, L. A. Ngah, O. Dănilă, H. Herrmann, W. Sohler, A. Martin, and S. Tanzilli, “High-quality polarization entanglement state preparation and manipulation in standard telecommunication channels,” *New Journal of Physics* **14**, 085015 (2012).
- [61] N. Matsuda, H. Le Jeannic, H. Fukuda, T. Tsuchizawa, W. J. Munro, K. Shimizu, K. Yamada, Y. Tokura, and H. Takesue, “A monolithically integrated polarization entangled photon pair source on a silicon chip,” *Scientific Reports* **2** (2012).
- [62] L. Orlslager, J. Safioui, S. Clemmen, K. P. Huy, W. Bogaerts, R. Baets, P. Emplit, and S. Massar, “Silicon-on-insulator integrated source of polarization-entangled photons,” *Optics Letters* **38**, 1960–1962 (2013).
- [63] K. Thyagarajan, J. Lugani, S. Ghosh, K. Sinha, A. Martin, D. B. Ostrowsky, O. Alibart, and S. Tanzilli, “Generation of polarization-entangled photons using type-II doubly periodically poled lithium niobate waveguides,” *Physical Review A* **80**, 052321 (2009).
- [64] R. T. Horn, P. Kolenderski, D. Kang, P. Abolghasem, C. Scarcella, A. Della Frera, A. Tosi, L. G. Helt, S. V. Zhukovsky, J. E. Sipe, G. Weihs, A. S. Helmy, and T. Jennewein, “Inherent polarization entanglement generated from a monolithic semiconductor chip,” *Scientific Reports* **3**, 2314 (2013).
- [65] T. Suhara, G. Nakaya, J. Kawashima, and M. Fujimura, “Quasi-phase-matched waveguide devices for generation of postselection-free polarization-entangled twin photons,” *IEEE Photonics Technology Letters* **21**, 1096–1098 (2009).
- [66] A. S. Solntsev and A. A. Sukhorukov, “Path-entangled photon sources on nonlinear chips,” *Reviews in Physics* **2**, 19–31 (2017).
- [67] H. Jin, F. M. Liu, P. Xu, J. L. Xia, M. L. Zhong, Y. Yuan, J. W. Zhou, Y. X. Gong, W. Wang, and S. N. Zhu, “On-chip generation and manipulation of entangled photons based on reconfigurable lithium-niobate waveguide circuits,” *Physical Review Letters* **113**, 103601 (2014).

- [68] J. W. Silverstone, D. Bonneau, K. Ohira, N. Suzuki, H. Yoshida, N. Iizuka, M. Ezaki, C. M. Natarajan, M. G. Tanner, R. H. Hadfield, V. Zwiller, G. D. Marshall, J. G. Rarity, J. L. O'Brien, and M. G. Thompson, "On-chip quantum interference between silicon photon-pair sources," *Nature Photonics* **8**, 104–108 (2014).
- [69] J. B. Spring, B. J. Metcalf, P. C. Humphreys, W. S. Kolthammer, X.-M. Jin, M. Barbieri, A. Datta, N. Thomas-Peter, N. K. Langford, D. Kundys, J. C. Gates, B. J. Smith, P. G. R. Smith, and I. A. Walmsley, "Boson sampling on a photonic chip," *Science* **339**, 798–801 (2013).
- [70] A. S. Solntsev, F. Setzpfandt, A. S. Clark, C. W. Wu, M. J. Collins, C. Xiong, A. Schreiber, F. Katzschmann, F. Eilenberger, R. Schiek, W. Sohler, A. Mitchell, C. Silberhorn, B. J. Eggleton, T. Pertsch, A. A. Sukhorukov, D. N. Neshev, and Y. S. Kivshar, "Generation of nonclassical biphoton states through cascaded quantum walks on a nonlinear chip," *Physical Review X* **4**, 031007 (2014).
- [71] F. Setzpfandt, A. S. Solntsev, J. Titchener, C. W. Wu, C. Xiong, R. Schiek, T. Pertsch, D. N. Neshev, and A. A. Sukhorukov, "Tunable generation of entangled photons in a nonlinear directional coupler," *Laser & Photonics Reviews* **10**, 131–136 (2016).
- [72] A. S. Solntsev, A. A. Sukhorukov, D. N. Neshev, and Y. S. Kivshar, "Spontaneous parametric down-conversion and quantum walks in arrays of quadratic nonlinear waveguides," *Physical Review Letters* **108**, 023601 (2012).
- [73] W. P. Grice, A. B. U'Ren, and I. A. Walmsley, "Eliminating frequency and space-time correlations in multiphoton states," *Physical Review A* **64**, 063815 (2001).
- [74] A. B. U'Ren, K. Banaszek, and I. A. Walmsley, "Photon engineering for quantum information processing," *Quantum Information & Computation* **3**, 480–502 (2003).
- [75] J. Huang and P. Kumar, "Photon-counting statistics of multimode squeezed light," *Physical Review A* **40**, 1670–1673 (1989).
- [76] D. Achilles, C. Silberhorn, and I. A. Walmsley, "Direct, loss-tolerant characterization of nonclassical photon statistics," *Physical Review Letters* **97**, 043602 (2006).
- [77] W. Wasilewski, C. Radzewicz, R. Frankowski, and K. Banaszek, "Statistics of multiphoton events in spontaneous parametric down-conversion," *Physical Review A* **78**, 033831 (2008).
- [78] S. Fasel, O. Alibart, S. Tanzilli, P. Baldi, A. Beveratos, N. Gisin, and H. Zbinden, "High-quality asynchronous heralded single-photon source at telecom wavelength," *New Journal of Physics* **6**, 163 (2004).
- [79] O. Alibart, D. B. Ostrowsky, P. Baldi, and S. Tanzilli, "High-performance guided-wave asynchronous heralded single-photon source," *Optics Letters* **30**, 1539–1541 (2005).
- [80] C. Wagenknecht, C.-M. Li, A. Reingruber, X.-H. Bao, A. Goebel, Y.-A. Chen, Q. Zhang, K. Chen, and J.-W. Pan, "Experimental demonstration of a heralded entanglement source," *Nature Photonics* **4**, 549–552 (2010).

- [81] S. Barz, G. Cronenberg, A. Zeilinger, and P. Walther, “Heralded generation of entangled photon pairs,” *Nature Photonics* **4**, 553–556 (2010).
- [82] P. Aboussouan, O. Alibart, D. B. Ostrowsky, P. Baldi, and S. Tanzilli, “High-visibility two-photon interference at a telecom wavelength using picosecond-regime separated sources,” *Physical Review A* **81**, 021801 (2010).
- [83] E. Meyer-Scott, N. Montaut, J. Tiedau, L. Sansoni, H. Herrmann, T. J. Bartley, and C. Silberhorn, “Limits on the heralding efficiencies and spectral purities of spectrally filtered single photons from photon-pair sources,” *Physical Review A* **95**, 061803 (2017).
- [84] A. L. Migdall, D. Branning, and S. Castelletto, “Tailoring single-photon and multiphoton probabilities of a single-photon on-demand source,” *Physical Review A* **66**, 053805 (2002).
- [85] T. B. Pittman, B. C. Jacobs, and J. D. Franson, “Single photons on pseudodemand from stored parametric down-conversion,” *Physical Review A* **66**, 042303 (2002).
- [86] M. J. Collins, C. Xiong, I. H. Rey, T. D. Vo, J. He, S. Shahnian, C. Reardon, T. F. Krauss, M. J. Steel, A. S. Clark, and B. J. Eggleton, “Integrated spatial multiplexing of heralded single-photon sources,” *Nature Communications* **4**, 2582 (2013).
- [87] T. Meany, L. A. Ngah, M. J. Collins, A. S. Clark, R. J. Williams, B. J. Eggleton, M. J. Steel, M. J. Withford, O. Alibart, and S. Tanzilli, “Hybrid photonic circuit for multiplexed heralded single photons,” *Laser & Photonics Reviews* **8**, L42–L46 (2014).
- [88] C. Xiong, X. Zhang, Z. Liu, M. J. Collins, A. Mahendra, L. G. Helt, M. J. Steel, D.-Y. Choi, C. J. Chae, P. H. W. Leong, and B. J. Eggleton, “Active temporal multiplexing of indistinguishable heralded single photons,” *Nature Communications* **7**, 10853 (2016).
- [89] A. Christ and C. Silberhorn, “Limits on the deterministic creation of pure single-photon states using parametric down-conversion,” *Physical Review A* **85**, 023829 (2012).
- [90] A. Divochiy, F. Marsili, D. Bitauld, A. Gaggero, R. Leoni, F. Mattioli, A. Korneev, V. Seleznev, N. Kaurova, O. Minaeva, G. Gol’Tsmán, K. G. Lagoudakis, M. Benkhaoul, F. Lévy, and A. Fiore, “Superconducting nanowire photon-number-resolving detector at telecommunication wavelengths,” *Nature Photonics* **2**, 302–306 (2008).
- [91] D. Sahin, A. Gaggero, Z. Zhou, S. Jahanmirinejad, F. Mattioli, R. Leoni, J. Beetz, M. Lerner, M. Kamp, S. Höfling, and A. Fiore, “Waveguide photon-number-resolving detectors for quantum photonic integrated circuits,” *Applied Physics Letters* **103**, 111116 (2013).
- [92] <http://www.aureatechnology.com/en/products/twin-photons-source.html> .
- [93] M. F. Saleh, B. E. A. Saleh, and M. C. Teich, “Modal, spectral, and polarization entanglement in guided-wave parametric down-conversion,” *Physical Review A* **79**, 053842 (2009).
- [94] D. Kang, L. G. Helt, S. V. Zhukovsky, J. P. Torres, J. E. Sipe, and A. S. Helmy, “Hyperentangled photon sources in semiconductor waveguides,” *Physical Review A* **89**, 023833 (2014).

- [95] P. G. Kwiat, “Hyper-entangled states,” *Journal of Modern Optics* **44**, 2173–2184 (1997).
- [96] S. Tanzilli, W. Tittel, H. De Riedmatten, H. Zbinden, P. Baldi, M. DeMicheli, D. B. Ostrowsky, and N. Gisin, “PPLN waveguide for quantum communication,” *European Physical Journal D* **18**, 155–160 (2002).
- [97] A. Eckstein, A. Christ, P. J. Mosley, and C. Silberhorn, “Highly efficient single-pass source of pulsed single-mode twin beams of light,” *Physical Review Letters* **106**, 013603 (2011).
- [98] G. Harder, V. Ansari, B. Brecht, T. Dirmeier, C. Marquardt, and C. Silberhorn, “An optimized photon pair source for quantum circuits,” *Optics Express* **21**, 13975–13985 (2013).
- [99] R. Horn, P. Abolghasem, B. J. Bijlani, D. Kang, A. S. Helmy, and G. Weihs, “Monolithic source of photon pairs,” *Physical Review Letters* **108**, 153605 (2012).
- [100] C. Xiong, G. D. Marshall, A. Peruzzo, M. Lobino, A. S. Clark, D.-Y. Choi, S. J. Madden, C. M. Natarajan, M. G. Tanner, R. H. Hadfield, S. N. Dorenbos, T. Zijlstra, V. Zwiller, M. G. Thompson, J. G. Rarity, M. J. Steel, B. Luther-Davies, B. J. Eggleton, and J. L. O’Brien, “Generation of correlated photon pairs in a chalcogenide As₂S₃ waveguide,” *Applied Physics Letters* **98**, 051101 (2011).
- [101] X. Zhang, Y. Zhang, C. Xiong, and B. J. Eggleton, “Correlated photon pair generation in low-loss double-stripe silicon nitride waveguides,” *Journal of Optics* **18**, 074016 (2016).
- [102] V. Pasiskevicius, G. Strömqvist, F. Laurell, and C. Canalias, “Quasi-phase matched nonlinear media: Progress towards nonlinear optical engineering,” *Optical Materials* **34**, 513–523 (2012).
- [103] N. C. Harris, D. Grassani, A. Simbula, M. Pant, M. Galli, T. Baehr-Jones, M. Hochberg, D. Englund, D. Bajoni, and C. Galland, “Integrated source of spectrally filtered correlated photons for large-scale quantum photonic systems,” *Physical Review X* **4**, 041047 (2014).
- [104] T. Meany, M. Gräfe, R. Heilmann, A. Perez-Leija, S. Gross, M. J. Steel, M. J. Withford, and A. Szameit, “Laser written circuits for quantum photonics,” *Laser & Photonics Reviews* **9**, 363–384 (2015).
- [105] R. Schiek, Y. Baek, and G. I. Stegeman, “Second-harmonic generation and cascaded nonlinearity in titanium-indiffused lithium niobate channel waveguides,” *JOSA B* **15**, 2255–2268 (1998).
- [106] J. B. Spring, P. S. Salter, B. J. Metcalf, P. C. Humphreys, M. Moore, N. Thomas-Peter, M. Barbieri, X.-M. Jin, N. K. Langford, W. S. Kolthammer, M. J. Booth, and I. A. Walmsley, “On-chip low loss heralded source of pure single photons,” *Optics Express* **21**, 13522–13532 (2013).
- [107] H. Herrmann, X. Yang, A. Thomas, A. Poppe, W. Sohler, and C. Silberhorn, “Post-selection free, integrated optical source of non-degenerate, polarization entangled photon pairs,” *Optics Express* **21**, 27981–27991 (2013).

- [108] A. Christ, A. Eckstein, P. J. Mosley, and C. Silberhorn, “Pure single photon generation by type-I PDC with backward-wave amplification,” *Optics Express* **17**, 3441–3446 (2009).
- [109] C. Canalias, V. Pasiskevicius, M. Fokine, and F. Laurell, “Backward quasi-phase-matched second-harmonic generation in submicrometer periodically poled flux-grown KTiOPO₄,” *Applied Physics Letters* **86**, 181105 (2005).
- [110] M. C. Booth, M. Atatüre, G. Di Giuseppe, B. E. A. Saleh, A. V. Sergienko, and M. C. Teich, “Counterpropagating entangled photons from a waveguide with periodic nonlinearity,” *Physical Review A* **66**, 023815 (2002).
- [111] A. De Rossi and V. Berger, “Counterpropagating twin photons by parametric fluorescence,” *Physical Review Letters* **88**, 043901 (2002).
- [112] Z. D. Walton, A. V. Sergienko, B. E. A. Saleh, and M. C. Teich, “Generation of polarization-entangled photon pairs with arbitrary joint spectrum,” *Physical Review A* **70**, 052317 (2004).
- [113] L. Lanco, S. Ducci, J.-P. Likforman, X. Marcadet, J. A. W. van Houwelingen, H. Zbinden, G. Leo, and V. Berger, “Semiconductor waveguide source of counterpropagating twin photons,” *Physical Review Letters* **97**, 173901 (2006).
- [114] A. Orieux, A. Eckstein, A. Lemaître, P. Filloux, I. Favero, G. Leo, T. Coudreau, A. Keller, P. Milman, and S. Ducci, “Direct Bell states generation on a III-V semiconductor chip at room temperature,” *Physical Review Letters* **110**, 160502 (2013).
- [115] X. Caillet, V. Berger, G. Leo, and S. Ducci, “A semiconductor source of counterpropagating twin photons: a versatile device allowing the control of the two-photon state,” *Journal of Modern Optics* **56**, 232–239 (2009).
- [116] J. Belhassen, F. Baboux, Q. Yao, M. Amanti, I. Favero, A. Lemaître, W. Kolthammer, I. Walmsey, and S. Ducci, “On-chip III-V monolithic integration of heralded single photon sources and beamsplitters,” *Applied Physics Letters* **112**, 071105 (2018).
- [117] J. Monroy-Ruz, K. Garay-Palmett, and A. B. U’Ren, “Counter-propagating spontaneous four wave mixing: photon-pair factorability and ultra-narrowband single photons,” *New Journal of Physics* **18**, 103026 (2016).
- [118] J. Cardenas, C. B. Poitras, K. Luke, L.-W. Luo, P. A. Morton, and M. Lipson, “High coupling efficiency etched facet tapers in silicon waveguides,” *IEEE Photonics Technology Letters* **26**, 2380–2382 (2014).
- [119] J. Notaros, F. Pavanello, M. T. Wade, C. M. Gentry, A. Atabaki, L. Alloatti, R. J. Ram, and M. A. Popović, “Ultra-efficient cmos fiber-to-chip grating couplers,” in “Optical Fiber Communications Conference and Exhibition (OFC),” (IEEE, 2016), pp. 1–3.
- [120] K. Moutzouris, S. Venugopal Rao, M. Ebrahimzadeh, A. De Rossi, M. Calligaro, V. Ortiz, and V. Berger, “Second-harmonic generation through optimized modal phase matching in semiconductor waveguides,” *Applied Physics Letters* **83**, 620–622 (2003).

- [121] K.-i. Harada, H. Takesue, H. Fukuda, T. Tsuchizawa, T. Watanabe, K. Yamada, Y. Tokura, and S.-i. Itabashi, “Generation of high-purity entangled photon pairs using silicon wire waveguide,” *Optics Express* **16**, 20368–20373 (2008).
- [122] J. Wang, D. Bonneau, M. Villa, J. W. Silverstone, R. Santagati, S. Miki, T. Yamashita, M. Fujiwara, M. Sasaki, H. Terai, M. G. Tanner, C. M. Natarajan, R. H. Hadfield, J. L. O’Brien, and M. G. Thompson, “Chip-to-chip quantum photonic interconnect by path-polarization interconversion,” *Optica* **3**, 407–413 (2016).
- [123] A. Valles, M. Hendrych, J. Svozilík, R. Machulka, P. Abolghasem, D. Kang, B. J. Bijlani, A. S. Helmy, and J. P. Torres, “Generation of polarization-entangled photon pairs in a Bragg reflection waveguide,” *Optics Express* **21**, 10841–10849 (2013).
- [124] D. Kang, M. Kim, H. He, and A. S. Helmy, “Two polarization-entangled sources from the same semiconductor chip,” *Physical Review A* **92**, 013821 (2015).
- [125] J. Svozilík, M. Hendrych, A. S. Helmy, and J. P. Torres, “Generation of paired photons in a quantum separable state in Bragg reflection waveguides,” *Optics Express* **19**, 3115–3123 (2011).
- [126] D. Kang, A. Pang, Y. Zhao, and A. S. Helmy, “Two-photon quantum state engineering in nonlinear photonic nanowires,” *JOSA B* **31**, 1581–1589 (2014).
- [127] J. D. Joannopoulos, S. G. Johnson, J. N. Winn, and R. D. Meade, *Photonic crystals: molding the flow of light* (Princeton university press, 2011).
- [128] J. Li, T. P. White, L. O’Faolain, A. Gomez-Iglesias, and T. F. Krauss, “Systematic design of flat band slow light in photonic crystal waveguides,” *Optics Express* **16**, 6227–6232 (2008).
- [129] T. F. Krauss, “Slow light in photonic crystal waveguides,” *Journal of Physics D: Applied Physics* **40**, 2666 (2007).
- [130] T. Baba, “Slow light in photonic crystals,” *Nature Photonics* **2**, 465–473 (2008).
- [131] M. Soljačić, S. G. Johnson, S. Fan, M. Ibanescu, E. Ippen, and J. D. Joannopoulos, “Photonic-crystal slow-light enhancement of nonlinear phase sensitivity,” *JOSA B* **19**, 2052–2059 (2002).
- [132] C. Monat, M. De Sterke, and B. Eggleton, “Slow light enhanced nonlinear optics in periodic structures,” *Journal of Optics* **12**, 104003 (2010).
- [133] R. Iliew, C. Etrich, T. Pertsch, and F. Lederer, “Slow-light enhanced collinear second-harmonic generation in two-dimensional photonic crystals,” *Physical Review B* **77**, 115124 (2008).
- [134] K. Rivoire, S. Buckley, F. Hatami, and J. Vučković, “Second harmonic generation in GaP photonic crystal waveguides,” *Applied Physics Letters* **98**, 263113 (2011).
- [135] K. Lenglé, L. Bramerie, M. Gay, J.-C. Simon, S. Combrié, G. Lehoucq, and A. De Rossi, “Efficient second harmonic generation in nanophotonic waveguides for optical signal processing,” *Applied Physics Letters* **102**, 151114 (2013).

- [136] B. Corcoran, C. Monat, C. Grillet, D. J. Moss, B. J. Eggleton, T. White, L. O’Faolain, and T. F. Krauss, “Green light emission in silicon through slow-light enhanced third-harmonic generation in photonic-crystal waveguides,” *Nature Photonics* **3**, 206–210 (2009).
- [137] C. Monat, M. Spurny, C. Grillet, L. O’Faolain, T. F. Krauss, B. J. Eggleton, D. Bulla, S. Madden, and B. Luther-Davies, “Third-harmonic generation in slow-light chalcogenide glass photonic crystal waveguides,” *Optics Letters* **36**, 2818–2820 (2011).
- [138] C. Monat, C. Grillet, M. Collins, A. Clark, J. Schroeder, C. Xiong, J. Li, L. O’Faolain, T. F. Krauss, B. J. Eggleton, and D. J. Moss, “Integrated optical auto-correlator based on third-harmonic generation in a silicon photonic crystal waveguide,” *Nature Communications* **5**, 3246 (2014).
- [139] C. Husko, T. D. Vo, B. Corcoran, J. Li, T. F. Krauss, and B. J. Eggleton, “Ultracompact all-optical XOR logic gate in a slow-light silicon photonic crystal waveguide,” *Optics express* **19**, 20681–20690 (2011).
- [140] J. Li, L. O’Faolain, and T. F. Krauss, “Four-wave mixing in slow light photonic crystal waveguides with very high group index,” *Optics Express* **20**, 17474–17479 (2012).
- [141] C. Monat, B. Corcoran, D. Pudo, M. Ebnali-Heidari, C. Grillet, M. D. Pelusi, D. J. Moss, B. J. Eggleton, T. P. White, L. O’Faolain, and T. F. Krauss, “Slow light enhanced nonlinear optics in silicon photonic crystal waveguides,” *IEEE Journal of Selected Topics in Quantum Electronics* **16**, 344–356 (2010).
- [142] K. Suzuki and T. Baba, “Nonlinear light propagation in chalcogenide photonic crystal slow light waveguides,” *Optics Express* **18**, 26675–26685 (2010).
- [143] C.-Y. Lin, X. Wang, S. Chakravarty, B. S. Lee, W. Lai, J. Luo, A. K.-Y. Jen, and R. T. Chen, “Electro-optic polymer infiltrated silicon photonic crystal slot waveguide modulator with 23 dB slow light enhancement,” *Applied Physics Letters* **97**, 093304 (2010).
- [144] A. Yariv and P. Yeh, “Electromagnetic propagation in periodic stratified media. II. Birefringence, phase matching, and x-ray lasers,” *JOSA* **67**, 438–447 (1977).
- [145] R. Iliew, C. Etrich, T. Pertsch, F. Lederer, and Y. S. Kivshar, “Huge enhancement of backward second-harmonic generation with slow light in photonic crystals,” *Physical Review A* **81**, 023820 (2010).
- [146] C. Xiong, C. Monat, A. S. Clark, C. Grillet, G. D. Marshall, M. J. Steel, J. Li, L. O’Faolain, T. F. Krauss, J. G. Rarity, and B. J. Eggleton, “Slow-light enhanced correlated photon pair generation in a silicon photonic crystal waveguide,” *Optics Letters* **36**, 3413–3415 (2011).
- [147] C. Xiong, M. J. Collins, M. J. Steel, T. F. Krauss, B. J. Eggleton, and A. S. Clark, “Photonic crystal waveguide sources of photons for quantum communication applications,” *IEEE Journal of Selected Topics in Quantum Electronics* **21**, 205–214 (2015).

- [148] A. S. Clark, C. Husko, M. J. Collins, G. Lehoucq, S. Xavier, A. De Rossi, S. Combrié, C. Xiong, and B. J. Eggleton, “Heralded single-photon source in a III-V photonic crystal,” *Optics Letters* **38**, 649–651 (2013).
- [149] M. J. A. De Dood, W. T. M. Irvine, and D. Bouwmeester, “Nonlinear photonic crystals as a source of entangled photons,” *Physical Review Letters* **93**, 040504 (2004).
- [150] W. T. M. Irvine, M. J. A. de Dood, and D. Bouwmeester, “Bloch theory of entangled photon generation in nonlinear photonic crystals,” *Physical Review A* **72**, 043815 (2005).
- [151] M. Corona and A. B. U’Ren, “Parametric down-conversion with optimized spectral properties in nonlinear photonic crystals,” *Physical Review A* **76**, 043829 (2007).
- [152] P. Sanchis, P. Bienstman, B. Luysaert, R. Baets, and J. Marti, “Analysis of butt coupling in photonic crystals,” *IEEE Journal of Quantum Electronics* **40**, 541–550 (2004).
- [153] J.-P. Hugonin, P. Lalanne, T. P. White, and T. F. Krauss, “Coupling into slow-mode photonic crystal waveguides,” *Optics Letters* **32**, 2638–2640 (2007).
- [154] C. M. De Sterke, K. B. Dossou, T. P. White, L. C. Botten, and R. C. McPhedran, “Efficient coupling into slow light photonic crystal waveguide without transition region: role of evanescent modes,” *Optics Express* **17**, 17338–17343 (2009).
- [155] H. S. Dutta, A. K. Goyal, V. Srivastava, and S. Pal, “Coupling light in photonic crystal waveguides: A review,” *Photonics and Nanostructures-Fundamentals and Applications* **20**, 41–58 (2016).
- [156] S. Hughes, L. Ramunno, J. F. Young, and J. E. Sipe, “Extrinsic optical scattering loss in photonic crystal waveguides: Role of fabrication disorder and photon group velocity,” *Physical Review Letters* **94**, 033903 (2005).
- [157] L. O’Faolain, T. P. White, D. O’Brien, X. Yuan, M. D. Settle, and T. F. Krauss, “Dependence of extrinsic loss on group velocity in photonic crystal waveguides,” *Optics Express* **15**, 13129–13138 (2007).
- [158] N. Matsuda, H. Takesue, K. Shimizu, Y. Tokura, E. Kuramochi, and M. Notomi, “Slow light enhanced correlated photon pair generation in photonic-crystal coupled-resonator optical waveguides,” *Optics Express* **21**, 8596–8604 (2013).
- [159] S. Azzini, D. Grassani, M. Galli, D. Gerace, M. Patrini, M. Liscidini, P. Velha, and D. Bajoni, “Stimulated and spontaneous four-wave mixing in silicon-on-insulator coupled photonic wire nano-cavities,” *Applied Physics Letters* **103**, 031117 (2013).
- [160] S. Azzini, D. Grassani, M. J. Strain, M. Sorel, L. G. Helt, J. E. Sipe, M. Liscidini, M. Galli, and D. Bajoni, “Ultra-low power generation of twin photons in a compact silicon ring resonator,” *Optics Express* **20**, 23100–23107 (2012).

- [161] E. Engin, D. Bonneau, C. M. Natarajan, A. S. Clark, M. G. Tanner, R. H. Hadfield, S. N. Dorenbos, V. Zwiller, K. Ohira, N. Suzuki, H. Yoshida, N. Iizuka, M. Ezaki, J. L. O'Brien, and M. G. Thompson, "Photon pair generation in a silicon micro-ring resonator with reverse bias enhancement," *Optics Express* **21**, 27826–27834 (2013).
- [162] S. Rogers, X. Lu, W. C. Jiang, and Q. Lin, "Twin photon pairs in a high-Q silicon microresonator," *Applied Physics Letters* **107**, 041102 (2015).
- [163] X. Lu, W. C. Jiang, J. Zhang, and Q. Lin, "Biphoton statistics of quantum light generated on a silicon chip," *ACS Photonics* **3**, 1626–1636 (2016).
- [164] K.-H. Luo, H. Herrmann, S. Krapick, B. Brecht, R. Ricken, V. Quiring, H. Suche, W. Sohler, and C. Silberhorn, "Direct generation of genuine single-longitudinal-mode narrowband photon pairs," *New Journal of Physics* **17**, 073039 (2015).
- [165] C. Reimer, L. Caspani, M. Clerici, M. Ferrera, M. Kues, M. Peccianti, A. Pasquazi, L. Razzari, B. E. Little, S. T. Chu, D. J. Moss, and R. Morandotti, "Integrated frequency comb source of heralded single photons," *Optics Express* **22**, 6535–6546 (2014).
- [166] F. Bussi eres, N. Sangouard, M. Afzelius, H. de Riedmatten, C. Simon, and W. Tittel, "Prospective applications of optical quantum memories," *Journal of Modern Optics* **60**, 1519–1537 (2013).
- [167] S. Ramelow, L. Ratschbacher, A. Fedrizzi, N. K. Langford, and A. Zeilinger, "Discrete tunable color entanglement," *Physical Review Letters* **103**, 253601 (2009).
- [168] D. Cruz-Delgado, R. Ramirez-Alarcon, E. Ortiz-Ricardo, J. Monroy-Ruz, F. Dominguez-Serna, H. Cruz-Ramirez, K. Garay-Palmett, and A. B. U'Ren, "Fiber-based photon-pair source capable of hybrid entanglement in frequency and transverse mode, controllably scalable to higher dimensions," *Scientific Reports* **6**, 27377 (2016).
- [169] K. Busch, G. Von Freymann, S. Linden, S. Mingaleev, L. Tkeshelashvili, and M. Wegener, "Periodic nanostructures for photonics," *Physics Reports* **444**, 101–202 (2007).
- [170] H. Takesue, N. Matsuda, E. Kuramochi, W. J. Munro, and M. Notomi, "An on-chip coupled resonator optical waveguide single-photon buffer," *Nature Communications* **4**, 2725 (2013).
- [171] P. J. Shadbolt, M. R. Verde, A. Peruzzo, A. Politi, A. Laing, M. Lobino, J. C. Matthews, M. G. Thompson, and J. L. O'Brien, "Generating, manipulating and measuring entanglement and mixture with a reconfigurable photonic circuit," *Nature Photonics* **6**, 45–49 (2012).
- [172] R. S. Weis and T. K. Gaylord, "Lithium niobate: summary of physical properties and crystal structure," *Applied Physics A* **37**, 191–203 (1985).
- [173] L. Arizmendi, "Photonic applications of lithium niobate crystals," *physica status solidi (a)* **201**, 253–283 (2004).

- [174] E. L. Wooten, K. M. Kissa, A. Yi-Yan, E. J. Murphy, D. A. Lafaw, P. F. Hallemeier, D. Maack, D. V. Attanasio, D. J. Fritz, G. J. McBrien, and D. E. Bossi, "A review of lithium niobate modulators for fiber-optic communications systems," *IEEE Journal of Selected Topics in Quantum Electronics* **6**, 69–82 (2000).
- [175] K. R. Parameswaran, R. K. Route, J. R. Kurz, R. V. Roussev, M. M. Fejer, and M. Fujimura, "Highly efficient second-harmonic generation in buried waveguides formed by annealed and reverse proton exchange in periodically poled lithium niobate," *Optics Letters* **27**, 179–181 (2002).
- [176] F. Lacour, N. Courjal, M.-P. Bernal, A. Sabac, C. Bainier, and M. Spajer, "Nanostructuring lithium niobate substrates by focused ion beam milling," *Optical Materials* **27**, 1421–1425 (2005).
- [177] H. Hartung, R. Geiss, T. Gischkat, F. Schrepel, R. Iliew, T. Pertsch, F. Lederer, W. Wesch, E.-B. Kley, and A. Tünnermann, "Photonic crystals in lithium niobate by ion-beam enhanced etching," in "IEEE/LEOS Winter Topicals Meeting Series, 2009," (IEEE, 2009), pp. 64–65.
- [178] H. Hartung, E.-B. Kley, T. Gischkat, F. Schrepel, W. Wesch, and A. Tünnermann, "Ultra thin high index contrast photonic crystal slabs in lithium niobate," *Optical Materials* **33**, 19–21 (2010).
- [179] R. Geiss, S. Diziain, M. Steinert, F. Schrepel, E.-B. Kley, A. Tünnermann, and T. Pertsch, "Photonic crystals in lithium niobate by combining focussed ion beam writing and ion-beam enhanced etching," *physica status solidi (a)* **211**, 2421–2425 (2014).
- [180] P. Rabiei and P. Gunter, "Optical and electro-optical properties of submicrometer lithium niobate slab waveguides prepared by crystal ion slicing and wafer bonding," *Applied Physics Letters* **85**, 4603–4605 (2004).
- [181] A. Guarino, G. Poberaj, D. Rezzonico, R. Degl'Innocenti, and P. Günter, "Electro-optically tunable microring resonators in lithium niobate," *Nature Photonics* **1**, 407–410 (2007).
- [182] H. Hu, R. Ricken, and W. Sohler, "Lithium niobate photonic wires," *Optics Express* **17**, 24261–24268 (2009).
- [183] H. Lu, B. Sadani, N. Courjal, G. Ulliac, N. Smith, V. Stenger, M. Collet, F. Baida, and M.-P. Bernal, "Enhanced electro-optical lithium niobate photonic crystal wire waveguide on a smart-cut thin film," *Optics Express* **20**, 2974–2981 (2012).
- [184] R. Geiss, S. Diziain, R. Iliew, C. Etrich, H. Hartung, N. Janunts, F. Schrepel, F. Lederer, T. Pertsch, and E.-B. Kley, "Light propagation in a free-standing lithium niobate photonic crystal waveguide," *Applied Physics Letters* **97**, 131109 (2010).
- [185] S. Diziain, R. Geiss, M. Zilk, F. Schrepel, E.-B. Kley, A. Tünnermann, and T. Pertsch, "Mode analysis of photonic crystal L3 cavities in self-suspended lithium niobate membranes," *Applied Physics Letters* **103**, 251101 (2013).

- [186] S. Diziain, R. Geiss, M. Zilk, F. Schrepel, E.-B. Kley, A. Tünnermann, and T. Pertsch, “Second harmonic generation in free-standing lithium niobate photonic crystal L3 cavity,” *Applied Physics Letters* **103**, 051117 (2013).
- [187] www.nanoln.com .
- [188] G. Poberaj, H. Hu, W. Sohler, and P. Guenter, “Lithium niobate on insulator (LNOI) for microphotonic devices,” *Laser & Photonics Reviews* **6**, 488–503 (2012).
- [189] R. Luo, H. Jiang, S. Rogers, H. Liang, Y. He, and Q. Lin, “On-chip second-harmonic generation and broadband parametric down-conversion in a lithium niobate microresonator,” *Optics Express* **25**, 24531–24539 (2017).
- [190] H. Liang, R. Luo, Y. He, H. Jiang, and Q. Lin, “High-quality lithium niobate photonic crystal nanocavities,” *Optica* **4**, 1251–1258 (2017).
- [191] C. Wang, M. Zhang, B. Stern, M. Lipson, and M. Lončar, “Nanophotonic lithium niobate electro-optic modulators,” *Optics Express* **26**, 1547–1555 (2018).
- [192] C. Wang, X. Xiong, N. Andrade, V. Venkataraman, X.-F. Ren, G.-C. Guo, and M. Lončar, “Second harmonic generation in nano-structured thin-film lithium niobate waveguides,” *Optics Express* **25**, 6963–6973 (2017).
- [193] L. G. Helt and M. J. Steel, “Effect of scattering loss on connections between classical and quantum processes in second-order nonlinear waveguides,” *Optics Letters* **40**, 1460–1463 (2015).
- [194] A. N. Poddubny, I. V. Iorsh, and A. A. Sukhorukov, “Generation of photon-plasmon quantum states in nonlinear hyperbolic metamaterials,” *Physical Review Letters* **117**, 123901 (2016).
- [195] A. Solntsev, L. Carletti, L. Xu, A. Poddubny, C. De Angelis, G. Leo, Y. Kivshar, D. N. Neshev, and A. A. Sukhorukov, “Quantum-classical correspondence for photon-pair generation in nonlinear dielectric nano-resonators,” in “Nonlinear Photonics,” (2016), pp. NT3A–4.
- [196] F. Lenzini, A. N. Poddubny, J. Titchener, P. Fisher, A. Boes, S. Kasture, B. Haylock, M. Villa, A. Mitchell, A. S. Solntsev, A. A. Sukhorukov, and M. Lobino, “Direct characterization of a nonlinear photonic circuit’s wave function with laser light,” *Light: Science & Applications* **7**, 17143 (2018).
- [197] A. W. Snyder and J. D. Love, *Optical Waveguide Theory* (Chapman and Hall, 1983).
- [198] C. Sauvan, J. P. Hugonin, I. S. Maksymov, and P. Lalanne, “Theory of the spontaneous optical emission of nanosize photonic and plasmon resonators,” *Physical Review Letters* **110**, 237401 (2013).
- [199] C. Sauvan, J.-P. Hugonin, R. Carminati, and P. Lalanne, “Modal representation of spatial coherence in dissipative and resonant photonic systems,” *Physical Review A* **89**, 043825 (2014).

- [200] P. Y. Chen, R. C. McPhedran, C. M. de Sterke, C. G. Poulton, A. A. Asatryan, L. C. Botten, and M. J. Steel, “Group velocity in lossy periodic structured media,” *Physical Review A* **82**, 053825 (2010).
- [201] D. E. Zelmon, D. L. Small, and D. Jundt, “Infrared corrected Sellmeier coefficients for congruently grown lithium niobate and 5 mol.% magnesium oxide-doped lithium niobate,” *JOSA B* **14**, 3319–3322 (1997).
- [202] R. Schiek and T. Pertsch, “Absolute measurement of the quadratic nonlinear susceptibility of lithium niobate in waveguides,” *Optical Materials Express* **2**, 126–139 (2012).
- [203] R. S. Klein, G. E. Kugel, A. Maillard, K. Polgár, and A. Péter, “Absolute non-linear optical coefficients of LiNbO₃ for near stoichiometric crystal compositions,” *Optical Materials* **22**, 171–174 (2003).
- [204] D. Duchesne, K. A. Rutkowska, M. Volatier, F. Légaré, S. Delprat, M. Chaker, D. Modotto, A. Locatelli, C. De Angelis, M. Sorel, D. N. Christodoulides, G. Salamo, R. Arès, V. Aimez, and R. Morandotti, “Second harmonic generation in AlGaAs photonic wires using low power continuous wave light,” *Optics Express* **19**, 12408–12417 (2011).
- [205] RF Module User’s Guide, version 4.3a, COMSOL, Inc, www.comsol.com .
- [206] A. M. Zheltikov, “Limiting efficiencies of second-harmonic generation and cascaded $\chi^{(2)}$ processes in quadratically nonlinear photonic nanowires,” *Optics Communications* **270**, 402–406 (2007).
- [207] C. Monat, C. Grillet, B. Corcoran, D. J. Moss, B. J. Eggleton, T. P. White, and T. F. Krauss, “Investigation of phase matching for third-harmonic generation in silicon slow light photonic crystal waveguides using Fourier optics,” *Optics Express* **18**, 6831–6840 (2010).
- [208] A. Cowan and J. F. Young, “Mode matching for second-harmonic generation in photonic crystal waveguides,” *Physical Review B* **65**, 085106 (2002).
- [209] A. R. Cowan and J. F. Young, “Nonlinear optics in high refractive index contrast periodic structures,” *Semiconductor Science and Technology* **20**, R41–R56 (2005).
- [210] Q. Rolland, S. Dupont, J. Gazalet, J.-C. Kastelik, Y. Pennec, B. Djafari-Rouhani, and V. Laude, “Simultaneous bandgaps in LiNbO₃ photonic crystal slab,” *Optics Express* **22**, 16288–16297 (2014).
- [211] L. H. Frandsen, A. V. Lavrinenko, J. Fage-Pedersen, and P. I. Borel, “Photonic crystal waveguides with semi-slow light and tailored dispersion properties,” *Optics Express* **14**, 9444–9450 (2006).
- [212] J. Liang, L. Y. Ren, M. J. Yun, X. Han, and X. J. Wang, “Wideband ultraflat slow light with large group index in a W1 photonic crystal waveguide,” *Journal of Applied Physics* **110**, 063103 (2011).

- [213] F. Wang, J. S. Jensen, and O. Sigmund, “High-performance slow light photonic crystal waveguides with topology optimized or circular-hole based material layouts,” *Photonics and Nanostructures-Fundamentals and Applications* **10**, 378–388 (2012).
- [214] K. Cui, Y. Huang, G. Zhang, Y. Li, X. Tang, X. Mao, Q. Zhao, W. Zhang, and J. Peng, “Temperature dependence of minitop band in double-slots photonic crystal waveguides,” *Applied Physics Letters* **95**, 191901 (2009).
- [215] N. Gutman, W. H. Dupree, Y. Sun, A. A. Sukhorukov, and C. M. de Sterke, “Frozen and broadband slow light in coupled periodic nanowire waveguides,” *Optics Express* **20**, 3519–3528 (2012).
- [216] C. Canalias and V. Pasiskevicius, “Mirrorless optical parametric oscillator,” *Nature Photonics* **1**, 459–462 (2007).
- [217] M. Conforti, C. De Angelis, U. K. Sapaev, and G. Assanto, “Pulse shaping via backward second harmonic generation,” *Optics Express* **16**, 2115–2121 (2008).
- [218] M. Conforti, A. Locatelli, C. De Angelis, A. Parini, G. Bellanca, and S. Trillo, “Self-pulsing instabilities in backward parametric wave mixing,” *JOSA B* **22**, 2178–2184 (2005).
- [219] D. Michaelis, U. Peschel, C. Wächter, and A. Bräuer, “Reciprocity theorem and perturbation theory for photonic crystal waveguides,” *Physical Review E* **68**, 065601 (2003).
- [220] M. Santagiustina, C. G. Someda, G. Vadala, S. Combrie, and A. De Rossi, “Theory of slow light enhanced four-wave mixing in photonic crystal waveguides,” *Optics Express* **18**, 21024–21029 (2010).
- [221] G. Lecamp, J.-P. Hugonin, and P. Lalanne, “Theoretical and computational concepts for periodic optical waveguides,” *Optics Express* **15**, 11042–11060 (2007).
- [222] A. A. Sukhorukov, A. S. Solntsev, S. S. Kruk, D. N. Neshev, and Y. S. Kivshar, “Nonlinear coupled-mode theory for periodic plasmonic waveguides and metamaterials with loss and gain,” *Optics Letters* **39**, 462–465 (2014).
- [223] A. E. Siegman, “Orthogonality properties of optical resonator eigenmodes,” *Optics Communications* **31**, 369–373 (1979).
- [224] L. C. Botten, M. S. Craig, R. C. McPhedran, J. L. Adams, and J. R. Andrewartha, “The finitely conducting lamellar diffraction grating,” *Optica Acta: International Journal of Optics* **28**, 1087–1102 (1981).
- [225] C. Wolff, K. Busch, and N. A. Mortensen, “Modal expansions in periodic photonic systems with material loss and dispersion,” *Physical Review B* **97**, 104203 (2018).
- [226] Z. Ruan, G. Veronis, K. L. Vodopyanov, M. M. Fejer, and S. Fan, “Enhancement of optics-to-THz conversion efficiency by metallic slot waveguides,” *Optics Express* **17**, 13502–13515 (2009).

- [227] C. De Angelis, G. Nalesso, D. Modotto, M. Midrio, A. Locatelli, and J. S. Aitchison, “Multiple-scale coupled-mode theory for second-harmonic generation in one-dimensional periodic structures,” *JOSA B* **20**, 1853–1865 (2003).
- [228] L. Tkeshelashvili and K. Busch, “Nonlinear three-wave interaction in photonic crystals,” *Applied Physics B* **81**, 225–229 (2005).
- [229] P. T. Leung, S. Y. Liu, and K. Young, “Completeness and time-independent perturbation of the quasinormal modes of an absorptive and leaky cavity,” *Physical Review A* **49**, 3982–3989 (1994).
- [230] A. E. Siegman, “Eigenmodes in nonnormal optical systems,” in “Wave-Optical Systems Engineering,” (vol. 4436 of SPIE Conference Series, 2001), pp. 1–15.
- [231] C. De Angelis, F. Gringoli, M. Midrio, D. Modotto, J. Aitchison, and G. Nalesso, “Conversion efficiency for second-harmonic generation in photonic crystals,” *JOSA B* **18**, 348–351 (2001).
- [232] M. Liscidini, A. Locatelli, L. C. Andreani, and C. De Angelis, “Maximum-exponent scaling behavior of optical second-harmonic generation in finite multilayer photonic crystals,” *Physical Review Letters* **99**, 053907 (2007).
- [233] F. Schreppe, T. Gischkat, H. Hartung, E.-B. Kley, and W. Wesch, “Ion beam enhanced etching of LiNbO₃,” *Nuclear Instruments and Methods in Physics Research Section B: Beam Interactions with Materials and Atoms* **250**, 164–168 (2006).
- [234] R. Regener and W. Sohler, “Loss in low-finesse Ti: LiNbO₃ optical waveguide resonators,” *Applied Physics B: Lasers and Optics* **36**, 143–147 (1985).
- [235] P. T. Kristensen, C. Van Vlack, and S. Hughes, “Generalized effective mode volume for leaky optical cavities,” *Optics Letters* **37**, 1649–1651 (2012).
- [236] J. R. de Lasson, P. T. Kristensen, J. Mørk, and N. Gregersen, “Roundtrip matrix method for calculating the leaky resonant modes of open nanophotonic structures,” *JOSA A* **31**, 2142–2151 (2014).
- [237] P. T. Kristensen, J. R. de Lasson, and N. Gregersen, “Calculation, normalization, and perturbation of quasinormal modes in coupled cavity-waveguide systems,” *Optics Letters* **39**, 6359–6362 (2014).
- [238] R. A. Sammut and A. W. Snyder, “Leaky modes on a dielectric waveguide: orthogonality and excitation,” *Applied Optics* **15**, 1040–1044 (1976).
- [239] J. G. Pedersen, S. Xiao, and N. A. Mortensen, “Limits of slow light in photonic crystals,” *Physical Review B* **78**, 153101 (2008).
- [240] J. Grgić, J. G. Pedersen, S. Xiao, and N. A. Mortensen, “Group index limitations in slow-light photonic crystals,” *Photonics and Nanostructures-Fundamentals and Applications* **8**, 56–61 (2010).

- [241] T. P. White and A. A. Sukhorukov, “Transition from slow and frozen to superluminal and backward light through loss or gain in dispersion-engineered waveguides,” *Physical Review A* **85**, 043819 (2012).
- [242] N. Gutman, C. M. de Sterke, A. A. Sukhorukov, and L. C. Botten, “Slow and frozen light in optical waveguides with multiple gratings: Degenerate band edges and stationary inflection points,” *Physical Review A* **85**, 033804 (2012).
- [243] M. Patterson, S. Hughes, S. Schulz, D. M. Beggs, T. P. White, L. O’Faolain, and T. F. Krauss, “Disorder-induced incoherent scattering losses in photonic crystal waveguides: Bloch mode reshaping, multiple scattering, and breakdown of the Beer-Lambert law,” *Physical Review B* **80**, 195305 (2009).
- [244] Z. Yang, M. Liscidini, and J. E. Sipe, “Spontaneous parametric down-conversion in waveguides: a backward heisenberg picture approach,” *Physical Review A* **77**, 033808 (2008).
- [245] J. E. Sipe, N. A. R. Bhat, P. Chak, and S. Pereira, “Effective field theory for the nonlinear optical properties of photonic crystals,” *Physical Review E* **69**, 016604 (2004).
- [246] J. Garrison and R. Chiao, *Quantum optics* (Oxford University Press, 2008).
- [247] C. K. Law, I. A. Walmsley, and J. H. Eberly, “Continuous frequency entanglement: effective finite Hilbert space and entropy control,” *Physical Review Letters* **84**, 5304–5307 (2000).
- [248] X. Caillet, A. Orioux, A. Lemaître, P. Filloux, I. Favero, G. Leo, and S. Ducci, “Two-photon interference with a semiconductor integrated source at room temperature,” *Optics Express* **18**, 9967–9975 (2010).
- [249] A. G. White, D. F. V. James, P. H. Eberhard, and P. G. Kwiat, “Nonmaximally entangled states: Production, characterization, and utilization,” *Physical Review Letters* **83**, 3103–3107 (1999).
- [250] C. M. Caves and D. D. Crouch, “Quantum wideband traveling-wave analysis of a degenerate parametric amplifier,” *JOSA B* **4**, 1535–1545 (1987).
- [251] D. A. Antonosyan, A. S. Solntsev, and A. A. Sukhorukov, “Effect of loss on photon-pair generation in nonlinear waveguide arrays,” *Physical Review A* **90**, 043845 (2014).
- [252] L. G. Helt, M. J. Steel, and J. E. Sipe, “Spontaneous parametric downconversion in waveguides: what’s loss got to do with it?” *New Journal of Physics* **17**, 013055 (2015).
- [253] A. Siegman, “Lasers without photons—or should it be lasers with too many photons?” *Applied Physics B* **60**, 247–257 (1995).
- [254] A. Judge, J. Brownless, N. Bhat, J. Sipe, M. Steel, and C. M. de Sterke, “Effective photons in weakly absorptive dielectric media and the beer–lambert–bouguer law,” *New Journal of Physics* **16**, 043028 (2014).

- [255] T. Gruner and D.-G. Welsch, “Green-function approach to the radiation-field quantization for homogeneous and inhomogeneous Kramers-Kronig dielectrics,” *Physical Review A* **53**, 1818–1829 (1996).
- [256] H. T. Dung, L. Knöll, and D.-G. Welsch, “Three-dimensional quantization of the electromagnetic field in dispersive and absorbing inhomogeneous dielectrics,” *Physical Review A* **57**, 3931 (1998).
- [257] S. Scheel, L. Knöll, and D.-G. Welsch, “QED commutation relations for inhomogeneous Kramers-Kronig dielectrics,” *Physical Review A* **58**, 700 (1998).
- [258] H. T. Dung, L. Knöll, and D.-G. Welsch, “Intermolecular energy transfer in the presence of dispersing and absorbing media,” *Physical Review A* **65**, 043813 (2002).
- [259] W. Vogel and D.-G. Welsch, *Quantum optics* (John Wiley & Sons, 2006).
- [260] L. Knöll, S. Scheel, and D.-G. Welsch, “QED in dispersing and absorbing media,” in “Coherence and Statistics of Photons and Atoms,” (edited by J. Peřina (Wiley, New York, 2001), p. 1.).
- [261] N. Vats, S. John, and K. Busch, “Theory of fluorescence in photonic crystals,” *Physical Review A* **65**, 043808 (2002).
- [262] A. Goban, C.-L. Hung, S.-P. Yu, J. D. Hood, J. A. Muniz, J. H. Lee, M. J. Martin, A. C. McClung, K. S. Choi, D. E. Chang, O. Painter, and H. J. Kimble, “Atom-light interactions in photonic crystals,” *Nature Communications* **5**, 3808 (2014).
- [263] J. S. Douglas, H. Habibian, C.-L. Hung, A. V. Gorshkov, H. J. Kimble, and D. E. Chang, “Quantum many-body models with cold atoms coupled to photonic crystals,” *Nature Photonics* **9**, 326–331 (2015).
- [264] A. Asenjo-Garcia, J. D. Hood, D. E. Chang, and H. J. Kimble, “Atom-light interactions in quasi-one-dimensional nanostructures: A Green’s-function perspective,” *Physical Review A* **95**, 033818 (2017).
- [265] R. C. McPhedran, L. C. Botten, J. McOrist, A. A. Asatryan, C. M. de Sterke, and N. A. Nicorovici, “Density of states functions for photonic crystals,” *Physical Review E* **69**, 016609 (2004).
- [266] S. John and J. Wang, “Quantum electrodynamics near a photonic band gap: Photon bound states and dressed atoms,” *Physical Review Letters* **64**, 2418–2421 (1990).
- [267] A. Yariv and P. Yeh, *Optical waves in crystals* (Wiley, New York, 1984).
- [268] S. Combrié, E. Weidner, A. DeRossi, S. Bansropun, S. Cassette, A. Talneau, and H. Benisty, “Detailed analysis by Fabry-Perot method of slab photonic crystal line-defect waveguides and cavities in aluminium-free material system,” *Optics Express* **14**, 7353–7361 (2006).

- [269] A. Asatryan, K. Busch, R. McPhedran, L. Botten, C. M. de Sterke, and N. Nicorovici, “Two-dimensional Green’s function and local density of states in photonic crystals consisting of a finite number of cylinders of infinite length,” *Physical Review E* **63**, 046612 (2001).
- [270] E. Yeganegi, A. Lagendijk, A. P. Mosk, and W. L. Vos, “Local density of optical states in the band gap of a finite one-dimensional photonic crystal,” *Physical Review B* **89**, 045123 (2014).
- [271] C. W. Wu, A. S. Solntsev, D. N. Neshev, and A. A. Sukhorukov, “Photon pair generation and pump filtering in nonlinear adiabatic waveguiding structures,” *Optics Letters* **39**, 953–956 (2014).
- [272] H. J. Kimble, “The quantum internet,” *Nature* **453**, 1023–1030 (2008).
- [273] J. Nunn, N. K. Langford, W. S. Kolthammer, T. F. M. Champion, M. R. Sprague, P. S. Michelberger, X.-M. Jin, D. G. England, and I. A. Walmsley, “Enhancing multiphoton rates with quantum memories,” *Physical Review Letters* **110**, 133601 (2013).
- [274] D. A. Kalashnikov, A. V. Paterova, S. P. Kulik, and L. A. Krivitsky, “Infrared spectroscopy with visible light,” *Nature Photonics* **10**, 98–101 (2016).
- [275] S. G. Johnson and J. D. Joannopoulos, “Block-iterative frequency-domain methods for Maxwell’s equations in a planewave basis,” *Optics Express* **8**, 173–190 (2001).
- [276] A. F. Oskooi, D. Roundy, M. Ibanescu, P. Bermel, J. D. Joannopoulos, and S. G. Johnson, “Meep: A flexible free-software package for electromagnetic simulations by the FDTD method,” *Computer Physics Communications* **181**, 687–702 (2010).
- [277] K. C. Huang, E. Lidorikis, X. Jiang, J. D. Joannopoulos, K. A. Nelson, P. Bienstman, and S. Fan, “Nature of lossy Bloch states in polaritonic photonic crystals,” *Physical Review B* **69**, 195111 (2004).
- [278] I. B. Udagedara, I. D. Rukhlenko, and M. Premaratne, “Complex- ω approach versus complex- k approach in description of gain-assisted surface plasmon-polariton propagation along linear chains of metallic nanospheres,” *Physical Review B* **83**, 115451 (2011).
- [279] S. Ha, A. A. Sukhorukov, K. B. Dossou, L. C. Botten, C. M. D. Sterke, and Y. S. Kivshar, “Bloch-mode extraction from near-field data in periodic waveguides,” *Optics Letters* **34**, 3776–3778 (2009).
- [280] A. F. Oskooi, L. Zhang, Y. Avniel, and S. G. Johnson, “The failure of perfectly matched layers, and towards their redemption by adiabatic absorbers,” *Optics Express* **16**, 11376–11392 (2008).

Appendix A

Details and methods of the simulations

In this appendix, I describe the details regarding the use of numerical codes for solving the Maxwell's equations, that were utilized in this work for finding the band diagram and the field profile of the modes, along with performing nonlinear simulations. The Mode Analysis engine of COMSOL is used only once in this work to find the band diagram and field profile of the LN ridge WG. The use of COMSOL for finding modes of a ridge WG is straightforward, and its description can be found in its user guide [205]. Two freely available software packages are mainly used throughout this work: The MPB eigenvalue solver [275] and the Meep FDTD code [276]. I will describe the details of using these two codes for simulations in this work, with a focus on the FDTD method, as most of the simulations in this work are done with it.

On the quasi-normal Bloch modes of the system and finding them

The eigenmodes of periodic WGs used in this work are quasi-normal Bloch modes (QNBM) [221], where the propagation of modes along the propagation direction is governed by the Floquet-Bloch boundary condition with a complex-valued wave-vector in general, and in the transverse direction to the WG there are open boundary conditions. In the work by Lecamp et al. [221], where this basis was introduced, QNBMs refer to all eigenmodes that are surrounded by an open boundary condition, which numerically is implemented through a choice of the perfectly-matched-layer (PML) boundary condition. These eigenmodes can be classified based on how the specific choice of PML properties affects them. One category consists of the continuum of the radiation modes that is discretized in the presence of PMLs. These modes strongly depend on the PML properties. The other category are the modes that are not sensitive to the choice of the PMLs and can be thought of as the true modes of the WG structure. These modes can be bound, leaky, or in general decaying with a complex wave-vector. This includes evanescent modes that do not carry power. In this work, the term QNBM is used to refer only to this second category of modes, that are not affected by the choice of the PMLs.

Although the above QNBM definition includes all the different types of modes dealt with throughout this work, a universal numerical method is not used in this work for finding different types of modes. For finding the band diagram and field profile of the evanescent modes of a 1D periodic stack, used in chapter 5 for analyzing atom-mediated SPDC, an exact analytical formulation is used, which is explained in appendix C. For finding the band diagram of a mode near the band edge that suffers from material absorption, used in section 3.4, a perturbative analytical method was used, which is

explained in that section. For finding the QNBMs in chapter 2, which include the fully guided modes and also leaky modes, numerical simulations using MPB and Meep are used. The MPB eigenvalue solver [275] is only suited for finding fully guided and lossless modes of a structure with Floquet-Bloch boundary condition on all its domain boundaries. The Meep FDTD code [276], which is a time-domain solver, can in principle find all manners of QNBMs with real- or complex-valued wave-vectors, with a surrounding open boundary condition. For the most part FDTD is used in chapter 2, as in addition to being able to find the leaky mode, it is also a quicker solver compared to MPB when one has a specific target frequency. MPB is mainly used to find a large number of real- k modes over a large frequency range without missing any.

A note on material dispersion

In all the designs of the LN periodic WGs with MPB and FDTD, two different sets of refractive indices are used for finding the modes at the FH and the SH frequencies, and the material dispersion around each of the frequencies is neglected. This is a good approximation, considering that the modal dispersion of a periodic structure dominates that of the material over small frequency ranges. The reason for doing this is that the material dispersion cannot be taken into account with MPB, and taking it into account with FDTD makes the simulation slower. With COMSOL, used for the LN ridge WG, it is straightforward to take into account material dispersion, as it is a frequency-domain solver.

MPB eigensolver

MPB is an eigenvalue solver, that uses the plane-wave-expansion method to find the eigenmodes of a structure with periodic boundary conditions. It is capable of finding real-valued eigenfrequencies, where the periodic boundary condition on the boundaries of the system's unitcell is set by a real-valued wave-vector. For every given k , that sets the boundary condition, the method finds a set of eigenfrequencies, corresponding to the Bloch modes of the system with the said wave-vector. This solver is only capable of finding the fully guided modes for a lossless system with a real-valued permittivity, and is not capable of finding evanescent or lossy modes, which have complex-valued wave-vectors. MPB can be used to find lossless guided modes under the light line, especially if there are a number of them to be found over a large frequency range without missing any, such as the band diagram shown in Fig. 2.2(b). To find fully-guided modes using MPB, a supercell is chosen, such that it is large enough in the yz -plane that a guided mode that is confined to the center of the supercell has very little of the tail of its field profile reaching the supercell's transverse boundaries. The Floquet-Bloch boundary condition is then set along the x -direction with k as the wave-vector. Periodic boundary conditions must also be set on the y - and z -directions, as MPB requires it, but they are inconsequential, as long as we are only interested in finding fully guided modes with negligible fields at the transversal edges of the supercell.

MPB can also be used to find the partial gap of the PCSW, such as shown in Fig. 2.6(b), as it will find all the propagating modes of the PC slab and surrounding air, projected along the x -direction. These modes should theoretically form a continuous region in the projected band diagram, but the

finite-sized yz -extent of the supercell will discretize these bands. The exact positions of the dots corresponding to the modes of air and slab really depend on the yz -extent chosen for the supercell in the simulation, as these modes are extended over the whole volume of the supercell. The guided mode band is independent of the supercell yz -size, as it has a confined profile in the yz -plane. Hence, if the yz -extent of the supercell is chosen large enough for the guided mode's profile to decay sufficiently at the supercell's boundaries, the guided mode band will be independent of it. Moreover, with a large yz -extent for the supercell, there will be a dense packing of the air and slab modes in the projected band diagram, such as shown in Fig. 2.6(b), which allows us to clearly identify the partial gap region.

Meep FDTD

FDTD is a time-domain solver of the Maxwell's equations, which is used in this work for finding the band diagram of fully guided and leaky modes, and also performing the nonlinear simulations. If we have a certain target frequency range, the FDTD code in Meep is a more efficient method compared to the eigenvalue solver in MPB for finding fully guided modes. This is because MPB has to find all the eigenfrequencies below the target frequency before getting to it, which could make the simulation very time consuming. FDTD on the other hand, as will be explained below, can target a frequency range of interest by using a pulsed excitation. For this reason, most of the band diagrams in this work are found using FDTD, except when the target is the band diagram for a large number of lossless guided modes, for which MPB is used. FDTD is also used here for finding the band diagram and field profile of leaky modes above the light line. For this, two different methods will be used, called the complex- ω and the complex- k methods, both of which will be explained and compared here. Moreover, the correct use of PMLs for properly normalizing leaky QNBMs will be explained. Finally, FDTD is used for the direct nonlinear SHG simulations in the undepleted-pump approximation, as was explained in chapter 3. Here, some extra details will be added to that explanation.

Finding complex- ω -real- k modes using a pulsed excitation

In this method, a pulse is excited inside the supercell, positioned spatially where the mode has the strongest field profile. The supercell has Floquet-Bloch boundary condition on its boundaries along the propagation direction, set by a real-valued wave-vector, and it has PML boundary conditions on its transverse boundaries. The pulse excites all modes within its spectral bandwidth. The system evolves for some time after the pulse, during which only the true modes of the system survive. The fully guided modes will have a constant amplitude during this evolution, and the lossy/leaky modes will have a decaying amplitude over time. By analyzing the time-dependent field in the supercell, done automatically by Meep, complex-valued frequencies $\omega = \omega' + i\omega''$ and amplitudes can be found for the modes. The fully confined modes will have a real-valued ω , and lossy/leaky modes will have a complex-valued ω . This method is referred to as the complex- ω method in this work. The main use of this method in this work is to find the band diagram and field profile of fully guided modes under the light line, with real-valued wave-vectors and real-valued frequencies. This includes most of the band diagrams and field profiles found for the FH modes or the signal and idler modes shown in chapter 2. The modes with a complex-valued frequency that are found here, corresponding to leaky

or lossy modes, are not exactly the QNBMs, although they are similar for low loss modes [277, 278]. The desired QNBMs have real-valued frequencies and complex-valued wave-vectors, and they are found using a complex-k method.

Finding complex-k-real- ω modes using CW excitation

To find complex-k-real- ω modes with FDTD, one can excite the structure from one end using a CW source, and use a Bloch-mode-extraction algorithm [279] on the resulting field to find the complex wave-vector and field profile of all the modes that were excited at that frequency. In this method, the PCSW must be long enough to provide enough detail in the spatial-frequency domain that is required for finding the complex-valued wave-vectors accurately, which for our purposes this happens to be in the order of a hundred periods long. In this work, a type of Bloch mode extraction is used, although in a less elaborate way, such that when the PCSW is excited, only the mode of interest is dominantly excited. I use two similar ways of implementing this. The first method is as follows: If we know the field profile of the mode, which could be found approximately from the complex- ω simulation, we can excite the PCSW from one end with a CW source that has the same spatial profile. This dominantly excites our mode of interest, which will then propagate and look like Fig. 2.9(b). We can then take a Fourier transform from the complex-valued field along the propagation direction, and find the real part of the wave-vector of the mode k' . To find the imaginary part k'' , we can fit the decaying exponential function $e^{-k''x}$ to the field envelope and find the k'' that results in the best fit. In this way, the band diagram of the pump mode of the W1 PCSW shown in Fig. 2.9(a) is found. The second method can be done without using any specific knowledge from the complex- ω simulation. We can first excite the structure from one end with a CW source of a certain frequency ω with a spatial profile that can excite all our modes of interest, but this does not have to be a dominant excitation for a specific mode and can include many modes. We then take a Fourier transform from the field profile along the propagation direction, which will show the k' of all the modes that were excited. We then pick a k' corresponding to a mode we want to focus on, create a line source over a finite length along the propagation direction with the spatial profile $e^{ik'x}$ and a region after that where there is no source, and run a simulation with a CW source of the same frequency with this extended spatial profile. This extended line source is phase-matched to our mode of interest, and its purpose is to dominantly excite the mode, and after the line source ends at some point, our dominantly excited mode of interest will start decaying. From this decay we can find its k'' . This method is used to find the band diagram of the pump mode of the double-slot PCSW shown in Fig. 2.12(c). Although for the most cases with leaky modes here, it happens that the k' found from the complex-k case is very close to the real-valued k of the complex- ω simulation, so the k' of a leaky mode can already be found efficiently using the complex- ω simulation. Hence, the main purpose of both these complex-k methods is finding the k'' of the leaky mode. Finally, the profile of the mode in the decaying region will be that of the QNBM of interest. Although in this way, a large transversal extent of the infinitely extended leaky mode cannot be easily reproduced, and the mode profile can only be found accurately in and around the line defect, which does the job for most of the calculations of this work, especially for finding the Bloch harmonics of the mode.

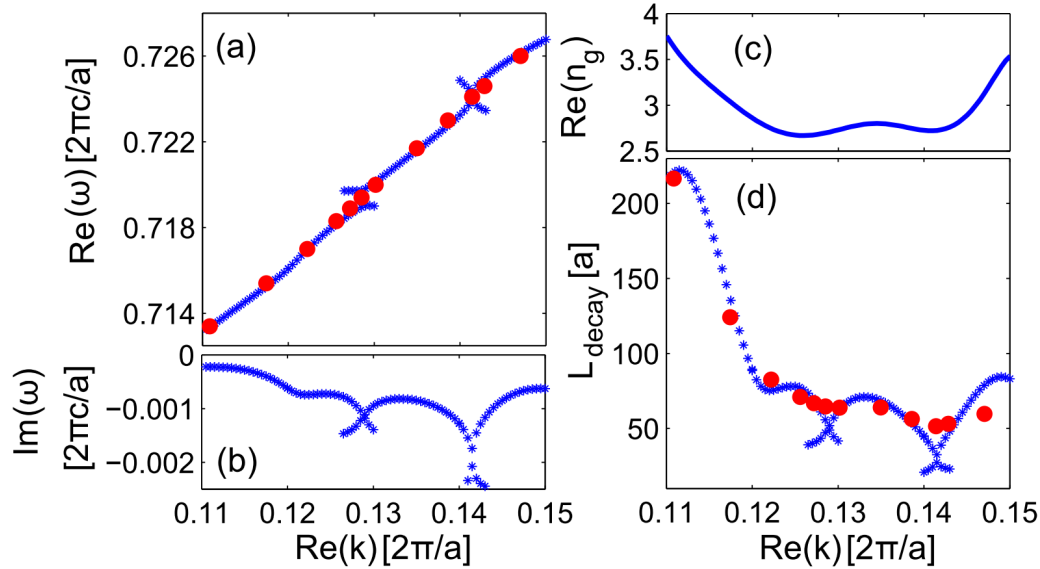


Figure A.1: (a) Band diagram of the TE₀₂ mode of the W1 PCSW around the SH frequency. The blue crosses are the complex- ω band. The red solid circles are from the complex- k method; (b) The imaginary part of frequency of the mode from the complex- ω method; (c) $\text{Re}[n_g]$ from the complex- k band; (d) L_{decay} of the mode, found from the complex- k method and the approximation from the complex- ω method.

Comparing the complex- ω and the complex- k method

It is evident that the complex- ω method, which needs only a supercell as the simulation domain, is much more efficient than the complex- k method, which needs a long PCSW. But we cannot always use the complex- ω method instead of the complex- k method, as the results of the two methods actually refer to two different physical situations, which only have exactly equivalent results for lossless guided modes with real-valued wave-vectors and real-valued frequencies [277, 278]. This allows us to find all the band diagrams and field profiles of the fully guided QNBMs under the light line using the efficient complex- ω method. For accurately finding the QNBM modes above the light we use the complex- k method as explained. However, the complex- ω method can find approximate results for the bands above the light line, which could be a starting point for the complex- k simulations as explained. Especially if a mode has low leakage, or equivalently a long decay length, the complex- ω method can predict the results of the complex- k simulations with good approximations. Here we show where this could be a good approximation by making a comparison between the results of the two case for the TE₀₂ mode of the W1 PCSW, whose complex- k band was shown in Fig. 2.9(a). The real and imaginary parts of the frequency found from the complex- ω method are shown in Figs. A.1(a) and (b), respectively. One could with a good approximation, relate the complex frequency to the decay length, using the real part of the group index through the relation $L_{\text{decay}} = -c/n'_g \omega''$, where $n'_g = \text{Re}[n_g] = c \frac{dk'}{d\omega}$ is found from the complex- k band diagram [277]. Although if one only has done the complex- ω simulation, one will not have access to the n_g from the complex- k method, but nonetheless here we have both cases and we follow the recipe of Ref. [277] for making the comparison. Because we have few points for the complex- k band, we fit a polynomial to the points, from which we can get the derivative. The result is shown in Fig. A.1(c). From this, we find the decay length predicted by the complex- ω simulation, shown in Fig. A.1(d), overlapped with the decay length found from the complex- k for comparison. By looking at Figs. A.1(a) and (d), we see that the complex- ω method predicts the complex- k results very closely, except for places where the complex- ω band exhibits

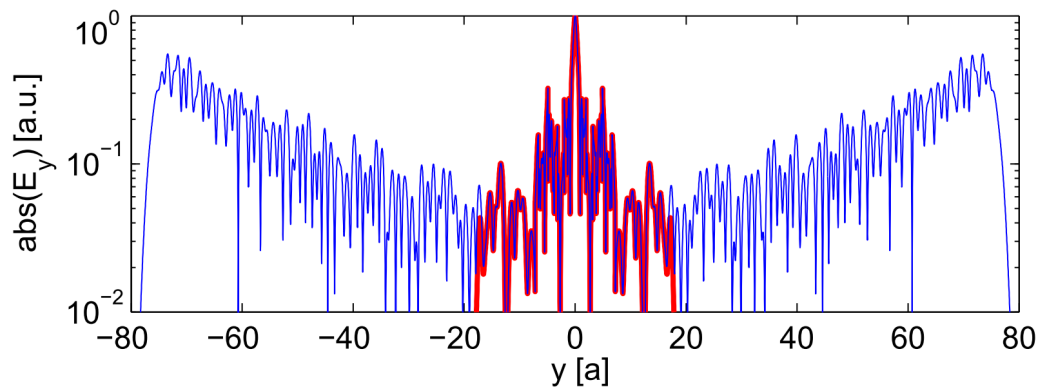


Figure A.2: Absolute value of the E_y field component of the leaky SH mode, on the $x = 0.5a, z = 0$ line, comparing the steady state field profile for two different supercell sizes of $40a$ and $160a$ in the y -direction.

frequency splitting in the band. At these places the complex- k band shows a smoother band diagram. Consequently, if we are looking for a complex- k band, for which we know there are no places of band splitting, which in general would be places of high losses and short decay lengths, we can rely on the predictions of the complex- ω method as a good approximation of the complex- k modes.

The conclusion from this analysis is that, one can even use the complex- ω method as a computationally efficient way of finding the SH/pump bands with a very good approximation, assuming that we are looking for low leakage modes, which are indeed what we are interested in for the pump. This means we can optimize a design for reaching phase-matching in a computationally efficient way using the complex- ω method. Once we are settled on a design, then we can find the band diagram of the leaky pump mode more accurately using the complex- k method, which is computationally more demanding.

Considerations in finding a leaky mode's field profile

For finding the field profile of leaky QNBMs over small regions around the line defect, we can use the complex- k method. However, finding the field over a large transversal dimension, which is wanted for observing the rising tail of a leaky QNBM, would require a long propagation direction together with a large transversal extent of the simulation domain, making the simulation not practical. For this, we use the complex- ω as an approximation in finding the field. To find the field profile with the complex- ω method, a narrow frequency-bandwidth pulse centered around the QNBM frequency, is excited in a supercell with the periodic boundary condition set by k' . After the pulse ends, enough time is given to the leaky mode to radiate and reach steady state. Steady state here for the leaky mode has a slightly different definition compared to a lossless mode. For a leaky QNBM, steady state is reached when the Bloch mode field profile $\mathbf{e}(\mathbf{r})$ is not changing any longer, and it is only the amplitude envelope of the field that decays along the propagation direction with $e^{-k''x}$. For a complex- ω leaky mode this amplitude decays in time with $e^{\omega''t}$, where ω'' is a negative number. The mode found in this way, is the solution to the source-free wave equation in the given geometry. The Bloch mode profile found from this method, for a supercell of size $160a$ in the y -direction, was shown in Fig. 3.3. To verify that this is indeed a steady state profile, the field profile for the same mode is found in a supercell with a different transverse dimension of $40a$ in the y -direction. The absolute value of the fields are plotted on a line for both cases of $40a$ and $160a$ supercells in Fig. A.2, which shows the exponentially rising tail, looking linear in a logarithmic plot. It also shows that the two field profiles

found using two different simulations match exactly over the domain they have in common, verifying that the fields are indeed the steady-state profiles.

Analogy between QNMs and QNBMs for describing the origin of the rising tail of the field

The problem of dealing with leaky modes has attracted much attention in recent years in the field of nano-optics in studying the dynamics of nano-resonators and cavities [198, 199, 235, 236, 237]. Quasi-normal modes (QNMs), introduced by Leung et al. [229], are used as the basis for modal expansion in open resonators, where eigenmodes have complex-valued frequencies as their eigenvalue. A type of analogy can be made, between the QNMs of a resonator and the leaky QNBMs of a PCSW, to help us explain the rising tail of the field profile of the leaky QNBMs through the more well-understood QNMs of a cavity. The QNM with a complex-valued frequency is a leaky mode that is mainly concentrated in the cavity region and the leaky QNBM with a complex-valued wave-vector is concentrated in the line defect region. QNMs are mainly concentrated in and around the cavity area, and have rising radiation tails away from the cavity. This is understood by imagining the resonator starting with a very large field amplitude that is concentrated in the cavity region, and then this field amplitude will gradually decrease through radiation, and this radiation will accumulate in regions far away from the cavity. The more time passes, the higher the amplitude of the tail of the mode becomes away from the cavity compared to its center, as more and more radiation accumulates in the tails. One can imagine in a similar way, why a leaky QNBM should have rising tails away from the line defect. If we excite the leaky mode with a large amplitude concentrated near the line defect, as the mode propagates, more of the field will leak towards and accumulate in the tails of the mode in the transverse directions, while the amplitude of the mode in the line defect region reduces. In this way, the mode approaches its steady state profile.

A more quantitative explanation can also be given to explain the rising tail, following what is done with QNMs, based on why a complex-valued eigenfrequency that reduces the amplitude of the mode in time should result in an exponentially rising field profile away from the resonator [235, 198]. We do this for QNBMs, and explain why a complex-valued wave-vector for the mode that decays the amplitude of the mode along the propagation direction should result in an exponentially rising field profile away from the line defect in the transverse direction. The explanation is as follows: Assume we have a leaky QNBM above the light line propagating in the x-direction with the complex-valued wave-vector $\mathbf{k} = (k'_x + ik''_x)\mathbf{x}$ in the first BZ. Assume that it is the 0th BH of this mode with the same wave-vector \mathbf{k} that is coupling to a plane-wave in the surrounding air. This plane-wave in air will have a wave-vector $\mathbf{k}_0 = k_{x_0}\mathbf{x} + k_{z_0}\mathbf{z}$, where $k_{x_0} = k'_x + ik''_x$, as the plane-wave mode must be phase-matched to the QNBM in the x-direction. It is important to note, that both k_{x_0} and k_{z_0} for this plane-wave could be complex-valued quantities, but together they must satisfy the dispersion relation for a plane-wave propagating in air at that frequency $\mathbf{k}_0 \cdot \mathbf{k}_0 = k_{x_0}^2 + k_{z_0}^2 = \frac{\omega^2}{c^2}$. This tells us that $k_{x_0}^2 + k_{z_0}^2$ must be a real number. Let us assume that $k_{z_0} = k'_z + ik''_z$. Hence we get $k_{x_0}^2 + k_{z_0}^2 = (k'_x)^2 - (k''_x)^2 + (k'_z)^2 - (k''_z)^2 + i2(k'_x k''_x + k'_z k''_z)$, which for it to be a real-valued quantity we must have $k'_x k''_x + k'_z k''_z = 0$. In other words, $k'_x k''_x$ must have the opposite sign compared to $k'_z k''_z$. For a QNBM decaying in the +x-direction, we have $k''_x > 0$. If $k'_x > 0$, which means a FP BH is coupling to the radiation, we then have $k'_x k''_x > 0$. Hence, the radiating plane-wave must have $k'_z k''_z < 0$, and this

results in a increasing amplitude in the $\pm z$ -direction for the plane-wave: For the wave in the $+z$ -direction with $k'_z > 0$, propagating on the $z > 0$ side of the line defect, we must have $k''_z < 0$, which means increasing amplitude with $e^{|k''_z|z}$. For the wave in the $-z$ -direction with $k'_z < 0$, propagating on the $z < 0$ side of the line defect, we must have $k''_z > 0$, which means increasing amplitude with $e^{|k''_z|z}$. It is interesting to note, that if we have a BP BH with $k'_x < 0$ in a forward-decaying mode, the same argument will show that the radiating plane-wave will be decaying away from the line defect, not rising. This means that the leaky QNBM will have rising radiation tails if the FP BHs are contributing to the radiation. This matches the intuitive explanation given beforehand: If the radiation is to accumulate in the transverse direction, it has to be radiated forward, such that the early radiations can accumulate on the later radiations. If the radiation is going backward, the later radiations will never reach the early radiations. For the case of the leaky SH mode whose rising field profile in the y -direction is shown in Fig. A.2, the BHs where shown in Fig. 2.10. We can see that both the FP C_0 and C_1 BHs are radiating in the y -direction into the slab, and hence the leaky mode should have a rising tail in that direction.

Use of PMLs for leaky modes

Since we are dealing with a leaky mode at the SH/pump frequency, for the numerical simulations it is essential to use a boundary condition that absorbs the radiation field. There are two solutions that Meep offers for implementing such a boundary condition: the PML and the absorbing boundary conditions. An absorbing boundary is simply an absorbing material with a gradually rising loss. This is an effective solution for having reflectionless boundaries, although one cannot use the fields in the absorbing region for an adjoint flux or adjoint density integral. For that purpose, the PML boundary condition must be used. However, it is known that PMLs do not work properly when a periodic structure is entering them [280]. The solution is, instead of using an infinite number of rows in the transverse direction that makes the rows of holes enter the PMLs, to use a finite number of rows in the transverse direction, after which there exists the unstructured slab, which will also be the case in any realistic experimental scheme. In the case of this work, I usually use 6 – 8 rows of holes on each side of the line defect, which is more than enough to confine the FH/signal/idler modes in the transverse direction through the PC bandgap effect. After these rows, the slab will have no inhomogeneity and PMLs can effectively do their job.

It was mentioned previously, that to get convergent results in calculating the adjoint flux or the adjoint density integrals, appearing in the denominator of Eqs. (3.19) and Eq. (3.21), for leaky QNBMs whose profile is infinitely extended in the transversal direction, the field inside the PML layers must be used. The reason is, that PMLs are complex coordinate transformations on ϵ and μ of the medium, that will preserve the value of such integrals [221, 198]. Especially, if the integrals have no explicit inclusion of ϵ and μ , there is no need to know the actual transformation that created the PML layer, and one can just use the field in the PML for the integral. This is the advantage of using the displacement field in Eq. (3.21). So all we need to know is the electric, magnetic, and displacement fields, which are all output by Meep everywhere, including in the PML region. We also do a test to verify that fields in the PML layer output by Meep are of physical significance. For this, we calculate the complex group index n_g from Eq. (3.15), by using the fields found from both of the $40a$ and $160a$ sim-

ulations, and compare the results. The presence of the large tails of the field in these large supercell simulations ensures that if a wrong method for handling the fields is used, we will get very different values for n_g from the two simulations. However, as a property of the mode, group index calculated from the fields has to remain unchanged in both the cases, and also match the value calculated from the complex- ω band diagram (given that these fields are found from a complex- ω simulation). For the $40a$ and $160a$ supercells we find $n_g = 3.1132 + i1.1923$ and $n_g = 3.1134 + i1.1921$, respectively. These values are very close to each other and to that calculated directly from the complex- ω band diagram, $n_g = 3.1377 + i1.1756$. This test verifies that the fields in the PML layer are correctly used.

Nonlinear FDTD

It was explained in section 3.3, how the nonlinear FDTD simulation is performed for SHG in this work. In essence, the field at the FH is used to generate the nonlinear current source, and that source is used as a volume source to drive the simulation at the SH frequency, which is a method valid under the UPA. Meep is capable of accepting analytical or numerically specified functions to use them as spatial profiles of the source. For the nonlinear simulations, I have used Meep's C++ interface, as C++ seemed a more straightforward interface for feeding matrix variables for the volume source to Meep compared to Meep's Scheme interface. The Scheme interface, which is better documented, has been used for linear simulations for finding the bands and the field profiles of modes. There is an important point in analyzing the results of such nonlinear simulations in Meep, which is how the results are turned into physical units, as Meep itself uses dimensionless variables for simulations [276]. The following transformations should be done to relate dimensionless electric e and magnetic h fields and current j in Meep to physical fields E and H and current J expressed in SI units: If we assume the value of e in Meep is that of the physical electric field E expressed in unit of V/m, then the magnetic field in Meep is related to the physical one by $h = \mu_0 c H$, and the current in Meep is related to the physical one by $j = \mu_0 c a J$, where the variables vacuum magnetic permeability μ_0 , speed of light in vacuum c , and the characteristic length that is used to normalize all the input dimensions in Meep which we always set to the periodicity of the structure a , are all expressed in SI units. These unit transformations should be carried out correctly, so that we can find the generated SH power from this nonlinear simulation in SI units, as shown in Fig. 3.4(d).

Appendix B

Intermediate calculations in the formulation of atom-mediated SPDC

Intermediate calculation steps for finding P of Eq. (5.7)

Here I present the Intermediate calculation steps to get from Eq. (5.6) to Eq. (5.7). Eq. (5.6) is repeated here:

$$P = \sum_{\sigma_i, \sigma_s} \int d^3 \mathbf{r}_s \int_0^\infty d\omega_s \int d^3 \mathbf{r}_i \int_0^\infty d\omega_i \left| \langle f | V^{(1)} | i \rangle \right|^2, \text{ with } V^{(1)} = \frac{-i}{\hbar} \int_{-\infty}^{+\infty} dt \hat{H}_{\text{NL}}(t), \quad (\text{B.1})$$

First step of the calculation is evaluating $\langle f | V^{(1)} | i \rangle$:

$$\begin{aligned} \langle f | V^{(1)} | i \rangle &= \langle 0 | \hat{f}_{\sigma_i}(\mathbf{r}_i, \omega_i) \hat{f}_{\sigma_s}(\mathbf{r}_s, \omega_s) \frac{-i}{\hbar} \int_{-\infty}^{+\infty} dt \hat{H}_{\text{NL}}(t) | 0 \rangle \\ &= \frac{i\epsilon_0}{\hbar} \int_{-\infty}^{+\infty} dt \int d^3 \mathbf{r} \sum_{\alpha, \beta, \gamma} \chi_{\alpha\beta\gamma}^{(2)}(\mathbf{r}) E_{\text{P}, \gamma}(\mathbf{r}, t) \langle 0 | \hat{f}_{\sigma_i}(\mathbf{r}_i, \omega_i) \hat{f}_{\sigma_s}(\mathbf{r}_s, \omega_s) \hat{E}_\alpha^-(\mathbf{r}, t) \hat{E}_\beta^-(\mathbf{r}, t) | 0 \rangle. \end{aligned} \quad (\text{B.2})$$

Substituting $\mathbf{E}_{\text{P}}(\mathbf{r}, t) = \int_0^{+\infty} d\omega_{\text{P}} \mathbf{E}_{\text{P}}(\mathbf{r}, \omega_{\text{P}}) e^{-i\omega_{\text{P}} t}$ and the electric field operators from Eqs. (5.1) and (5.2) into Eq. (B.2) gives:

$$\begin{aligned} \langle f | V^{(1)} | i \rangle &= \frac{-i}{\pi} \sum_{\alpha, \beta, \gamma} \sum_{\beta'} \sum_{\beta''} \int_0^{+\infty} d\omega' \int_0^{+\infty} d\omega'' \int_0^{+\infty} d\omega_{\text{P}} \int_{-\infty}^{+\infty} dt e^{-i(\omega_{\text{P}} - \omega' - \omega'')t} \int d^3 \mathbf{r} \chi_{\alpha\beta\gamma}^{(2)}(\mathbf{r}) \\ &\times E_{\text{P}, \gamma}(\mathbf{r}, \omega_{\text{P}}) \frac{\omega'^2}{c^2} \int d^3 \mathbf{s}' \sqrt{\epsilon''(\mathbf{s}', \omega')} G_{\alpha\beta'}^*(\mathbf{r}, \mathbf{s}', \omega') \frac{\omega''^2}{c^2} \int d^3 \mathbf{s}'' \sqrt{\epsilon''(\mathbf{s}'', \omega'')} G_{\beta\beta''}^*(\mathbf{r}, \mathbf{s}'', \omega'') \\ &\times \langle 0 | \hat{f}_{\sigma_i}(\mathbf{r}_i, \omega_i) \hat{f}_{\sigma_s}(\mathbf{r}_s, \omega_s) \hat{f}_{\beta'}^\dagger(\mathbf{s}', \omega') \hat{f}_{\beta''}^\dagger(\mathbf{s}'', \omega'') | 0 \rangle \\ &= -2i \sum_{\alpha, \beta, \gamma} \sum_{\beta'} \sum_{\beta''} \int_0^{+\infty} d\omega' \int_0^{+\infty} d\omega'' \int d^3 \mathbf{r} \chi_{\alpha\beta\gamma}^{(2)}(\mathbf{r}) E_{\text{P}, \gamma}(\mathbf{r}, \omega' + \omega'') \\ &\times \frac{\omega'^2}{c^2} \int d^3 \mathbf{s}' \sqrt{\epsilon''(\mathbf{s}', \omega')} G_{\alpha\beta'}^*(\mathbf{r}, \mathbf{s}', \omega') \frac{\omega''^2}{c^2} \int d^3 \mathbf{s}'' \sqrt{\epsilon''(\mathbf{s}'', \omega'')} G_{\beta\beta''}^*(\mathbf{r}, \mathbf{s}'', \omega'') \\ &\times \langle 0 | \hat{f}_{\sigma_i}(\mathbf{r}_i, \omega_i) \hat{f}_{\sigma_s}(\mathbf{r}_s, \omega_s) \hat{f}_{\beta'}^\dagger(\mathbf{s}', \omega') \hat{f}_{\beta''}^\dagger(\mathbf{s}'', \omega'') | 0 \rangle, \end{aligned} \quad (\text{B.3})$$

where the expression $\int_{-\infty}^{+\infty} dt e^{-i(\omega_{\text{P}} - \omega' - \omega'')t} = 2\pi\delta(\omega_{\text{P}} - \omega' - \omega'')$ was used, which allows taking the integral over ω_{P} . The expectation value of the combination of the bosonic operators in Eq. (B.3) can

be calculated by using the commutation relations in Eq. (5.4), giving:

$$\begin{aligned}
& \langle 0 | \hat{f}_{\sigma_i}(\mathbf{r}_i, \boldsymbol{\omega}_i) \hat{f}_{\sigma_s}(\mathbf{r}_s, \boldsymbol{\omega}_s) \hat{f}_{\beta'}^\dagger(\mathbf{s}', \boldsymbol{\omega}') \hat{f}_{\beta''}^\dagger(\mathbf{s}'', \boldsymbol{\omega}'') | 0 \rangle \\
&= [\hat{f}_{\sigma_i}(\mathbf{r}_i, \boldsymbol{\omega}_i), \hat{f}_{\beta'}^\dagger(\mathbf{s}', \boldsymbol{\omega}')] [\hat{f}_{\sigma_s}(\mathbf{r}_s, \boldsymbol{\omega}_s), \hat{f}_{\beta''}^\dagger(\mathbf{s}'', \boldsymbol{\omega}'')] + [\hat{f}_{\sigma_i}(\mathbf{r}_i, \boldsymbol{\omega}_i), \hat{f}_{\beta''}^\dagger(\mathbf{s}'', \boldsymbol{\omega}'')] [\hat{f}_{\sigma_s}(\mathbf{r}_s, \boldsymbol{\omega}_s), \hat{f}_{\beta'}^\dagger(\mathbf{s}', \boldsymbol{\omega}')] \\
&= \delta_{\sigma_i \beta'} \delta(\mathbf{r}_i - \mathbf{s}') \delta(\boldsymbol{\omega}_i - \boldsymbol{\omega}') \delta_{\sigma_s \beta''} \delta(\mathbf{r}_s - \mathbf{s}'') \delta(\boldsymbol{\omega}_s - \boldsymbol{\omega}'') \\
&+ \delta_{\sigma_i \beta''} \delta(\mathbf{r}_i - \mathbf{s}'') \delta(\boldsymbol{\omega}_i - \boldsymbol{\omega}'') \delta_{\sigma_s \beta'} \delta(\mathbf{r}_s - \mathbf{s}') \delta(\boldsymbol{\omega}_s - \boldsymbol{\omega}'). \tag{B.4}
\end{aligned}$$

Substituting Eq. (B.4) into Eq. (B.3) and taking the integrals gives:

$$\begin{aligned}
\langle f | V^{(1)} | i \rangle &= -4i \sum_{\alpha, \beta, \gamma} \int d^3 \mathbf{r} \chi_{\alpha \beta \gamma}^{(2)}(\mathbf{r}) E_{P, \gamma}(\mathbf{r}, \boldsymbol{\omega}_i + \boldsymbol{\omega}_s) \\
&\times \frac{\omega_s^2}{c^2} \frac{\omega_i^2}{c^2} \sqrt{\varepsilon''(\mathbf{r}_s, \boldsymbol{\omega}_s) \varepsilon''(\mathbf{r}_i, \boldsymbol{\omega}_i)} G_{\alpha \sigma_i}^*(\mathbf{r}, \mathbf{r}_i, \boldsymbol{\omega}_i) G_{\beta \sigma_s}^*(\mathbf{r}, \mathbf{r}_s, \boldsymbol{\omega}_s), \tag{B.5}
\end{aligned}$$

where the fact was used that $\chi_{\alpha \beta \gamma}^{(2)} = \chi_{\beta \alpha \gamma}^{(2)}$ is valid under the Kleinman's symmetry. Substituting Eq. (B.5) into Eq. (B.1) gives:

$$\begin{aligned}
P &= 16 \int_0^\infty d\omega_s \int_0^\infty d\omega_i \frac{\omega_s^2}{c^2} \frac{\omega_i^2}{c^2} \sum_{\alpha, \beta, \gamma} \sum_{\alpha', \beta', \gamma'} \int d^3 \mathbf{r} \chi_{\alpha \beta \gamma}^{(2)}(\mathbf{r}) \int d^3 \mathbf{r}' \chi_{\alpha' \beta' \gamma'}^{(2)}(\mathbf{r}') \\
&\times E_{P, \gamma'}^*(\mathbf{r}', \boldsymbol{\omega}_i + \boldsymbol{\omega}_s) E_{P, \gamma}(\mathbf{r}, \boldsymbol{\omega}_i + \boldsymbol{\omega}_s) \sum_{\sigma_s} \frac{\omega_s^2}{c^2} \int d^3 \mathbf{r}_s \varepsilon''(\mathbf{r}_s, \boldsymbol{\omega}_s) G_{\beta' \sigma_s}(\mathbf{r}', \mathbf{r}_s, \boldsymbol{\omega}_s) G_{\beta \sigma_s}^*(\mathbf{r}, \mathbf{r}_s, \boldsymbol{\omega}_s) \\
&\times \sum_{\sigma_i} \frac{\omega_i^2}{c^2} \int d^3 \mathbf{r}_i \varepsilon''(\mathbf{r}_i, \boldsymbol{\omega}_i) G_{\alpha' \sigma_i}(\mathbf{r}', \mathbf{r}_i, \boldsymbol{\omega}_i) G_{\alpha \sigma_i}^*(\mathbf{r}, \mathbf{r}_i, \boldsymbol{\omega}_i). \tag{B.6}
\end{aligned}$$

To simplify this result more, the following GF identity is used [256]:

$$\sum_j \frac{\omega^2}{c^2} \int d^3 \mathbf{s} \varepsilon''(\mathbf{s}, \boldsymbol{\omega}) G_{\alpha j}(\mathbf{r}, \mathbf{s}, \boldsymbol{\omega}) G_{\beta j}^*(\mathbf{r}', \mathbf{s}, \boldsymbol{\omega}) = \text{Im} [G_{\alpha \beta}(\mathbf{r}, \mathbf{r}', \boldsymbol{\omega})]. \tag{B.7}$$

This simplifies Eq. (B.6) to the result in Eq. (5.7):

$$\begin{aligned}
P &= 16 \int_0^\infty d\omega_s \int_0^\infty d\omega_i \frac{\omega_s^2}{c^2} \frac{\omega_i^2}{c^2} \sum_{\alpha, \beta, \gamma} \sum_{\alpha', \beta', \gamma'} \int d^3 \mathbf{r} \int d^3 \mathbf{r}' \chi_{\alpha \beta \gamma}^{(2)}(\mathbf{r}) \chi_{\alpha' \beta' \gamma'}^{(2)}(\mathbf{r}') \\
&\times E_{P, \gamma}(\mathbf{r}, \boldsymbol{\omega}_i + \boldsymbol{\omega}_s) E_{P, \gamma'}^*(\mathbf{r}', \boldsymbol{\omega}_i + \boldsymbol{\omega}_s) \text{Im} [G_{\beta' \beta}(\mathbf{r}', \mathbf{r}, \boldsymbol{\omega}_s)] \text{Im} [G_{\alpha' \alpha}(\mathbf{r}', \mathbf{r}, \boldsymbol{\omega}_i)]. \tag{B.8}
\end{aligned}$$

Intermediate calculation steps for finding P_{is} of Eq. (5.9)

Here I present the Intermediate calculation steps to get from Eq. (5.8) to Eq. (5.9). Eq. (5.8) is repeated here:

$$P_{\text{is}} = |\langle f | V^{(3)} | i \rangle|^2, \text{ with } V^{(3)} = \left(\frac{-i}{\hbar}\right)^3 \int_{-\infty}^{+\infty} dt_1 \int_{-\infty}^{t_1} dt_2 \int_{-\infty}^{t_2} dt_3 \hat{H}_{\text{int}}(t_1) \hat{H}_{\text{int}}(t_2) \hat{H}_{\text{int}}(t_3), \tag{B.9}$$

First, $\hat{H}_{\text{int}}(t_1) \hat{H}_{\text{int}}(t_2) \hat{H}_{\text{int}}(t_3)$ is expanded into $[\hat{H}_{\text{NL}}(t_1) + \hat{H}_i(t_1) + \hat{H}_s(t_1)][\hat{H}_{\text{NL}}(t_2) + \hat{H}_i(t_2) + \hat{H}_s(t_2)][\hat{H}_{\text{NL}}(t_3) + \hat{H}_i(t_3) + \hat{H}_s(t_3)]$, which gives 9 different terms. It can be shown that only the ones that

have $\hat{H}_{\text{NL}}(t_3)$ in the last term have a non-zero contribution. This physically means that the SPDC Hamiltonian should act first for the atoms to be excited later. This is the so-called intuitive order [246]. The counterintuitive order in which the atoms are excited before the SPDC takes place will have zero contribution at infinite interaction times. Moreover, we want only terms that result in both signal and idler atoms excited, as only these terms will give us a non-zero contribution. Hence the only terms we have to consider are $[\hat{H}_i(t_1)\hat{H}_s(t_2) + \hat{H}_s(t_1)\hat{H}_i(t_2)]\hat{H}_{\text{NL}}(t_3)$, and in there only the terms that have $\hat{b}_{i,s}^\dagger$. The first step in evaluating Eq. (B.9) would be to eliminate the atomic operators:

$$\begin{aligned}
\langle f|V^{(3)}|i\rangle &= \langle 0|\hat{b}_s\hat{b}_i\left(\frac{-i}{\hbar}\right)^3 \int_{-\infty}^{+\infty} dt_1 \int_{-\infty}^{t_1} dt_2 \int_{-\infty}^{t_2} dt_3 [\hat{H}_i(t_1)\hat{H}_s(t_2) + \hat{H}_s(t_1)\hat{H}_i(t_2)]\hat{H}_{\text{NL}}(t_3)|0\rangle \\
&= \left(\frac{-i}{\hbar}\right)^3 \int_{-\infty}^{+\infty} dt_1 \int_{-\infty}^{+\infty} dt_2 \int_{-\infty}^{+\infty} dt_3 \Theta(t_1 - t_2)\Theta(t_1 - t_3)\Theta(t_2 - t_3) \langle 0|\hat{b}_s\hat{b}_i[e^{i\omega_i t_1}e^{i\omega_s t_2} \\
&\quad \times \hat{b}_i^\dagger \mathbf{d}_i^* \cdot \hat{\mathbf{E}}(\mathbf{r}_i, t_1)\hat{b}_s^\dagger \mathbf{d}_s^* \cdot \hat{\mathbf{E}}(\mathbf{r}_s, t_2) + e^{i\omega_i t_2}e^{i\omega_s t_1}\hat{b}_s^\dagger \mathbf{d}_s^* \cdot \hat{\mathbf{E}}(\mathbf{r}_s, t_1)\hat{b}_i^\dagger \mathbf{d}_i^* \cdot \hat{\mathbf{E}}(\mathbf{r}_i, t_2)]\hat{H}_{\text{NL}}(t_3)|0\rangle \\
&= \left(\frac{-i}{\hbar}\right)^3 \int_{-\infty}^{+\infty} dt_1 \int_{-\infty}^{+\infty} dt_2 \int_{-\infty}^{+\infty} dt_3 \Theta(t_1 - t_2)\Theta(t_1 - t_3)\Theta(t_2 - t_3) \langle 0|[e^{i\omega_i t_1}e^{i\omega_s t_2} \\
&\quad \times \mathbf{d}_i^* \cdot \hat{\mathbf{E}}(\mathbf{r}_i, t_1)\mathbf{d}_s^* \cdot \hat{\mathbf{E}}(\mathbf{r}_s, t_2) + e^{i\omega_i t_2}e^{i\omega_s t_1}\mathbf{d}_s^* \cdot \hat{\mathbf{E}}(\mathbf{r}_s, t_1)\mathbf{d}_i^* \cdot \hat{\mathbf{E}}(\mathbf{r}_i, t_2)]\hat{H}_{\text{NL}}(t_3)|0\rangle, \quad (\text{B.10})
\end{aligned}$$

where Θ is the Heaviside function. The next step is to calculate $\langle 0|\mathbf{d}_i^* \cdot \hat{\mathbf{E}}(\mathbf{r}_i, t_1)\mathbf{d}_s^* \cdot \hat{\mathbf{E}}(\mathbf{r}_s, t_2)\hat{H}_{\text{NL}}(t_3)|0\rangle$, where the only non-zero term comes from the following field operator combinations $\langle 0|\hat{E}^+\hat{E}^+\hat{E}^-\hat{E}^-|0\rangle$:

$$\begin{aligned}
\langle 0|\mathbf{d}_i^* \cdot \hat{\mathbf{E}}(\mathbf{r}_i, t_1)\mathbf{d}_s^* \cdot \hat{\mathbf{E}}(\mathbf{r}_s, t_2)\hat{H}_{\text{NL}}(t_3)|0\rangle &= -\varepsilon_0 \int d^3\mathbf{r} \sum_{\alpha, \beta, \gamma} \chi_{\alpha\beta\gamma}^{(2)}(\mathbf{r}) E_{\text{P}, \gamma}(\mathbf{r}, t_3) \sum_{\sigma_i, \sigma_s} d_{i, \sigma_i}^* d_{s, \sigma_s}^* \\
&\quad \times \langle 0|\hat{E}_{\sigma_i}^+(\mathbf{r}_i, t_1)\hat{E}_{\sigma_s}^+(\mathbf{r}_s, t_2)\hat{E}_{\alpha}^-(\mathbf{r}, t_3)\hat{E}_{\beta}^-(\mathbf{r}, t_3)|0\rangle. \quad (\text{B.11})
\end{aligned}$$

The expectation value in Eq. (B.11) can be evaluated using the identity:

$$\begin{aligned}
&\langle 0|\hat{E}_{\sigma_i}^+(\mathbf{r}_i, t_1)\hat{E}_{\sigma_s}^+(\mathbf{r}_s, t_2)\hat{E}_{\alpha}^-(\mathbf{r}, t_3)\hat{E}_{\beta}^-(\mathbf{r}, t_3)|0\rangle \\
&= [\hat{E}_{\sigma_i}^+(\mathbf{r}_i, t_1), \hat{E}_{\alpha}^-(\mathbf{r}, t_3)][\hat{E}_{\sigma_s}^+(\mathbf{r}_s, t_2), \hat{E}_{\beta}^-(\mathbf{r}, t_3)] + [\hat{E}_{\sigma_i}^+(\mathbf{r}_i, t_1), \hat{E}_{\beta}^-(\mathbf{r}, t_3)][\hat{E}_{\sigma_s}^+(\mathbf{r}_s, t_2), \hat{E}_{\alpha}^-(\mathbf{r}, t_3)] \\
&= 2[\hat{E}_{\sigma_i}^+(\mathbf{r}_i, t_1), \hat{E}_{\beta}^-(\mathbf{r}, t_3)][\hat{E}_{\sigma_s}^+(\mathbf{r}_s, t_2), \hat{E}_{\alpha}^-(\mathbf{r}, t_3)], \quad (\text{B.12})
\end{aligned}$$

where in that last line the fact that $\chi_{\alpha\beta\gamma}^{(2)} = \chi_{\beta\alpha\gamma}^{(2)}$ is used. The following commutation relation is then used, which can be found from Eqs. (5.1), (5.2), (5.4), and (B.7):

$$[\hat{E}_{\alpha}^+(\mathbf{r}, t), \hat{E}_{\beta}^-(\mathbf{r}', t')] = \int_0^{\infty} d\omega \frac{\hbar\omega^2}{\pi c^2 \varepsilon_0} e^{-i\omega(t-t')} \text{Im} [G_{\alpha\beta}(\mathbf{r}, \mathbf{r}', \omega)]. \quad (\text{B.13})$$

Substituting Eq. (B.13) in Eqs. (B.12) and (B.11) and back into Eq. (B.10) and rearranging terms, Eq. (B.10) can be rewritten to get:

$$\begin{aligned} \langle f|V^{(3)}|i\rangle &= \frac{-2i}{\hbar\epsilon_0\pi^2} \sum_{\alpha,\beta,\gamma} \sum_{\sigma_i,\sigma_s} \int d^3\mathbf{r} \chi_{\alpha\beta\gamma}^{(2)}(\mathbf{r}) d_{i,\sigma_i}^* d_{s,\sigma_s}^* \int_0^\infty d\omega' \int_0^\infty d\omega \int_0^{+\infty} d\omega_P \frac{\omega'^2}{c^2} \frac{\omega^2}{c^2} \\ &\times \int_{-\infty}^{+\infty} dt_1 e^{i(\omega_i-\omega)t_1} \Theta(t_1-t_3) \int_{-\infty}^{+\infty} dt_2 e^{i(\omega_s-\omega')t_2} \Theta(t_2-t_3) \int_{-\infty}^{+\infty} dt_3 e^{-i(\omega_P-\omega-\omega')t_3} \\ &\times E_{P,\gamma}(\mathbf{r}, \omega_P) \text{Im} [G_{\sigma_i\beta}(\mathbf{r}_i, \mathbf{r}, \omega)] \text{Im} [G_{\sigma_s\alpha}(\mathbf{r}_s, \mathbf{r}, \omega')]. \end{aligned} \quad (\text{B.14})$$

In the above equation, we have turned the two terms in the expectation value of Eq. (B.10) to one term, while getting rid of the step function $\Theta(t_1-t_2)$. This can be done by exchanging the label of t_1 and t_2 for one of the two terms, which would then produce the same integrand for each term, except that one will have $\Theta(t_1-t_2)$ and the other will have $\Theta(t_2-t_1)$, and summing them up gives $\Theta(t_1-t_2) + \Theta(t_2-t_1) = 1$. This physically means that it does not matter for this coincidence detection scheme which one of the atoms has been excited first. To simplify Eq. (B.14) we take the time integrals first:

$$\begin{aligned} &\int_{-\infty}^{+\infty} dt_1 e^{i(\omega_i-\omega)t_1} \Theta(t_1-t_3) \int_{-\infty}^{+\infty} dt_2 e^{i(\omega_s-\omega')t_2} \Theta(t_2-t_3) \int_{-\infty}^{+\infty} dt_3 e^{-i(\omega_P-\omega-\omega')t_3} \\ &= \int_{-\infty}^{+\infty} dT_1 e^{i(\omega_i-\omega)T_1} \Theta(T_1) \int_{-\infty}^{+\infty} dT_2 e^{i(\omega_s-\omega')T_2} \Theta(T_2) \int_{-\infty}^{+\infty} dt_3 e^{-i(\omega_P-\omega_i-\omega_s)t_3} \\ &= \zeta(\omega_i-\omega) \zeta(\omega_s-\omega') 2\pi\delta(\omega_P-\omega_i-\omega_s), \end{aligned} \quad (\text{B.15})$$

where $\zeta(\omega) = \pi\delta(\omega) + iP\frac{1}{\omega} = \int_{-\infty}^{+\infty} dt e^{i\omega t} \Theta(t)$ is the Fourier transform of the step function. P in this formula is the Cauchy's principal value. Substituting Eq. (B.15) back into Eq. (B.14) we can take the integrals over the frequency. We use the following GF identity for taking integrals involving $\zeta(\omega)$:

$$\int_0^\infty d\omega \zeta(\omega_0-\omega) \text{Im} [G_{\alpha\beta}(\mathbf{r}, \mathbf{r}', \omega)] = -i\pi G_{\alpha\beta}(\mathbf{r}, \mathbf{r}', \omega_0). \quad (\text{B.16})$$

The result of taking the frequency integrals is:

$$\begin{aligned} \langle f|V^{(3)}|i\rangle &= \frac{4i\pi}{\hbar\epsilon_0} \frac{\omega_s^2}{c^2} \frac{\omega_i^2}{c^2} \sum_{\alpha,\beta,\gamma} \sum_{\sigma_i,\sigma_s} d_{i,\sigma_i}^* d_{s,\sigma_s}^* \\ &\times \int d^3\mathbf{r} \chi_{\alpha\beta\gamma}^{(2)}(\mathbf{r}) E_{P,\gamma}(\mathbf{r}, \omega_i + \omega_s) G_{\sigma_i\beta}(\mathbf{r}_i, \mathbf{r}, \omega_i) G_{\sigma_s\alpha}(\mathbf{r}_s, \mathbf{r}, \omega_s). \end{aligned} \quad (\text{B.17})$$

This is then used to write the expression for $P_{\text{is}} = |\langle f|V^{(3)}|i\rangle|^2$, which results in Eq. (5.9):

$$P_{\text{is}} = \left| \frac{4\pi}{\hbar\epsilon_0} \frac{\omega_s^2 \omega_i^2}{c^4} \sum_{\alpha,\beta,\gamma} \sum_{\sigma_i,\sigma_s} d_{i,\sigma_i}^* d_{s,\sigma_s}^* \int d^3\mathbf{r} \chi_{\alpha\beta\gamma}^{(2)}(\mathbf{r}) E_{P,\gamma}(\mathbf{r}, \omega_i + \omega_s) G_{\sigma_i\beta}(\mathbf{r}_i, \mathbf{r}, \omega_i) G_{\sigma_s\alpha}(\mathbf{r}_s, \mathbf{r}, \omega_s) \right|^2. \quad (\text{B.18})$$

Appendix C

Green's function of an infinite periodic waveguide

Analytical evaluation of the Green's function based on the QNBMs

An external polarization source $\mathbf{P}_{\text{ex}}(\mathbf{r}, \omega)$ excites the system according to the wave equation, such that $\left[(\nabla \times \nabla \times) - \frac{\omega^2}{c^2 \epsilon_0} \epsilon \right] \mathbf{E}(\mathbf{r}, \omega) = \frac{\omega^2}{c^2 \epsilon_0} \mathbf{P}_{\text{ex}}(\mathbf{r}, \omega)$, which can be found from Eq. (3.3), where the nonlinear polarization is substituted with \mathbf{P}_{ex} . The GF of the system satisfies $\left[(\nabla \times \nabla \times) - \frac{\omega^2}{c^2} \epsilon \right] \bar{\mathbf{G}}(\mathbf{r}, \mathbf{r}', \omega) = \bar{\mathbf{I}} \delta(\mathbf{r} - \mathbf{r}')$, hence we can find the electric field of the excited system through:

$$E_\alpha(\mathbf{r}, \omega) = \sum_\beta \frac{\omega^2}{c^2 \epsilon_0} \int d^3 \mathbf{r}' G_{\alpha\beta}(\mathbf{r}, \mathbf{r}', \omega) P_{\text{ex},\beta}(\mathbf{r}', \omega). \quad (\text{C.1})$$

With a specific source of polarization $\mathbf{P}_{\text{ex}}(\mathbf{r}, \omega) = \delta(\mathbf{r} - \mathbf{r}_0) \mathbf{j}$, where \mathbf{j} is the unit vector along x, y, or z, then the electric field it will generate will be $E_\alpha(\mathbf{r}, \omega) = \frac{\omega^2}{c^2 \epsilon_0} G_{\alpha j}(\mathbf{r}, \mathbf{r}_0, \omega)$. Now we will find the electric field in the system generated from this same excitation source, using the unconjugated reciprocity theorem, and by equating the result to what we have just found with the GF approach, we can have an expression for the GF of the system. This is done as follows: If we have a point source $\mathbf{P}_{\text{ex}}(\mathbf{r}, \omega) = \delta(\mathbf{r} - \mathbf{r}_0) \mathbf{j}$, the generated electric field will be of the form:

$$\mathbf{E}(\mathbf{r}, \omega) = \begin{cases} \sum_q A_q^+ \mathbf{E}_q^+(\mathbf{r}, \omega) = \sum_q A_q^+ \mathbf{e}_q^+(\mathbf{r}, \omega) e^{ik_q^+ x}, & \text{for } x > x_0 \\ \sum_q A_q^- \mathbf{E}_q^-(\mathbf{r}, \omega) = \sum_q A_q^- \mathbf{e}_q^-(\mathbf{r}, \omega) e^{ik_q^- x}, & \text{for } x < x_0 \end{cases}, \quad (\text{C.2})$$

where q runs over the QNBMs of the system, and + and - correspond to the forward- and backward-propagating counterpart of a mode, respectively. Since we have a point source at $x = x_0$, we will only have modes propagating forward for $x > x_0$ and modes propagating backward for $x < x_0$. We must find the coefficients A_q for each excited mode. To find them, we use the result of the unconjugated reciprocity theorem of Eq. (3.6):

$$\oint_S (\mathbf{E} \times \mathbf{H}_q^\pm - \mathbf{E}_q^\pm \times \mathbf{H}) \cdot d\mathbf{S} = -i\omega \int d^3 \mathbf{r} \mathbf{E}_q^\pm \cdot \mathbf{P}_{\text{ex}}, \quad (\text{C.3})$$

where the surface integral is over a box that includes the point $\mathbf{r} = \mathbf{r}_0$. For evaluating this, we need the orthogonality relation of QNBMs:

$$\iint_{-\infty}^{+\infty} (\mathbf{e}_m^- \times \mathbf{h}_n^+ - \mathbf{e}_n^+ \times \mathbf{h}_m^-) \cdot \mathbf{x} dy dz = \delta_{nm} \mathcal{F}_n. \quad (\text{C.4})$$

Now we can put the ansatz for the electric field from Eq. (C.2) in Eq. (C.3), one time use the + sign in Eq. (C.3) to find $A_q^- = i\omega E_{q,j}^+(\mathbf{r}_0, \omega) / \mathcal{F}_q$ and another time use the - sign in Eq. (C.3) to find $A_q^+ = i\omega E_{q,j}^-(\mathbf{r}_0, \omega) / \mathcal{F}_q$. Putting these results in Eq. (C.2), we find the α -component of the generated electric field as follows:

$$E_\alpha(\mathbf{r}, \omega) = \begin{cases} \sum_q \frac{i\omega}{\mathcal{F}_q} E_{q,j}^-(\mathbf{r}_0, \omega) E_{q,\alpha}^+(\mathbf{r}, \omega), & \text{for } x > x_0 \\ \sum_q \frac{i\omega}{\mathcal{F}_q} E_{q,j}^+(\mathbf{r}_0, \omega) E_{q,\alpha}^-(\mathbf{r}, \omega), & \text{for } x < x_0 \end{cases} = \frac{\omega^2}{c^2 \epsilon_0} G_{\alpha j}(\mathbf{r}, \mathbf{r}_0, \omega), \quad (\text{C.5})$$

which we put equal to the one found from the GF calculation. We rewrite this GF in a more compact form with Heaviside functions, and we also substitute for \mathcal{F}_q from the group velocity definition of Eq. (3.15). The result is:

$$G_{\alpha\beta}(\mathbf{r}, \mathbf{r}', \omega) = \sum_q [e_{q,\alpha}^+(\mathbf{r}, \omega) e_{q,\beta}^-(\mathbf{r}', \omega) e^{ik_q^+(\omega)(x-x')} \Theta(x-x') + e_{q,\alpha}^-(\mathbf{r}, \omega) e_{q,\beta}^+(\mathbf{r}', \omega) e^{ik_q^+(\omega)(x'-x)} \Theta(x'-x)] \frac{iac}{2\omega} \frac{n_{gq}^+(\omega)}{\int_\Omega d^3\mathbf{r} \epsilon \mathbf{e}_q^+ \cdot \mathbf{e}_q^-}. \quad (\text{C.6})$$

Analytical evaluation of the QNBMs of a 1D periodic waveguide

To evaluate the GF from Eq. (C.6), we need to evaluate the QNBMs of the system first. Here I analytically evaluate the band and the field profile for a 1D periodic waveguide, which is then used in chapter 5 in combination with Eq. (C.6) for evaluating the GF used in the study of atom-mediated SPDC. The 1D periodic structure under study is shown schematically in Fig. C.1(a). This is a periodic stack of two layers $\epsilon(x) = \begin{cases} \epsilon_1, & \text{for } 0 < x < d_1 \\ \epsilon_2, & \text{for } d_1 < x < d_1 + d_2 = a \end{cases}$, with $\epsilon(x) = \epsilon(x+a)$, where $\epsilon_{1,2}$ can be complex-valued quantities. We can then use standard methods for finding the dispersion relation of the Bloch modes of this structure and their electric field profile [267]. To do this analytical calculation, the following electric field ansatz is assumed for a mode:

$$E(x) = \begin{cases} E_1(x) = Ae^{ik_1x} + Be^{-ik_1x}, & \text{for } 0 < x < d_1 \\ E_2(x) = Ce^{ik_2x} + De^{-ik_2x}, & \text{for } d_1 < x < a \end{cases}, \quad (\text{C.7})$$

with $k_{1,2} = \sqrt{\epsilon_{1,2}} \frac{\omega}{c}$. We define $n_{1,2} \equiv \sqrt{\epsilon_{1,2}}$. From this ansatz, using the Maxwell's equation we can find the magnetic field ansatz:

$$H(x) = \frac{1}{i\omega\mu_0} \begin{cases} H_1(x) = ik_1Ae^{ik_1x} - ik_1Be^{-ik_1x}, & \text{for } 0 < x < d_1 \\ H_2(x) = ik_2Ce^{ik_2x} - ik_2De^{-ik_2x}, & \text{for } d_1 < x < a \end{cases}. \quad (\text{C.8})$$

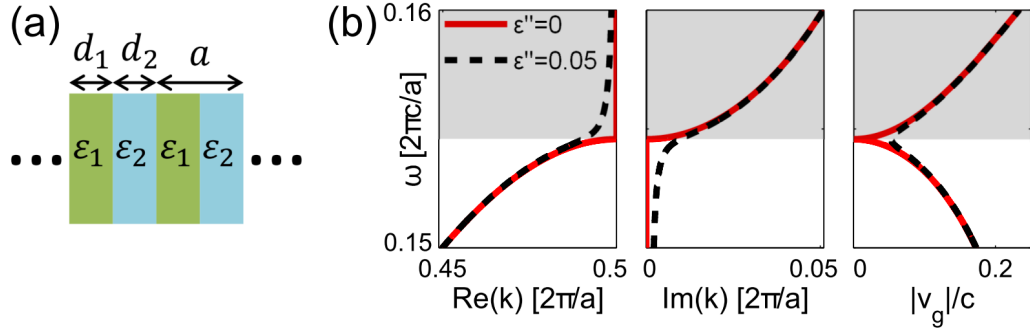


Figure C.1: (a) Schematic of the 1D periodic WG. We assume a structure with $\epsilon_1 = 3 + i\epsilon''$, $\epsilon_2 = 12 + i\epsilon''$, and $d_1 = d_2 = 0.5a$; (b) The band diagram and the group velocity of the mode of the periodic structure with and without loss, incorporated through introducing material absorption $\epsilon'' = 0.05$ and $\epsilon'' = 0$. The gray shaded area is the bandgap region.

We have four boundary condition equations we can use. We have the continuity of the electric and magnetic fields at the point between the two dielectric slabs at $x = d_1$, which gives $E_1(d_1) = E_2(d_1)$ and $H_1(d_1) = H_2(d_1)$. We also have the periodic Floquet-Bloch boundary condition between the start of a unitcell at $x = 0$ and its end at $x = a$ that the ansatzs should satisfy, which gives $E_1(0)e^{ika} = E_2(a)$ and $H_1(0)e^{ika} = H_2(a)$, where k is the complex-valued wave-vector of the QNBM. Putting the ansatzs of Eqs. (C.7) and (C.8) in these four boundary condition equations and rearranging the terms, we can

find a matrix equation $M \begin{bmatrix} A \\ B \\ C \\ D \end{bmatrix} = 0$, where M is a 4×4 matrix whose arrays are a function of $k_1(\omega)$,

$k_2(\omega)$, d_1 , d_2 , and k . To find the non-trivial answer of this set of equations we set $\det|M| = 0$, which gives us an equation that specifies k as a function of k_1 , k_2 , d_1 , and d_2 :

$$\cos(ka) = \cos(k_1 d_1) \cos(k_2 d_2) - \frac{1}{2} \left(\frac{n_1}{n_2} + \frac{n_2}{n_1} \right) \sin(k_1 d_1) \sin(k_2 d_2). \quad (\text{C.9})$$

For a specific structure, we can find $k(\omega)$ numerically from the above equation. With k known, we can find the relation between the $\{A, B, C, D\}$ coefficients:

$$B = -A \frac{2n_2 e^{ika} e^{-ik_1 d_1} - (n_1 + n_2) e^{ik_2 d_2} + (n_1 - n_2) e^{-ik_2 d_2}}{2n_2 e^{ika} e^{ik_1 d_1} + (n_1 - n_2) e^{ik_2 d_2} - (n_1 + n_2) e^{-ik_2 d_2}} \quad (\text{C.10})$$

$$C = A \frac{n_1 + n_2}{2n_2} + B \frac{n_2 - n_1}{2n_2} \quad (\text{C.11})$$

$$D = B \frac{n_1 + n_2}{2n_2} + A \frac{n_2 - n_1}{2n_2} \quad (\text{C.12})$$

By fixing one of these coefficients to an arbitrary value, which in this work is $A = 1$, we can find the other three, being B , C , and D . Having these coefficients means having the Bloch mode profiles.

Numerical evaluation of the Green's function of a 1D periodic waveguide

Here the GF of the 1D periodic WG shown in Fig. C.1(a) is evaluated numerically. This numerically evaluated GF is used in chapter 5, for investigating the effect of loss on the heralding excitation mechanism in the atom-mediated SPDC proposal. The band and the v_g for the mode of this 1D periodic WG around its first bandgap are shown in Fig. C.1(b), for two cases of with and without

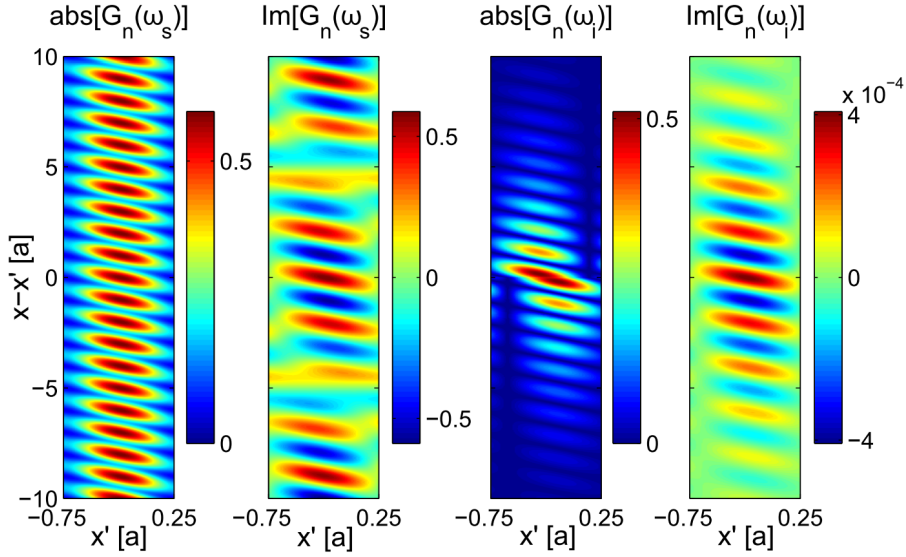


Figure C.2: The absolute and imaginary part of the normalized GF $G_n(x, x', \omega)$ for $\epsilon'' = 0.001$ at $\omega_i = 0.16 \frac{2\pi c}{a}$ and $\omega_s = 0.15 \frac{2\pi c}{a}$. GF is periodic as a function of x and x' and is also a function of the difference between them, hence we plot G_n as a function of x' over one period and an extended $x - x'$.

loss, calculated from Eq. (C.9). It is clear from the band diagram, that without loss there is a sharp transition from the guided part of the mode to the evanescent part in the bandgap. The presence of loss makes the transition less sharp, adding a decay to the guided part of the mode before the bandgap and adding a frequency variation to the $\text{Re}(k)$ in the bandgap region, which is a sign that the evanescent mode in the bandgap is no longer purely evanescent. The electric field profile of the QNBM in this structure is found from Eq. (C.7), where the coefficients B , C , and D are found from Eqs. (C.10) to (C.12). These numerically evaluated band diagram and Bloch mode profiles are then inserted in the expression for a single-mode 1D GF:

$$G(x, x', \omega) = [e^+(x, \omega)e^-(x', \omega)e^{ik^+(\omega)(x-x')} \Theta(x-x') + e^-(x, \omega)e^+(x', \omega)e^{ik^+(\omega)(x'-x)} \Theta(x'-x)] \times \frac{iac}{2\omega} \frac{n_g^+(\omega)}{\mathcal{S} \int_0^a dx \epsilon(x) e^+(x) e^-(x)} \equiv \frac{a}{\mathcal{S}} G_n(x, x', \omega), \quad (\text{C.13})$$

to numerically evaluate the normalized GF G_n for different value of ϵ'' . The 1D GF is found from Eq. (C.6) without the polarization dependencies, where \mathcal{S} is some transverse normalization area perpendicular to the propagation direction. Any volume integral can then be written as $\int d^3\mathbf{r} = \mathcal{S} \int dx$. The normalized Green's function G_n is defined as a unitless quantity that is independent of \mathcal{S} , and can be constructed with periodicity-normalized dimensions and frequencies, which are common variables to use for a periodic structure. The result is shown in Fig. C.2. The absolute value and the imaginary part of the GF for two different frequencies are plotted, with ω_i in the bandgap range and ω_s in the band. With a lossless structure, the in-band and the bandgap modes will be purely guided and evanescent, respectively. Here we plot them for a small amount of loss, so the modes are not purely guided or evanescent anymore, but still retain their guided and evanescent nature for the most part. Firstly, we see that the evanescent mode has a small imaginary part, due to the presence of loss. More importantly, we see that $\text{Im}[G]$ for the lossy evanescent mode is much smaller than its $\text{abs}[G]$, whereas for the guided mode $\text{Im}[G]$ and $\text{abs}[G]$ are of comparable magnitudes.

Abbreviations and conventions

Abbreviations

BH:	Bloch harmonic	S:	Signal
BP:	Backward-propagating	SEM:	Scanning electron microscope
BZ:	Brillouin zone	SFG:	Sum-frequency generation
CP:	Counterpropagating	SFWM:	Spontaneous four-wave mixing
CW:	Continuous wave	SH:	Second-harmonic
DFG:	Difference-frequency generation	SHG:	Second-harmonic generation
DOF:	Degree of freedom	SPDC:	Spontaneous parametric down-conversion
FDTD:	Finite-difference time-domain	TE:	Transverse electric
FH:	Fundamental-harmonic	TH:	Third-harmonic
FP:	Forward-propagating	THG:	Third-harmonic generation
FWHM:	Full-width-at-half-maximum	TIR:	Total internal reflection
GF:	Green's function	TM:	Transverse magnetic
I:	Idler	TWM:	Three-wave mixing
JPS:	Joint phase-matching spectrum	UPA:	Undepleted-pump approximation
JSA:	Joint spectral amplitude	WG:	Waveguide
LN:	Lithium niobate		
P:	Pump		
PC:	Photonic crystal		
PCSW:	Photonic crystal slab waveguide		
PML:	Perfectly-matched-layer		
QNBM:	Quasi-normal Bloch mode		
QNM:	Quasi-normal mode		
QPM:	Quasi-phase-matching		

Conventions

- x :** Bold variables indicate vectors. When specifically used on letters x , y , and z , to give \mathbf{x} , \mathbf{y} , and \mathbf{z} , they refer to unit-vectors of the Cartesian coordinates.
- \hat{x} : The hat sign indicates an operator variable used in quantum mechanical calculations.
- \bar{x} : The bar sign is used on tensorial or matrix variables. This includes variables such as the linear permittivity, nonlinear susceptibility, or the Green's function tensor.
- x^* : This is the complex-conjugate of variable x .
- \hat{x}^\dagger : The dagger sign is used on an operator variable and it refers to its Hermitian conjugate.
- x', x'' : When x is a complex-valued quantity, like wave-vector k or relative permittivity ϵ , then x' is its real part and x'' its imaginary part. When prime and double prime are used on a real-valued quantity, like the position vector \mathbf{r} or sometimes the real-valued frequency ω , it is simply to indicate different variables. This can be recognized from the context.
- $\text{Re}[x], \text{Im}[x]$: Another way of showing the real and imaginary part of x .
- $\hat{x}^\pm(t)$: When $+$ or $-$ signs are the superscript of a time-domain operator $\hat{x}(t)$, they refer to its positive or negative frequency components, respectively.
- x^\pm : When $+$ or $-$ signs are the superscript of non-operator variables, they associate that variable to a forward-propagating or backward-propagating mode, respectively.

Acknowledgement

Coming to fruition of a PhD project requires a hospitable environment. This includes the presence of a wise and supportive supervisor, a group consisting of competent colleagues, a handful of brilliant individuals to bounce your ideas off, and the mood for failing and trying again, the maintenance of which is overall a job for friends and family. My PhD project is no exception. Hence, I would like to express my gratitude to the following people:

- Prof. Thomas Pertsch, who was not only a supervisor to me, but truly a mentor. I could always rely on Thomas for advice and support, and I count myself lucky to have been trained by him.
- Dr. Frank Setzpfandt, who I have worked closely with during my PhD and was effectively a second supervisor to me. From Frank, I learned how to do good science, and most of my great ideas are the result of countless hours of discussion with him.
- Dr. Reinhard Geiss, for the fabrication of the lithium niobate ridge waveguides.
- Dr. Frank Setzpfandt, for guiding me in the construction of the setup for the characterization of the lithium niobate ridge waveguides.
- Matthias Zilk, who taught me how to work with the cluster computer server at our university. I performed most of my numerical simulations using this parallel-computation facility.
- Dr. Shakeeb Bin Hasan, who helped me with using Comsol for the design of ridge waveguides.
- Rafael Quintero-Bermudez, my former master student, for his work on the design of nanobeam structures during his master thesis.
- Prof. Niels Asger Mortensen, in particular for sharing his knowledge on the effect of loss on slow-light modes in periodic structures, and in general for the many interesting discussions we had during his stay in Jena as a guest professor and on many other occasions.
- Prof. Andrey A. Sukhorukov, in particular for suggesting the study of evanescent modes for pair-generation, which eventually resulted in the emergence of the atom-mediated SPDC concept, and in general for our many insightful discussions. I also thank Andrey for hosting my two weeks scientific visit at his group in Australian National University in Canberra, Australia, during which I have worked on the study of evanescent modes.
- Dr. Alexander N. Poddubny from Ioffe Institute in St. Petersburg, Russia, who helped me understand his formulation of the Green's function method for SPDC calculations involving atomic detectors.

- Dr. Falk Eilenberger, Dr. Christoph Menzel, Dr. Thomas Kaiser, Dr. Reinhard Geiss, Dr. Frank Setzpfandt, Benny Walther, Matthias Zilk, Jan Sperrhake, Nils Geib, and others in our group for many useful scientific and many equally useful non-scientific discussions we had over the years.
- Najmeh Abbasirad and Mohammadreza Younesi, my Iranian colleagues, who have made sure my Farsi speaking skills stay at peak performing conditions.
- Dr. Dorit Schmidt and Szilvia Mammel, who on countless occasions guided me through the complicated world of German bureaucracy. I am forever grateful for all their help and care during my studies in Jena.
- Brenda, who during this time brought color to my life.
- My family, who during all my studies supplied me with an endless source of confidence, which was a fuel to my engine and kept it going on non-stop.
- And finally thanks to anyone I unintentionally forgot to mention.

Ehrenwörtliche Erklärung

Ich erkläre hiermit ehrenwörtlich, dass ich die vorliegende Arbeit selbständig, ohne unzulässige Hilfe Dritter und ohne Benutzung anderer als der angegebenen Hilfsmittel und Literatur angefertigt habe. Die aus anderen Quellen direkt oder indirekt übernommenen Daten und Konzepte sind unter Angabe der Quelle gekennzeichnet.

Bei der Auswahl und Auswertung folgenden Materials haben mir die nachstehend aufgeführten Personen in der jeweils beschriebenen Weise unentgeltlich geholfen:

- Dr. Reinhard Geiss von Institut für Angewandte Physik war verantwortlich für die Herstellung der Lithiumniobat-Wellenleitern.
- Prof. Andrey A. Sukhorukov von Australian National University hat mir die Untersuchung des "evanescent modes" für "pair-generation" vorgeschlagen.
- Rafael Quintero-Bermudez hat die Simulationen für die Nanobeam Strukturen als Teil seiner Masterarbeit unter meiner Betreuung gemacht.

Weitere Personen waren an der inhaltlich-materiellen Erstellung der vorliegenden Arbeit nicht beteiligt. Insbesondere habe ich hierfür nicht die entgeltliche Hilfe von Vermittlungs- bzw. Beratungsdiensten (Promotionsberater oder andere Personen) in Anspruch genommen. Niemand hat von mir unmittelbar oder mittelbar geldwerte Leistungen für Arbeiten erhalten, die im Zusammenhang mit dem Inhalt der vorgelegten Dissertation stehen.

Die Arbeit wurde bisher weder im In- noch im Ausland in gleicher oder ähnlicher Form einer anderen Prüfungsbehörde vorgelegt.

Die geltende Promotionsordnung der Physikalisch-Astronomischen Fakultät ist mir bekannt.

Ich versichere ehrenwörtlich, dass ich nach bestem Wissen die reine Wahrheit gesagt und nichts verschwiegen habe.